



RIBLET EFFECTS ON GÖRTLER VORTEX  
DEVELOPMENT OVER A  
CONCAVE SURFACE

DISSERTATION

JAMES A. ROTHENFLUE

AFIT/DS/ENY/96-4

**DISTRIBUTION STATEMENT A**

Approved for public release;  
Distribution Unlimited

DEPARTMENT OF THE AIR FORCE  
AIR UNIVERSITY  
**AIR FORCE INSTITUTE OF TECHNOLOGY**

Wright-Patterson Air Force Base, Ohio

DTIC QUALITY INSPECTED 1

19970214 027

AFIT/DS/ENY/96-4

RIBLET EFFECTS ON GÖRTLER VORTEX  
DEVELOPMENT OVER A  
CONCAVE SURFACE

DISSERTATION

JAMES A. ROTHENFLUE

AFIT/DS/ENY/96-4

Approved for public release: distribution unlimited

AFIT/DS/ENY/96-4

RIBLET EFFECTS ON GÖRTLER VORTEX DEVELOPMENT  
OVER A CONCAVE SURFACE

DISSERTATION

Presented to the Faculty of the School of Engineering  
of the Air Force Institute of Technology

Air University

In Partial Fulfillment of the  
Requirements for the Degree of  
Doctorate of Philosophy in Aeronautical Engineering

JAMES A. ROTHENFLUE

February 1996

Approved for public release: distribution unlimited.

### Acknowledgments

This dissertation is the culmination efforts of many people. Principle among these contributors was my research advisor, Dr. Paul King. His guidance was indispensable throughout all phases of this research. I would also like to thank the members of my research committee, Dr. William Elrod, Dr. Milton Franke, Maj. Glenn Perram, and Dr. Richard Rivir, who endured several long committee meetings and whose individual contributions are too numerous to list here. The entire staff of the AFIT Model Shop is due considerable praise for the craftsmanship they demonstrated in the construction of the Boundary Layer Research Facility. They developed ingenious manufacturing techniques and stretched material limits to turn my rough sketches into a facility which has hopefully just begun to make its contribution to AFIT and the aeronautical research community in general. The AFIT laboratory technicians, led by Mr. Jay Anderson, were always there to bend, twist, cut, break, mend, drill, lift, and otherwise be an extra brain or set of hands on those frequent occasions when my progress ground to a halt.

However, my sincerest gratitude goes to my wife, Lisa, who spent many days and nights alone with our new baby while Dad was cloistered away in the study or putting in extra hours in the laboratory. On countless occasions, she put her own education and research on hold to free me to complete my work. Without her, I would never have completed this project.

JAMES ANDREW ROTHENFLUE

## Table of Contents

	Page
Acknowledgments.....	ii
List of Figures.....	vi
List of Tables.....	ix
List of Symbols.....	x
Abstract.....	xvi
I. Introduction.....	1
Scope.....	1
Objectives.....	2
II. Görtler Theory and Riblet Behavior.....	5
The Görtler Instability.....	5
History.....	5
Physics of the Görtler Instability.....	6
Mathematical Model of the Görtler Instability.....	8
Classical Theory.....	9
Influence of Pressure Gradient and Variable Wall Curvature.....	19
Görtler Vortices in Turbulent Boundary Layers.....	21
Empirical Relationships.....	21
Neutral Curve Location.....	22
Wavelength Selection.....	23
Transition.....	24
Riblet Properties.....	25
Description and General Properties.....	25
Riblet-Boundary Layer Interactions.....	28
Riblet Flat Plate TBL Properties.....	28
Riblet Flat Plate LBL Properties.....	30
Riblet Curved Surface Properties.....	31
Riblet-GV Interaction.....	32
Chapter Summary.....	37
III. Apparatus.....	38
The Boundary Layer Research Facility.....	38
Design Requirements.....	38
BLRF Design.....	39
Air Supply System.....	39
Stilling Chamber.....	41
Nozzle.....	42

Test Section.....	42
Straight Test Section.....	43
Curved Test Section.....	46
BLRF Characterization.....	47
Velocity Range.....	47
Flow Uniformity.....	48
Turbulence and Open Slot Influence.....	48
Data Acquisition Equipment.....	50
LDA Configuration.....	51
Optical.....	51
Electronic.....	52
Central Computer.....	53
Chapter Summary.....	53
IV. Experimental Procedure.....	55
Overview.....	55
Optical Alignment.....	55
Laser Tuning.....	55
Probe Alignment.....	58
BSA Configuration.....	59
Burst Frequency Bandwidth and Number of Samples.....	60
Data Acquisition Mode.....	62
Oversize Rejection.....	63
Hardware Coincidence Filtering.....	64
Software Configuration.....	65
Data Acquisition.....	65
Data Conversion.....	69
Data Transformation.....	69
Data Reduction.....	69
Data Acquisition Conditions and Methodology.....	70
Test Conditions.....	70
Data Collection Method.....	71
Data Analysis and Presentation.....	72
Confidence Interval Calculation.....	72
Outlier Rejection.....	74
Chapter Summary.....	76
V. Discussion of Results.....	77
Overview.....	77
Boundary Layer Transition Locations.....	78
Skin Friction Measurements.....	85
Boundary Layer Perturbation Measurements.....	88
Overview.....	88
Flat/Ribletted Plate.....	89
Curved Smooth Plate.....	92

Curved/Ribletted Plate.....	94
Lower Boundary Layer.....	95
Upper Boundary Layer.....	98
Summary of Results.....	100
Figures.....	104
VI. Conclusions and Recommendations.....	135
Conclusions.....	135
Recommendations.....	136
References.....	138
Appendix A. Component Listing.....	142
Appendix B. BLRF Component Specifications.....	143
Appendix C. Laser Doppler Anemometry - Basic Principles.....	145
Appendix D. Optical to Test Section Coordinate Transformation.....	151
Appendix E. Boundary Layer Turbulence Profiles.....	155
Appendix F. Boundary Layer Velocity Profiles.....	163
Vita.....	171

## List of Figures

	Page
Figure 1. Flow Geometry.....	7
Figure 2. Force Balance on Particle "A".....	8
Figure 3. Sample Shear Layers Over Curved Surfaces.....	9
Figure 4. $O\eta\xi$ and $O\phi\psi$ Coordinate Systems. (Floryan and Saric, 1982).....	10
Figure 5. GV Geometry and Definitions. (Floryan and Saric, 1982).....	15
Figure 6. Görtler Stability Diagram, Fundamental Mode. (Floryan and Saric, 1982).....	17
Figure 7. Lines of Constant $\Lambda$ . (data from Tani and Sakagami, 1964).....	20
Figure 9. Riblet Shapes.....	26
Figure 10. TBL Riblet Vortices from Suzuki and Kasagi (1994): a.) $h^+ = 9.1$ and $s^+ = 15$ , b.) and $h^+ = 19$ and $s^+ = 31$ , reference vector = $0.005U$ . ....	30
Figure 11. Proposed Riblet - GV Interaction.....	33
Figure 12. Test Conditions, Based on $\Lambda_s$ .....	35
Figure 13. BLRF Schematic Overview (PM = Photomultiplier).....	39
Figure 14. Air Supply System Schematic. ....	40
Figure 15. Stilling Chamber Internal Arrangement, Air Travels Left to Right. ....	41
Figure 16. Aluminum Connecting Piece 2-View.....	44
Figure 17. Straight Test Section. ....	45
Figure 18. Flat/Ribletted Plate. ....	45
Figure 19. Curved Test Section Dimensions.....	47
Figure 23. Laser Manipulation - Laser Enters Fiber-Optic Cable at Right. ....	57
Figure 24. 3-D Probe Volume, 2-D Probe at Top, 1-D Probe at Bottom. ....	58
Figure 25. Passing 6 Laser Beams Through Pinhole for Coarse Alignment. ....	59
Figure 26. Velocity Component Oscillations Induced by Streamwise Vortices.....	73
Figure 27. Outlier Examples, $u$ vs. $z$ , Curved/smooth, $U = 7.5$ m/s.....	75
Figure 28. $Tu$ vs. $y$ , flat/ribletted, $U = 7.5$ m/s.....	104
Figure 29. Boundary Layer Peak $Tu$ vs. $x$ , flat/smooth.....	104
Figure 30. Transition Reynolds Number vs. $U$ .....	105
Figure 31. Transition Data Comparison to Method of Michel (1952). ....	105
Figure 32. Average Skin Friction Coefficient vs. $U$ for $x = 105 - 400$ mm. ....	106
Figure 33. Spanwise Shear, $u$ vs. $z$ , flat/ribletted, $x = 105$ mm, $y = 0.5$ mm. ....	106
Figure 34. Spanwise Shear, $u$ vs. $z$ , flat/ribletted, $x = 200$ mm, $y = 0.5$ mm. ....	107
Figure 35. Spanwise Shear, $u$ vs. $z$ , flat/ribletted, $x = 300$ mm, $y = 0.5$ mm. ....	107
Figure 36. Spanwise Shear, $u$ vs. $z$ , flat/ribletted, $x = 400$ mm, $y = 0.5$ mm. ....	108
Figure 37. Spanwise Shear, $u$ vs. $z$ , flat/ribletted, $x = 500$ mm, $y = 0.5$ mm. ....	108
Figure 38. Paired Riblet Valley Vortices Schematic.....	109
Figure 39. Riblet Peak $u$ vs. $y$ , flat/ribletted, $x = 105$ mm. ....	109
Figure 40. Riblet Valley, $u$ vs. $y$ , flat/ribletted, $x = 105$ mm.....	110
Figure 41. $w$ vs. $z$ , flat/ribletted, $y = 0.5$ mm, $x = 105$ mm. ....	110
Figure 42. $w$ vs. $z$ , flat/ribletted, $y = 0.5$ mm, $x = 200$ mm. ....	111
Figure 43. $w$ vs. $z$ , flat/ribletted, $y = 0.5$ mm, $x = 300$ mm. ....	111
Figure 44. $w$ vs. $z$ , flat/ribletted, $y = 0.5$ mm, $x = 400$ mm. ....	112
Figure 45. $w$ vs. $z$ , flat/ribletted, $y = 0.5$ mm, $z = 500$ mm.....	112



Figure 46. v vs. z, flat/ribletted, $y = 0.5$ mm, $x = 105$ mm. ....	113
Figure 47. v vs. z, flat/ribletted, $y = 0.5$ mm, $x = 200$ mm. ....	113
Figure 48. v vs. z, flat/ribletted, $y = 0.5$ mm, $x = 300$ mm. ....	114
Figure 49. v vs. z, flat/ribletted, $y = 0.5$ mm, $x = 400$ mm. ....	114
Figure 50. v vs. z, flat/ribletted, $y = 0.5$ mm, $x = 500$ mm. ....	115
Figure 51. Peak and Valley Comparison, v vs. y, flat/ribletted, $x = 300$ mm. ....	115
Figure 52. Measured GV's, Curved/Smooth Plate. ....	116
Figure 53. u vs. z, curved/smooth, $U \cong 3.5$ m/s, $y = 3.0$ mm. ....	116
Figure 54. u vs. z, curved/smooth, $U \cong 7.5$ m/s, $y = 3.0$ mm. ....	117
Figure 55. u vs. z, curved/smooth, $U \cong 15.0$ m/s, $y = 1.0$ mm. ....	117
Figure 56. v vs. z, curved/smooth, $U \cong 3.5$ m/s, $y = 3.0$ mm. ....	118
Figure 57. v vs. z, curved/smooth, $U \cong 7.5$ m/s, $y = 3.0$ mm. ....	118
Figure 58. v vs. z, curved/smooth, $x = 300$ mm, $U \cong 15.0$ m/s, $y = 1.0$ mm. ....	119
Figure 59. v vs. z, curved/smooth, $x = 400$ mm, $U \cong 14.9$ m/s, $y = 0.5$ mm. ....	119
Figure 60. v vs. z, curved/smooth, $x = 500$ mm, $U \cong 15.1$ m/s, $y = 0.5$ mm. ....	120
Figure 61. w vs. z, curved/smooth, $U \cong 3.5$ m/s, $y = 1.0$ mm. ....	120
Figure 62. w vs. z, curved/smooth, $U = 7.5$ m/s, $y = 1.0$ mm. ....	121
Figure 63. w vs. z, curved/smooth, $U = 15.0$ m/s, $x = 300$ mm, $y = 1.0$ mm. ....	121
Figure 64. w vs. z, curved/smooth, $U = 14.9$ m/s, $x = 400$ mm, $y = 1.0$ mm. ....	122
Figure 65. w vs. z, curved/smooth, $U = 15.1$ m/s, $x = 500$ mm, $y = 1.0$ mm. ....	122
Figure 66. Spanwise Shear, u vs. z, curved/ribletted, $x = 105$ mm, $y = 0.5$ mm. ....	123
Figure 67. Spanwise Shear, u vs. z, curved/ribletted, $x = 200$ mm, $y = 0.5$ mm. ....	123
Figure 68. Spanwise Shear, u vs. z, curved/ribletted, $x = 300$ mm, $y = 0.5$ m/s. ....	124
Figure 69. Spanwise Shear, u vs. z, curved/ribletted, $x = 400$ mm, $y = 0.5$ mm. ....	124
Figure 70. Spanwise Shear, u vs. z, curved/ribletted, $x = 500$ mm, $y = 0.5$ mm. ....	125
Figure 71. Lower Boundary Layer, w vs. z, curved/ribletted, $x = 105$ mm, $y = 0.5$ mm. ....	125
Figure 72. Lower Boundary Layer, w vs. z, curved/ribletted, $x = 200$ mm, $y = 0.5$ mm. ....	126
Figure 73. Lower Boundary Layer, w vs. z, curved/ribletted, $x = 300$ mm, $y = 0.5$ mm. ....	126
Figure 74. Lower Boundary Layer, w vs. z, curved/ribletted, $x = 400$ mm, $y = 0.5$ mm. ....	127
Figure 75. Lower Boundary Layer, w vs. z, curved/ribletted, $x = 500$ mm, $y = 0.5$ mm. ....	127
Figure 76. Lower Boundary Layer, v vs. z, curved/ribletted, $x = 105$ mm, $y = 0.5$ mm. ....	128
Figure 77. Lower Boundary Layer, v vs. z, curved/ribletted, $x = 200$ mm, $y = 0.5$ mm. ....	128
Figure 78. Lower Boundary Layer, v vs. z, curved/ribletted, $x = 300$ mm, $y = 0.5$ mm. ....	129
Figure 79. Lower Boundary Layer, v vs. z, curved/ribletted, $x = 400$ mm, $y = 0.5$ mm. ....	129
Figure 80. Lower Boundary Layer, v vs. z, curved/ribletted, $x = 500$ mm, $y = 0.5$ mm. ....	130
Figure 81. Upper Boundary Layer GV Formation Example. ....	130
Figure 82. Upper Boundary Layer, u vs. z, curved/ribletted, $U \cong 3.5$ m/s, $y = 3.0$ mm. ....	131
Figure 83. Upper Boundary Layer, u vs. z, curved/ribletted, $U \cong 7.5$ m/s, $y = 3.0$ mm. ....	131
Figure 84. v and w vs. z, curved/ribletted, $U \cong 3.5$ m/s, $x = 300$ mm, $y = 3.0$ mm. ....	132
Figure 85. v and w vs. z, curved/ribletted, $U \cong 3.5$ m/s, $x = 400$ mm, $y = 3.0$ mm. ....	132
Figure 86. v and w vs. z, curved/ribletted, $U \cong 3.5$ m/s, $x = 500$ mm, $y = 3.0$ mm. ....	133
Figure 87. v and w vs. z, curved/ribletted, $U \cong 7.5$ m/s, $x = 300$ mm, $y = 3.0$ mm. ....	133
Figure 88. v and w vs. z, curved/ribletted, $U \cong 7.5$ m/s, $x = 400$ mm, $y = 3.0$ mm. ....	134
Figure 89. v and w vs. z, curved/ribletted, $U \cong 7.5$ m/s, $x = 500$ mm, $y = 3.0$ mm. ....	134
Figure 90. Nozzle Top View Shop Drawing. ....	143

Figure 91. Stilling Chamber Stand. ....	144
Figure 92. Doppler Burst as Seen on Oscilloscope. ....	146
Figure 93. Direction of $U_N$ . ....	147
Figure 94. Velocity-Frequency Relationship with Frequency Shift. ....	148
Figure 95. 2-D Fringe Pattern from Two Coherent Beams. ....	148
Figure 96. 3-D Fringe Pattern. ....	149
Figure 97. Laser Probe Angles. ....	151
Figure 98. Laboratory Coordinates. ....	152
Figure 99. LDA Measurement Axes. ....	152
Figure 100. After 1st Rotation. ....	152
Figure 101. Second Rotation. ....	153
Figure 100. Tu vs. y: Curved/Smooth, $U = 3.5$ m/s. ....	155
Figure 101. Tu vs. y: Curved/Smooth, $U = 7.5$ m/s. ....	156
Figure 102. Tu vs. y: Curved/Smooth, $U = 15.0$ m/s. ....	156
Figure 103. Tu vs. y: Flat/Ribletted, $U = 3.5$ m/s, Riblet Peak. ....	157
Figure 104. Tu vs. y: Flat/Ribletted, $U = 3.5$ m/s, Riblet Valley. ....	157
Figure 105. Tu vs. y: Flat/Ribletted, $U = 7.5$ m/s, Riblet Peak. ....	158
Figure 106. Tu vs. y: Flat/Ribletted, $U = 7.5$ m/s, Riblet Valley. ....	158
Figure 107. Tu vs. y: Flat/Ribletted, $U = 15.0$ m/s, Riblet Peak. ....	159
Figure 108. Tu vs. y: Flat/Ribletted, $U = 15.0$ m/s, Riblet Valley. ....	159
Figure 109. Tu vs. y: Curved/Ribletted, $U = 3.5$ m/s, Riblet Peak. ....	160
Figure 110. Tu vs. y: Curved/Ribletted, $U = 3.5$ m/s, Riblet Valley. ....	160
Figure 111. Tu vs. y: Curved/Ribletted, $U = 7.5$ m/s, Riblet Peak. ....	161
Figure 112. Tu vs. y: Curved/Ribletted, $U = 7.5$ m/s, Riblet Valley. ....	161
Figure 113. Tu vs. y: Curved/Ribletted, $U = 15.0$ m/s, Riblet Peak. ....	162
Figure 114. Tu vs. y: Curved/Ribletted, $U = 15.0$ m/s, Riblet Valley. ....	162
Figure 115. u vs. y: Curved//Smooth, $U = 3.5$ m/s. ....	163
Figure 116. u vs. y: Curved/Smooth, $U = 7.5$ m/s. ....	163
Figure 117. u vs. y: Curved/Smooth, $U = 15.0$ m/s. ....	164
Figure 118. u vs. y: Flat/Ribletted, $U = 3.5$ m/s, Riblet Peak. ....	165
Figure 119. u vs. y: Flat/Ribletted, $U = 3.5$ m/s, Riblet Valley. ....	165
Figure 120. u vs. y: Flat/Ribletted, $U = 7.5$ m/s, Riblet Peak. ....	166
Figure 121. u vs. y: Flat/Ribletted, $U = 7.5$ m/s, Riblet Valley. ....	166
Figure 122. u vs. y: Flat/Ribletted, $U = 15.0$ m/s, Riblet Peak. ....	167
Figure 123. u vs. y: Flat/Ribletted, $U = 15.0$ m/s, Riblet Valley. ....	167
Figure 124. u vs. y: Curved/Ribletted, $U = 3.5$ m/s, Riblet Peak. ....	168
Figure 125. u vs. y: Curved/Ribletted, $U = 3.5$ m/s, Riblet Valley. ....	168
Figure 126. u vs. y: Curved/Ribletted, $U = 7.5$ m/s, Riblet Peak. ....	169
Figure 127. u vs. y: Curved/Ribletted, $U = 7.5$ m/s, Riblet Valley. ....	169
Figure 128. u vs. y: Curved/Ribletted, $U = 15.0$ m/s, Riblet Peak. ....	170
Figure 129. u vs. y: Curved/Ribletted, $U = 15.0$ m/s, Riblet Valley. ....	170

## List of Tables

	Page
Table 1. Streamwise Observed Boundary Layer Transition Locations .....	81
Table 2. Summary of Riblet Effects on GV Wavelength and Location. ....	103

## List of Symbols

### Symbol

AFIT	Air Force Institute of Technology
BLRF	Boundary Layer Research Facility
DFT	Discrete Fourier Transform
GV	Görtler Vortex
LBL	Laminar Boundary Layer
LDA	Laser-Doppler Anemometry
LPA	Laser Probe Alignment
OM	Optical Misalignment
OTT	Optical to Test Section
TBL	Turbulent Boundary Layer
T-S	Tollmein-Schlichting
uns.	Unstable Region

### Arabic Symbols

$C_f$	skin friction coefficient, $= 2\tau_w/(\rho U^2)$ , (dimensionless)
$D$	streamwise length of curved wall; (m)
$f$	Doppler frequency; (Hz)
$f_o$	frequency shift of one laser beam
$f_k$	$k$ -th member of discrete frequency spectrum (dimensionless)
$G$	Görtler number; $= (U\theta/\nu)(\theta/R)^{1/2}$ , (dimensionless)
$G_{cr}$	critical Görtler number, (dimensionless)
$G_{tr}$	transition Görtler number, (dimensionless)
$g$	functional form for the $O(\epsilon_c)$ term in expression for metric coefficients, (dimensionless)

$H(Q)$	complex potential function of flow over slightly curved surface, (dimensionless)
$h, h_\phi, h_\psi$	metric coefficients; $=  dQ/dH $ , (dimensionless)
$h$	riblet height; (mm)
$h^+$	non-dimensional riblet height; $= hu_\tau/\nu$ , (dimensionless)
$i$	$(-1)^{1/2}$
$\text{Im}(H(Q))$	imaginary component of complex function $H(Q)$ , (dimensionless)
$k$	enumerator
$L$	reference length scale; (m)
$n$	summation variable
$N$	number of samples
$O$	origin location of $O\eta\xi$ and $O\phi\psi$ coordinate systems
$p$	static pressure; (Pa)
$p_k$	$k$ -th value of discrete power spectrum, (dimensionless)
$\tilde{p}$	static pressure; $p/\rho U^2$ , (dimensionless)
$\tilde{p}'$	disturbance component of static pressure; (dimensionless)
$\hat{p}$	$\psi$ dependent static pressure disturbance component; (Pa)
$\tilde{P}$	base (Blasius) flow static pressure; (dimensionless)
$Q$	complex variable $\eta + i\xi$ , (dimensionless)
$Q(H)$	inverse complex potential function of flow over slightly curved surface, (dimensionless)
$r$	probable error, (dimensionless)
$R$	radius of curvature of concave surface; (m)
$Re_\delta$	Reynolds number wrt $\delta$ ; $= U\delta/\nu$ , (dimensionless)
$Re_x$	Reynolds number wrt $x$ ; $= Ux/\nu$ , (dimensionless)
$Re_{x,tr}$	Reynolds number wrt $x$ at boundary layer transition, (dimensionless)
$Re_\theta$	Reynolds number wrt $\theta$ ; $= U\theta/\nu$ , (dimensionless)

$Re_{\theta, tr}$	Reynolds number wrt $\theta$ at boundary layer transition, (dimensionless)
$ReH(Q)$	real component of complex function $H(Q)$ ; (dimensionless)
$s$	riblet spacing; (m)
$s_F$	fringe pattern spacing; (m)
$s^+$	non-dimensional riblet spacing; $su_\tau/\nu$ , (dimensionless)
$U$	freestream velocity; (m/s)
$u$	velocity in x direction; (m/s)
$u_i$	velocity of the i-th particle; (m/s)
$u_\tau$	friction velocity; $= (\tau_w/\rho)^{1/2}$ ; (m/s)
$u_1$	fluid velocity at element "A's" initial position, $y = y_1$ ; (m/s)
$u_2$	fluid velocity at element "A's" final position, $y = y_2$ ; (m/s)
$u'$	disturbance velocity in x direction from the mean; (m/s)
$\tilde{u}$	velocity in the $\phi$ direction; $= u^*/U$ (dimensionless)
$\tilde{u}'$	velocity perturbation in the $\phi$ direction; (dimensionless)
$u''$	u velocity after second coordinate transformation; (m/s)
$u^*$	velocity in the $\phi$ direction; (m/s)
$\hat{u}$	$\psi$ dependent $\phi$ component of disturbance velocity; (dimensionless)
$\bar{u}_{weighted}$	residence time weighted mean velocity; (m/s)
$U$	freestream velocity; (m/s)
$U_N$	velocity normal to fringe pattern relative to fringes; (m/s)
$\tilde{U}$	Blasius boundary layer solution for velocity in $\phi$ direction; (dimensionless)
$v$	velocity in the y direction; (m/s)
$v'$	disturbance velocity in the y-direction; (m/s)
$v''$	v velocity after 2nd coordinate transformation; (m/s)
$v^*$	velocity in the $\psi$ direction; (m/s)
$\tilde{v}$	velocity in the $\psi$ direction; $= v^*/U$ , (dimensionless)

$\tilde{v}'$	velocity perturbation in the $\psi$ direction; (dimensionless)
$\hat{v}$	$\psi$ dependent $\psi$ component of disturbance velocity; (dimensionless)
$\tilde{V}$	Blasius flow profile in the $\psi$ direction; (dimensionless)
$w$	velocity in the $z$ direction; (m/s)
$w'$	disturbance velocity in the $z$ direction; (m/s)
$w''$	$w$ velocity after 2nd coordinate transformation; (m/s)
$\tilde{w}$	velocity in the $z$ direction; $= w/U$ , (dimensionless)
$\tilde{w}'$	velocity perturbation in the $z$ direction; (dimensionless)
$\hat{w}$	$\psi$ dependent $z$ component of disturbance velocity; (dimensionless)
$x$	streamwise coordinate (m)
$x'$	streamwise coordinate after first rotation; (m)
$x''$	streamwise coordinate after second rotation; (m)
$x_o$	$x$ location corresponding to chordwise location, $\eta_o$ ; (m)
$x_1$	upstream $x$ location for momentum thickness measurement; (m)
$x_2$	downstream $x$ location for momentum thickness measurement; (m)
$y$	normal to surface coordinate (m)
$y^+$	wall unit in $y$ direction; $= yu_\tau/\nu$ , (dimensionless)
$y'$	normal coordinate after first rotation, (m)
$y''$	normal coordinate after second rotation, (m)
$y_1$	initial $y$ station of particle "A"; (m)
$y_2$	final $y$ station of particle "A"; (m)
$z$	spanwise coordinate; (m)
$z^+$	wall unit in $z$ direction; $= zu_\tau/\nu$ , (dimensionless)
$\tilde{z}$	spanwise coordinate; $z/D$ , (dimensionless)

#### Greek Symbols

$\alpha$	GV non-dimensional wavenumber; $= (2\pi\theta)/\lambda$ , (dimensionless)
----------	---

$\beta$	GV spatial amplification rate, (dimensionless)
$\delta$	boundary layer thickness; (m)
$\delta_r$	non-dimensionalized length scale; $(\nu\eta_o/U)^{1/2} \cong (\nu x_o/U)^{1/2}$ ; (m)
$\Delta t_i$	residence time in probe volume of i-th particle; (sec)
$\epsilon_c$	curvature scaling factor; $= D/R$ , (dimensionless)
$\epsilon_v$	viscous scaling factor; $= (\nu/U_\infty L)^{1/2}$ , (dimensionless)
$\eta$	Cartesian coordinate in the chordwise direction; (dimensionless)
$\eta_l$	smallest predicted turbulence scale; (m)
$\eta_o$	particular chordwise location; (m)
$\xi$	Cartesian coordinate in the normal to chordwise direction; (dimensionless)
$\theta$	boundary layer momentum thickness; (m)
$\theta_h$	half angle between laser beams; (radians)
$\theta_{x1}$	momentum thickness at location x1; (m)
$\theta_{x2}$	momentum thickness at location x2; (m)
$\theta_1$	angle between bisector and 1-D probe optical axis; (radians)
$\theta_2$	angle between bisector and 2-D probe optical axis; (radians)
$\rho$	local fluid density; (kg/m <sup>3</sup> )
$\rho_\infty$	freestream fluid density; (kg/m <sup>3</sup> )
$\Lambda$	non-dimensional wavelength parameter; $= (U_\infty \lambda/\nu)(\lambda/R)^{1/2}$ , (dimensionless)
$\Lambda_s$	wavelength parameter of riblet spacing; $= (U_\infty s/\nu)(s/R)^{1/2}$ , (dimensionless)
$\lambda$	vortex wavelength; (m)
$\lambda_L$	laser wavelength (m)
$\mu$	fluid viscosity; (kg/m*sec)
$\nu$	kinematic viscosity; $= \mu/\rho$ ; (m <sup>2</sup> /sec)
$\sigma$	standard deviation
$\tau_w$	shear stress at wall; $= \mu(u_y + v_x)_{y=0} \cong \mu(u_y)_{y=0}$ ; (N/m <sup>2</sup> )



$\phi$	coordinate corresponding to streamlines; (dimensionless)
$\phi_1$	scaled $\phi$ coordinate; (dimensionless)
$\psi$	coordinate corresponding to equipotential lines; (dimensionless)

## Abstract

Riblet effects on Görtler vortex development in laminar and transitional flows were measured using three dimensional laser-Doppler anemometry. Three freestream velocities were tested such that riblet spacing corresponded to Görtler vortex (GV) wavelengths which presumably would be either strongly amplified, weakly amplified, or attenuated by centrifugal forces on a curved surface. Experiments revealed the development of paired, counterrotating vortices within the riblet valleys over both flat and concave surfaces. For riblet spacings equivalent to weakly or non-amplified GV wavelengths, GV development on a curved surface was above the riblets and was delayed by the addition of riblets. The GV wavelength was larger than the riblet spacing, but was approximately the same as for the smooth surface. For the strongly amplified case, streamwise vorticity developed earlier than for the smooth plate and was confined to paired, counterrotating, riblet valley vortices with wavelength equal to the riblet spacing. Boundary layer transition was accelerated by the addition of riblets to the curved surface for the strongly amplified case, but was delayed for the other two cases. Thus, riblets with spacing equal to strongly amplified GV wavelengths accelerate boundary layer transition; whereas, riblet spacings equal to smaller, less strongly amplified or attenuated GV wavelengths delay transition. Surface skin friction was increased in all test cases by the addition of riblets.

# RIBLET EFFECTS ON GÖRTLER VORTEX DEVELOPMENT OVER A CONCAVE SURFACE

## I. Introduction

### 1.1 Scope

The intent of this research is to investigate riblet effects on Görtler vortex wavelength and location in a laminar boundary layer over a concave surface and develop a method by which these effects can be predicted. The centrifugal instability within such a boundary layer is known as the Görtler instability, and the streamwise vortices which develop in response to it are Görtler vortices (GVs). It is proposed that riblets introduce a spanwise periodic disturbance into the boundary layer which will inhibit or reinforce GV development, depending on whether the disturbance wavelength is stable or unstable with respect to Görtler theory.

GVs evolve slowly in the streamwise direction, and are thus a weak disturbance. Despite this weakness, however, Barlow and Johnson (1985) showed that the presence of Görtler vortices increases the local skin friction drag on a surface by up to 20-40% over that of flat plate values. In addition, Floryan (1991) notes that Görtler vortices precipitate premature boundary layer transition to turbulence and increase surface heat transfer, and that the search for effective methods of controlling or eliminating GV's has been underway for several decades. Floryan (1991) also explains that the potential benefits of controlling these vortices extend into several technological areas, including turbomachinery, high lift airfoils, and other devices where laminar boundary layers exist over concave surfaces.

Görtler theory indicates that the rate at which GVs strengthen is a function of their wavelength; thus, if the presence of riblets inhibits or reinforces the most unstable vortex wavelengths, riblets may delay or accelerate GV development. This, in turn may offer a mechanism for controlling certain boundary layer characteristics, including heat transfer, skin friction, and transition location, which are affected by GVs. According to Floryan (1991), there has been some success at controlling GVs using active methods such as boundary layer removal; however, a simple, passive control mechanism such as riblets would be more practical in most engineering applications. The author has found no published experimental research explicitly directed at the riblet-GV interaction.

## 1.2 Objectives

Three objectives were accomplished in the course of this research. First, a predictive model was developed which can be used to predict whether riblets will accelerate or delay GV development and whether they will affect GV wavelength. Second, a wind tunnel was built and 3-D laser-Doppler anemometry (LDA) equipment was installed and configured so that non-intrusive velocity and turbulence measurements could be taken throughout the boundary layer over both smooth and ribletted surfaces. As a test case, the boundary layer over a flat/smooth plate was analyzed and compared to a known solution given in White (1991). The third and final objective was to corroborate the predicted riblet effects by investigating the riblet/Görtler instability interaction. This was achieved by measuring riblet effects on Görtler vortex wavelength and location over the plate. In addition, skin friction and boundary layer transition location over the surface were monitored so that the effects of this particular riblet geometry could be determined.

The riblet-GV interaction was investigated by analyzing zero streamwise pressure gradient boundary layers over curved/smooth, flat/ribletted, and curved/ribletted plates. The flat/ribletted plate tests were performed to provide a baseline from which centrifugally induced flow structures over the curved/ribletted plate could be discriminated from viscous effects. The curved/smooth plate tests were performed to provide a baseline for GV development in the absence of riblets. Although riblet geometry was not varied in this study, the relative size of the riblets with respect to the boundary layer was altered by changing freestream velocity in the test section. The riblets were v-shaped, and were 2.6 mm in height and spaced 3.0 mm apart. The radius of curvature for all curved plates was 1 meter. Three freestream velocities were investigated so that riblet induced perturbation wavelengths were strongly amplified, weakly amplified, and not amplified by boundary layer centrifugal forces, as predicted by Görtler theory for  $U = 15.0, 7.5, \text{ and } 3.5 \text{ m/s}$  respectively, where  $U$  is the freestream velocity at the edge of the boundary layer. Data were obtained at  $x = 105$  (upstream limit of data acquisition in test section), 200, 300, 400, and 500 mm over each plate, where  $x$  is the streamwise distance along the plate measured from the leading edge. These five locations allowed the streamwise evolution of flow structures within the boundary layer to be monitored. In particular, streamwise vortical structures within the boundary layer were compared between the test cases in order to determine riblet effects on centrifugally induced vortex wavelength and location. Turbulence intensity was measured within the boundary layer so that the  $x$  location of transition could be determined. Finally, boundary layer velocity profiles were acquired so that a momentum integral analysis could be applied over a portion of the test plate to

measure the effect of this riblet geometry on surface skin friction. To allow direct comparison of experimental results to existing theoretical predictions (Floryan, 1990), all tests were performed so that no pressure gradient existed over the test surface.

A laser-Doppler anemometer was ideally suited for this research because of the need to obtain non-intrusive, spatially precise, three-dimensional velocity measurements very near the surface, including within riblet valleys. LDA does not require the introduction of a physical probe into the boundary layer, which would disrupt delicate flow structures. In addition, the small size of the laser probe volume (approximately  $150 \times 150 \times 250$  microns) facilitates a high degree of spatial resolution. In addition, laser beam divergence has only a negligible effect on probe volume shape for this laser-Doppler equipment since beam divergence over the probe volume length (250 microns) creates only a 0.04% change in beam diameter.

The structure of this dissertation is such that the theory governing the Görtler instability is described first. The predictive method is developed in this section also. This is followed by a description of the purpose and design of the experimental apparatus. This dissertation then concludes with an examination of the experimental results and comparison to predictions.

## II. Görtler Theory and Riblet Behavior

This chapter provides the theoretical and empirical foundation on which the remainder of this dissertation is based. After reviews of the Görtler instability and riblet effects in both laminar and turbulent boundary layers, the mechanism by which riblets appear to affect GV development is described.

### 2.1 The Görtler Instability

In order to put this research into context, this description of the Görtler instability will begin with a brief historical review. A physical portrait of the instability is then presented, followed by a mathematical description. Since no published research to date addresses the ribletted surface condition, the theory presented herein is based on the classical assumption of a smooth/curved surface. The influence of riblets is treated later in the chapter through the introduction of a spanwise periodic velocity disturbance within the boundary layer. Therefore, particular attention is paid to the elements of Görtler theory relating disturbance wavelength to the rate at which the resulting GVs are intensified by centrifugal forces.

2.1.1 History. Clauser and Clauser (1937) discovered that the laminar boundary layer over a concave surface tends to become turbulent earlier than that over a flat surface. In 1940, Görtler (1954) proposed that this was the result of streamwise vortices within the boundary layer which form in response to a centrifugal instability. The theory he developed is an extension of the theory describing the Taylor vortices between concentric, rotating cylinders. Since Görtler's original work, a long list of researchers, including Liepmann (1943), Hall (1986), Floryan (1986), Smith (1988), and Bassom (1992), have

revised and extended his theory. Gregory and Walker (1956) experimentally verified the existence of Görtler vortices by placing china clay on a concave surface and observing the streaks that formed due to spanwise variations of surface skin friction across the vortices. However, Floryan (1991) noted that experimental verification of many aspects of Görtler theory, including the GV wavelength selection mechanism, has been difficult due to the weak nature of the disturbance. Thus, he concluded that additional experimental research into the effects of various boundary layer disturbances on GV development is needed. The following section presents a physical description of the Görtler instability devised by Liepmann (1943).

2.1.2 Physics of the Görtler Instability. Liepmann (1943) considered a 2-D, constant property, fluid flow over a concave surface as illustrated in Figure 1. The surface curvature is small, such that  $\delta/R \ll 1$ , where  $\delta$  is the laminar boundary layer thickness and  $R$  is the radius of curvature of the surface. The  $x$  coordinate of the curvilinear system is streamwise and tangent to the surface,  $y$  is normal to the surface and positive towards the center of curvature, and  $z$  is spanwise and consistent with a right-handed coordinate system. Velocities  $u$ ,  $v$ , and  $w$  are in the  $x$ ,  $y$ , and  $z$  directions respectively, although the 2-D assumption requires  $w = 0$  throughout. In addition, Liepmann (1943) neglected the streamwise growth of the boundary layer ( $v = 0$ ); thus, the streamlines are concentric arcs (parallel flow assumption).

The fluid within this flowfield experiences a volume specific centrifugal force in the negative  $y$  direction equal to  $\rho u^2/(R-y)$ , which is balanced by a local centripetal pressure gradient. With  $\delta$  sufficiently small, the radius of curvature of all streamlines within the



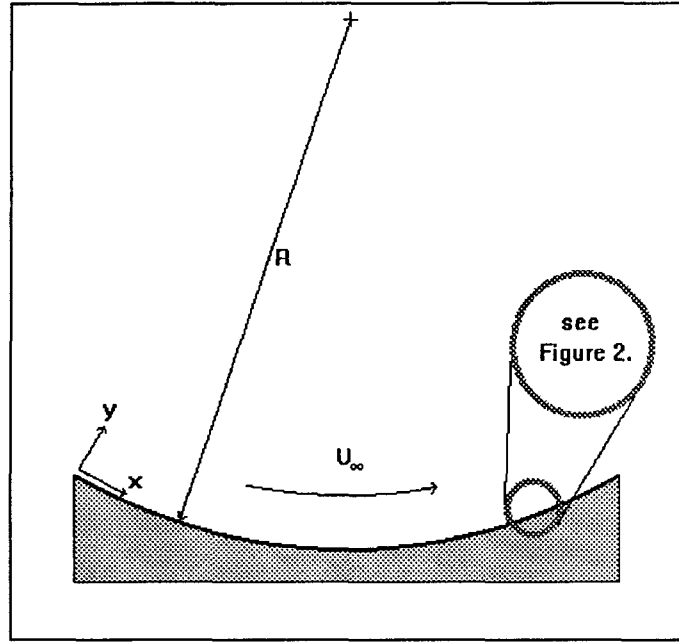


Figure 1. Flow Geometry.

boundary layer is approximately equal to  $R$ . Thus, the force balance on a boundary layer volumetric element becomes:

$$-\left(\frac{\rho u^2}{R}\right) = \frac{dp}{dy}. \quad (1)$$

Figure 2 depicts boundary layer fluid element "A" at two sequential locations. First "A" is at  $y = y_1$ , where the local velocity is  $u = u_1$ . If this element is perturbed in the negative  $y$  direction to  $y = y_2 < y_1$ , the centrifugal force acting on the element is unchanged since its velocity remains the same; however, the centripetal force at  $y_2$  is less than at  $y_1$  since the local fluid velocity,  $u_2$ , is less than  $u_1$ . This creates a force imbalance on the element which forces it towards the wall and further away from its original position. Thus, the element's motion is reinforced unstably with respect to this disturbance. Liepmann (1943) also showed that disturbances in the positive  $y$  direction are also unstably augmented.

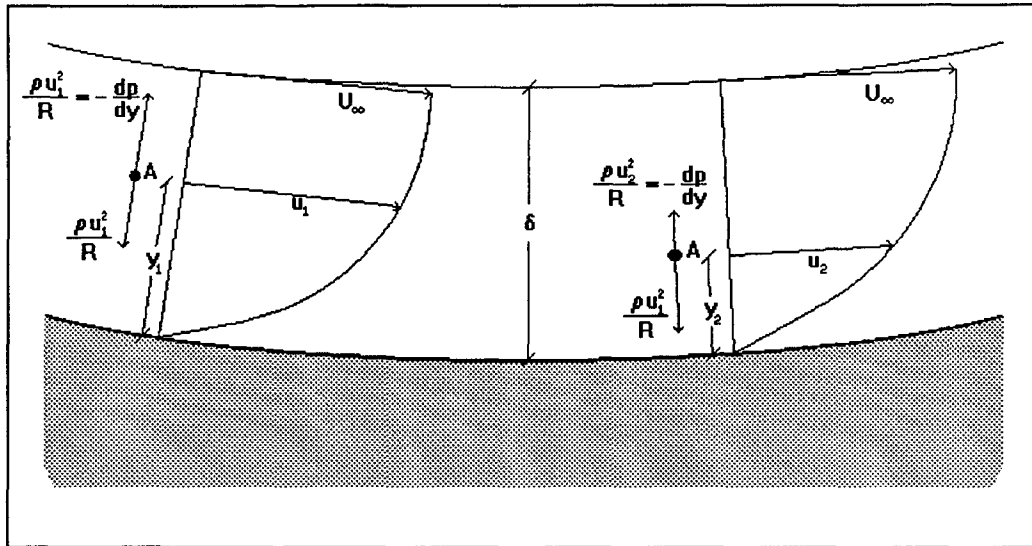


Figure 2. Force Balance on Particle "A".

Floryan (1986) used a small perturbation stability analysis and the parallel flow assumption to derive necessary and sufficient conditions for the inviscid stability of flows over a curved surface. He stated these as follows:

- (i)  $d(u^2)/dy < 0$  for concave walls, and
- (ii)  $d(u^2)/dy > 0$  for convex walls.

Four examples of shear layers are given in Figure 3. According to these criteria, flows A, C, and D are potentially unstable (denoted by the regions marked "uns.").

### 2.1.3 Mathematical Model of the Görtler Instability.

The previous section is sufficient to provide an intuitive understanding of the physical forces behind the Görtler instability, but does not address how this instability would manifest itself. This section provides a more rigorous treatment of the mathematical problem, including a description of the GVs which develop in response to the centrifugal forces. In particular, the relationship between GV wavelength and the rate

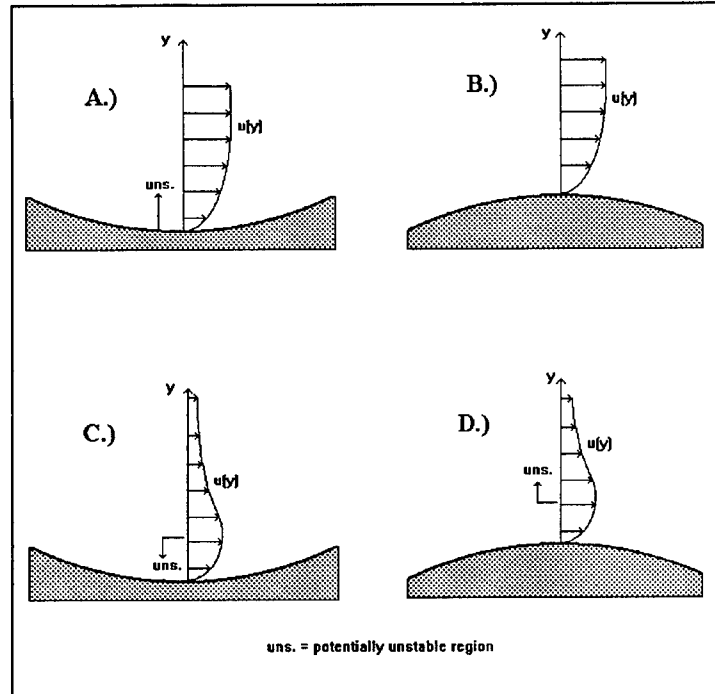


Figure 3. Sample Shear Layers Over Curved Surfaces.

of GV intensification is described. This information is used later in this chapter (page 32) to predict the effects of riblet-induced boundary layer disturbances.

**2.1.3.1 Classical Theory.** This analysis of the Görtler instability asymptotically matches a potential flow outer solution (i.e., the flow region away from the wall where viscous effects are negligible) for the flow over a curved wall to a viscous boundary layer inner solution near the wall (i.e., the region where viscous forces are non-negligible). Figure 4, taken from Floryan and Saric (1982), shows the pattern of streamlines and potential lines given by the potential flow solution over a surface with concave curvature. The  $O\eta\xi$  coordinate system is Cartesian, whereas the  $O\phi\psi$  coordinate system is aligned with the local streamlines ( $\psi = \text{constant}$ ) and potential lines ( $\phi = \text{constant}$ ). The wall has constant radius of curvature,  $R$ , and extends over streamwise

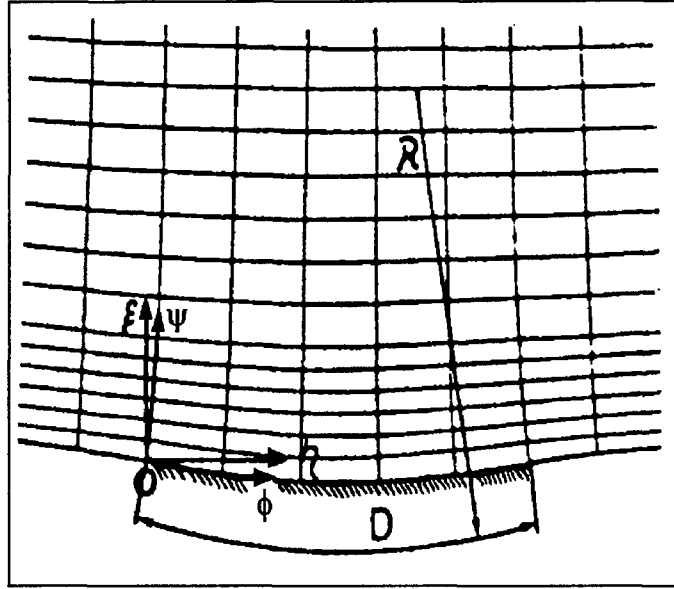


Figure 4.  $O\eta\xi$  and  $O\phi\psi$  Coordinate Systems. (Floryan and Saric, 1982)

distance,  $D$ . Both the  $O\eta\xi$  and  $O\phi\psi$  coordinate systems are non-dimensionalized by dividing each coordinate by the wall length,  $D$ .

Floryan and Saric (1982) used a series of conformal transformations, beginning with the potential function for the flow past a circular cylinder with vorticity, to generate a function,  $H(Q)$ , representing the complex potential of the flowfield in Figure 4.  $H$  was defined such that, given the complex variable,  $Q = \eta + i\xi$ ,  $\phi = \text{Re} [H(Q)]$  and  $\psi = \text{Im} [H(Q)]$ . Given this “ $Q$ -space”, scale factors were developed in order to provide reference scales for the inner and outer solutions.

Floryan and Saric (1982) defined two scaling factors to relate the small boundary layer and streamwise distance scales to the larger scale associated with the radius of curvature of the surface. First, they defined the viscous scale factor,  $\varepsilon_v \equiv (\nu/UL)^{1/2}$ , where  $L$  is a reference length scale of order of magnitude equal to  $D$ , and  $U$  is the freestream

velocity. Second, the curvature scale factor is  $\epsilon_c \equiv D/R \ll 1$ . The functional form for the metric coefficients is,

$$h_\phi = h_\psi = h = \left| \frac{dQ}{dH} \right| = 1 + \epsilon_c g(\phi, \psi) + \text{order}(\epsilon_c^2), \quad (2)$$

where  $g$  is the first order metric coefficient gauge function used in the Navier-Stokes equations (Floryan and Saric, 1982).

In order to develop the field equations, Floryan and Saric (1982) substituted the metric coefficients given in Equation (2) into the dimensionless form of the Navier-Stokes equations, including mass conservation, written in terms of generalized curvilinear coordinates. For an incompressible, two-dimensional, constant property flow, this yielded;

#### Mass

$$\tilde{u}_\phi + \tilde{v}_\psi + \epsilon_c (g_\phi \tilde{u} + g_\psi \tilde{v} + g_{\phi\psi} \tilde{u} + g_{\psi\phi} \tilde{v}) + \text{order}(\epsilon_c^2) = 0 \quad (3)$$

#### $\phi$ momentum

$$\tilde{u}_t + \tilde{u}\tilde{u}_\phi + \tilde{v}\tilde{u}_\psi + \epsilon_c (\tilde{u}\tilde{v}g_\psi + \tilde{v}^2g_\phi) = -\tilde{p}_\phi + \epsilon_v^2 [\tilde{u}_{\phi\phi} + \tilde{u}_{\psi\psi} + \epsilon_c (-3g\tilde{u}_{\phi\phi} - 2g\tilde{v}_{\phi\psi} - g\tilde{u}_{\psi\psi} - 4g_\phi\tilde{v}_\psi + 2g_\psi\tilde{v}_\phi - 2g_\phi\tilde{u}_\phi - g_{\psi\psi}\tilde{u} - g_{\phi\phi}\tilde{v})] + \text{order}(\epsilon_c^2) \quad (4)$$

#### $\psi$ momentum

$$\tilde{v}_t + \tilde{u}\tilde{v}_\phi + \tilde{v}\tilde{v}_\psi + \epsilon_c (\tilde{u}\tilde{v}g_\phi - \tilde{u}^2g_\psi) = -\tilde{p}_\psi + \epsilon_v^2 [\tilde{v}_{\phi\phi} + \tilde{v}_{\psi\psi} + \epsilon_c (-3g\tilde{v}_{\psi\psi} - 2g\tilde{u}_{\psi\psi} - g\tilde{v}_{\phi\phi} + 2g_\phi\tilde{u}_\psi - 4g_\psi\tilde{u}_\phi - 2g_\psi\tilde{v}_\psi - g_{\phi\phi}\tilde{v} - g_{\psi\psi}\tilde{u})] + \text{order}(\epsilon_c^2) \quad (5)$$

where  $\tilde{u}$  and  $\tilde{v}$  are the velocities in the  $\phi$  and  $\psi$  directions respectively, and subscripts denote partial differentiation with respect to the given variable. Velocities and pressures are non-dimensionalized as follows:

$$(\tilde{u}, \tilde{v}) = \frac{(u^*, v^*)}{U}, \quad \tilde{p} = \frac{p}{\rho U^2} \quad (6)$$

where  $u^*$  and  $v^*$  are dimensional velocities in the  $\phi$  and  $\psi$  directions, and  $p$  is the dimensional pressure. At this point, no disturbances have been introduced into the analysis, and the flow represented by these equations is the unperturbed base flow. Floryan and Saric (1982) showed that the inner (boundary layer) solution to these equations is the Blasius flat plate boundary layer solution for zero pressure gradient, incompressible flow to order( $\epsilon_c$ ) + order( $\epsilon_v$ ). This indicates that the influence of curvature on the boundary layer velocity profile is negligible as  $R$  approaches infinity. For the remainder of this analysis, the functions  $\tilde{U}(\phi, \psi)$  and  $\tilde{V}(\phi, \psi)$  will represent the non-dimensional velocities in the  $\phi$  and  $\psi$  directions for the base flow solution to Equations (3) - (5), and  $\tilde{P}(\phi, \psi)$  is the non-dimensional base flow static pressure. Thus, the following analysis is exact only in the limiting case as curvature approaches zero (i.e., approaching a flat plate).

Floryan and Saric (1982) defined 3-D, steady, spatially growing disturbances to be superimposed on the 2-D mean flow as follows:

$$\begin{aligned}\tilde{u} &= \tilde{U}(\phi, \psi) + \tilde{u}'(\phi, \psi, \tilde{z}) \\ \tilde{v} &= \tilde{V}(\phi, \psi) + \left(\frac{v}{\delta_r U}\right) \tilde{v}'(\phi, \psi, \tilde{z}) \\ \tilde{w} &= \left(\frac{v}{\delta_r U}\right) \tilde{w}'(\phi, \psi, \tilde{z}) \\ \tilde{p} &= \tilde{P}(\phi, \psi) + \left(\frac{v^2}{\delta_r^2 U^2}\right) \tilde{p}'(\phi, \psi, \tilde{z}),\end{aligned}\tag{7}$$

where primes denote the perturbation velocities and pressure, and the  $\tilde{z}$  coordinate and  $\tilde{w}$  velocity are non-dimensionalized by dividing by  $D$  and  $U$  respectively. The viscous length scale is defined by,  $\delta_r = (v\eta_0/U)^{1/2}$ , where  $\eta_0$  is the dimensional local value of the  $\eta$

coordinate ( $\eta_0 = \eta D$ ). Since  $\eta_0 \simeq x$  for  $\varepsilon_c \ll 1$ ,  $\delta_r \simeq (vx/U)^{1/2}$ , which is the expression for  $\delta_r$  used for the remainder of this study.

Equations (7) are substituted into Equations (3)-(5) and the resulting set of equations are linearized by neglecting all terms which are second or higher order in the primed variables. The result as given in Floryan and Saric (1982) is the set of linear disturbance equations:

Mass

$$\tilde{u}'_{\phi_1} + \tilde{v}'_{\psi} + \tilde{w}'_{\bar{z}} = 0 \quad (8)$$

$\phi$  momentum

$$\tilde{u}' \tilde{U}_{\phi_1} + \tilde{U} \tilde{u}'_{\phi_1} + \tilde{v}' \tilde{U}_{\psi} + \tilde{V} \tilde{u}'_{\psi} = \tilde{u}'_{\psi\psi} + \tilde{u}'_{\bar{z}\bar{z}} \quad (9)$$

$\psi$  momentum

$$\tilde{U} \tilde{v}'_{\phi_1} + \tilde{u}' \tilde{V}_{\phi_1} + \tilde{v}' \tilde{V}_{\psi} + \tilde{V} \tilde{v}'_{\psi} + 2G^2 \tilde{U} \tilde{u}' = -\tilde{p}'_{\psi} + \tilde{v}'_{\psi\psi} + \tilde{v}'_{\bar{z}\bar{z}} \quad (10)$$

$\bar{z}$  momentum

$$\tilde{U} \tilde{w}'_{\phi_1} + \tilde{V} \tilde{w}'_{\psi} = -\tilde{p}'_{\bar{z}} + \tilde{w}'_{\psi\psi} + \tilde{w}'_{\bar{z}\bar{z}} \quad (11)$$

where  $G$  is the Görtler number,

$$G = \left( \frac{U\theta}{\nu} \right) \sqrt{\frac{\theta}{R}}, \quad (12)$$

$\theta$  is the momentum thickness of the boundary layer, and  $\phi_1 = \varepsilon_v \phi$ . Note that these equations include a  $\bar{z}$  momentum component due to the three dimensionality of the disturbances defined in Equation (7). In addition, White (1991) notes that  $\theta = 0.664\delta_r$  for the Blasius boundary layer solution.

To solve this elliptic set of equations, one must assume a mathematical form for the disturbance. Insight regarding the experimentally observed characteristics of GVs led Floryan and Saric (1982) to define the following disturbance:

$$\begin{aligned}(\tilde{u}', \tilde{v}', \tilde{p}') &= (\hat{u}, \hat{v}, \hat{p}) \cos(\alpha \tilde{z}) e^{\beta \phi_1} \\ \tilde{w}' &= \hat{w} \sin(\alpha \tilde{z}) e^{\beta \phi_1},\end{aligned}\tag{13}$$

where,  $\alpha = 2\pi\theta/\lambda$ , is the dimensionless wavenumber,  $\beta$  is the dimensionless spatial amplification rate, and  $\lambda$  is the dimensional wavelength of the disturbance (spanning a pair of GVs). All hatted symbols are functions of  $\psi$  alone. This disturbance is consistent with a set of parallel, longitudinal vortices with physical dimensions that do not change in the streamwise direction. The geometry of these Görtler vortices is illustrated in Figure 5, taken from Floryan and Saric (1982). Floryan (1991) notes that the streamwise conservation of wavelength of GVs over walls of constant radius has been corroborated by all experimental observations to date.

Floryan and Saric (1982) substitute Equations (13) into Equations (8)-(11) to derive the following set of ordinary differential equations:

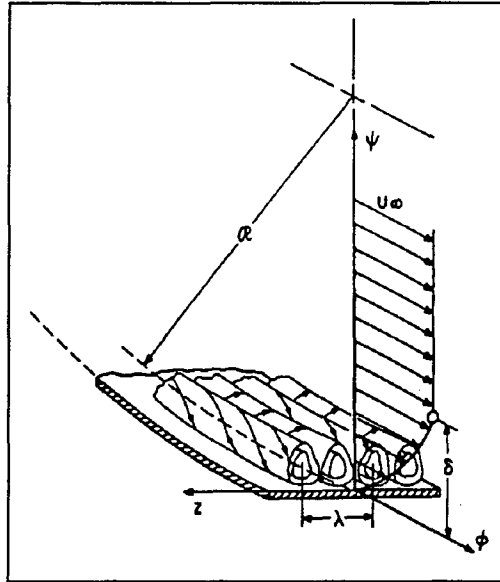
$$\beta \hat{u} + \frac{d\hat{v}}{d\psi} + \alpha \hat{w} = 0\tag{14}$$

$$\hat{u} \frac{\partial \tilde{U}}{\partial \phi_1} + \beta \tilde{U} \hat{u} + \frac{\partial \tilde{U}}{\partial \psi} \hat{v} + V \frac{d\hat{u}}{d\psi} = \frac{d^2 \hat{u}}{d\psi^2} - \alpha^2 \hat{u}\tag{15}$$

$$\beta \tilde{U} \hat{v} + \frac{\partial \tilde{V}}{\partial \phi_1} \hat{u} + \frac{\partial \tilde{V}}{\partial \psi} \hat{v} + \tilde{V} \frac{d\hat{v}}{d\psi} + 2G^2 \tilde{U} \hat{u} = -\frac{d\hat{p}}{d\psi} + \frac{d^2 \hat{v}}{d\psi^2} - \alpha^2 \hat{v}\tag{16}$$

$$\beta \tilde{U} \hat{w} + \tilde{V} \frac{d\hat{w}}{d\psi} = \alpha \hat{p} + \frac{d^2 \hat{w}}{d\psi^2} - \alpha^2 \hat{w}\tag{17}$$





downstream. Although the physical dimensions of the GVs remain constant, the associated perturbation velocities increase. Conversely, solutions for which  $\beta < 0$  represent disturbances which are attenuated. Finally,  $\beta = 0$  implies neutral stability.

Floryan (1985) defined the first, or fundamental, disturbance mode as that solution for a particular  $G$ - $\alpha$  combination that has the largest value of  $\beta$ . Therefore, this solution defines the vortices that are least stable, implying that they will develop faster than the vortices associated with any other mode. He noted that the first mode is always associated with a single layer of vortices over the surface, implying that the hatted functions are non-zero only for  $0 < \psi < \lambda/D$ . For the above example, when  $G = 10.0$  and  $\alpha = 0.9$ , the amplification rate of the first disturbance mode (a single vortex layer) is  $\beta = 2.0$ . In theory, the higher modes of the disturbance, which describe perturbations composed of multiple layers of vortices, are superimposed on the fundamental mode; however, Floryan (1985) proved that the amplification rates of the second and higher modes are negligibly small compared to that of the fundamental. Therefore, he stated that the first mode of the disturbance is the only mode of practical significance.

One can plot contours of constant  $\beta$  on a  $G$  vs.  $\alpha$  chart for any mode of the instability. This is called the stability diagram for that mode, and such a diagram for the first mode of the linearized Görtler theory based on Equations (14)-(17) is shown in Figure 6. The GV wavelength on this figure corresponding to the largest value of  $\beta$  for a given Görtler number,  $G$ , is least stable; and, therefore, is most likely to develop. The maximum amplification curve in Figure 6 denotes the locus of these most unstable  $G$ - $\alpha$  combinations with a dashed line. Floryan (1991) notes that current Görtler instability

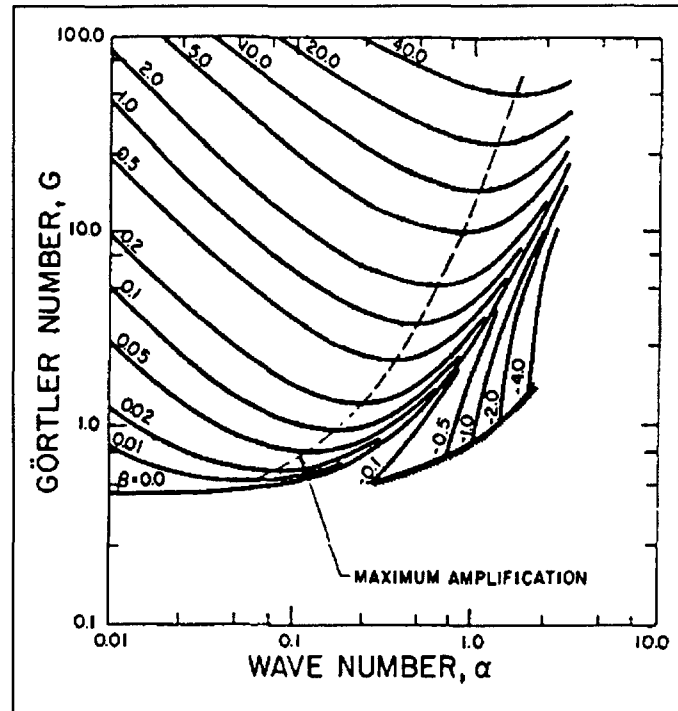


Figure 6. Görtler Stability Diagram, Fundamental Mode. (Floryan and Saric, 1982)

theory cannot predict the precise wavelength of GV's which will develop in a given flow situation; it can only estimate a wavelength near which GV development will likely occur. This ambiguity is due largely to an inadequate understanding of the GV wavelength selection mechanism, particularly regarding how various types of flow disturbances interact with boundary layer centrifugal forces.

As is evident from the diagram, this theory predicts a critical Görtler number,  $G_{cr}$ , below which no GV's are amplified regardless of wavelength. Boundary layers in this regime are stable with respect to centrifugal effects. Floryan and Saric (1982) report  $G_{cr} = 0.4638$ ; however, other mathematical approaches (such as that by Herbert (1976)) to this problem predict different values. These theories differ in the base flow assumptions (i.e., non-Blasius boundary layers), linearization assumptions (i.e. which terms are neglected), potential flow geometry (i.e. conditions upstream and downstream of the curved surface),

and assumed mathematical form for the disturbances. Herbert (1976) summarizes the results of several different approaches and finds that the location of the low wavenumber portion of the neutral stability curve ( $\alpha < 0.2$ ) differs markedly from one analysis to the next. Floryan (1991) concludes that this region of the stability diagram ( $\alpha < 0.2$  and  $G < 2.0$ ) is particularly sensitive to changes in the aforementioned assumptions; thus, the true location of the neutral curve ( $\beta = 0$  line) for  $\alpha < 0.2$ , and the actual value of  $G_{cr}$  are unknown. He also states that the shape of the low wavenumber neutral curve and the value of  $G_{cr}$  are probably configuration-dependent, and thus vary from one flow situation to another.

Herbert (1976) and Floryan (1985) show that for  $\alpha > 0.2$ , all current theories converge towards a single solution, thus establishing that portion of the stability diagram with some certainty. The experimental corroboration of this portion of the diagram is presented in Section 2.1.5.1.

The wave number,  $\alpha$ , of a given Görtler vortex increases as the vortex propagates downstream because with  $\lambda$  constant,  $\alpha \sim \theta \sim x^{1/2}$  for laminar boundary layers (Floryan, 1991). In addition,  $G$  also increases downstream and is proportional to  $x^{3/4}$  in accordance with Equation (12). Thus, if one were to measure GV wavelength at a particular location over a curved surface and plot the  $G$ - $\alpha$  combination associated with those GVs on a stability diagram, one could determine the  $G$ - $\alpha$  trajectory on the stability diagram at locations further downstream. With logarithmic scales on both the vertical and horizontal axes, the  $G$ - $\alpha$  combinations associated with these vortices will trace a line with slope =  $(3/4)(1/2)^{-1} = 3/2$ . Thus, on a Görtler stability diagram, a constant wavelength GV will be

represented by values along a straight line of slope  $3/2$  as it propagates downstream. Thus, Floryan (1991) indicates that for a given vortex wavelength, the spatial amplification rate history and future can be obtained.

Since the physical dimensions of a Görtler vortex do not change with  $x$ , it is convenient to define a non-dimensional, Görtler number-like, wavelength parameter which is also independent of  $x$ :  $\Lambda = (U_{\infty} \lambda / \nu)(\lambda / R)^{1/2}$ . The  $G-\alpha$  trace described above for a set of GVs is now a line of constant  $\Lambda$  on the stability diagram. In Figure 7, some experimental results from Tani and Sakagami (1964) are plotted on a stability diagram to illustrate this point. As can be seen, the plotted points follow lines of constant  $\Lambda$  quite closely. Also evident in this figure is that a GV generally experiences an increasing amplification rate as the flow progresses downstream.

Floryan (1991) shows that the GV wavelength which is most amplified by the Görtler instability corresponds to  $\Lambda = 210$ . In addition, Floryan (1991) notes that for non-dimensional wavenumbers in the approximate range  $100 < \Lambda < 400$  (indicated by dashed lines in Figure 7), the amplification experienced by GVs is relatively insensitive to wavelength. He further shows that GV wavelengths tend to correspond to  $\Lambda$ s in this range, since the amplification experienced by these vortices is larger than the amplification experienced by GVs for which  $\Lambda < 100$  and  $\Lambda > 400$ .

**2.1.3.2 Influence of Pressure Gradient and Variable Wall Curvature.** The above constant wall curvature, zero pressure gradient treatment of the Görtler problem resulted in a set of ordinary differential equations. Kalburgi et al. (1989) show that the generalized Görtler instability theory which accounts for both variable wall curvature and

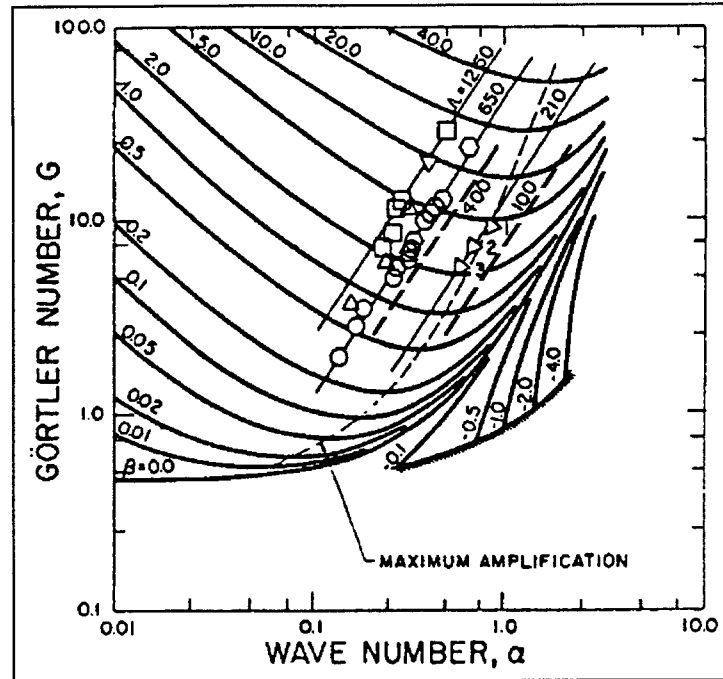


Figure 7. Lines of Constant  $\Lambda$ . (data from Tani and Sakagami, 1964)

non-zero pressure gradients results in a set of streamwise parabolic, partial differential equations which must be solved numerically. However, Floryan (1991) suggests that the analysis of Kalburgi et al. (1989) may be inconsistent in that it neglects certain terms in the derivation of the disturbance equations which may have a significant influence on the solution. Nevertheless, the experimental data presented by Kalburgi et al. (1989) appears to corroborate the predicted trends. First, an adverse pressure gradient reinforces the Görtler instability, causing the GVs to experience a higher amplification rate and develop more rapidly than those in a zero pressure gradient. Second, a favorable pressure gradient stabilizes the flow, reducing  $\beta$  and inhibiting GV development. Third, the effects of variable wall curvature are strongly dependent on flow geometry upstream of a given point on the surface. Although the GVs tend to maintain a constant wavelength once they develop, the streamwise location and amplification rate of the GVs over a given concave

section will vary depending on  $dR/dx$ . Convex curvatures immediately upstream tend to reduce  $\beta$ ; whereas, relatively large upstream concave curvatures increase  $\beta$ .

Floryan (1991) notes that most GV research to date has been performed at zero pressure gradient and constant wall curvature to minimize the number of experimental variables. The research herein was also performed at zero pressure gradient since this simplifies the task of discriminating the effects of any particular control variable.

2.1.4 Görtler Vortices in Turbulent Boundary Layers. The subject of this dissertation is riblet effects on the Görtler instability in a laminar boundary layer; however, Floryan (1991) reports that GVs develop in turbulent boundary layers over walls of relatively high curvature ( $\delta_r/R > 0.002$ ). He notes that these curvature values are similar to those experienced on the pressure surfaces of turbine blades in steam turbines and some turbojet and turbofan engines. He further explains that turbulent boundary layer GVs tend to meander in the spanwise direction due to the influence of vortical structures in the outer region of the boundary layer, and that the mathematical tools used to predict the size and strength of these GVs rely heavily on empirical formulas.

2.1.5 Empirical Relationships. Although the linear theory presented in the previous sections provides insight into the nature of the Görtler instability and defines many of the important parameters governing GV behavior, Floryan (1991) describes many aspects of GV behavior that remain primarily within the purview of experimental empiricism. Among these are the precise location of the neutral curve, the selection mechanisms for GV wavelength, and the prediction of transition due to the influence of the Görtler instability on the laminar boundary layer. The primary intent of this research is

to determine if riblets can inhibit or enhance the development of GVs through appropriate selection of riblet dimensions. Since the proposed mechanism for the riblet effects involves the interaction of riblet-induced boundary layer disturbances with the GV wavelength selection mechanism, this section will describe those GV characteristics that are germane to this topic.

2.1.5.1 Neutral Curve Location. One of the continuing goals of GV research has been to confirm the location of the neutral curve predicted by linear theory. Floryan (1991) states that most of the published GV research to date has been performed at wavenumbers of order (1) and higher due to the extreme difficulty of detecting the weakly amplified vortices with  $\alpha \leq 0.1$ . Unfortunately, if one extends the lines of constant  $\Lambda$  in Figure 7 down to the neutral stability curve ( $\beta = 0$ ), it is evident that the upstream wavenumbers are of order (0.1) and smaller. Floryan (1991) notes that the inability to measure such weak vortices has not confirmed or refuted the  $G_{cr} \simeq 0.5$  criteria predicted by the theory presented in the previous sections. However, Bippes (1978) experimentally located the neutral curve for  $\alpha \geq 1$  and found it to be near, but not coincident with the curve predicted by linear theory, as illustrated in Figure 8. In that work, artificial streamwise vortices of specific wavelengths were introduced into the flow over the concave surface, and the rate of vortex amplification measured. The cause of this discrepancy between the experimental and theoretical neutral curves is unclear, but Floryan (1991) suggests that it may be due to the simplifying approximations used in the linear theory.



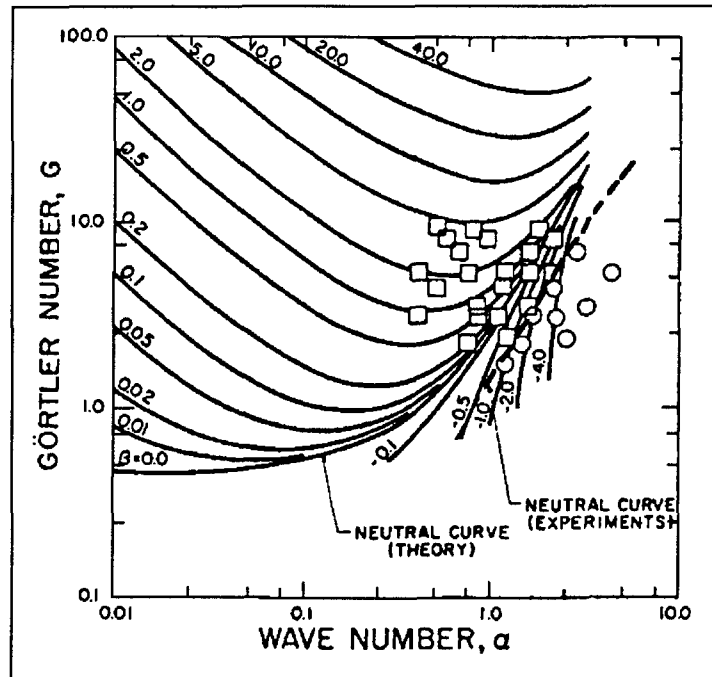


Figure 8. Experimental vs. Theoretical Neutral Curves:  $\square$  = Amplified Disturbance,  $\circ$  = Attenuated Disturbance. (Bippes, 1978)

**2.1.5.2 Wavelength Selection.** According to Floryan (1991), the mechanism by which the Görtler instability selects vortices of a particular wavelength is not clearly understood. He notes that this selection mechanism appears to be only weakly governed by the local streamline curvature because there exists a demonstrably strong coupling between the oncoming disturbances in the flow and the wavelength of the GVs which appear.

This receptivity of the Görtler instability to oncoming disturbances has been exploited by researchers who wish to select particular GV wavelengths for study. For example, while investigating the heat transfer over a concave surface, Kottke (1986) placed a wire grid upstream of the curved test section in order to generate GVs of a specific wavelength. He adjusted the mesh spacing to equal the desired wavelength, and through trial and error, determined the optimum upstream grid location for GV

wavelength selection. In a similar study, Crane and Umut (1990) placed small triangular fins upstream of the test section at regular intervals, and oriented them to introduce a vortical motion in the fluid traversing them. The size and spacing of the fins determined the GV wavelength which appeared over the concave test surface.

In some analyses, researchers wish to minimize external influences on the wavelength selection process. For example, Goglia and Mangalam (1985) constructed an isolated cambered airfoil and placed it in a low turbulence wind tunnel. The vortices which appeared over the concave surface of the airfoil were very near the maximum amplification line ( $\Lambda \simeq 210$ ) on the Görtler stability diagram. Thus, Goglia and Mangalam (1985) concluded that, under controlled conditions where external influences are minimized, the GVs which develop over a concave surface have wavelengths very close to the wavelength which is most amplified by the Görtler instability as predicted by linear theory. However, Floryan (1991) states that in “noisy” environments, a given disturbance in the flow may stimulate the development of GVs with a wavelength significantly different than  $\Lambda = 210$  (typically within the  $100 < \Lambda < 400$  range), perhaps because of a disproportionate amount of energy associated with the initial disturbance wavelength.

**2.1.5.3 Transition** According to Floryan (1991), current research indicates that GVs accelerate transition by destabilizing the laminar boundary layer in the upwash region between two counterrotating vortices. In this region, low speed fluid from near the wall is lifted into the freestream, creating an inflectional  $u(y)$  profile and developing a region of high shear between the low speed fluid and the fast moving

freestream. According to White (1991), these are ideal conditions for the onset of turbulence within a boundary layer.

Liepmann (1945) suggested that the location of transition due to the centrifugal instability could be predicted using an empirically determined transition Görtler number,  $G_{tr} \approx 7$ . However, he notes that as  $R$  approaches infinity (very low curvature walls), boundary layer transition must be predicted using flat plate criteria, since the influence of centrifugal forces becomes negligible. White (1991) suggested that the flat plate correlation of Van Driest and Blumer (1963) provides good agreement with experimental observations for flows with no pressure gradient. This correlation will be described in detail in the Discussion of Results chapter and was used in this research to compare flat plate transition predictions to observed transition locations over a curved surface to discriminate the effects of curvature on transition. Finally, in flows of intermediate curvature, curved and flat plate correlations predict similar transition locations. In these cases, Liepmann (1945) notes that transition tends to occur sooner than predicted by either theory alone. The author has found no correlations which are designed to predict transition for these intermediate curvature cases.

## 2.2 Riblet Properties

Riblet theory is the second major discipline addressed in this research. The following sections provide a physical description of riblets and characterize riblet properties in both turbulent and laminar boundary layers.

2.2.1 Description and General Properties. Riblets are small surface ridges which are usually oriented so that the fluid flow over the riblet surface runs parallel to the peaks.

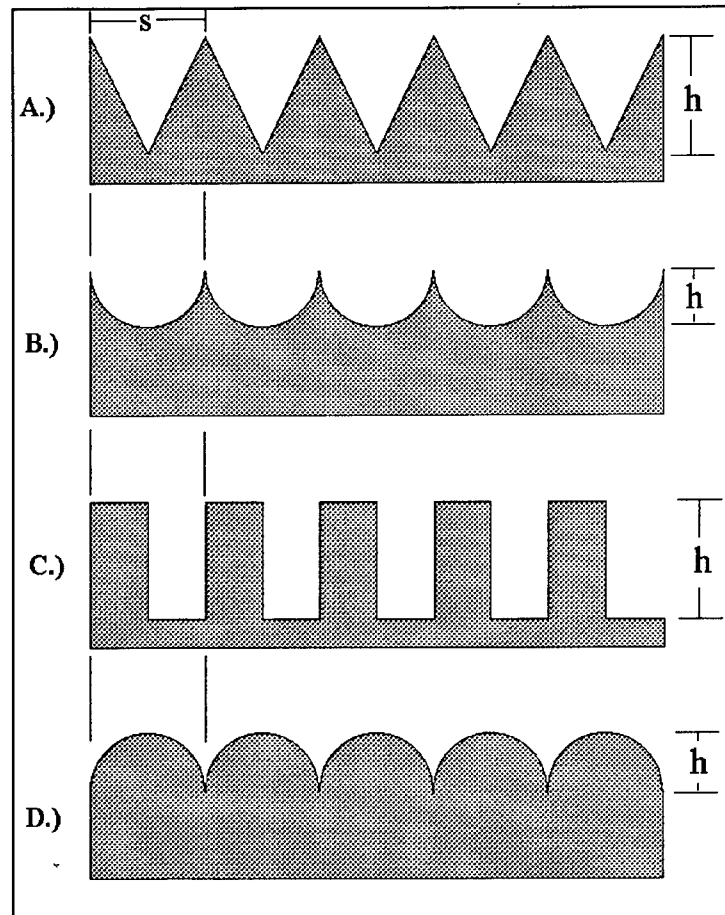


Figure 9. Riblet Shapes.

Several possible riblet profiles are illustrated in Figure 9. Walsh (1990) states that riblets were conceived and are used primarily to reduce skin friction drag in turbulent boundary layers (TBLs). Although the amount of literature available on riblet behavior is extensive, most of it is directed at the TBL problem; therefore, much of the following discussion is placed in the context of turbulent boundary layers.

Walsh (1990) notes that the appropriate riblet dimensions for drag reduction vary depending on their shape and the state of the boundary layer in which they are placed. These dimensions are expressed in terms of dimensionless wall variables (denoted with the “+” superscript) which Walsh gives as

$$h^+ = \frac{hu_\tau}{\nu} \quad \text{and} \quad s^+ = \frac{su_\tau}{\nu}, \quad (18)$$

where  $h$  and  $s$  are riblet height and spacing respectively. White (1991) gives the following definition for the friction velocity:

$$u_\tau = \sqrt{\frac{\tau_w}{\rho}}. \quad (19)$$

The wall shear stress,  $\tau_w$ , is defined by

$$\tau_w = \mu \left( \frac{\partial u}{\partial y} + \frac{\partial v}{\partial x} \right)_{y=0} \approx \mu \left( \frac{\partial u}{\partial y} \right)_{y=0}. \quad (20)$$

Walsh (1990) indicates that the most commonly tested riblet shape is the V-groove shown in Figure 9A. He gives the optimum dimensions for maximum TBL skin friction reduction over a flat plate as  $h^+ \approx s^+ \approx 8-12$ , which is slightly larger than the laminar sublayer thickness as given by White (1991). The majority of skin friction measurements have been performed over flat plates due to the simplified flow geometry, for which TBL skin friction reductions of up to seven to eight percent have been achieved. Walsh (1990) notes that riblet shapes other than the V-groove, such as the rectangular profile of Figure 9c, may further decrease skin friction an additional two percent in some situations; however, current experimental evidence suggests that potential skin friction reductions for riblets alone are below ten percent.

Walsh (1990) reports that no riblet-induced skin friction drag reductions in laminar boundary layers (LBLs) have been measured. Very little published research exists in this area due, in part, to the lack of motivation to reduce the already low skin friction in the LBL environment. However, the laminar flow numerical calculations of Desaint Victor

(1987) suggest that LBL skin friction reductions of up to four percent may be possible with the geometry  $h/s = 2.5$  and  $h/\delta = 0.2$ . However, wall curvature introduces flow structures into the boundary layer which may be affected by riblets, potentially changing the riblet-induced drag reduction mechanism.

The author has found no published research addressing the interaction of riblets and the Görtler instability, hence the motivation for this research. Therefore, all following discussions regarding the appropriate riblet dimensions for riblet-GV interactions are based solely on the author's suggested mechanisms by which riblets affect GV development.

**2.2.2 Riblet-Boundary Layer Interactions.** The following sections address several specific mechanisms of riblet-boundary layer interactions for turbulent and laminar boundary layers which are applicable to riblet-GV interactions. As previously mentioned, since most riblet research to date has been motivated by skin friction studies, much of the following discussion is couched in those terms.

**2.2.2.1 Riblet Flat Plate TBL Properties.** Walsh (1990) discusses a number of mechanisms through which riblets influence the near-wall flow structure within a TBL. Of these mechanisms, two are of primary interest to this research: the ability of riblets to resist the spanwise movement of the fluid near the wall and to constrain the development of longitudinal vortices within the TBL.

Coustols and Savill (1992) showed that the flow within the laminar sublayer of a TBL is characterized by the spanwise movement of low speed fluid which results in the pooling of this fluid into longitudinal streaks spaced approximately  $z^+ = 100$  wall units

apart, where  $z^+ = (zu_r/\nu)$ . They further showed that these regions of localized sublayer thickening are ultimately responsible for much of the turbulence production and skin friction generated within the TBL. Choi (1990) reported that appropriately sized riblets appear to constrain this lateral movement of the fluid, interfering with the growth of the elongated regions of low speed fluid in the lower boundary layer. This also interferes with the development of the longitudinal vortices which exist just above the laminar sublayer within a TBL. Choi (1990) concluded that these vortices were constrained in both location and strength due to the presence of riblets.

Two studies published since the inception of this research document the presence of streamwise vortical motion within and above the riblet valleys in a turbulent boundary layer. The experimental results of Suzuki and Kasagi (1994), reproduced in Figure 10, illustrate the instantaneous cross-stream velocity components near a riblet surface measured using three-dimensional particle tracking velocimetry. These riblets have flat valleys and measure  $h^+ = 9.1$  and  $s^+ = 15$  for Figure 10a, and  $h^+ = 19$  and  $s^+ = 31$  for Figure 10b (all "+" variables are dimensionless). The counterrotating vortices present in the figure are the ensemble average of time-dependent, turbulently fluctuating vortices in that region. The smaller riblets of Figure 10a have a maximum cross stream component less than 0.1% of  $U$ , whereas the larger riblets of Figure 10b have a maximum cross stream component of approximately 0.8% of  $U$ . The riblets of Figure 10a were appropriately sized to reduce drag, whereas the larger riblets of Figure 10b had no effect on drag. Suzuki and Kasagi (1994) conclude that the strengthening of these vortices in

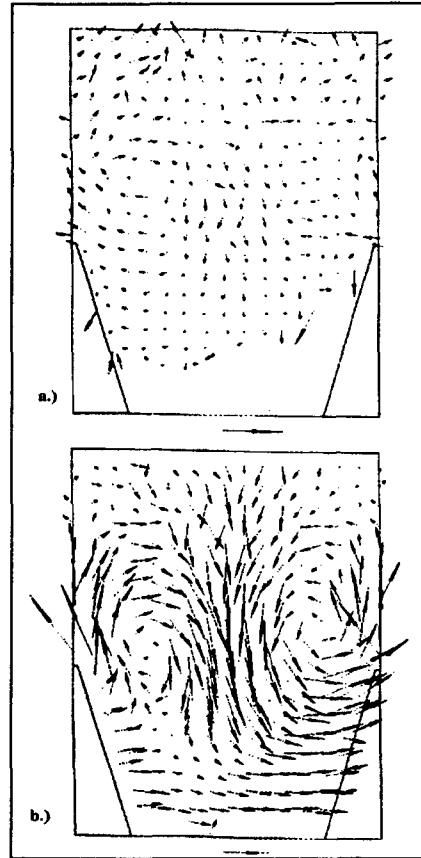


Figure 10. TBL Riblet Vortices from Suzuki and Kasagi (1994): a.)  $h^+ = 9.1$  and  $s^+ = 15$ , b.) and  $h^+ = 19$  and  $s^+ = 31$ , reference vector =  $0.005U$ .

Figure 10b increases momentum transport within the lower TBL, negating any potential drag reductions.

**2.2.2.2 Riblet Flat Plate LBL Properties.** The flat plate LBL does not contain any of the time-dependent structures, such as migrating vortices and low speed streaks, that the TBL contains. Riblets create regions of low speed flow in the riblet valleys in which very little shear stress is produced. If this local reduction in shear stress is more than sufficient to balance the relatively large stress at the riblet peaks and the increased wetted surface area of the riblets compared to the smooth surface, then drag reductions are possible. However, Walsh (1990) reported that the only measurable effect



to date of riblets on LBL properties has been an acceleration of boundary layer transition to turbulence. The acceleration of transition as was also observed in the research documented herein.

A boundary layer undergoing the transition to turbulence can still be considered laminar, although the flow within such a boundary layer may experience intermittent turbulent bursts. Results from this research will show that the TBL counterrotating vortices illustrated in Figure 10 actually develop during the transition process, while the boundary layer is still laminar.

2.2.2.3 Riblet Curved Surface Properties. The works of Rothenflue (1991) and Fang et al. (1990) suggest that riblets reduce cascade total pressure losses by 10-15 percent when riblets are applied to the concave surfaces of the cascade blades. The reason for this relatively large decrease in cascade pressure loss remains unclear, since it is larger than would be predicted by presuming an 8-10 percent decrease in the skin friction coefficient over that surface. Among several possible explanations, Fang et al. (1990) speculated that the riblets were inhibiting the development of GVs over the pressure surface. This theory is predicated on the assumption that the boundary layer over that surface is laminar, since the curvature values on the blades of both Rothenflue (1991) and Fang et al. (1990),  $\delta_r/R \approx 0.0007$ , are insufficient for TBL GV development. Since the pressure gradient over the majority of the concave surfaces of their blades is either favorable or only slightly adverse (DeCook (1991)) and the Reynolds number values are relatively low ( $Re_x \leq 400,000$ ), it is likely that the boundary layer is laminar. The Görtler number range over the blades in the studies of Fang et al. (1990) and Rothenflue (1991)

was approximately  $0 \leq G \leq 9$ , which is ideal for GV development in a LBL according to Floryan (1991).

It is possible that the riblets were imposing a particular disturbance wavenumber on the Görtler instability, thus initiating the development of GVs that were less strongly amplified than those that appeared over the smooth surface. It is also possible that the riblets simply delayed GV development. Therefore, the works of Rothenflue (1991) and Fang et al. (1990) suggested the need for a more detailed investigation of riblets' effects on a boundary layer subject to the Görtler instability.

### 2.3 Riblet-GV Interaction

This section describes the suggested mechanisms of riblet-GV interaction investigated in this research, and defines important boundary layer parameters to be used in data analysis in the Discussion of Results chapter. Riblets will create a spanwise periodic disturbance in the LBL with a wavelength equal to the riblet spacing,  $s$ . How this disturbance interacts with the Görtler instability will be strongly dependent on the disturbance wavelength relative to the wavelength of GVs which would have appeared over a smooth surface under identical flow conditions. To quantify this relationship, a variation on the non-dimensional wavelength parameter,  $\Lambda$ , is defined:

$$\Lambda_s = \left( \frac{Us}{\nu} \right) \sqrt{\frac{s}{R}} \quad (21)$$

Since the Görtler instability is highly receptive, it follows that the wavelength and location of any streamwise vortices which develop in response to it will be affected by appropriately sized riblets. If the Görtler instability were not receptive, or if the riblets were not sized properly, the vortices would develop over a ribletted plate exactly as they

would have over a smooth plate. Therefore, riblets for which  $100 < \Lambda_s < 400$ , for example, should result in GV wavelengths corresponding to  $\lambda = s$  ( $\Lambda = \Lambda_s$ ), as illustrated in Figure 11, since disturbances of this wavelength are highly unstable with respect to the centrifugal instability. Note that these vortices are similar to the TBL vortices in Figure 10. In addition, results from this research will show that similar vortices develop within the riblet valleys in a laminar boundary layer over a flat plate due to viscous forces. Thus, taking into account viscous and centrifugal forces, it is likely that the only steady, streamwise vortical structures in a laminar boundary layer over a curved surface with riblets, with  $100 < \Lambda_s < 400$ , will be these paired, counterrotating, riblet-valley vortices.

For  $\Lambda_s < 100$ , the riblets are small compared to the GVs which would normally develop over a smooth surface. Although the Görtler instability will induce the development of relatively large streamwise vortices over the riblets, the riblets will resist

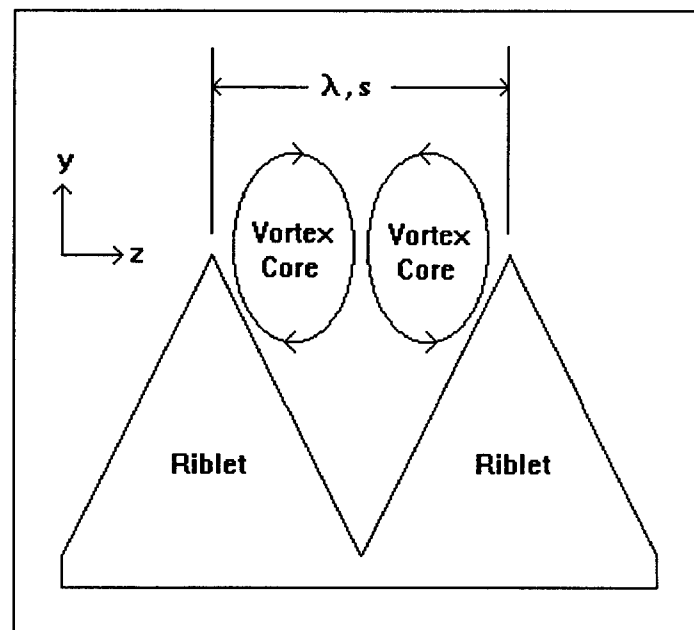


Figure 11. Proposed Riblet - GV Interaction.

the spanwise movement of fluid over the peaks. In such a situation, it is likely that riblets will hinder Görtler vortex development, resulting in a streamwise delay in their appearance.

For  $\Lambda_s > 400$ , riblet dimensions become large with respect to boundary layer dimensions, and the assumptions built into the flow equations derived in the first half of this chapter break down. Flows in this regime are perhaps best characterized as fluid traveling through a set of curved channels, rather than the flow over a ribletted surface. For this reason, this  $\Lambda_s$  regime was not investigated in this research.

The  $s = 3.0$  mm riblets used in this research correspond to  $\Lambda_s = 39, 79$ , and  $157$  for  $U = 3.5$  m/s,  $7.5$  m/s, and  $15.0$  m/s, respectively. Thus, riblet induced disturbances for  $U = 15.0$  m/s were strongly reinforced by centrifugal forces, while the riblet disturbances for  $U = 7.5$  m/s were weakly reinforced. For  $U = 3.5$  m/s,  $\Lambda_s$  lies very near the neutral stability curve on the Görtler stability diagram (Figure 7); thus, the disturbances introduced by these riblets were not centrifugally reinforced.

One can define another parameter based on  $\alpha$ :  $\alpha_s = 2\pi\theta/s$ . Unlike  $\Lambda_s$ , the value of  $\alpha_s$  changes with  $x$  (it increases as  $x$  increases). For  $U = 3.5$  m/s, this wavenumber increased from  $\alpha_s = 0.951$  at  $x = 105$  mm ( $G = 2.17$ ) to  $\alpha_s = 2.07$  at  $x = 500$  mm ( $G = 6.98$ ). For  $U = 7.5$  m/s, it increased from  $\alpha_s = 0.649$  at  $x = 105$  mm ( $G = 2.62$ ) to  $\alpha_s = 1.42$  at  $x = 500$  mm ( $G = 8.47$ ). For  $U = 15.0$  m/s,  $\alpha_s = 0.445$  at  $x = 105$  mm ( $G = 3.12$ ) and increased to  $\alpha_s = 1.00$  at  $x = 500$  mm ( $G = 10.08$ ). These test ranges are plotted as lines of constant  $\Lambda_s$  in Figure 12. In this figure, conditions at the entry of the test region

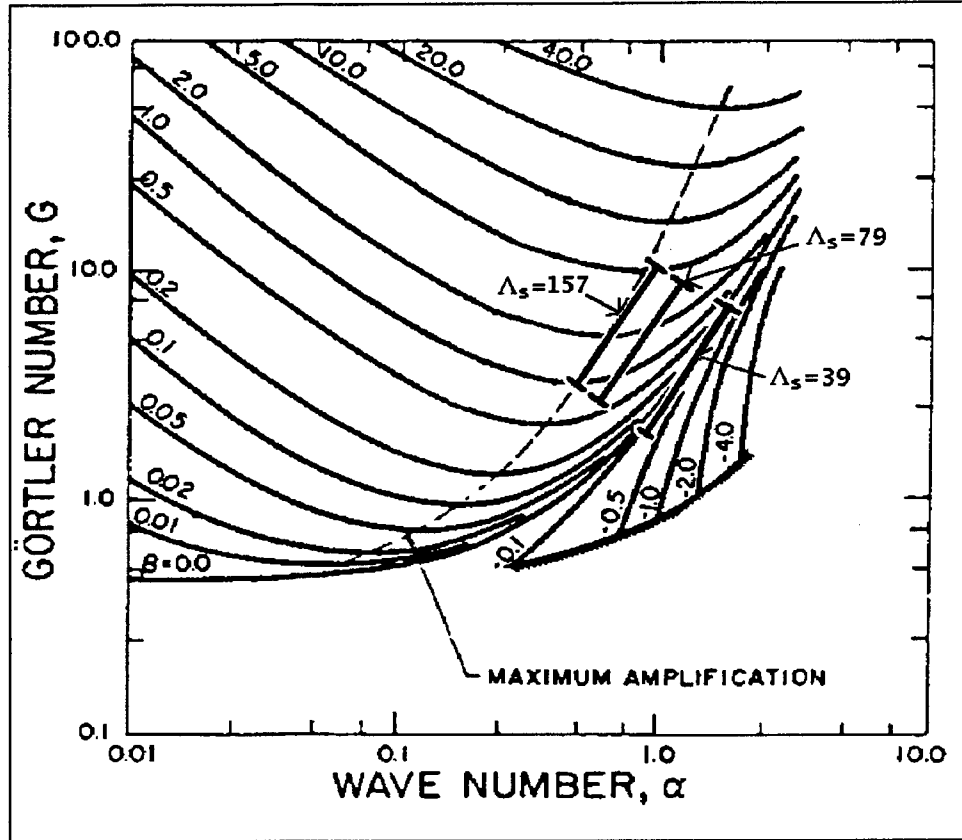


Figure 12. Test Conditions, Based on  $\Lambda_s$ .

( $x = 105$  mm) are at the bottom left end of the  $\Lambda_s$  lines, and conditions at the test region exit ( $x = 500$  mm) are at the upper right end of the lines.

In addition to documenting vortex development through direct measurement of vortical velocity components, riblet effects on boundary layer momentum thickness and skin friction will be presented herein. The boundary layer momentum thickness, as given by White (1991), is:

$$\theta = \int_0^{\infty} \frac{u}{U} \left( 1 - \frac{u}{U} \right) dy. \quad (22)$$

In the course of this research, the momentum thickness was calculated from the boundary layer  $u$  vs.  $y$  profiles and will be used in the Discussion of Results chapter for boundary

layer transition correlations and for the calculation of the skin friction coefficient,  $C_f$ . The skin friction coefficient is given by White (1991) as:

$$C_f = \frac{2\tau_w}{\rho U^2} \quad (23)$$

where  $\tau_w$  is the surface shear stress, given by,

$$\tau_w = \mu \left( \frac{\partial u}{\partial y} + \frac{\partial v}{\partial x} \right)_{y=0} \approx \mu \left( \frac{\partial u}{\partial y} \right)_{y=0} \quad (24)$$

and  $\mu$  is the fluid viscosity. White (1991) shows that for a zero pressure gradient,

$$C_f = 2 \frac{d\theta}{dx}. \quad (25)$$

This relationship can be integrated over a portion of a surface from streamwise location  $x_1$  to  $x_2$  to yield an expression for the average skin friction coefficient,

$$C_{f,ave} = \frac{2(\theta_{x_2} - \theta_{x_1})}{(x_2 - x_1)} \quad (26)$$

where  $\theta_{x_1}$  and  $\theta_{x_2}$  are the momentum thicknesses of the boundary layer at  $x_1$  and  $x_2$ , respectively.

Finally, the turbulence intensity,  $Tu$ , was used in this research to determine whether the boundary layer was laminar, transitional, or turbulent. The form of  $Tu$  used herein is given in White (1991) as:

$$Tu = \left( \frac{1}{U} \right) \sqrt{\frac{\overline{u'^2} + \overline{v'^2} + \overline{w'^2}}{3}}, \quad (27)$$

where primed variables are the fluctuating velocity components. The use of this parameter to determine the boundary layer state will be described in the Discussion of Results chapter.

## 2.4 Chapter Summary

This chapter consisted of three sections, and was intended to provide the theoretical foundation upon which the experimental work presented in the following chapters is to be based. The Görtler instability was described in the opening section. Next, riblets were described and their effects on laminar and turbulent boundary layers were presented. In addition, a model was developed with which riblet effects on GV wavelength and streamwise location can be predicted. Finally, the third section of this chapter defined the flow quantities which will be used in later chapters as part of the experimental analysis. The most important conclusion to be drawn from this chapter is that the Görtler instability is a highly receptive phenomenon; and, thus, riblet-induced disturbances in the boundary layer should modify Görtler vortex development in a manner depending on the value of  $\Lambda_s$ . Therefore, the research documented in this dissertation is directed at measuring the effects of riblets on Görtler vortex wavelength and location; thus, corroborating the predicted behavior. Since Görtler vortices accelerate boundary layer transition, increase heat transfer, and increase skin friction (Floryan, 1991), techniques may be developed by which riblets will control these quantities over concave surfaces. Thus, the primary contribution of this research is that it introduces the concept that riblets can, in fact, be used to predictably affect GV development.

### III. Apparatus

#### 3.1 The Boundary Layer Research Facility

The AFIT Boundary Layer Research Facility (BLRF) which was designed and constructed for this project allowed precise, high spatial resolution, non-intrusive 3-D velocity measurements throughout the boundary layers over curved and flat surfaces. It offered a continuously variable freestream velocity range from approximately 3 to 18 m/s, employed two adjustable test section walls which allowed control of the pressure gradient along the test surface, and used an ejector assembly to seed the flow for laser Doppler anemometry. Due to wind tunnel geometry, measurements throughout the boundary layer were possible for streamwise Reynolds numbers in the range  $20,000 \leq Re_x \leq 560,000$  for both curved and flat surfaces. A detailed listing of component specifications and serial numbers is given in Appendix A.

#### 3.2 Design Requirements

The design of the BLRF was influenced by a number of experimental requirements. Precise velocity measurements were necessary within laminar boundary layers over smooth and ribletted surfaces on both flat and curved plates, including the requirement to take flow measurements within the riblet valleys. Since the Görtler instability is highly receptive, flow disturbances from the data acquisition equipment needed to be minimized. Finally, to allow for a variety of test conditions, the freestream velocity within the test section was to be controllable over as wide a range as possible. A schematic overview of



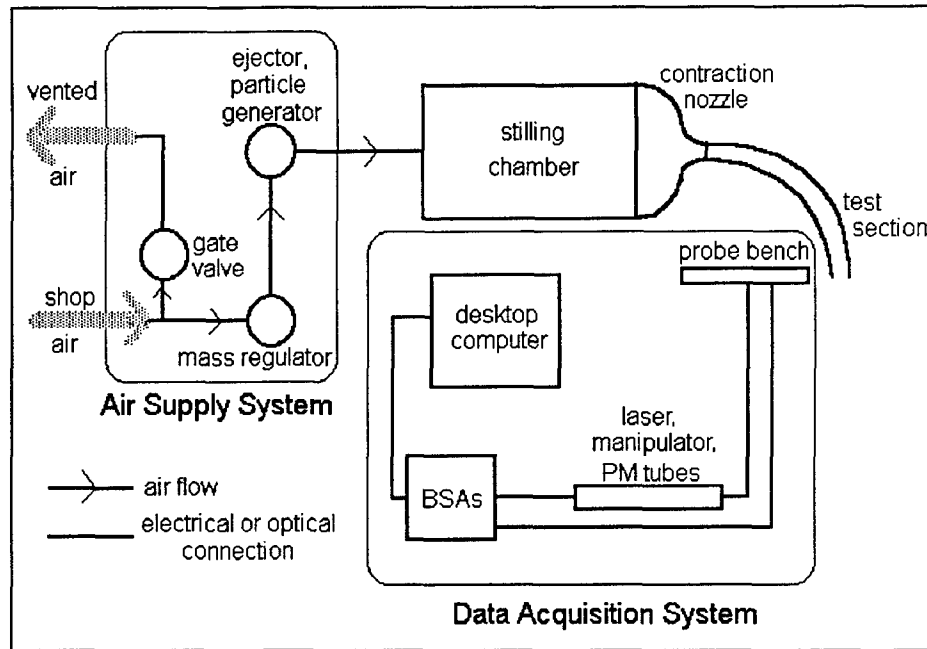


Figure 13. BLRF Schematic Overview (PM = Photomultiplier).

the BLRF is given in Figure 13 (PM tubes = photomultiplier tubes), and the following sections describe the subsystem designs in detail.

### 3.3 BLRF Design

3.3.1 Air Supply System. The BLRF air supply system performed two functions:

1) provide steady air velocities in the test section for extended runs by delivery of a constant mass flow rate, and 2) introduction of LDA flow seeding particles. The air source for the BLRF was the AFIT compressed air supply (shop air), which was nominally maintained at 100 psi and was capable of delivering 1 lbm/s continuously. This mass flow rate was increased to 2 lbm/s in the test section by the incorporation of an ejector assembly. The major components of the BLRF air supply system are depicted in Figure

14.

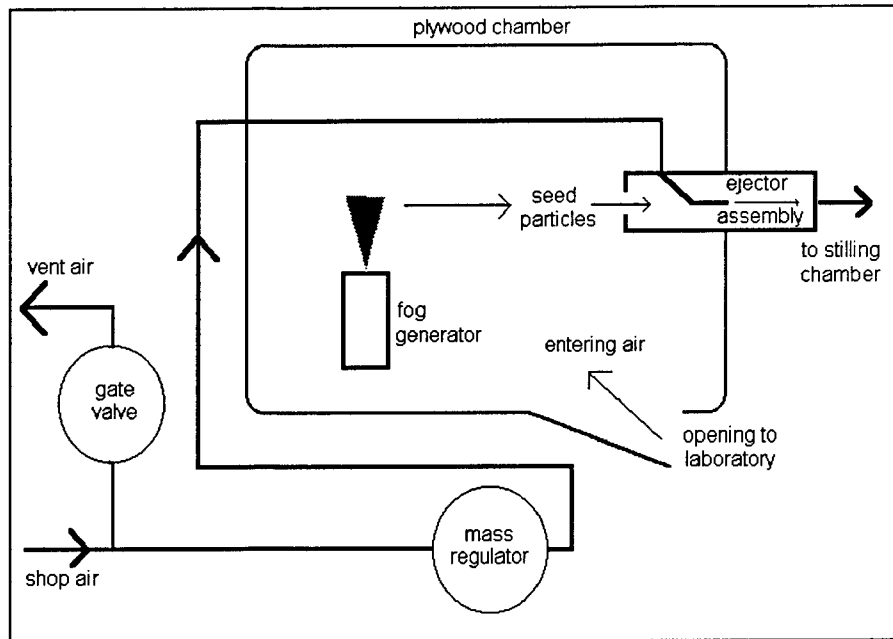


Figure 14. Air Supply System Schematic.

To maintain steady flow in the test section, the pressure upstream of the gate valve in Figure 14 must be constant for the entire duration of a run (0.5 - 3.0 hr.). This was achieved by setting the mass regulator to the required test section flow rate, then opening the gate valve to vent sufficient air from the shop air system so that the AFIT compressors were running at full capacity. Once this condition was achieved, the compressors ran continuously and the pressure upstream of the gate valve remained constant (typically 80 psi). The mass regulator was chosen over a pressure regulator because it was more capable of compensating for small upstream pressure variations with minimum impact on test section air velocity in the BLRF, and it did not require a separate pressurized air supply (i.e. bottled air) for a control regulator.

Flow seeding was performed between the mass regulator and ejector. A remotely operated DANTEC fog machine (model number 2522) was housed in a plywood chamber open to the laboratory. During operation, the ejector drew seeded air from the plywood

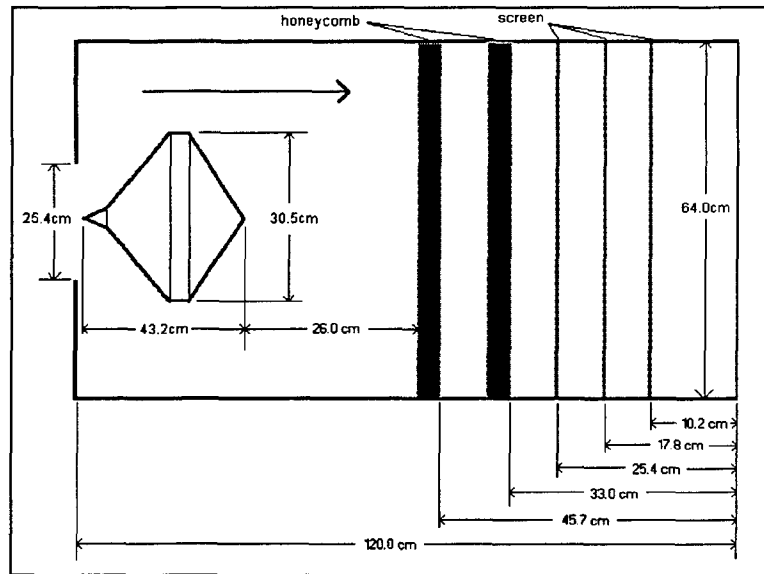


Figure 15. Stilling Chamber Internal Arrangement, Air Travels Left to Right.

chamber (and, hence, from the laboratory) and delivered it, along with unseeded shop air, to the stilling chamber where the seed particles were evenly distributed.

**3.3.2 Stilling Chamber.** The stilling chamber performed two functions: 1) evenly distributing the seed particles, and 2) flow straightening. The internal layout of the Stilling chamber is given in Figure 15.

Flow entering the stilling chamber was the unmixed effluent from the ejector assembly. This air was abruptly diffused by an axially symmetric plug, creating a highly turbulent, low speed region ( $< 3.0$  m/s) between the plug and the first honeycomb mesh. The combination of high turbulence and long dwell time assured uniform mixing of the seed particles throughout the flow.

The turbulent flow from the mixing region was smoothed and straightened by two honeycomb mesh/wire screen combinations, followed by three wire screens. Both honeycombs had 0.635 cm (1/4 inch) cells and were 5.08 cm (2 inches) thick, creating the

8 to 1 cell length to width ratio suggested by Huber (1982). All screens were 30 mesh with 0.015 cm (0.006 inch) wires. These wires were thin enough to assure that the Reynolds number based on wire diameter was less than 40 for all test conditions; which, according to Huber (1982), assured that the wire wakes were fully laminar, thus optimizing the turbulence reducing characteristics of the screens.

3.3.3 Nozzle. Air exiting the stilling chamber was directed into the test section by the nozzle. The nozzle contracted from the 64 cm square cross section of the stilling chamber to the  $16 \times 40$  cm test section, resulting in a 6.4:1 contraction ratio. Bi-circular wall contours were used, and the corners between the walls were filleted, as suggested by Huber (1982), to aid in the transverse fluid motion resulting from the transition from a square to rectangular cross section. Detailed dimensions for the nozzle are given in Appendix B.

3.3.4 Test Section. Two test sections were used for this research. Flat plate measurements were taken with a 1 meter long straight test section, and curved plate measurements were taken with a curved test section which had a centerline radius of curvature of 1 meter and turned through 90 degrees, giving a length of 1.6 meters. Both test sections measured  $16 \times 40$  cm at the inlet and were subdivided into two equal  $8 \times 40$  cm channels by the test plate. The velocity within the test section could be selected anywhere from approximately 3.0 m/s to 15.0 m/s. Due to the limited range of movement of the LDA traversing system, data acquisition was limited to the upstream 0.5 meters ( $x \leq 500$  mm) of the test sections. At the furthest downstream data acquisition location ( $x = 500$  mm), the streamwise Reynolds numbers ranged from 112,000 at  $U = 3.0$  m/s to

560,000 at  $U = 15.0$  m/s. Turbulence levels entering both test sections were approximately 1.0 percent and rose to 3.0 percent at  $x = 500$  mm. This rise in turbulence was due to the development of a turbulent mixing region in an open slot in the test section sidewall which was needed to provide for uninterrupted passage of the laser beams. Finally, boundary layer thicknesses at  $x = 500$  mm over the test plate never exceeded 20 mm, and, thus, were less than one quarter of the total channel width.

An aluminum inlet piece, illustrated in Figure 16, was shared by both sections and was pierced by 10 static pressure taps along the sidewalls which were used to assure that no top-to-bottom pressure gradients existed along the 40 cm axis of the test section. In addition, a total pressure tap was installed at the top of the inlet piece to allow redundant confirmation of measured freestream velocities within the test section.

**3.3.4.1 Straight Test Section.** The straight test section was constructed primarily of plexiglass and is shown in Figure 17. Both 40 cm sidewalls were hinged at the upstream edge to allow pressure balancing along the test plate by moving the trailing edge of the sidewalls towards or away from the test plate until no pressure gradient was detected from the static pressure taps that were installed along the top endwall. Both endwalls were cut with 1.27 cm (0.5 inch) grooves for insertion of the test plate. The static pressure within the test section was equal to atmospheric pressure, and rubber seals were used between the plexiglass walls to keep air from escaping or entering the test section. The test section walls were attached to one another by clamps which could easily be loosened when sidewall adjustments were necessary and then re-tightened. The pivoting joints (denoted by the "pin" annotation in Figure 17) between the upstream edges

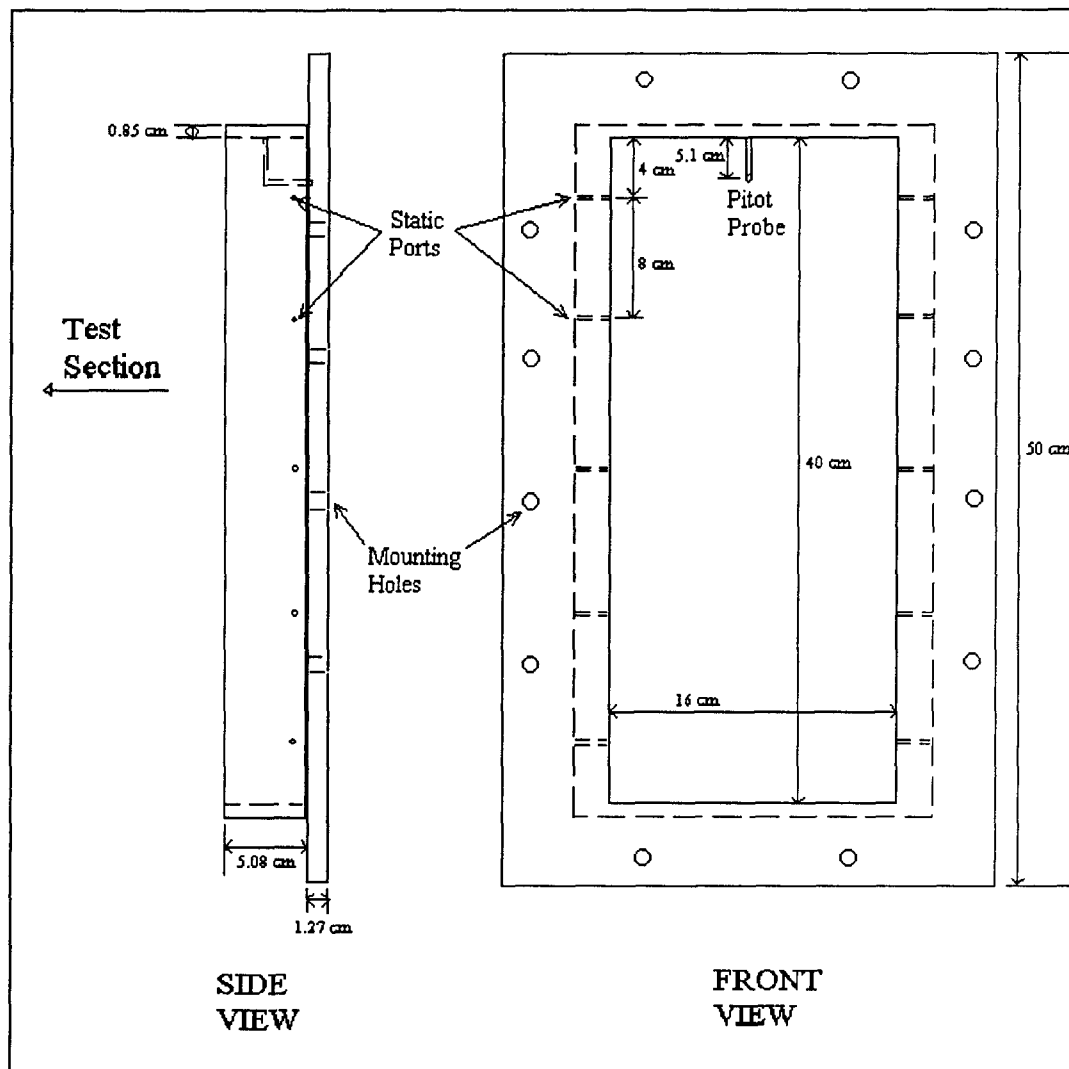


Figure 16. Aluminum Connecting Piece 2-View.

of the movable sidewalls and the aluminum inlet piece also used rubber seals. A 5.08 cm slot is cut along the length of the inner sidewall to allow uninterrupted passage of the lasers from the LDA equipment.

The flat test plates used with the straight test section were machined from 1.3 cm ( $\cong 0.5$  inch) thick plexiglass with a sharp leading edge, cut to 30 degrees. The ribletted plate, illustrated in Figure 18, had V-groove riblets machined over the center 25.4 cm span for entire length of the test section. The riblets measured  $s = 3.0 \pm 0.1$  mm and  $h = 2.6 \pm$

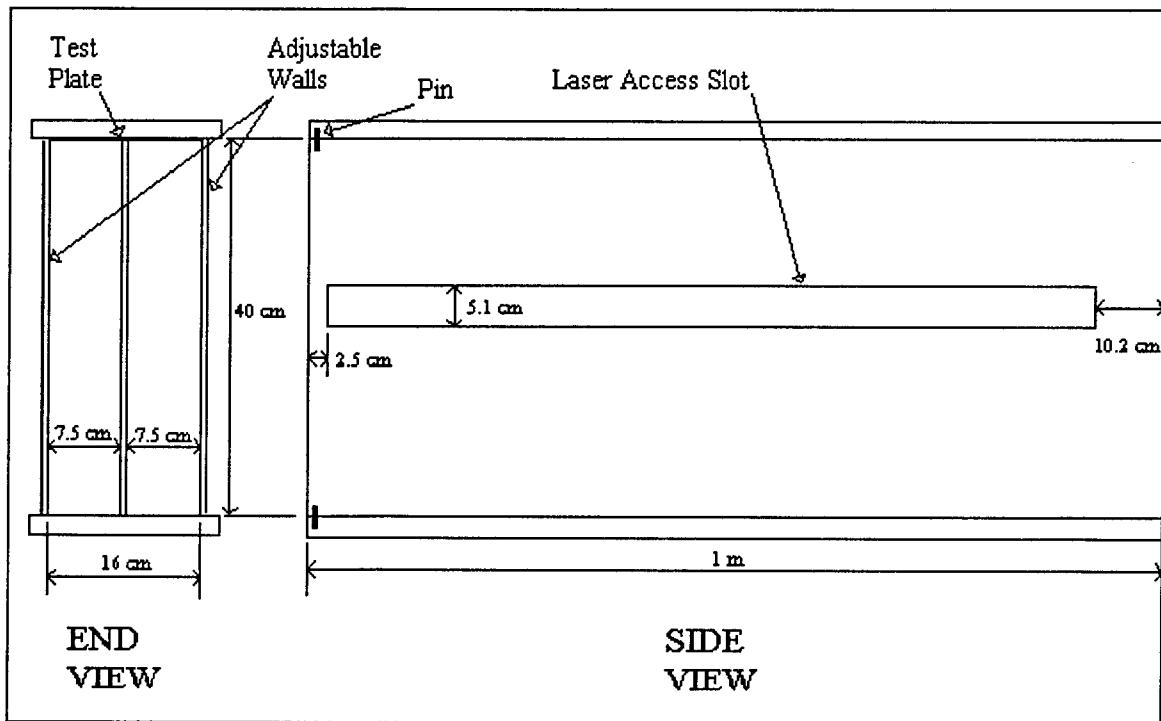


Figure 17. Straight Test Section.

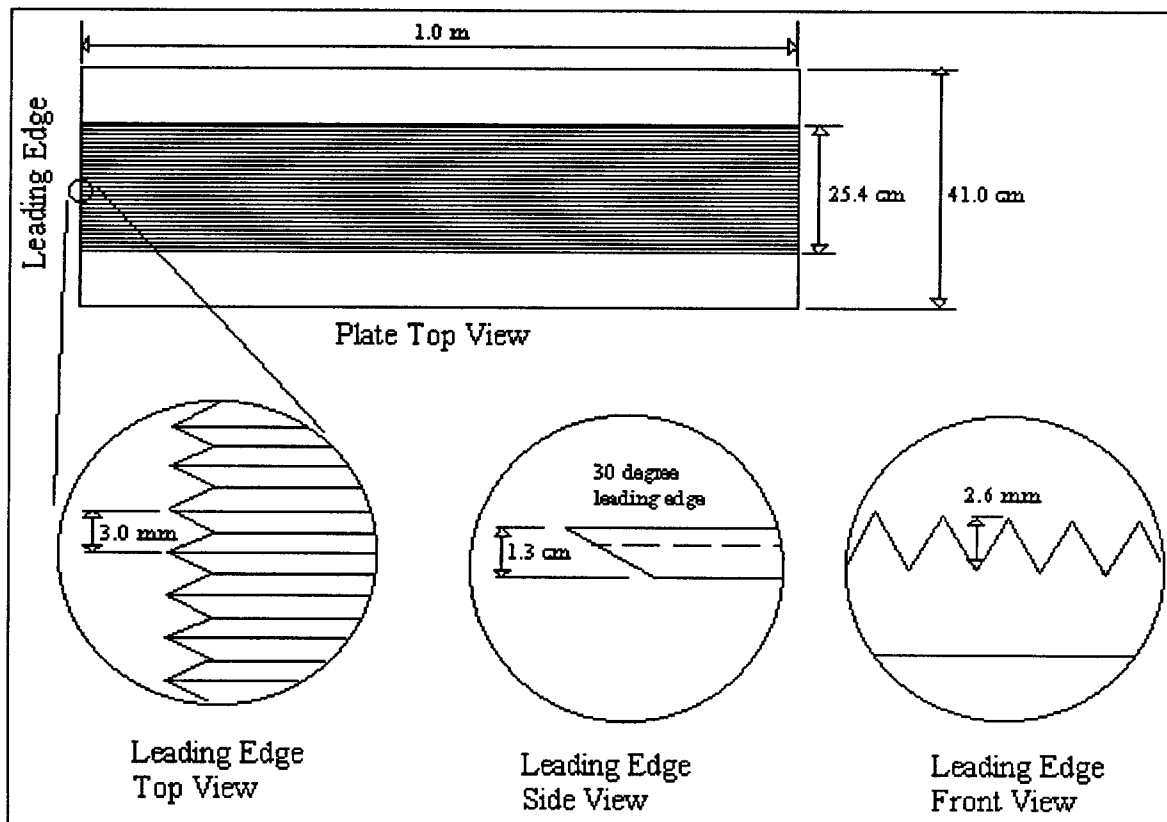


Figure 18. Flat/Ribletted Plate.

0.1 mm. To prevent flow separation at the leading edge of the plate, the sidewall position on the “back” side of the test section (i.e. the side opposite from where data acquisition occurred) was adjusted to produce a pressure that was slightly lower than atmospheric on the back side of the test plate leading edge. This turned the flow slightly at the test plate leading edge, reducing the angle of attack of what was effectively a wedge airfoil.

3.3.4.2 Curved Test Section. The curved test section, also constructed of plexiglass, is illustrated in Figure 19. The sidewalls were constructed of 0.318 cm (1/8 inch) thick plexiglass sheets cemented to rigid plexiglass frames. As for the straight test section, the upstream edges of these sidewalls were pinned so that they could be rotated about the leading edge to create a zero pressure gradient in the test section. However, no static pressure taps were present because of the expected secondary flows near the top and bottom of the test section due to the curvature. Instead, static pressure measurements were made using the static pressure ports of a pitot-static tube inserted through the sidewall slot. As for the straight test section, the 5.1 cm wide sidewall slot was cut along the length of the test section in the center of the sidewall so that the laser beams could enter the test section unobstructed. The endwalls at the top and bottom of the test section had 0.318 cm grooves to allow insertion of a curved test plate, and seals between the test section sidewalls and endwalls were maintained using a rubber gasket.

The smooth test plate for this section was a piece of 0.318 cm thick plexiglass cut to a 30 degree sharp leading edge (the edge incident to the oncoming flow of air). The ribletted plate, with riblets identical to the flat plate, was constructed of 0.521 cm (0.205



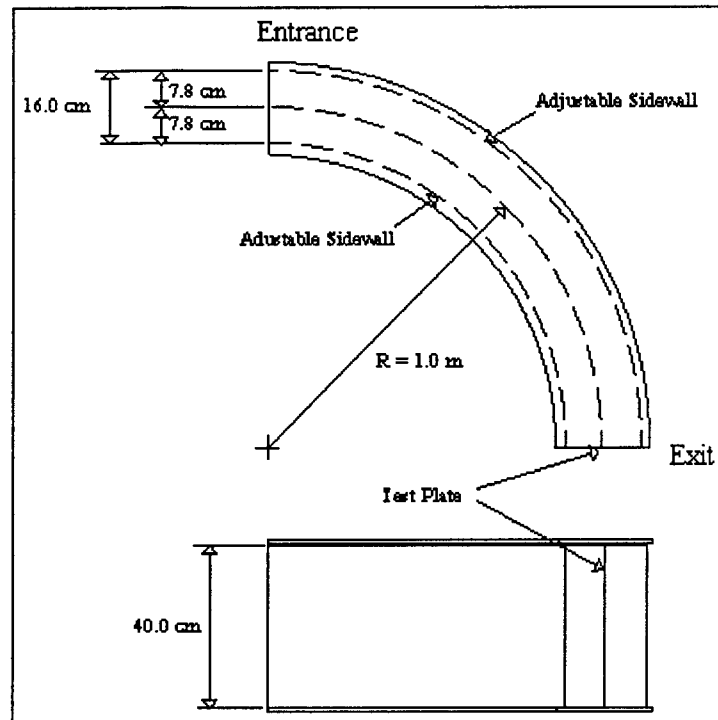


Figure 19. Curved Test Section Dimensions.

inch) thick Plexiglas cut to the same 30 degree leading edge. Both plates were flexed by hand and inserted into the  $R = 1$  meter endwall grooves.

### 3.3.5 BLRF Characterization.

3.3.5.1 Velocity Range. The usable velocity range in the test section (both flat and curved) was determined by measuring test section velocities with the LDA equipment. Velocities below  $U = 3.0 \text{ m/s}$  (measured in the freestream immediately above the test plate at the entrance of the test section) were unsustainable because of the unacceptably long stabilization time of the mass regulator valve. The lower the mass flow rate, the longer the valve took to settle, yielding a constant velocity in the test section. Velocities above  $U = 15.0 \text{ m/s}$  could not be reliably maintained because this is near the absolute air flow limitation of the AFIT compressors. Small variations in shop air demands throughout the AFIT building created unacceptably large pressure variations

upstream of the gate valve if velocities in excess of  $U = 15.0$  m/s were being maintained in the test section. Thus, the effective velocity range of the BLRF is approximately  $3.0 \leq U \leq 15.0$  m/s.

3.3.5.2 Flow Uniformity. Measurement of the nozzle exit plane (test section entrance) velocities were performed with a pitot-static tube attached to a slant oil manometer accurate to 0.005 inches of water, and were conducted over the full range of exit velocities. At no location outside of the nozzle sidewall boundary layers did the velocity in the exit plane vary from the mean by more than 1.5 percent, with the velocity in the region near the exit plane centerline about 1.5 percent lower than that near the nozzle walls. Huber (1982) states that a small centerline velocity deficit is characteristic of this type of nozzle.

3.3.5.3 Turbulence and Open Slot Influence. The LDA equipment was used to measure freestream turbulence levels throughout the test region over all test plates. The test region is defined as the streamwise range over the test plate in which boundary layer measurements were to be taken. For this research, this range was  $105 \leq x \leq 500$  mm. For  $x < 105$  mm, there was no optical path to the boundary layer for the LDA equipment; and, for  $x > 500$  mm, the LDA traversing mechanism was incapable of moving downstream. For all freestream velocities, turbulence levels entering the test region were in the range of 0.8 to 1.0 percent (as determined using equation (27)). The turbulence level increased to 3.0 - 3.5 percent at the exit plane of the test region ( $x = 500$  mm) due to the influence of the mixing region in the laser access slot.

As already mentioned, this open slot was required to allow an unobstructed path for the laser beams into the test section. The ability to take velocity measurement very near (within approximately 0.3 mm) of the test surface required that the laser beams from the LDA apparatus be very nearly diffraction limited (i.e., focusable to within the theoretical limits of the optics used). Attempts to acquire data through the plexiglass or through transparent mylar placed over the slot demonstrated that data acquisition within 1 mm of the test surface was impossible because of diffraction of the beams through the material. Cutting small windows in paper covers placed over the slot proved to be impractical since the pitot-static probe used for pressure balancing required free access to the length of the test section. Placing paper over the slot after test section pressure balancing was completed would likely have changed the streamwise pressure distribution within the test section so that a zero pressure gradient no longer existed over the plate. It was decided to reproduce a known flow condition within the test section with an open laser access slot to determine if the slot had a measurable effect on boundary layer development.

The final phase of BLRF characterization involved the reproduction of a known solution for a laminar boundary layer. This was intended to confirm that the presence of an open slot in the test section sidewall was not significantly influencing laminar boundary layer development over the plate in the test region. As a test case, a flat plate, zero pressure gradient, laminar boundary layer was produced and measured under a several test conditions. The resulting measured profiles were compared to the Blasius similarity solution given in White (1991), and agreement with theory was found to be very good.

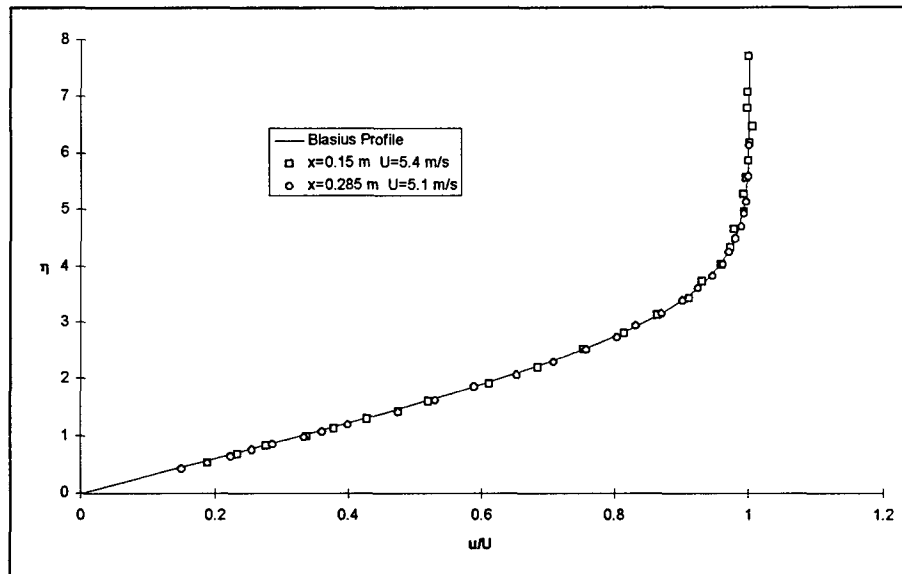


Figure 20. Boundary Layer Data Compared to Blasius Solution.

Figure 20 presents the data for two typical test cases, where the dimensionless vertical coordinate is  $\eta = y[U/(\nu x)]^{1/2}$ . The small scatter in the data, most noticeable for  $\eta > 5$  since the profile is nearly vertical in that region, was most likely due to small oscillations in the freestream velocity as other researchers at AFIT placed demands on the air supply. This was corrected for the remainder of the data in this work by arranging to operate the BLRF only at certain hours when other researchers agreed not to disturb the AFIT 100 psi air supply system.

### 3.4 Data Acquisition Equipment

A DANTEC 40 MHz, 3-axis laser Doppler anemometry system (components specified in Appendix A) was the primary instrument used for data acquisition. This device consisted of 3 Burst Spectrum Analyzers (BSAs), a 300 mW laser, a laser manipulator deck with 40 MHz Bragg cell, 1-D and 2-D laser probes and associated optics, a traversing system, and a desktop computer. Nearly all laser components were interconnected by fiber-optic cables, and the computer controlled the system using a GPIB

RS-232 serial connection. Position accuracy of the traversing system in all three axes is  $\pm 0.05$  mm.

### 3.4.1 LDA Configuration.

3.4.1.1 Optical. LDA basic principles are presented in Appendix C, where definitions of several important terms such as Doppler frequency and signal pedestal are given. In order to achieve 3-D measurements, two laser probes were used: one measuring a single velocity component (1 pair of lasers), and the other measuring two components (2 pairs of lasers). This required six lasers, each with a unique wavelength (one laser at  $\lambda = 514.5$  nm, another at  $\lambda = 488.0$  nm, and another at  $\lambda = 476.5$  nm, and then three other lasers with frequencies shifted upwards by 40 MHz from the first three). The DANTEC laser manipulator deck created these six lasers by splitting the single, multi-frequency laser beam emanating from the 300 mW Argon laser source into three distinct colors. These colors and their associated wavelengths are as follows: green ( $\lambda = 514.5$  nm), blue ( $\lambda = 488.0$  nm), and purple ( $\lambda = 476.5$  nm). Each of these three beams was passed through a vibrating Bragg cell which further split each into two beams, one of which was frequency shifted by the 40 MHz vibrating frequency of the cell. The resulting six beams were then directed into fiber-optic cables which conducted them to the laser probes. The 1-D probe received the shifted and unshifted purple beams, and the 2-D probe received the blue and green pairs.

The angle between the optical axes of the two probes was 70 degrees, and the focal length of the transmitting/receiving optics of each probe was 600 mm. The off-axis backscatter measurement technique was employed, which means that radiation scattered

by seed particles from the lasers emitted by one probe was being detected by the other probe (e.g., the purple laser probe picked up signals from the green and blue lasers). This configuration resulted in a probe volume, defined as the region of intersection of the six laser beams which was detectable by the receiving optics, which was approximately  $150 \times 150 \times 250 \mu\text{m}$ . These probe volume dimensions are approximate because the exact dimensions vary with the quality of laser probe alignment, nearness of the probe volume to a solid surface (which affects background light levels due to scattered laser light from the surface), and the user selected amplification of the signals from the photomultipliers (the higher the amplification, the larger the probe volume).

Details regarding the LDA system alignment, spot location, data acquisition, and data reduction techniques used for this research are given in Chapter 4.

3.4.1.2 Electronic. The electronic systems of the DANTEC 3-D LDA equipment included three DANTEC model 57×08 photomultiplier tubes and three burst spectrum analyzers (BSAs). The light scattered from seed particles within the flow was received by the optical probes and transmitted by fiber optic cable to the photomultiplier (PM) tubes. The PM tubes had a current limitation of 1.6 mA and operated at a maximum input voltage from the BSAs of 1306 V. These tubes converted the optical signal into an electronic voltage which was sent to the BSAs. The BSAs then digitized the time varying voltage from the PM tubes and converted the resulting data into velocities.

This LDA system used three burst spectrum analyzers (one model 55N20 BSA enhanced master and two model 57N35 BSA enhanced slaves). The master BSA operated as the clock source for all three BSAs. The user-selected measurement velocity

bandwidth (Doppler frequency range) was interpolated at 14-bit word precision, and the input filters to prevent spectral aliasing were 4th-order Butterworth filters. Transit time of a particle through the probe volume was given by a 12-bit time counter and arrival time of the particle was measured by a 14-bit arrival time counter. The number of discrete samples taken from a given burst (record length) was user selectable from 4, 8, 16, 32, or 64 samples. These samples were processed through a hardware fast Fourier transform to yield the Doppler frequency of the interference pattern of the light scattered from the particle, which then yielded particle velocity. According to the BSA documentation, these BSAs could yield measured velocities within 1 percent of actual velocity for a single particle given a record length of 64 samples. Smaller record lengths resulted in slightly less accuracy.

3.4.2 Central Computer. The computer controlling the data acquisition equipment and reducing the raw data from the BSAs was a Gateway 2000 486DX/33 MHz desktop. The 200 MB hard drive on this computer was insufficient to contain all of the data produced during the entire data acquisition process (which was in excess of 600 MB); thus, a Valtek 250 MB tape backup unit was used for data archival and storage.

### 3.5 Chapter Summary

The design and operation of the BLRF were described in this chapter. The design requirements were given first, followed by a detailed description of the BLRF components. Next, the flow characteristics within the test section were given, including velocity range, freestream turbulence levels, and flow uniformity. In addition, to test the facility, laminar boundary layer profiles were measured over a flat plate, and the results compared to the known solution given in White (1991). Finally, the three-dimensional

laser-Doppler anemometry data acquisition equipment was described. The BLRF was designed and the LDA equipment was configured to allow non-intrusive flow measurements to be taken throughout the boundary layer over both flat and curved plates, including within riblet valleys.



## IV. Experimental Procedure

### 4.1 Overview

This discussion of experimental procedure will first address tuning and alignment of the laser manipulator deck and probes. The operational settings for the BSAs and desktop software will then be described, followed by a complete description of a data acquisition cycle.

### 4.2 Optical Alignment

4.2.1 Laser Tuning. Proper LDA alignment is critical to maximizing fringe pattern regularity and brightness, which optimizes the data acquisition rate and the ability to acquire data near a solid surface. The beam emanating from the Argon laser was approximately 300 mW in power and was directed into the laser manipulator deck, also known as the transmitter. The transmitter is depicted in Figure 21. The first step in aligning the system was to assure that the beam was entering the transmitter precisely

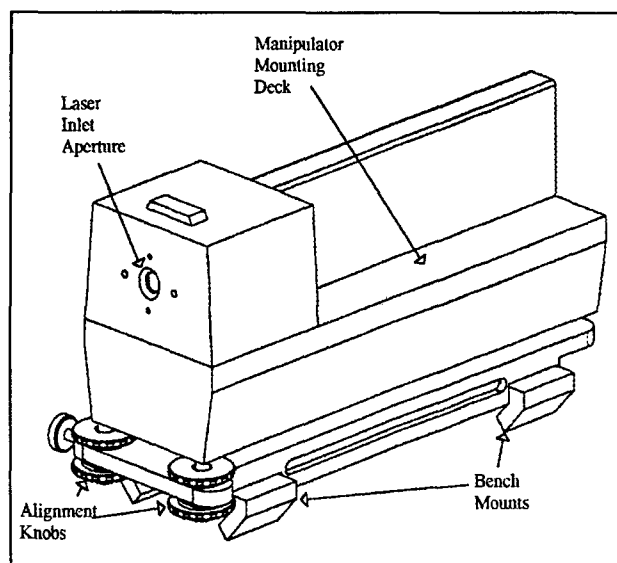


Figure 21. Transmitter.

along its axis. This was performed by throwing a switch on the transmitter which removed the Bragg cell from the beam path, allowing the laser beam to travel the transmitter's length, reflect off a mirror on the far side from the laser entry port, and exit the transmitter via the same hole through which it entered. A semi-transparent plate (provided with the transmitter) with a small hole in the middle, was installed in the entry port to allow the beam exit location to be monitored. Adjustments were made at the feet of the transmitter until the beam exited precisely through the same spot it entered. Once this alignment was achieved, tuning of the six manipulators installed on the top of the transmitters was possible.

The arrangement of the manipulators on the transmitter is illustrated in Figure 22. "Tuning" refers to the process of maximizing the effectiveness with which the laser beams were directed into the fiber optic cables which carried them to the laser probes. This was accomplished by adjusting the four alignment screws on each manipulator while monitoring laser power (using a US Instruments triple scale power meter, given in component listing in Appendix A) emanating from the probe. When maximum power was obtained, tuning for that manipulator was complete. The manipulator adjustment screws modify the orientation of a glass cylinder within the manipulator, as shown in Figure 23, so that the beam enters the cable precisely along its axis. Experience has shown that the green laser power from the probes was up to 30 mW per beam, the blue approximately 12 mW, and the purple was less than 3 mW. These differences are the result of the relative power produced at each wavelength by the Argon laser. Since the purple channel was the

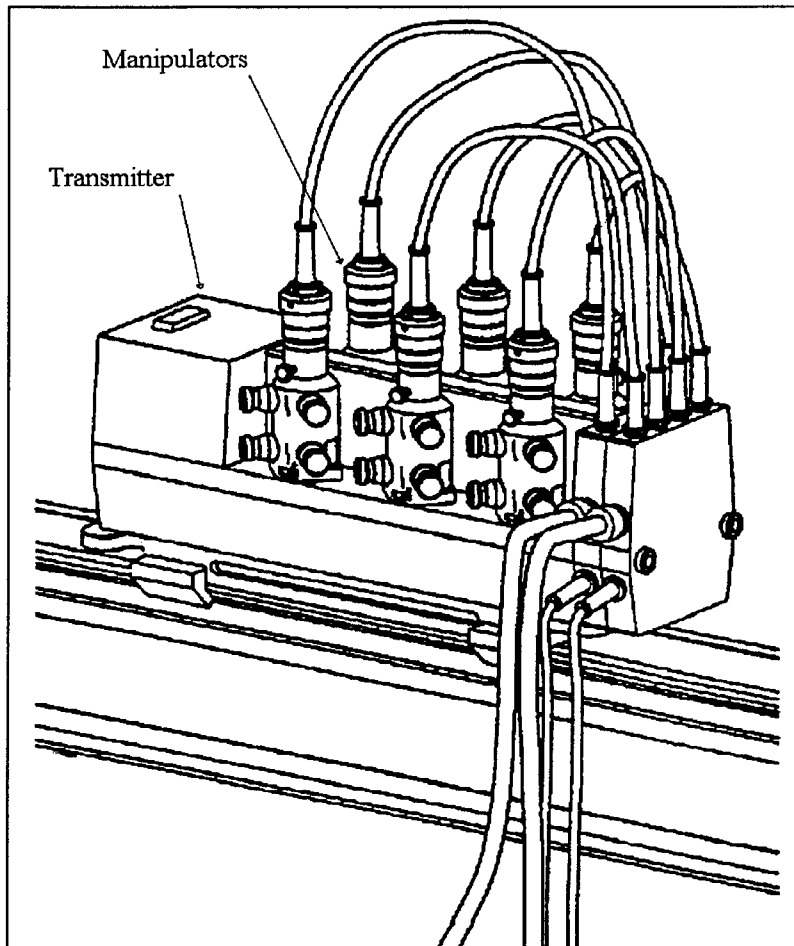


Figure 22. 3-D Configuration of Manipulators on Transmitter.

weakest, daily tuning of that color was critical to maximize the quality and rate of data output from the LDA apparatus.

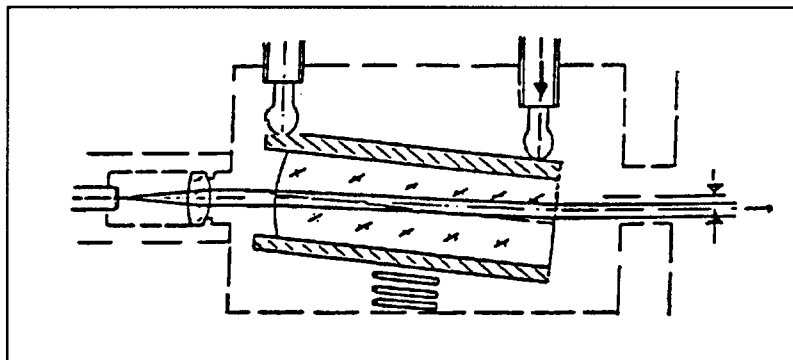


Figure 23. Laser Manipulation - Laser Enters Fiber-Optic Cable at Right.

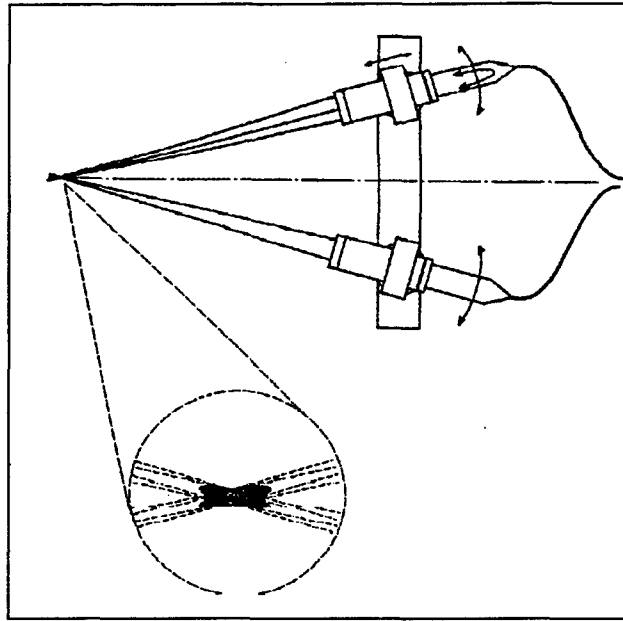


Figure 24. 3-D Probe Volume, 2-D Probe at Top, 1-D Probe at Bottom.

4.2.2 Probe Alignment. The fiber optic cables from the manipulator deck transmitted the laser light to the two probes and returned received light to the photomultipliers. The green and blue pairs of lasers were sent to the 2-D probe, and the 1-D probe received the purple pair of lasers from the transmitter. The probe optics directed the laser beams to a focal point 600 mm away, and the process of probe alignment assured that both probes were focused on the same point in space. Thus, the "probe volume" was the region of intersection of all six beams and is illustrated in Figure 24.

Coarse alignment was achieved by passing all six beams through a 100 micron pinhole as shown in Figure 25. Refining the alignment required a particle generator, such as any brand of ultrasonic humidifier or a TSI six jet atomizer (which was used for this research, model 9306, listed in Appendix A). The probe volume was placed directly over the exit of the generator and data acquisition was performed as if for a seeded flow. The

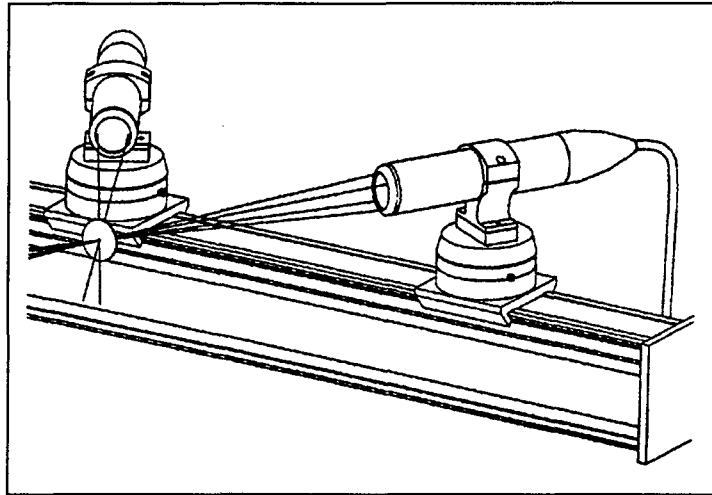


Figure 25. Passing 6 Laser Beams Through Pinhole for Coarse Alignment.

relatively large particles produced by an atomizer or humidifier resulted in very strong bursts which were easily detectable, even for roughly aligned laser probes. While monitoring the data rate on the front panel of the BSA or on the computer screen, small adjustments were made to the 1-D probe's orientation using the three adjustment knobs on the probe mount. These adjustments were made until a maximum data rate was obtained.

Fine adjustment of the probe alignment was performed with the probe volume situated in the seeded flow to be analyzed. The smaller particles from the DANTEC fog generator produced smaller bursts and were therefore more sensitive to small probe misalignments. Adjustments were made as for the atomizer until the data rate was maximized. The LDA was then ready to perform data acquisition.

#### 4.3 BSA Configuration

Although the user controlled data acquisition from the desktop computer, the BSAs governed the entire process of acquiring each individual burst, based on user-defined parameters. Proper choice of these parameters for the particular flow in question was critical to acquiring meaningful data from the LDA. Important flow qualities included

minimum and maximum expected particle velocity, turbulence intensity, proximity to reflective surfaces, seed particle density, and seed particle size. The BSA settings used for this research and reasons for their use are described in the following paragraphs.

4.3.1 Burst Frequency Bandwidth and Number of Samples. The fringe model approximation to LDA described in Appendix C states that an intersecting pair of lasers of identical frequency will create stationary planes of alternating light and dark regions called fringes. Fringe spacing is a function of laser wavelength and the angle of beam intersection, and is given by

$$s_F = \frac{\lambda_L}{2 \sin(\theta_h / 2)}, \quad (28)$$

where  $s_F$  is the distance between fringes,  $\lambda_L$  is laser wavelength, and  $\theta_h$  is the angle between the two beams. Shifting the frequency of one of the lasers will cause the fringes to scroll through the probe volume at a frequency equal to the frequency shift of the laser. A particle passing through this region will “flash” at a frequency related to its velocity given by

$$f = \frac{U_N}{s_F}, \quad (29)$$

where  $U_N$  is the particle velocity component relative to the fringes which is normal to the fringe planes, and  $f$  is the Doppler frequency of the burst. As previously mentioned, the BSAs are configured to take a set number of samples of a particle's Doppler burst, from which the Doppler frequency is calculated using a Discrete Fourier Transform (DFT),

$$f_k = \sum_{n=0}^{n=N-1} x_n e^{-i2\pi nk/N}, \quad (30)$$

where  $N$  is the number of samples,  $k$  enumerates the samples,  $n$  is the summation variable,  $x_n$  is the  $n$ -th sample of the time varying signal, and  $f_k$  is the  $k$ -th sample of the frequency spectrum. The global peak value in the power spectrum,  $p_k = |f_k|^2$ , is the Doppler frequency of the burst and was estimated using a 2nd order polynomial interpolating technique which was hardwired into the DANTEC Burst Spectrum Analyzers. Kreyzig (1987) shows that the greater the sampling frequency of  $x_n$ , the larger the frequency bandwidth defined by  $f_k$ . However, for a given number of samples, the frequency resolution of  $f_k$  decreases as the bandwidth increases. Thus, the BSAs must be configured, using the DANTEC supplied software, to detect a Doppler frequency range which encompasses the expected burst frequency (velocity) range of the particles in the flow, without exceeding that range so much as to reduce frequency (velocity) resolution significantly. For example, a frequency bandwidth corresponding to a  $U$  velocity bandwidth of 8 m/s, centered at 4 m/s, would result in velocity measurements being taken over the interval,  $0 \leq U \leq 8$  m/s. A 4 m/s bandwidth would yield more precise velocities, but would be limited to the range  $2 \leq U \leq 6$  m/s.

An additional consideration in bandwidth selection is sampling time. For the DANTEC BSAs, the rate at which samples of the time varying signal from the PM tubes were acquired (sampling frequency) was equal to 1.5 times the burst frequency bandwidth. A small bandwidth resulted in a long sampling time due to the lower sampling rate. If the sampling time exceeded the time that it took particles to traverse the widest point of the probe volume, the samples taken at the end of the BSAs sampling time were all approximately zero volts and corrupted the velocity calculation by adding noise to the

frequency spectrum. In practice, this resulted in very low data rates from the BSAs since they were designed to reject bursts which did not have a clearly defined absolute maximum in the power spectrum which was at least 4 times larger than the next largest local maximum. To avoid this, bandwidth was increased and/or the number of samples was reduced; however, these solutions were both at the expense of frequency resolution.

Determination of the optimum combination of bandwidth and number of samples was made from a calculation of the transit time of the fastest expected particles across the probe volume. Sampling time should not exceed approximately 50 to 75 percent of transit time to avoid selective rejection of the higher speed particles by the BSAs. For this research, several combinations were used, depending on the expected velocity range and signal quality for each test condition. However, the great majority of the data was acquired using 32 samples and a velocity bandwidth from approximately 8 m/s (resulting in a measured velocity range,  $0 \leq u \leq 8$  m/s) for the low speed tests ( $U_{\infty} = 3.5$  and  $7.5$  m/s) to 16 m/s (resulting in  $0 \leq u \leq 16$  m/s) for the high speed tests ( $U_{\infty} = 15.0$  m/s). This resulted in sampling times less than 50 percent of the minimum particle transit time. In some cases where signal quality from the PM tubes was poor due to light scattered from the nearby wall ( $y < 0.5$  mm), the number of samples was reduced to 16 to account for the effective shrinking of the useful probe volume to only its brightest central region.

**4.3.2 Data Acquisition Mode.** The BSAs can be configured to operate in one of three modes: continuous, controlled dead time, and burst. Continuous mode corresponds to flows where particle seeding is so dense that at least one particle can reasonably be expected to occupy the probe volume at all times. Controlled dead time mode is used in



flows with relatively low particle densities, and specifies a minimum amount of time between any two consecutive bursts to be collected by the BSAs. Finally, burst mode is also intended for sparsely seeded flows, but it instructs the BSAs to collect data on every burst which is detected.

For this research, seed particles occupied the control volume only approximately 0.01 to 0.1 percent of the time, which indicates one of the latter two modes was applicable. Since the BSA documentation suggests that controlled dead time mode is applicable only to certain specific flow situations such as reacting flows, burst mode was chosen for all data acquisition in this study.

**4.3.3 Oversize Rejection.** Larger particles will generally scatter more light than smaller particles, and will thus create brighter bursts. In high speed, turbulent flows, the larger particles may not follow the streamlines within the smallest turbulent eddies due to particle inertia. In these cases, the BSAs can be programmed to reject bursts above a certain brightness level, thus only measuring the movement of the smaller particles. The aerosol created by the DANTEC fog generator consists of roughly spherical particles which are no larger than approximately 1 micron in diameter. Tennekes and Lumley (1990) show that the smallest turbulence length scale,  $\eta_l$ , in a given flow can be estimated using the calculation  $\eta_l \approx \delta Re_\delta^{-3/4}$ . By this calculation, the smallest turbulent eddies expected for any flow condition in this research (i.e. for  $U = 15$  m/s and  $\delta = 5$  mm) were approximately 9 microns in diameter. Since the largest seed particles are an order of magnitude smaller than this scale, no oversize rejection was employed.

4.3.4 Hardware Coincidence Filtering. Coincidence filtering is the process of discriminating which bursts detected by the BSAs are from particles which traversed the 3-D probe volume defined by the simultaneous intersection of all six laser beams. The intersecting regions of each pair of lasers for this equipment (i.e. the 1-D probe volumes) were ellipsoidal and approximately 0.15 mm wide and 2.5 mm long. The long axis of the 1-D volumes were oriented along the optical centerline of the transmitting and receiving optics. LDA probes can be arranged to detect bursts from this region in one of two general ways: backscatter and forward scatter. Forward scatter requires the receiving optics be placed on the opposite side of the probe volume from the transmitting optics. This generally results in brighter bursts than for backscatter, but requires an optical path on both sides of the test section. In the backscatter technique, the receiving optics are placed on the same side of the probe volume as the transmitting optics. On-axis backscatter requires that the transmitting optics also serve as the receiving optics; whereas, in off-axis backscatter, a separate set of optics is used. The primary disadvantage of on-axis backscatter is that the receiving optics are looking down the long axis of the 1-D probe volume, resulting in a 2.5 mm ambiguity in particle transit location. Off-axis backscatter reduces this ambiguity by placing the optical axis of the receiving optics at some angle to the probe volume's long axis; thus, only bursts from that portion of the probe volume in the field of view of the receiving optics are detected. Off-axis backscatter was the technique employed in this study.

The 1-D probe, which emitted the purple lasers, was configured to detect the bursts from the blue and green lasers of the 2-D probe, and visa versa. The BSAs were

instructed (using the DANTEC supplied software, Burstware version 3.0, DANTEC (1990)) to employ a coincidence filtering scheme in which bursts would be accepted only if simultaneously detected by all three BSAs. This assured that only particles traversing the 3-D probe volume were considered. Since the angles between the 1-D and 2-D probes was 70 degrees, the irregularly shaped region of overlap of the three 1-D probe volumes was roughly ellipsoidal and approximately  $0.15 \times 0.15 \times 0.25$  mm in size.

#### 4.4 Software Configuration

Once the LDA equipment was optically aligned and the BSAs were properly configured, the controlling software (Burstware 3.0) on the desktop computer was configured. Although the BSAs controlled the data acquisition process for each burst, the Burstware controlled the overall acquisition process, including number of bursts collected, and traverse system positions. Once data acquisition was complete, the Burstware was used to convert, transform, and reduce the raw data to arrive at the velocity and turbulence values presented in the Discussion of Results chapter. The use of the Burstware in data acquisition and reduction is covered in the following three sections.

4.4.1 Data Acquisition. The procedure for data acquisition for a given day was as follows.

4.4.1.1 LDA Preparation. After warming up the Argon laser and fog generator, the manipulators were tuned, particularly if laboratory temperatures varied more than  $\pm 5$  °F since the previous day. If laboratory temperatures had remained fairly constant, it was usually necessary to tune only the purple channel, since it was weakest.

After tuning, spot location was determined, i.e. the location of the probe volume with respect to the test surface. The x location was determined by visually aligning the spot on the plate surface with guide marks placed on the transparent top and bottom endwalls. Repeated direct measurements of x distance indicate that guide mark spot location was accurate to  $\pm 1$  mm in the x direction. This error is less than 1 percent of the magnitude of all x coordinates within the test section, making the magnitude of the uncertainty relative to the x scale of the experiment no larger than that of the y and z uncertainties relative to their respective scales. For smooth surfaces, z location is arbitrary and  $z = 0$  was defined near the middle of the test plate over a region of the plate which was relatively clear of surface defects such as scratches, which could create unwanted reflections.

The y location procedure was performed carefully to avoid damage to the PM tubes. First, the voltage to the PM tube for BSA #1 (the green channel) was lowered to approximately 350-900 V using the Burstware software. This was done to prevent damage to the tube when the spot touched the surface, and the precise voltage was determined by the observed strength of the reflections from the surface. The signal from that channel was then monitored on an oscilloscope while the spot was moved toward the surface in 0.05 mm increments. When the spot touched the surface, this was noted by a large spike in the signal on the oscilloscope. The maximum voltage to the PM tube meter on the front panel of BSA #1 was monitored to prevent this from exceeding approximately 50% of saturation. If it exceeded 50%, the PM tube voltage was dropped to a lower number. When the spike reached a maximum, the brightest central portion of the probe

volume was on the surface, and the  $y = 0$  datum was defined. The PM tube was then turned off, the traversing system backed away from the surface a known distance, and the PM voltage restored to 1304 V, which is required for data acquisition. Experience indicated that  $y$  location of the spot was measurable to approximately  $\pm 0.05$  mm using this method. Over ribletted surfaces, this process is essentially the same except that both  $z$  and  $y$  adjustments were used to locate either the top of a riblet peak or the bottom of a riblet valley.

The spot was then moved 2.5 cm above the surface (or riblet peaks) to measure the freestream velocity. This distance is at least 0.5 cm larger than the maximum boundary layer thickness for any test condition in this research. The air mass flow rate was set, as described in the BLRF description, while freestream velocity was monitored. Once the proper freestream velocity was attained, it was monitored for at least five minutes to assure that "settling" of the mass regulator was complete. The settling process at low freestream velocities could take more than 30 minutes.

After the freestream velocity was set, velocity profiles were acquired while the pressure upstream of the gate valve was monitored to assure that variations did not exceed approximately  $\pm 1$  psi (the resolution of the pressure gauge). Data acquisition for a single profile required from 15 - 45 minutes, depending on the number of data points and proximity to the wall. At the end of acquisition, the freestream velocity was rechecked to assure it had not changed more than  $\pm 0.05$  m/s during acquisition. The entire procedure, from spot location on, was then repeated for each data set to be taken that day.

4.4.1.2 Software Preparation. The primary role of the Burstware in data acquisition was to control the traverse positions for each set of data, and fix the number of bursts to be collected at each position. In this software, the user defines a 1, 2, or 3 dimensional grid in space over which data is to be obtained, and selects whether or not the user is consulted before acquisition proceeds from one grid point to the next. For this work, only 1-D profiles were utilized and user control was maintained over the entire process to assure that optimal BSA settings were maintained as acquisition proceeded from one flow region to the next. The number of bursts to be collected at each grid point was determined by available data storage space and time considerations. Each grid point ultimately produced 10 data files: one binary data file from each photomultiplier containing particle transit times and Doppler frequencies (3 files), a binary data file for each photomultiplier containing particle velocities calculated from the measured Doppler frequencies (3 files), one binary file for each velocity component containing particle velocities in the laboratory coordinate system (3 files), and one ASCII file containing the average velocities and turbulence intensities calculated from all observed bursts for all three laboratory coordinate directions (1 file). The length of each data file was determined by the number of bursts collected, and machine limitations in disk capacity and file management were easily exceeded. For this research, 1000 bursts were collected per data point, which ultimately resulted in total data storage of over 600 MB in approximately 75,000 files. Total acquisition time for each 1-D profile (typically containing 50 grid points), not including BLRF configuration and warm-up, was approximately 30 minutes.

4.4.1.3 Data Conversion. The raw binary data files produced during data acquisition included particle arrival time, transit time, and Doppler frequency for all three channels for every validated burst. Bursts for which the absolute maximum of the power spectrum was less than 4 times in magnitude than the next largest maximum were automatically rejected. The data conversion process converted this data into particle velocities with respect to the three *measured* velocity components. This involved little user control beyond initiating the conversion process.

4.4.1.4 Data Transformation. The validation process used by the BSAs during acquisition resulted in a certain number of bursts for which data in one or two channels was rejected. Since 3-D data no longer existed for those bursts, the data from the remaining channels needed to be identified and rejected. This is referred to as software coincidence filtering and is the first step of the data transformation process. The second step is to take the remaining coincident data and transform the velocity components into the test section coordinates using an appropriate transformation matrix. The software for this transformation was supplied by DANTEC, but the transformation matrix was user-generated. The derivation and application of the transformation matrix for this research is described in Appendix D.

4.4.1.5 Data Reduction. The end product of the data transformation process was a set of binary files, each of which described the particle velocities for all validated, coincident bursts for one test section velocity component at one traverse location. This data included the arrival time and traverse time of each particle, and the magnitude of the transformed velocity component. During data reduction, this data was

used to produce a single file containing a summary of the important characteristics, including mean velocities, and turbulence intensities.

The method used for mean velocity calculations in this research was residence time weighting (DANTEC, 1990), which weights the contribution of each burst to the mean calculation by its transit time as follows:

$$\bar{u}_{\text{weighted}} = \frac{\sum (u_i \Delta t_i)}{\sum \Delta t_i}. \quad (31)$$

where  $u_i$  is the velocity and  $\Delta t_i$  is the transit time of the  $i$ -th particle. This diminishes the contribution of high speed particles and increases the contribution of low speed particles. This compensates for the fact that a disproportionately large number of high speed particles traverse the probe volume due solely to their higher speed, not to their greater number density in the flow.

#### 4.5 Data Acquisition Conditions and Methodology

The previous sections described the operation of the LDA equipment used in this research. The purpose of this section is to describe the test conditions and experimental procedures used during data acquisition.

4.5.1 Test Conditions. Although the test conditions were described and located on a Görtler stability diagram in Chapter II, this paragraph summarizes these conditions and includes a few extra details. Velocity and turbulence profiles, normal to and parallel to the surface of the test plate, were taken at five streamwise locations and three freestream velocities. The five streamwise locations, measured from the leading edge of the test plate, were  $x = 105, 200, 300, 400,$  and  $500$  mm. Riblet dimensions were chosen so that  $\Lambda_s$  values, given the achievable freestream velocities within the BLRF and the 1



meter radius of curvature of the test section, spanned a range from the highly amplified disturbances given by  $100 < \Lambda_s < 400$  to the non-amplified disturbances near  $\Lambda_s = 39$ . The 3 mm riblet spacing that was chosen resulted in  $\Lambda_s = 39, 79$ , and 157 for  $U_\infty = 3.5, 7.5$ , and 15.0 m/s respectively. Maximum Görtler numbers in the test section (at  $x = 500$  mm) were  $G = 7.0, 8.5$ , and 10.1 for  $U_\infty = 3.5, 7.5$  and 15.0 m/s respectively; and minimum Görtler numbers in the test section (at  $x = 105$  mm) for each velocity were  $G = 2.2, 2.6$ , and 3.1, respectively. These values of  $G$  span the range of likely GV development as outlined by Floryan (1990) and can be expected to initiate boundary layer transition within the test section, based on the  $G_{tr} \cong 7$  criteria proposed by Liepmann (1945).

4.5.2 Data Collection Method. Four test plates were used for data acquisition: a flat/smooth plate, a flat/ribletted plate, a curved/smooth plate, and a curved/ribletted plate. Flat/smooth plate data was obtained to test-out the BLRF and to determine streamwise boundary layer transition location. Data over the flat/ribletted plate was obtained to allow comparisons with both the curved/smooth and curved/ribletted plates in order to isolate the effects of curvature from the effects of riblets on boundary layer development. This data was obtained at all flow conditions and streamwise locations (same  $Re_x$ ) used for the curved plate tests. Tests over the curved/smooth plate were then performed; and, finally, the curved/ribletted tests were performed.

At each streamwise location, several velocity profiles were acquired. Vertical boundary layer profiles ( $u, v$ , and  $w$  vs.  $y$ ) were taken over the smooth surface (to within 0.4 mm from the surface) and over both riblet valleys (to within 0.6 mm from the valley bottom) and peaks (to within 0.2 mm from the riblet peak). Spanwise profiles ( $u, v$ , and  $w$

vs.  $z$ ) were taken at  $y = 1.0$  and  $3.0$  mm above the smooth surface. The  $y = 1.0$  mm station was the lowest station where data could consistently be taken over a significant spanwise range without losing data due to surface reflections, and was used to monitor vortex induced spanwise  $w$  variations, as illustrated in Figure 26. Surface reflections were smaller over the ribletted surfaces, allowing the lower station to be moved to  $y = 0.5$  mm above the peaks. For both the smooth and ribletted/curved plates, the  $y = 3.0$  mm station (where  $y = 0$  is at the smooth surface or the riblet peaks) was the location where the largest  $u$  and  $v$  velocity variations due to GVs were expected, since this was in a region of the boundary layer where the  $u$  vs.  $y$  velocity gradient was steep, but the solid surface was sufficiently far away so that vertical movement of fluid was less restricted by the wall.

#### 4.6 Data Analysis and Presentation

4.6.1 Confidence Interval Calculation. The data points in the velocity and turbulence profiles are the arithmetic mean of two measurements. Each velocity measurement was the residence time-weighted mean of the validated data from 1000 bursts, and each turbulence measurement was based on the 3-D mean-squared velocity values of those bursts as suggested by White (1991),

$$Tu = \left( \frac{1}{U} \right) \sqrt{\frac{\overline{u'^2} + \overline{v'^2} + \overline{w'^2}}{3}}, \quad (32)$$

where primed variables are the fluctuating velocity components.

It is impossible to calculate a meaningful confidence interval around a data point based on only two samples. Therefore, instead of calculating confidence intervals for each individual point, a mean confidence interval for all points within a given velocity or

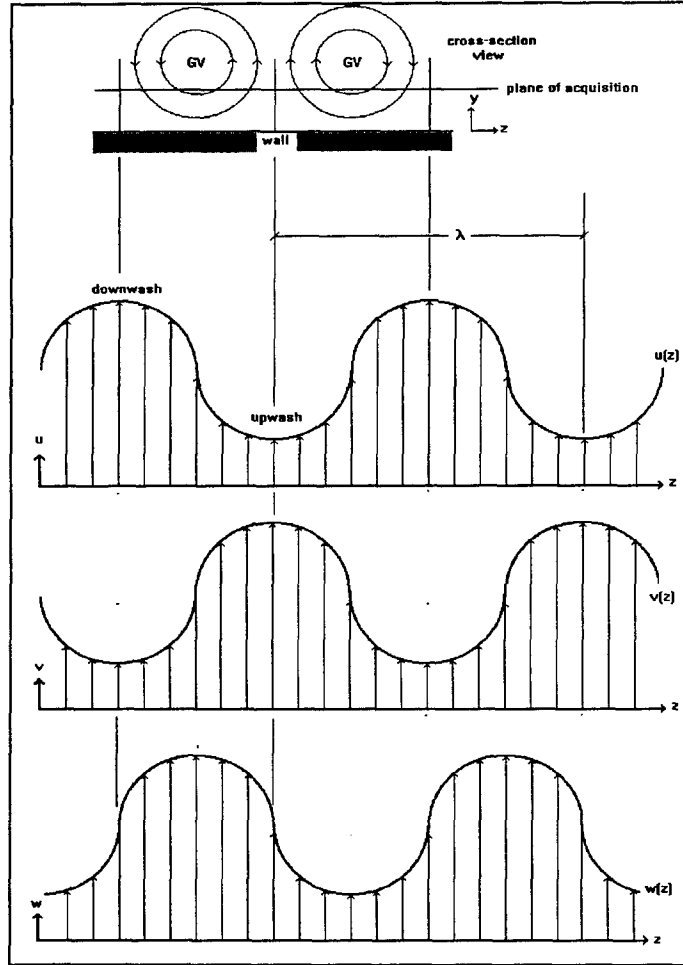


Figure 26. Velocity Component Oscillations Induced by Streamwise Vortices.

turbulence profile was estimated using the following procedure. The 90 percent confidence interval around a mean is given by Walpole and Myers (1989) as,

$$90\% \text{ confidence interval} = \pm \frac{\sigma t_{(N-1),0.05}}{\sqrt{N}}, \quad (33)$$

where  $\sigma$  is the estimate of standard deviation in the measurement,  $N$  is the number of samples, and  $t_{(N-1),0.05}$  is a value read from the Student  $t$  Distribution table.  $(N-1)$  is an integer equal to one less than the number of samples taken, and 0.05 is one-half the difference between 1.00 and the desired confidence interval (0.90 in this case). Together,

they define the row and column coordinates read from the table. To obtain a mean confidence interval for a set of data,  $\sigma$  was estimated for each velocity and turbulence profile by using the set of error values defined by the absolute value of the difference between the two measurements at each point in the profile. Thus, a 40 point velocity profile would yield a set of 40 error values. The average of this set of errors is an estimate of the probable error,  $r$ , of each measurement. This implies there is an even chance that the true velocity at a given point lies within the span  $\pm r$  around each measurement. For example, 50 measurements out of a set of 100 measurements would fall within the span about the mean ( $m$ ) given by:  $m-r < m < m+r$ . Eshbach (1975) shows that, if one assumes a normal (Gaussian) distribution in the measured values about the true value, the standard deviation of the measurement population is  $\sigma = 1.483r$ . Using this estimate for  $\sigma$ , the 90 percent confidence interval estimate for all points in the profile is given by Equation (33). To reduce clutter in certain figures, a confidence interval was included with only one of the profiles, and it represents the 90% confidence interval for all data in the figure. In figures where another method was used to produce the confidence intervals, that method is described in the corresponding text.

4.6.2 Outlier Rejection. The LDA equipment is susceptible to the occasional detection of spurious bursts due to laser reflections off the test surface. It was necessary to develop a statistical criterion for identifying and rejecting measurements which were corrupted by these bursts. An example of a velocity profile which contains two such spurious measurements is given in Figure 27. Individual measurements instead of averages are plotted on this figure, and the two "outliers" are clearly evident at  $z = -4$  mm

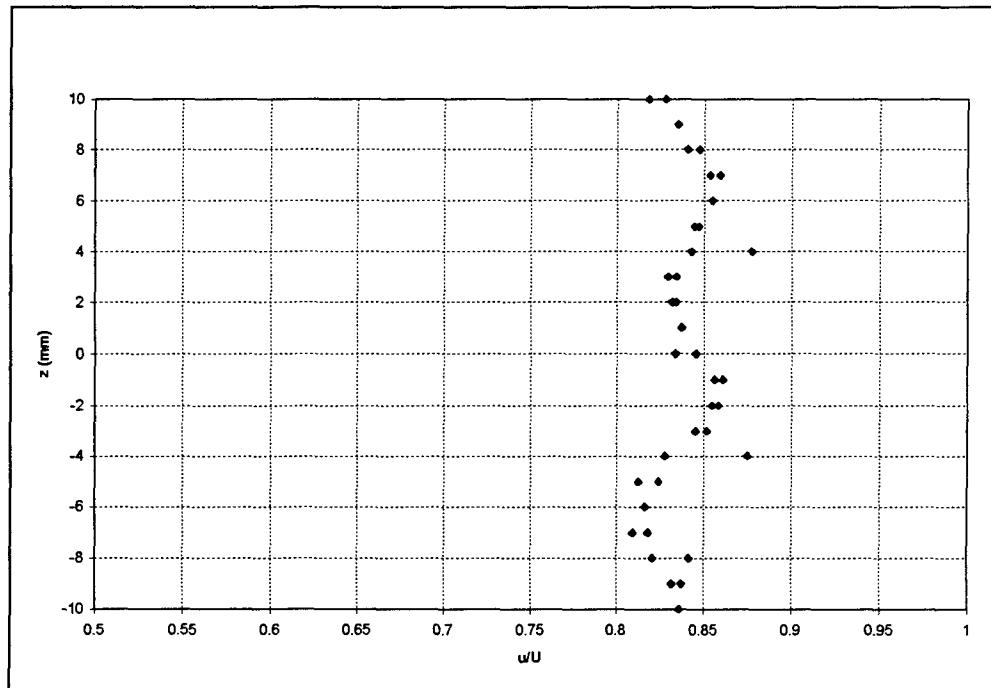


Figure 27. Outlier Examples,  $u$  vs.  $z$ , Curved/smooth,  $U = 7.5$  m/s.

and +4 mm. Eshbach (1975) notes that it is impossible to use a traditional rejection criterion such as Chauvenet with only two measurements available at each point. Therefore, outliers were identified based on the confidence interval similar to that defined in Equation (33) for this dissertation. That is, if the difference between two measurements at a given point was greater than the 99% confidence interval for the data in the profile, the point was removed. The 99% confidence interval was chosen because it implies that, given a normal distribution in measurement error, only 1 in 100 measurements could reasonably be expected to lie outside of this range. Since no profile in this research exceeded 50 points, this implies that a measurement was rejected only if one could reasonably expect such an observed difference in a measured value from the mean to exist in a set of data composed of twice as many samples as the actual set.

#### 4.7 Chapter Summary

This chapter described the experimental techniques and procedures used for the research documented in this dissertation. Alignment of the laser-Doppler equipment was addressed first, followed by a description of the BSA configurations employed. Next, the data acquisition process was described, including the methods used to adjust the BSA configuration to allow measurements to be taken very near the wall. Finally, the statistical methods used to reduce the data were documented, including methods used to weight the data, reject outliers, and calculate confidence interval estimates. In particular, a single confidence interval estimate was obtained for all points in a given velocity and turbulence profile since only two measurements of the mean were available at each point.

## V. Discussion of Results

### 5.1 Overview

This chapter begins with a description of the statistical methods used for data analysis and presentation. The observed locations of boundary layer transition will then be presented, so that the data for the rest of the chapter can be examined in context of the turbulence state of the boundary layer. Since this research includes the first ever documented measurements of GV velocity component measurements in the presence of riblets, the turbulence state of the boundary layer at each streamwise measurement station was monitored and documented. The measured surface skin friction over both ribletted and curved plates will then be presented and compared to theoretical predictions. Again, this dissertation documents the first ever measurements of laminar boundary layer skin friction over a concave surface in the presence of riblets. Finally, the effects of riblets on Görtler vortex formation will be described by comparing GV development over the curved/smooth plate to that over the curved/ribletted plate. This is the primary contribution of this research since it is the first documented analysis of the riblet-Görtler vortex interaction in a laminar boundary layer. Of particular importance, this dissertation documents the first measurements of the cross-stream velocity components attributable to the developing Görtler vortices within a laminar boundary layer over a low curvature, concave surface for which the classical theory derived in Chapter 2 strictly applies. This analysis will include a comparison of the curved/ribletted data to that obtained over the flat/ribletted plate in order to discriminate viscosity-induced flow structures over the riblets from centrifugally-induced structures. This dissertation also contains the first

documented measurements of viscosity-induced vortical flow structures within the riblet valleys in a laminar boundary layer. Due to their large number, all figures in this chapter are contained in the final section, beginning on page 104.

In short, the data indicates that riblet effects on GV development are strongly influenced by  $\Lambda_s$ . For  $\Lambda_s = 39$  ( $U = 3.5$  m/s) and  $\Lambda_s = 79$  ( $U = 7.5$  m/s), curved plate riblets delayed GV formation as compared to the curved/smooth plate. However, for  $\Lambda_s = 157$  ( $U = 15.0$  m/s), GV development appeared to be accelerated by the riblets, although the GVs were located within the riblet valleys for this case, as opposed to above the riblet peaks as was observed for both  $\Lambda_s = 39$  and  $\Lambda_s = 79$ . Additionally, no riblet effects on transition were detected for  $\Lambda_s = 39$ , transition was delayed by riblets in the  $\Lambda_s = 79$  case, and transition was accelerated for  $\Lambda_s = 157$ . Finally, riblets increased the mean surface skin friction on both the flat and curved test plates when compared to flat/smooth plate theory and to the curved/smooth plate data.

## 5.2 Boundary Layer Transition Locations

The turbulence state of the boundary layer over the flat/ribletted, curved/smooth, and curved/ribletted plates was determined by its turbulence profile,  $Tu$  vs.  $y$ . The complete set of turbulence profiles used for this analysis is given in Appendix E, and the conventions illustrated in Figure 28 are used for identifying the boundary layer state throughout this discussion. The data in this figure are from the curved/smooth plate tests for  $U = 7.5$  m/s, and show example  $Tu$  profiles for laminar, transitional, and turbulent boundary layers at  $x = 105, 300$ , and  $500$  mm respectively. For the laminar case, elevated turbulence levels within the boundary layer were small. McCormack et. al (1970) suggest



that boundary layer turbulence levels below 3% are essentially laminar; thus, Tu profiles with peak intensities less than 3% were considered laminar for this discussion. A boundary layer may be laminar with intermittent turbulent bursts, so the term "transitional" was used in this research to describe a laminar boundary layer in which turbulent fluctuations were growing. When the peak turbulence intensity exceeded 3%, the boundary layer was considered transitional. The profiles in Appendix E (Figures 102 - 116) show that the peak turbulence intensity continued to rise downstream until it reached approximately 10 percent and the boundary layer was fully turbulent. For this research the threshold for a fully turbulent boundary layer was defined as the location at which  $Tu \geq 9\%$ . The one exception to this rule was the curved/ribletted plate, for which peak turbulence intensities did not exceed 8.3 percent, even after the boundary layer peak Tu ceased growing in the streamwise direction and the boundary layer was clearly fully turbulent. The cause of this decrease in turbulence remains unclear; however, Choi (1990) noted a decrease in freestream turbulence in a fully turbulent boundary layer over riblets which he suggested was a result of the decrease in the strength of streamwise vorticity above the riblets. It is possible that the delay in GV development observed over the riblets in this research for  $\Lambda_s = 39$  and 79 had a similar effect. Even for  $\Lambda_s = 157$  where GV development was accelerated, the GVs for that case were contained within the riblet valleys (as will be shown in the following sections) and no streamwise vorticity was detected above the riblet peaks. It is difficult to formulate an experimental research project that would either corroborate or disprove this conjecture regarding the observed relationship between streamwise vorticity and boundary layer turbulence; however, with

the advent of extremely fast supercomputers, a 3-D Navier-Stokes calculation of this phenomenon may be possible, and may yield additional insight. To account for the approximately 2 percentage point decrease in maximum  $Tu$  observed over the curved/ribletted plate, the fully turbulent  $Tu$  threshold was reduced from 9 percent to 7 percent for that test plate.

For reference during the remainder of the chapter, boundary layer transition locations for all test conditions are summarized in Table 1. The uncertainties in these measured values were calculated as follows. If the peak  $Tu$  in the boundary layer for some case was below 3 percent at say  $x = 200$  mm and above 3 percent at say  $x = 300$  mm, then clearly the boundary layer was transitional at  $x = 250 \pm 50$  mm. The symbol  $>500$  indicates that the a transitional or turbulent boundary layer state was not detected within the test section. Peak turbulence data acquired over the flat/smooth plate is included in this table, but, unlike the data from the three other test plates, the flat/smooth peak turbulence values were not obtained from  $Tu$  vs.  $y$  profiles, but were acquired by manually scanning the boundary layer from  $y = 0$  to  $y \cong \delta$  with the LDA equipment until a peak  $Tu$  was detected. This value of  $Tu$  was then logged by hand, along with the corresponding  $x$  location, and plotted in Figure 29, but no  $Tu$  vs.  $y$  profile was saved to disk. This table indicates that the boundary layer became transitional at  $x \cong 350, 250,$  and  $210$  mm for  $U = 3.5, 7.5,$  and  $15.0$  m/s, respectively. The boundary layer transition point (that point where the boundary layer became turbulent) was at  $x \cong 450$  mm for  $U = 15.0$  m/s, and a fully turbulent boundary layer was not detected within the test section for  $U = 3.5$  and  $7.5$  m/s. For the remainder of this document, the terms “transition” or “transition

Table 1. Streamwise Observed Boundary Layer Transition Locations

		U = 3.5 m/s x location (mm)	U = 7.5 m/s x location (mm)	U = 15.0 m/s x location (mm)
Transition Detected	flat/smooth	350 ± 10	250 ± 10	210 ± 10
	flat/ribletted	250 ± 50	250 ± 50	150 ± 50
	curved/smooth	300 ± 100	250 ± 50	250 ± 50
	curved/ribletted	450 ± 50	450 ± 50	52 ± 52
Transition Completed	flat/smooth	> 500	> 500	450 ± 10
	flat/ribletted	450 ± 50	350 ± 50	250 ± 50
	curved/smooth	> 500	450 ± 50	350 ± 50
	curved/ribletted	> 500	> 500	150 ± 50

point” refer to the “transition completed” data in Table 1. The “Transition Detected” data is given solely to illustrate that long before boundary layer transition occurs, turbulent fluctuations are indeed present in the laminar boundary layer. To infer that this data corresponds to the point at which the boundary layer becomes unstable is incorrect since, according to White (1991), laminar boundary layers generally become unstable well upstream of the development of turbulent fluctuations. Further, White (1991) states that the transition process begins for a boundary layer when it becomes unstable, not when the first turbulent fluctuations develop. Therefore, the phrase “Transition Detected” was used in Table 1 instead of the misleading “Transition Began.”

The streamwise Reynolds number of the location where the boundary layer became fully turbulent (transition completed) versus freestream velocity is plotted in Figure 30. The error bars in this figure correspond to uncertainties in the x locations in Table 1. Only the “Transition Completed” data is plotted in this figure since those are the points to which the given transition correlations (Van Driest and Blumer (1963), Liepmann (1945), and Michel (1952)) correspond. Two transition correlations (Van Driest and Blumer

(1963), and Liepmann (1945)) are included in this figure. First, a flat plate transition correlation developed by Van Driest and Blumer (1963) as offered by White (1991), and, second, a curved plate correlation by Liepmann (1945). Since turbulence levels in the test section varied from approximately 1 percent at the entrance to 3 percent at the exit, two Van Driest and Blumer (1963) lines, one for 1.0 percent freestream turbulence intensity and another for 3.0 percent freestream turbulence intensity, are given in the figure. Finally a line denoting the maximum Reynolds number achievable within the test section (denoted by "Test section upper limit" line) is plotted. Points on this line correspond to  $Re_x$  where  $x = 500$  mm.

According to White (1991), the correlation of Van Driest and Blumer (1963) is as follows:

$$\sqrt{Re_{x,tr}} = \frac{-1 + \sqrt{1 + 132500Tu^2}}{39.2Tu^2} \quad (34)$$

where  $Re_{x,tr}$  is the transition Reynolds number. This flat plate correlation was used because it was designed to predict boundary layer transition in flows with a zero pressure gradient, taking into account the effects of freestream turbulence. The two Van Driest and Blumer (1963) correlation lines plotted in Figure 30 show that all measured transition locations lie between the  $Tu = 1.0\%$  and  $3.0\%$  predictions for both the curved and flat plates. The only measured transition point for the flat/smooth plate, for which this correlation strictly applies because all other plates were either curved and/or ribletted, was for  $U = 15$  m/s where  $Re_{x,tr} = 432,000$ . The correlation of Van Driest and Blumer (1963) (Equation (34)) predicts this same  $Re_{x,tr}$  if one assumes a freestream turbulence level of 1.1 percent, which suggests that the rise in freestream turbulence near the end of the test

section had only a small effect on the transition location. Therefore, it is apparent from Figure 30 that the measured flat/smooth plate transition point is much nearer the  $Tu = 1.0$  % line than to the  $Tu = 3.0$  % line.

Flat plate transition was accelerated by the presence of riblets for all test cases ( $Re_{x,tr}$  for ribletted plate was lower than for the smooth plate). As evident in Figure 30, the acceleration of transition by the riblets was larger for the lower velocities, but was nevertheless significant at all velocities.

As expected, curvature accelerated transition. For  $U = 15.0$  m/s, transition moved from  $Re_{x,tr} = 432,000$  over the flat/smooth surface to  $Re_{x,tr} = 337,000$  over the curved/smooth surface. For  $u = 7.5$  m/s, transition occurred at  $Re_{x,tr} = 216,000$  over the curved/smooth plate, but was not detected within the test section for the flat/smooth plate ( $Re_{x,tr} > 240,000$ ). Transition data for  $U = 3.5$  m/s was inconclusive since the boundary layer did not become fully turbulent within the test section over either the flat or curved wall.

Liepmann (1945) suggested that transition over a curved surface can be predicted by defining a transition Görtler number,  $G_{tr}$ . He showed that  $G_{tr} \cong 7$  and that the precise value of  $G_{tr}$  was constant for a given test section but could differ from one wind tunnel to the next. He attributed this variation to subtle differences between wind tunnels in the magnitude and frequency distribution of the turbulent fluctuations in the test section freestream. Since this correlation takes into account wall curvature but not the presence of riblets; it strictly applies only to the curved/smooth plate data. The plotted curve indicates that the measured transition points for the curved/smooth plate agree well with

this correlation if one assumes  $G_{tr} = 7.7$ . This is within 10% of the  $G_{tr} \cong 7$  value suggested by Liepmann (1945). Further,  $G_{tr} = 7.7$  predicts that transition should not have been detected within the test section for  $U = 3.5$  m/s, which was, in fact, the case.

Transition over the curved plate was delayed by riblets for  $U = 7.5$  m/s, but was accelerated for  $U = 15.0$  m/s. Thus, riblets for which  $\Lambda_s = 79$ , i.e. ones for which GV growth was expected to be delayed, appeared to delay boundary layer transition; whereas,  $\Lambda_s = 157$  riblets, i.e. ones expected to accelerate GV development, accelerated transition. Once again, riblet effects for  $U = 3.5$  m/s were inconclusive since transition to turbulence was not detected for either the curved/smooth or the curved/ribletted case.

A one-step transition correlation by Michel (1952) was suggested by White (1991) as an effective method of predicting transition in flat and non-flat plate flows over smooth surfaces, and is given by

$$Re_{\theta, tr} \approx 2.9 Re_{x, tr}^{0.4} \quad (35)$$

where  $Re_{\theta, tr}$  is the Reynolds number at transition (recall that “transition” refers to the end of transition) based on the momentum thickness of the boundary layer. Measured boundary layer transition points are plotted against this correlation in Figure 31. As was the case for Figure 30, the error bars in this figure were calculated directly from the  $x$  uncertainties given in Table 1. The curved/smooth plate data is near the correlation; however, both the flat and curved/ribletted plate data lie above the correlation ( $Re_{\theta, tr}$  larger than predicted) except for the  $Re_x = 102,000$ , flat/ribletted case (which corresponds to  $U = 3.5$  m/s). This increase in  $Re_{\theta, tr}$  for the ribletted surfaces may be a result of the

method used in calculating  $Re_\theta$  over riblets or that this correlation simply cannot be applied to the ribletted plate.

Since the estimated values of  $\theta$  varied from riblet peaks to valleys, a method was required for deriving a single value of  $\theta$  to be used for comparison to theoretical correlations. Thus, the arithmetic mean of  $\theta$  measured over the riblet peaks and valleys was used to estimate the average  $\theta$  over a ribletted surface.  $\theta$  was estimated from the measured velocity profiles ( $u$  vs.  $y$ ) using the trapezoidal rule numerical integration technique over both the riblet peak and valley. Appendix F (Figures 117 - 131) is dedicated to the complete set of velocity profiles used in making these calculations.

Using this method for calculating  $\theta$ , differences between the observed and predicted values of  $Re_{\theta,tr}$  over riblets increased as  $Re_x$  increased. Large  $Re_x$  corresponded to large freestream velocities; and, hence, to larger values of  $\Lambda_s$ . Thus, this data implies that, for ribletted plates, as  $\Lambda_s$  increases,  $Re_{\theta,tr}$  grows large with respect to the value predicted for a smooth surface. Conversely, for riblets which have low values of  $\Lambda_s$  ( $\Lambda_s = 39$  for this data),  $Re_{\theta,tr}$  is nearly identical to the smooth plate prediction of Michel (1952).

### 5.3 Skin Friction Measurements

A sufficient number of  $u$  vs.  $y$  profiles was obtained to allow an estimate of the mean surface skin friction from  $x = 105 - 400$  mm to be calculated for each test case. To understand the procedure for measuring the mean surface skin friction, consider a flat plate with a fluid flowing parallel to the surface. Skin friction can be expressed in terms of the non-dimensional skin friction coefficient,  $C_f$ , defined as (White, 1991),

$$C_f = \frac{2\tau_w}{\rho U^2} \quad (36)$$

where  $\tau_w$  is the local surface shear stress, which is the drag force per unit surface area produced by the viscosity of the fluid flowing over it:

$$\tau_w = \frac{\text{Drag}}{\text{Area}} \quad (37)$$

The “Area” in this case refers to the geometric area, such as given by the length multiplied by the width of a rectangular surface for example. For a perfectly smooth surface, the wetted area of the surface is equal to the geometric area; however, for a rough or ribletted surface, the wetted area is larger than the geometric area. An increase in wetted area generally produces more drag on the surface, increasing the value of  $\tau_w$ , thereby increasing  $C_f$ . In other cases, such as when riblets in a turbulent boundary layer are appropriately sized so that the drag on the surface is decreased despite the increase in wetted surface area,  $C_f$  decreases.

White (1991) shows that, for a zero pressure gradient,

$$C_f = 2 \frac{d\theta}{dx} \quad (38)$$

This relationship can be integrated over a portion of a surface from streamwise location  $x_1$  to  $x_2$  to yield an expression for the average skin friction coefficient,

$$C_{f,ave} = \frac{2(\theta_{x_2} - \theta_{x_1})}{(x_2 - x_1)} \quad (39)$$

where  $\theta_{x_1}$  and  $\theta_{x_2}$  are the momentum thicknesses of the boundary layer at  $x_1$  and  $x_2$  respectively.



A plot of  $C_{f,ave}$  from  $x_1 = 105$  mm to  $x_2 = 400$  mm, calculated from the velocity profiles given in Appendix F (Figures 117-131), is given in Figure 32. Each point in this figure is labeled with the portion of the  $x_1$  to  $x_2$  range over which a turbulent boundary layer existed (i.e. “1/3t” designates that one-third of the surface, or more specifically,  $x > 300$  mm, was covered by a turbulent boundary layer). Also on this plot is a curve (solid line) representing the theoretical value of  $C_{f,ave}$  over this  $x$  range for a laminar boundary layer over a flat plate derived from the expression for  $C_f$  given by White (1991),

$$C_{f,laminar} = \frac{0.664}{\sqrt{Re_x}}. \quad (40)$$

In addition, White (1991) suggests the following expression for the local skin friction coefficient in a turbulent boundary layer:

$$C_{f,turbulent} = \frac{0.027}{Re_x^{1/7}}. \quad (41)$$

The average  $C_f$  calculated from this expression is plotted in Figure 32 with a dashed line. If one assumes constant  $\nu$ , both of these  $C_f$  expressions are functions of  $x$  and  $U$  since  $Re_x$  is a function of  $x$ ,  $U$ , and  $\nu$ . The location of the laminar and turbulent theoretical value lines was determined by numerically integrating the given  $C_f$  expression using an Excel 5.0 spreadsheet from  $x_1$  to  $x_2$  for a selected value of  $U$ , and the resulting number was divided by  $x_2 - x_1$ . These calculations were performed for 20 values of  $U$  between  $U = 0.5$  and  $15.0$  m/s to produce the plotted curves.

The curved/smooth plate data lies near the laminar  $C_{f,ave}$  curve. For  $U = 15.0$  m/s, the small increase in measured skin friction in the curved/smooth data compared to the laminar curve is a result of the contribution of the turbulent boundary layer over  $x = 350$

to 400 mm, since the skin friction in a turbulent boundary layer is nearly an order of magnitude higher than that for a laminar boundary layer (White, 1991). However,  $C_{f,ave}$  for the two ribletted cases is higher than the smooth plate data and increases with freestream velocity to values in excess of the fully turbulent curve at  $U = 15.0$  m/s. This effect is particularly pronounced for the curved/ribletted case and is due to both the rapid transition of the boundary layer to turbulence at  $U = 15.0$  m/s for this case and the doubling of the wetted surface area due to the presence of riblets. Even for  $U = 7.5$  m/s, the increase in wetted surface area due to the riblets resulted in a net increase in the average skin friction coefficient compared to the smooth plate data. This is significant because, for that case, the riblets delayed boundary layer transition over the curved plate, resulting in a laminar boundary layer over a larger portion of the  $x_1 - x_2$  regime. Even though laminar boundary layers produce much smaller values of  $C_f$ , this effect was apparently more than offset by the increase in drag produced by the increased wetted surface area of the riblets.

#### 5.4 Boundary Layer Perturbation Measurements

5.4.1 Overview. This section will describe the evolution of boundary layer disturbances over the flat/ribletted, curved/smooth, and curved/ribletted plates. Three types of disturbances were detected: 1.) centrifugally induced Görtler vortices, 2.) viscosity induced riblet-valley vortices, and 3.) spanwise periodic, non-vortical velocity perturbations over the curved/ribletted plate which appear to precede the development of GVs and may play a role in the delay of GV development. The data acquired over each

plate will be discussed separately, beginning with the flat/ribletted plate, proceeding to the curved/smooth plate, and concluding with the curved/ribletted plate.

5.4.2 Flat/Ribletted Plate. The flow over the upstream portion of this plate was characterized by the development of strong spanwise shear ( $du/dz$ ) in the  $y = \text{constant}$  plane immediately above the plane of the riblet peaks. This shear is illustrated by the  $u$  vs.  $z$  profiles taken 0.5 mm above the riblet peaks at  $x = 105$  mm given in Figure 33. The riblet peaks were located at  $z = 1.5$  and  $4.5$  mm on this figure, and the shear was particularly pronounced for the two higher speed cases. The shear relaxed downstream, as evidenced by Figures 34 - 37 which show the evolution of the  $u$  vs.  $z$  profiles at  $y = 0.5$  mm for  $x = 200 - 500$  mm.

The mechanism which replaced the high speed fluid over the riblet valleys in Figure 33 at  $z = 0.0, 3.0$ , and  $6.0$  mm with the relatively low speed fluid at the same  $z$  locations in Figure 37 appears to have been paired, counterrotating, riblet-valley vortices. A set of these vortices is shown schematically in Figure 38. Two pieces of evidence support this conclusion: 1.) much of the low speed fluid appearing over the riblet valleys appears to have been produced at the riblet peaks, and 2.) the cross stream ( $v$  and  $w$ ) velocity components associated with these riblet-valley vortices are consistent with the transport of fluid from the peak region to the valley region of the riblets. These two phenomena are described in detail in the following two paragraphs.

The majority of low speed fluid production in the boundary layer was occurring at the riblets peaks and not in the valleys because the wall shear stress,  $\tau_w$ , was an order of magnitude larger at the peaks than that at the base of the valleys. This is particularly true

over the upstream half of the plate and is illustrated in Figures 39 and 40 which show the  $u$  vs.  $y$  profiles over a riblet peak and valley, respectively, at  $x = 105$  mm ( $y = 0$  is at the peak and valley in Figures 39 and 40 respectively). The magnitude of  $du/dy$  at  $y = 0$  over the riblet peak (Figure 39) is approximately 30, 18, and 9 times the magnitude over the valley (Figure 40) for  $U = 3.5$ ,  $7.5$ , and  $15.0$  m/s respectively. Since the production of low speed fluid in a boundary layer is proportional to the magnitude of the shear stress at the wall (White (1991)), it appears the majority of low speed fluid within the boundary layer was being created at the riblet peaks. Thus, it follows that the decrease in fluid velocity noted over the riblet valleys in the  $u$  vs.  $z$  profiles was at least partially due to the spanwise transport of fluid from the riblet peaks to the valleys.

The second piece of evidence supporting the theory that riblet-valley vortices were responsible for the population of the riblet valleys with low momentum fluid was the detection of the cross stream velocity components associated with those vortices. The  $w$  vs.  $z$  profiles taken  $0.5$  mm over the riblet peaks at all five streamwise locations are given in Figures 41 - 45. As for previous spanwise profiles, the riblet peaks were located at  $z = 1.5$  and  $4.5$  mm and the valleys were located at  $z = 0.0$ ,  $3.0$ , and  $6.0$  mm. No perturbations were detected at  $x = 105$  or  $200$  mm; however, at  $x = 300$  mm, spanwise periodic  $w$  perturbations consistent with streamwise vorticity become evident for  $U \cong 7.5$  and  $15.0$  m/s. At  $x = 400$  and  $500$  mm, these perturbations are evident for all three freestream velocities. On Figure 38, one can see that, in a  $y = \text{constant}$  plane immediately above the riblet peaks, if data acquisition moves in a positive  $z$  direction from a location directly above a peak, then the  $w$  velocity component should be positive for the vortex

geometry illustrated. This is the observed trend in all  $w$  vs.  $z$  data given in Figures 41 - 45 for which  $w$  perturbations were detected.

In order to confirm vortical motion, spanwise periodic perturbations in the  $v$  velocity component must also exist. Specifically, the vortices illustrated in Figure 38 would induce positive  $v$  values over the riblet peaks and negative values over the valleys. Figures 46 - 50 depict the  $v$  vs.  $z$  profiles obtained 0.5 mm above the riblet peaks at all 5 streamwise locations. As before, riblet peaks are at  $z = 1.5$  and  $4.5$  mm, and the valleys are at  $z = 0.0$ ,  $3.0$ , and  $6.0$  mm. These figures indicate ascending fluid particles over the riblet peaks and descending particles over the valleys as predicted; thus, confirming the presence of the paired, riblet-valley vortices. The  $x = 300$  mm appearance of the  $v$  perturbation coincided with the  $w$  perturbation for  $U \cong 7.5$  and  $15.0$  m/s; however, for  $U \cong 3.5$  m/s, the  $v$  perturbations were not clearly evident until  $x = 500$  mm. Thus, paired riblet valley vortex formation for the flat plate occurred at  $x = 300$  mm for  $U \cong 7.5$  and  $15.0$  m/s, and at  $x = 500$  mm for  $U \cong 3.5$  m/s. Note that vortex development preceded final transition of the boundary layer to turbulence in all three cases, suggesting that the turbulent boundary layer (TBL) riblet-valley vortices observed by Suzuki and Kasagi (1994) (Figure 10) may actually form while the boundary layer is laminar. For all cases, the wavelength of these vortices was equal to the riblet spacing,  $s$ . Finally, the theory that these vortices were induced by the spanwise shear between the riblet peaks is corroborated by the fact that vortex formation occurred relatively late for the  $U \cong 3.5$  m/s case, where maximum values of  $du/dz$  were initially much lower in magnitude than for the other two velocities.

These paired, riblet-valley vortices appeared to extend approximately 1.5-2.0 mm above the plane of the riblet peaks. This is illustrated in the  $v$  vs.  $y$  profiles given in Figure 51, taken at  $x = 300$  mm. In this figure, the  $y$  datum is at the bottom of the riblet valley; thus, the riblet peaks correspond to  $y = 2.6$  mm (the dashed line on the figure). The vortex-induced  $v$  perturbations extend up to approximately  $y = 4.5$  mm, which is approximately 1.9 mm above the peaks. In addition, this data contrasts the  $v$  vs.  $y$  profiles for a case where no riblet-valley vortices were yet present ( $U \cong 3.5$  m/s) to two cases where they were present ( $U \cong 7.5$  and  $15.0$  m/s).

**5.4.3 Curved Smooth Plate.** This test configuration reproduced the flow conditions used in the formulation of the Görtler theory presented in Chapter 2. Its primary purpose was to generate GVs and measure the GV-induced velocity perturbations in all three directions. This information yielded GV wavelength and streamwise locations for each freestream velocity. Approximate observed GV wavelengths were  $\lambda \cong 12.3, 8.4,$  and  $4.1$  mm for  $U = 3.5, 7.5,$  and  $15.0$  m/s, and were calculated by measuring the peak-to-peak distances in the  $u, v,$  and  $w$  vs.  $z$  profiles at all locations where GVs were detected, and taking the average of those measurements. These wavelengths correspond to  $\Lambda = 306, 370, 252$  for  $U = 3.5, 7.5, 15.0$  m/s, respectively.

These wavelength estimates are approximate because GV wavelength tended to vary in the spanwise direction from one vortex to the next. Individual vortex wavelengths ranged from 10-15 mm for  $U \cong 3.5$  m/s, 7 - 9 mm for  $U \cong 7.5$  m/s, and 2 - 6 mm for  $U \cong 15.0$  m/s. The wide variation in measured wavelengths for  $U \cong 15.0$  m/s is probably

exaggerated by the limited spanwise resolution of the velocity profiles. Data was obtained at  $\Delta z = 1.0$  mm increments, which is fully half the size of the smallest detected GVs.

GV existence was confirmed only where spanwise periodic oscillations in all three velocity components were detected. GVs were first detected at  $x = 400$  mm for  $U \cong 3.5$  and  $7.5$  m/s, and at  $x = 300$  mm for  $U \cong 15.0$  m/s. In all three cases, these streamwise positions correspond with a transitional boundary layer; however, Floryan (1990) states that initial GV development begins well upstream of the location of earliest experimental detection since the early GVs are so weak. In all cases, GVs were detectable to the exit of the test section at  $x = 500$  mm. The data from each location at which GVs were detected are plotted on a Görtler stability diagram in Figure 52.

The spanwise  $u$  vs.  $z$  profiles given in Figures 53 - 55 illustrate the streamwise GV development for each freestream velocity. The  $y$  station chosen for the data in each of these figures is the station where oscillations in the  $u$  vs.  $z$  profile were first detected for that velocity, and the  $z$  datum is not necessarily consistent from one profile to the next in each figure. In Figures 53 and 54, the periodic variations are visible in the  $x = 400$  and  $500$  mm profiles and the average peak-to-peak distances are  $12.0$  mm for  $U = 3.5$  m/s, and  $8.5$  mm for  $U = 7.5$  m/s. In Figure 55, the  $u$  oscillations are visible at  $x = 300$ ,  $400$ , and  $500$  mm and have a mean peak-to-peak distance of  $4.6$  mm.

As previously discussed, the peaks (local maxima) in the  $u$  profiles correspond to downwash regions between two GVs; thus, the  $v$  velocity must be at a local minimum. Conversely, valleys (local minima) in the  $u$  profiles correspond to upwash regions between GVs where low speed fluid is moving away from the wall; thus, the  $v$  velocity in these

areas must be at a local maximum. The  $v$  vs.  $z$  profiles in Figures 56 - 60 are consistent with these trends. For every local maximum in Figures 53 - 55, there is a corresponding local minimum within  $z = \pm 1$  mm in Figures 56 - 60. To reduce clutter in the figures, only profiles in which spanwise periodic oscillations were detected are shown and the profiles for the  $U \cong 15.0$  m/s cases at  $x = 300, 400,$  and  $500$  mm are placed in separate figures. The relatively large uncertainty in these measurements, denoted by the large error bars, is a result of the small size of the GV-induced  $v$  velocities, which ranged from approximately 7 to 200 mm/s. The mean spanwise peak to peak distances in these profiles are 12.5 mm for  $U \cong 3.5$  m/s, 7.7 mm for  $U \cong 7.5$  m/s, and 4.0 mm for  $U \cong 15.0$  m/s.

Streamwise vorticity will also induce spanwise variations in the  $w$  velocity component with a wavelength identical to that of the vortices. The  $w$  vs.  $z$  profiles in which spanwise periodic perturbations were detected are given in Figures 61 - 65. These profiles were taken at  $y = 1.0$  mm, which was the station where  $w$  perturbations were most visible. As for the  $u$  and  $v$  vs.  $z$  data, the  $U \cong 15.0$  m/s profiles in Figures 63 - 65 illustrate the spanwise irregularity in GV wavelength because the data window ( $z = \pm 10$  mm) spans several vortices. The average peak-to-peak distances in these profiles are 12.5 mm, 9.0 mm, and 3.6 mm for  $U \cong 3.5$  m/s,  $U \cong 7.5$  m/s, and  $U \cong 15.0$  m/s respectively.

**5.4.4 Curved/Ribletted Plate.** This discussion will be split into two subsections, based on two regions within the boundary layer where the observed riblet-boundary layer interactions were qualitatively different: the lower boundary layer and the upper boundary layer. The lower boundary layer is defined as the region where  $y < 1.0$  mm above the riblet peaks; and, thus, it is the flow within and just above the riblets. Data from this



region will be compared to the data taken over the flat/riblet plate since riblet disturbances over the flat plate were primarily confined to the lower boundary layer. The upper boundary layer is defined as that region where  $y \geq 1$  mm. The data from this region will be compared to the curved/smooth plate data, since GV development took place primarily in this part of the boundary layer.

The data in this section indicates that paired riblet-valley vortices in the lower boundary layer did not coexist with GVs in the upper boundary layer at any of the freestream conditions and streamwise locations tested. For  $U \cong 3.5$  m/s, riblet-valley vortices never developed. Instead, only GVs of similar wavelength to the curved/smooth case were detected. For  $U \cong 7.5$  m/s, riblet-valley vortices developed upstream of the observed GV locations, but disappeared when the Görtler vortices formed in the upper boundary layer. For  $U \cong 3.5$  and  $7.5$  m/s, GV development was delayed compared to the curved/smooth plate. Finally, for  $U \cong 15.0$  m/s, riblet-valley vortices existed for the entire length of the test section, and no upper boundary layer GV development was detected.

5.4.4.1 Lower Boundary Layer. The spanwise shear in the  $u$  vs.  $z$  profiles which was noted over the flat/riblet plate also existed over the curved/riblet plate. Figures 66 - 70 depict the  $u$  vs.  $z$  profiles at each streamwise location. The maximum shear in the  $U \cong 15.0$  m/s data diminishes downstream more rapidly than for the flat/riblet case; however, the data otherwise resembles that for the flat/riblet plate from  $x = 105 - 400$  mm. At  $x = 500$  mm (Figure 70), the  $U \cong 3.5$  and  $7.5$  profiles exhibit a relatively large scale gradient in the  $z$  direction, as if under the influence of a long

wavelength disturbance. The upper boundary layer data will show that this was due to the development of relatively long wavelength GVs in the boundary layer.

The  $w$  vs.  $z$  profiles obtained over this test plate are given in Figures 71 - 75. At  $x = 105$  mm (Figure 71), strong  $w$  perturbations were present for  $U \cong 15.0$  m/s, which is 195 mm upstream of where perturbations were initially detected for the flat/ribletted case. These perturbations have an amplitude of  $w/U \cong \pm 0.03$ , which is larger than any observed  $w$  disturbances over the flat plate. At  $x = 200$  mm (Figure 72), the  $w$  perturbation for  $U \cong 15.0$  m/s was smaller in amplitude than at  $x = 105$  mm, but still large compared to any observed over the flat plate. In addition, a weak disturbance appeared for the  $U \cong 7.5$  m/s case, 100 mm upstream of earliest disturbance detection over the flat plate. At  $x = 300$  mm (Figure 73), the amplitude of the perturbation for  $U \cong 15.0$  m/s was approximately the same as for the flat plate; however, the disturbance present for  $U \cong 7.5$  m/s was still relatively weak. At  $x = 400$  mm (Figure 74), the  $U \cong 7.5$  m/s disturbance was no longer evident. Finally, at  $x = 500$  mm (Figure 75), the  $U \cong 15.0$  m/s disturbance remained essentially unchanged; however, evidence of a large scale disturbance with wavelength longer than the 6 mm width of the profiles existed for  $U \cong 7.5$  and 3.5 m/s. Again, the upper boundary layer data will show that this was due to the influence of GVs in the upper boundary layer.

The presence of vortical motion was confirmed by the  $v$  vs.  $z$  profiles given in Figures 76 - 80. As was the case for the flat/ribletted plate, the vortices were oriented so that  $v$  was positive over the peaks and negative over the valleys. Unlike the flat/ribletted plate,  $v$  perturbations were evident for  $U \cong 7.5$  and 15.0 m/s over the range  $x = 105 - 500$

mm. For the flat/ribletted plate, these perturbations were restricted to  $x \geq 300$  mm. At  $x = 500$  mm (Figure 80), disturbances for  $U \cong 3.5$  and  $7.5$  m/s appear to be a superposition of 3 mm wavelength riblet-induced velocities and a larger wavelength component similar to the GV-induced perturbations evident in the  $u$  and  $w$  vs.  $z$  data at  $x = 500$  mm. The  $U \cong 15.0$  m/s data exhibits the same 3 mm wavelength riblet-induced perturbation present in the data taken upstream, but no long wavelength disturbance similar to that observed for the lower speed cases is evident.

When analyzed in its entirety, the  $u$ ,  $v$ , and  $w$  vs.  $z$  data discussed above indicates that plate curvature affects riblet-valley vortex development in a manner depending on freestream velocity (or, alternately,  $\Lambda_s$ ). For  $U \cong 3.5$  m/s ( $\Lambda_s = 39$ ), riblet valley vortices had developed by  $x = 500$  mm over the flat plate, but none developed over the curved plate. For  $U \cong 7.5$  m/s ( $\Lambda_s = 79$ ), vortices developed 100 mm further upstream (at  $x = 200$  mm) as a result of curvature, but disappeared by  $x = 400$  mm. In addition, vortex induced  $v$  and  $w$  velocities were smaller in magnitude over the curved plate than they were over the flat plate for  $U \cong 7.5$  m/s. At  $x = 105$  and  $400$  mm,  $v$  perturbations with a 3 mm wavelength were detected for  $U \cong 7.5$  m/s, but no corresponding  $w$  perturbations were detected; therefore, the existence of vortices cannot be confirmed at those  $x$  stations. Finally, for  $U \cong 15.0$  m/s ( $\Lambda_s = 157$ ), riblet-valley vortices developed at least 195 mm further upstream as a result of curvature, and existed over the entire length of the test section. The  $v$  and  $w$  velocity perturbations were generally equal to or larger than those observed over the flat plate.

5.4.4.2 Upper Boundary Layer. Now that the lower boundary layer flow structures have been described, this section describes the flow patterns observed in the upper boundary layer ( $y > 1.0$  mm). Görtler vortices form in the upper boundary layer over the curved/ribletted plate only for the  $U \cong 3.5$  and  $7.5$  m/s cases. In addition, clearly defined GV induced  $u$ ,  $v$ , and  $w$  velocity perturbations existed only at the exit of the test section ( $x = 500$  mm) for these two freestream velocities, indicating a delay of approximately 100 mm in GV formation compared to the flat/ribletted plate. The geometry of this upper boundary layer GV formation is illustrated in Figure 81 for one pair of Görtler vortices with wavelength approximately equal to three times the riblet spacing. Under no test conditions were GVs detected in the upper boundary layer for  $U \cong 15.0$  m/s.

The  $u$  vs.  $z$  profiles at all streamwise locations where upper boundary layer disturbances were detected are given in Figures 82 and 83. The  $y$  stations chosen for these figures are those stations where velocity perturbations were first detected. The profiles for the  $U \cong 3.5$  m/s case in Figure 82 indicate that a small amplitude disturbance developed in the boundary layer at  $x = 300$  mm with a wavelength of approximately 5 - 8 mm. By  $x = 400$  mm, this disturbance was superimposed on a larger amplitude disturbance with a wavelength of about 15 mm. Finally, at  $x = 500$  mm, the shorter wavelength disturbance had nearly vanished, and only a relatively large amplitude disturbance with wavelength equal to approximately 13 mm remained. Cross stream velocity data will show that the 13 mm wavelength disturbance at  $x = 500$  mm was actually a set of streamwise vortices similar to the curved/smooth plate Görtler vortices.

The profiles for the  $U \cong 7.5$  m/s case given in Figure 83 indicate a similar evolution in the upper boundary layer from a relatively short wavelength disturbance at  $x = 300$  mm to a longer wavelength disturbance at  $x = 500$  mm. The initial disturbance at  $x = 300$  mm had a wavelength similar to the riblet spacing ( $\lambda = 3.0$  mm), and the final disturbance had a wavelength of  $\lambda \cong 9$  mm, which is approximately the same as the  $\lambda = 7 - 9$  mm GV's detected over the curved/smooth plate. Again, the cross stream velocities indicated that the  $x = 500$  mm disturbance was in fact associated with streamwise vortical motion.

The cross stream  $v$  and  $w$  vs.  $z$  velocity profiles associated with the above  $u$  vs.  $z$  profiles are given in Figures 84 - 89. For  $U \cong 3.5$  m/s (Figures 84 - 86), no clear  $v$  or  $w$  perturbations existed at  $x = 300$  mm; however, a  $v$  velocity perturbation with the same superimposed short and long wavelength disturbances as was observed in the  $u$  vs.  $z$  data in Figure 82 was evident at  $x = 400$  mm (Figure 85). Finally, at  $x = 500$  mm (Figure 86), both  $v$  and  $w$  oscillations with wavelength approximately equal to the smooth plate GV's and to the oscillation observed in the  $u$  vs.  $z$  data are evident. The  $x = 500$  mm station was the only station where  $w$  oscillations were visible; and, thus, it was the only station where vortices were detected. For  $U \cong 7.5$  m/s (Figures 87 - 89), a disturbance with a wavelength of approximately 2-3 mm is evident at  $x = 300$  mm in the  $v$  profile. At  $x = 400$  mm, this disturbance had nearly disappeared from the  $v$  profile, but a new, longer wavelength disturbance was becoming evident for  $z > 4$  mm and  $z < -4$  mm in both the  $v$  and  $w$  profiles. However, the spanwise periodic patterns in both the  $v$  and  $w$  profiles associated with the long wavelength disturbance was not clearly evident until  $x = 500$  mm (Figure 89), where the observed wavelength was approximately 9 mm. This wavelength is

approximately the same as the  $\lambda = 7 - 9$  mm disturbances observed in the GVs over the curved/smooth plate at this freestream velocity.

### 5.5 Summary of Results.

The major findings described in this chapter were supported by the use of a new wavelength parameter,  $\Lambda_s$ , to indicate the correlation of riblet spacing with GV wavelength and location. A new wind tunnel was constructed for the investigation of Görtler vortex development and three-dimensional velocity measurements within the boundary layer over four plates. This research yielded the following results:

#### 1. Flat-Smooth Plate

- Boundary layer transition points determined from turbulence profiles for three freestream velocities agreed with those found in the classical treatment of laminar boundary layer theory.

#### 2. Flat-Ribletted Plate

- Paired, counterrotating vortices, nested in the riblet-valleys, were found for three freestream velocities. High freestream velocities caused an earlier development of these vortices ( $x \cong 300$  mm for higher speeds in contrast with  $x \cong 500$  mm for the low-speed case).

- The location of transition as determined from turbulence profiles occurred upstream (earlier) than those found on the smooth plate. For the low-speed case ( $U = 3.5$  m/s), transition occurred approximately 50 mm earlier progressing to 200 mm earlier for the high-speed ( $U = 15.0$  m/s) case. A byproduct of the earlier transition with

riblets is an increased skin friction coefficient which was verified through the measurement of momentum thickness and the use of the Von Karman momentum integral.

### 3. Curved-Smooth Plate

- First-ever measurements of three velocity components in Görtler vortices for three freestream velocities identified the wavelength and location of initiation of the Görtler vortices. The vortices remained stationary (did not meander) for a period of time up to approximately 45 minutes. The non-dimensional wavelength,  $\Lambda$ , varied between 252 and 306, as shown in Table 2, a range for which Görtler stability theory predicts the greatest likelihood of GV development. For the high-speed case, GVs persisted through the transition region ( $105 < x < 400$  mm) and into the fully turbulent boundary layer region, though the beginnings of vortex breakup were indicated in this latter region.

- Skin friction coefficients as determined from boundary layer profiles indicated for the low-speed cases ( $U = 3.5$  and  $7.5$  m/s), where boundary layers were essentially laminar over the extent of the measurement region, agreement with values from laminar boundary layer theory for a flat plate. For the high-speed case, the boundary layer was in a transitional state, and the skin friction coefficient was larger than indicated by laminar flow theory but less than for a turbulent boundary layer over a flat plate.

### 4. Curved-Ribletted Plate

- For riblet spacing matching a GV wavelength which would likely occur ( $U = 15.0$  m/s,  $\Lambda_s = 157$ ) and be amplified according to Görtler stability theory, paired streamwise vortices developed and nested in riblet valleys in a similar manner to those observed for the flat-ribletted surface. For this case, both initiation of transition and

Görtler vortex formation occurred earlier than observed for the smooth plate.

Interestingly, the nested pairs persisted unattenuated in the turbulent boundary layer region up to the end of the measurement region. A byproduct of the earlier transition was an increased average skin friction coefficient over the plate.

- For riblet spacing matching riblet wavelengths not likely to occur or be amplified ( $U = 3.5$  and  $7.5$  m/s,  $\Lambda_s = 39$  and  $79$ , respectively), suppression did not occur; instead, vortices formed above the riblet surface with similar wavelength to those observed for the smooth surface. For these cases, vortex development and boundary layer transition occurred downstream of the location observed on the smooth surface.

- For riblet spacing intended to induce lightly amplified GV's ( $U = 7.5$  m/s,  $\Lambda_s = 79$ ), nested, paired vortices formed and disappeared early on the plate prior to the formation of the larger vortices external to the riblets. Subsequent skin friction measurements indicated a value approximately 2.5 times that for the smooth surface.

- For riblet spacing equivalent to an attenuated disturbance wavelength ( $U = 3.5$  m/s,  $\Lambda_s = 39$ ), no nested-paired vortices were seen, and skin friction was only slightly greater (11%) than for the smooth surface.

A riblet-spacing parameter was developed,  $\Lambda_s$ , which was used to predict riblet effects on GV development. Riblets for which  $\Lambda_s > 100$  correspond to strongly unstable disturbances, and were predicted to accelerate GV development and produce GV's with wavelengths corresponding to  $\Lambda = \Lambda_s$ .  $\Lambda_s = 157$  was the largest value investigated in this research. Riblets for which  $\Lambda_s < 100$  produce weakly reinforced disturbances, and were predicted to delay GV development, but not affect GV wavelength.



Table 2. Summary of Riblet Effects on GV Wavelength and Location.

U (m/s)	Without Riblets			With Riblets		
	GVs formed by $x =$ (mm)	$\lambda$ (mm)	$\Lambda$	GVs formed by $x =$ (mm)	$\lambda$ (mm)	$\Lambda$
3.5	400	12.3	306	500	13.0	332
7.5	400	8.4	370	500	9.0	410
15.0	300	4.1	252	105	3.0	157

The observed riblet effects on GV development follow the predicted trends based on the riblet spacing parameter,  $\Lambda_s$ . These results are summarized in Table 2. For  $U = 3.5$  m/s ( $\Lambda_s = 39$ ) and  $U = 7.5$  m/s ( $\Lambda_s = 79$ ), GV development was delayed by the addition of riblets to the curved surface, and GV wavelength over the ribletted surface was approximately the same as for the smooth surface. For  $\Lambda_s = 157$ , GV development was accelerated by the riblets and GV wavelength was changed by the riblets to equal the riblet spacing.

## 5.6 Figures

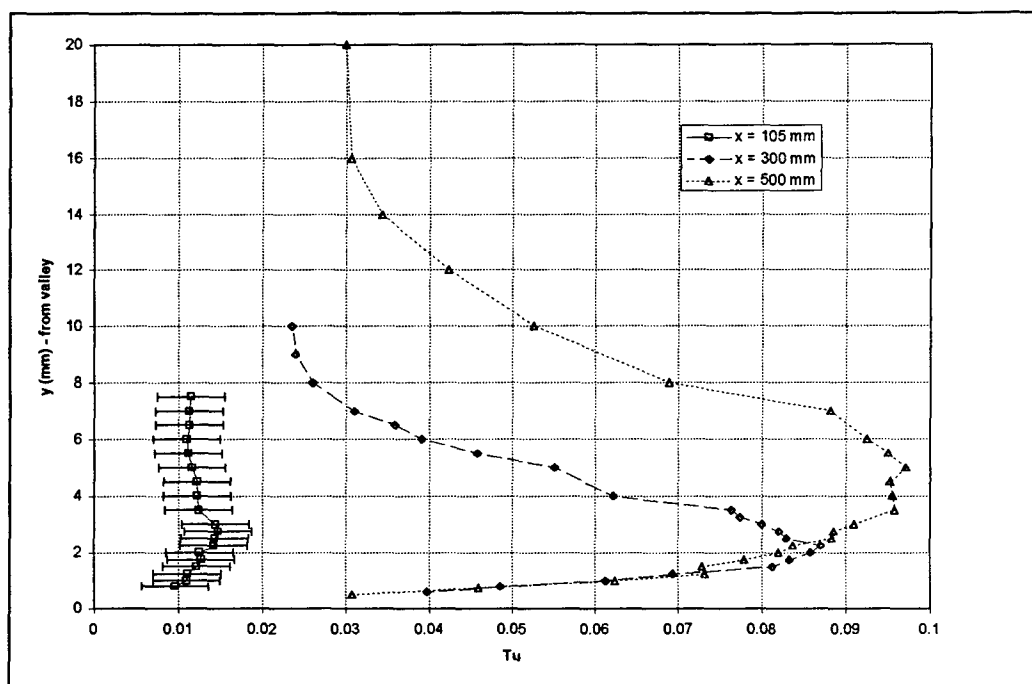


Figure 28.  $T_u$  vs.  $y$ , flat/ribletted,  $U = 7.5$  m/s.

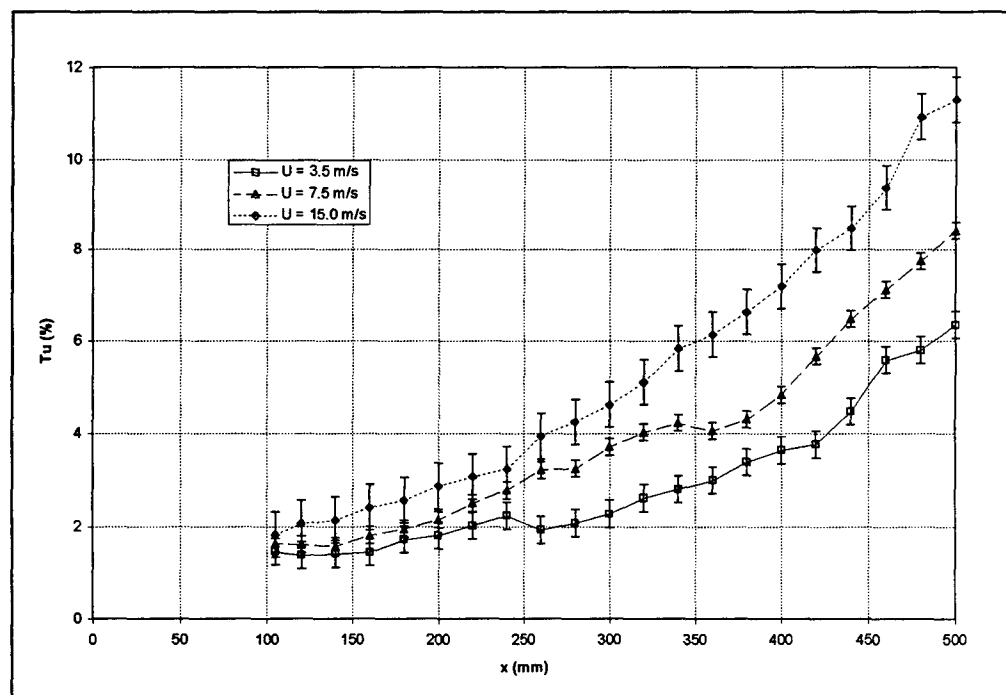


Figure 29. Boundary Layer Peak  $T_u$  vs.  $x$ , flat/smooth.

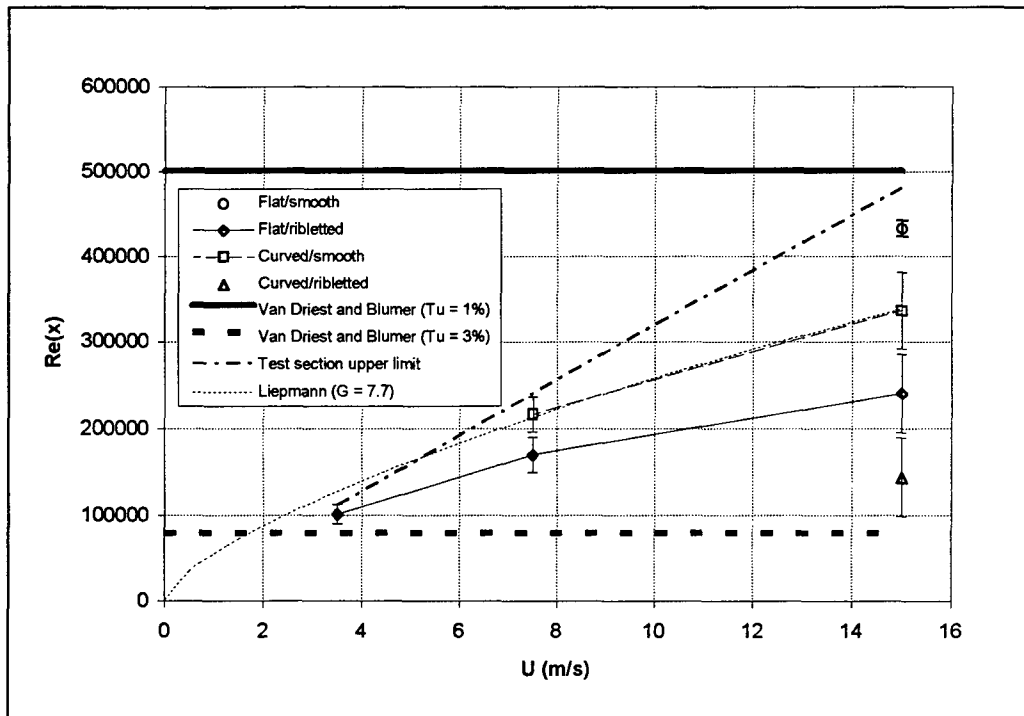


Figure 30. Transition Reynolds Number vs.  $U$

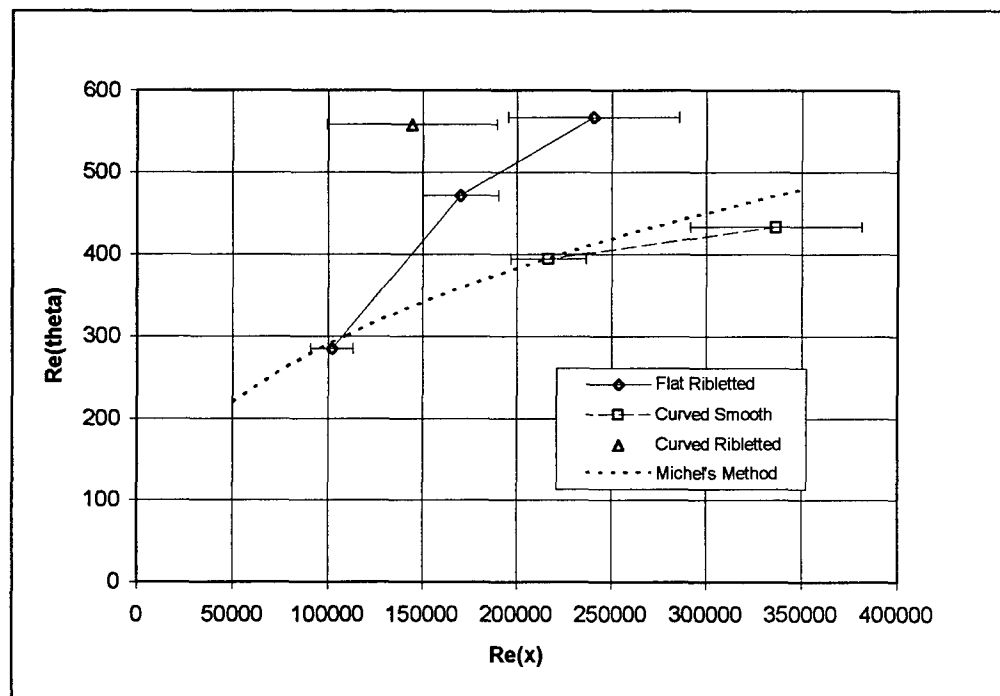


Figure 31. Transition Data Comparison to Method of Michel (1952).

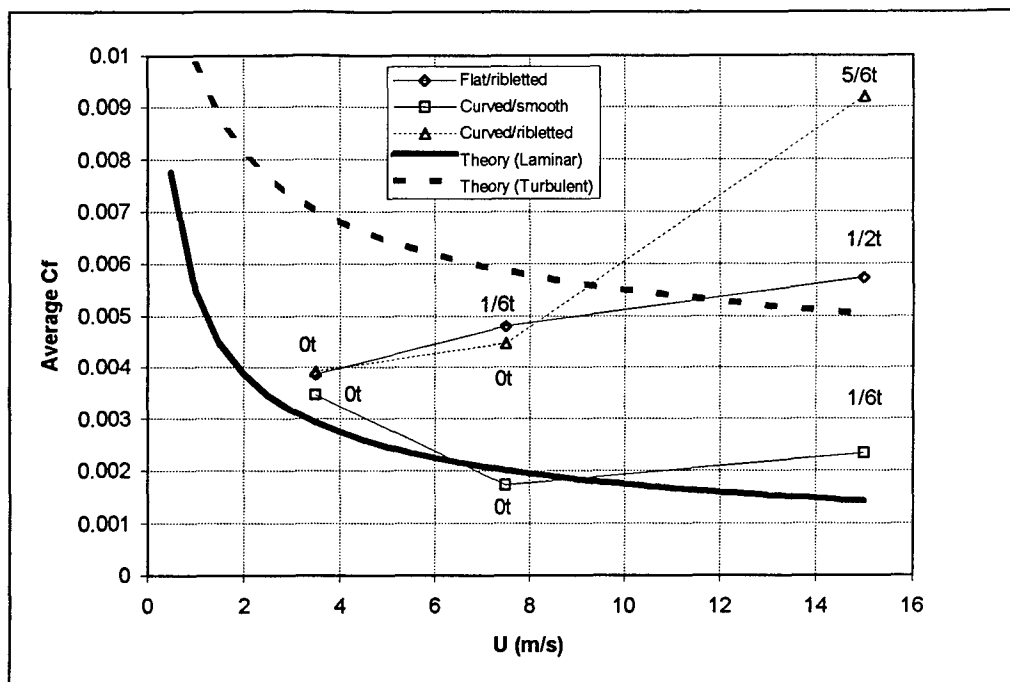


Figure 32. Average Skin Friction Coefficient vs.  $U$  for  $x = 105 - 400$  mm.

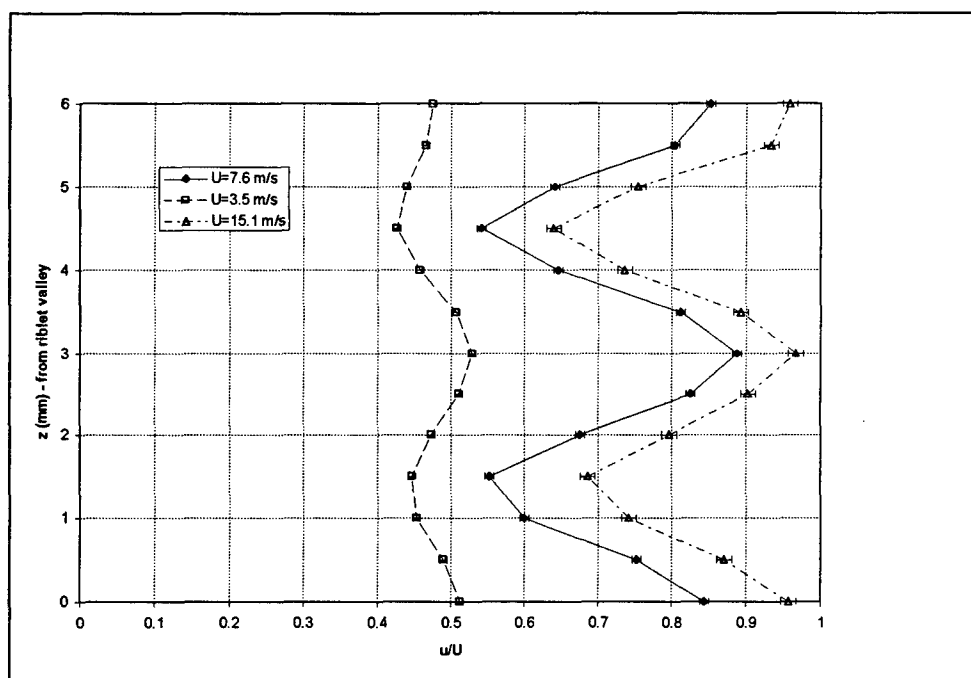


Figure 33. Spanwise Shear,  $u$  vs.  $z$ , flat/ribletted,  $x = 105$  mm,  $y = 0.5$  mm.

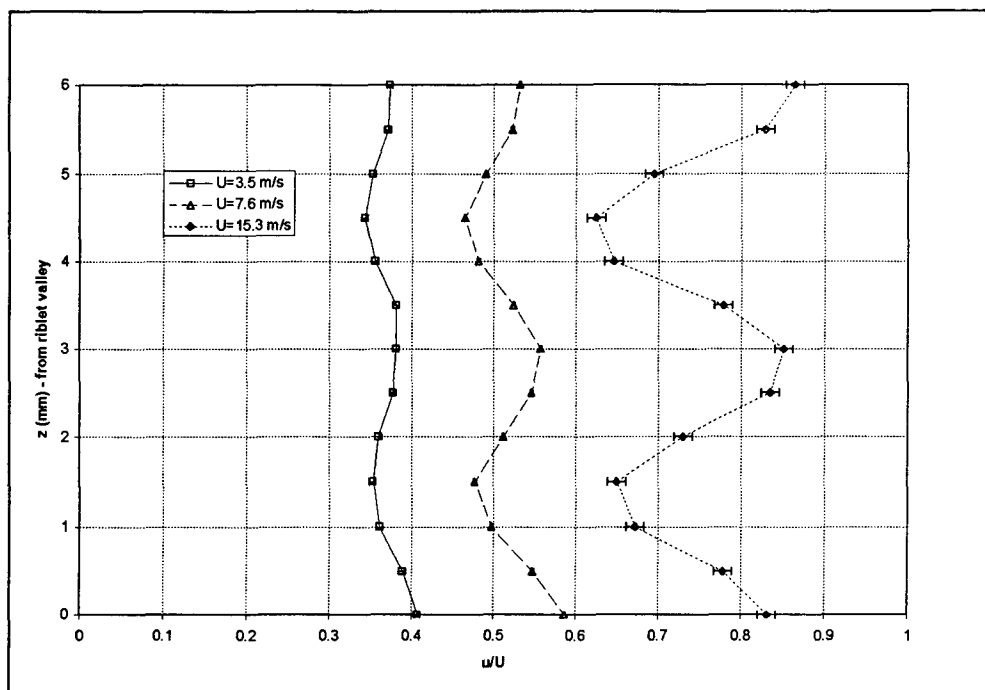


Figure 34. Spanwise Shear,  $u$  vs.  $z$ , flat/ribletted,  $x = 200$  mm,  $y = 0.5$  mm.

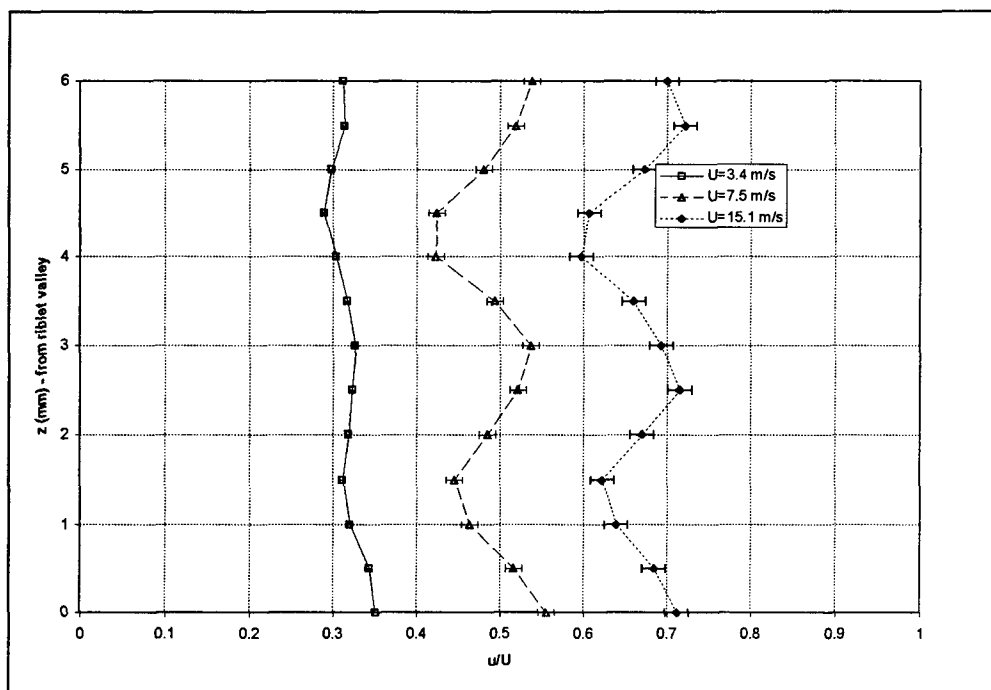


Figure 35. Spanwise Shear,  $u$  vs.  $z$ , flat/ribletted,  $x = 300$  mm,  $y = 0.5$  mm.

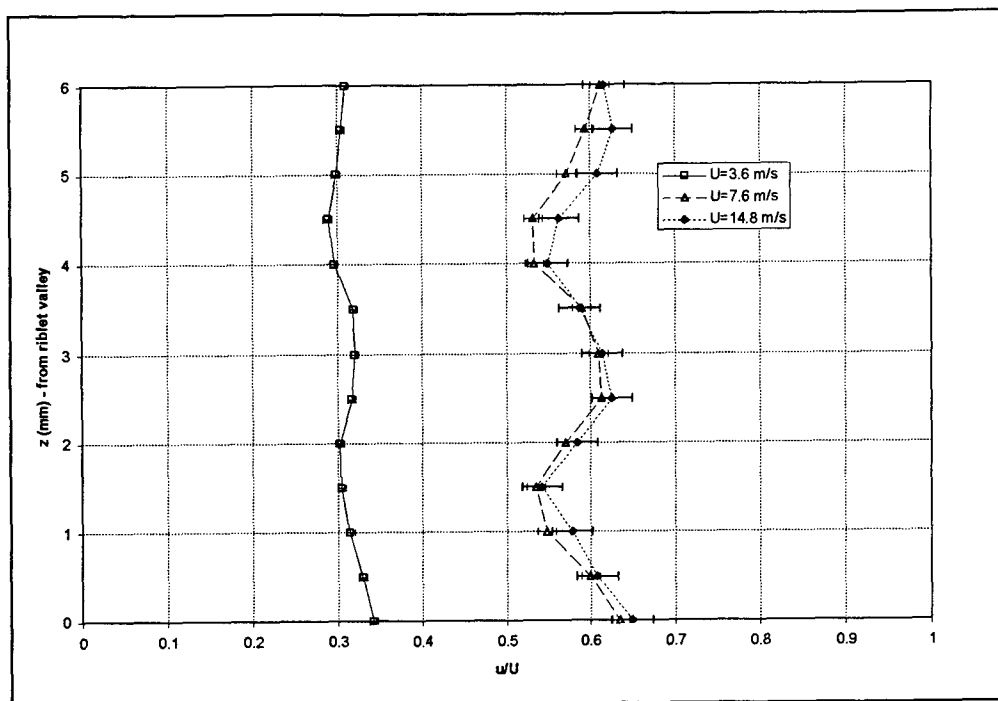


Figure 36. Spanwise Shear,  $u$  vs.  $z$ , flat/ribletted,  $x = 400$  mm,  $y = 0.5$  mm.

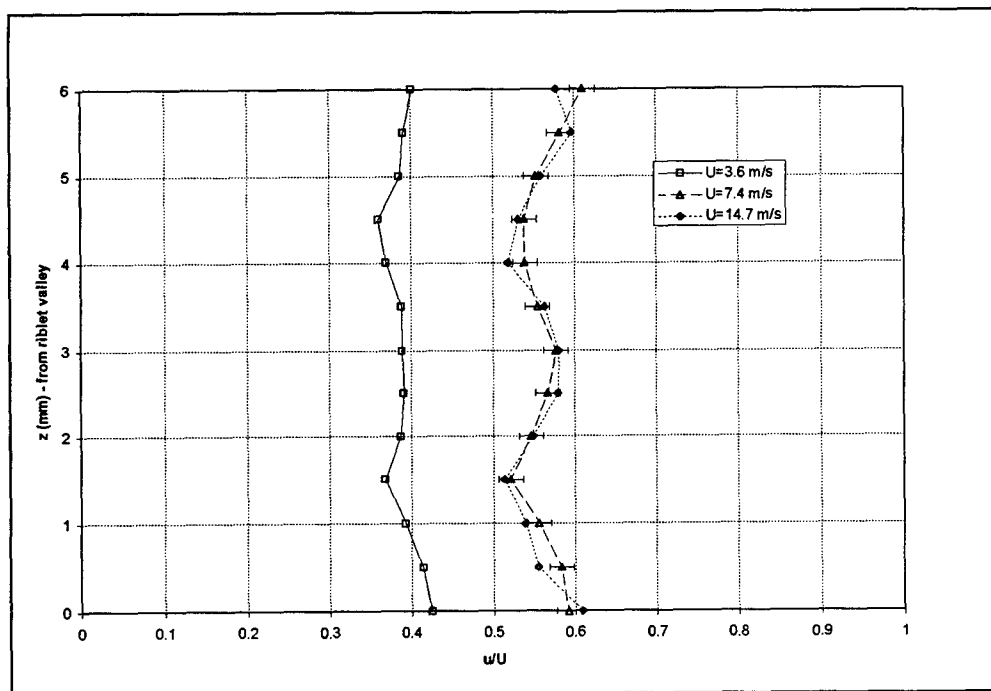


Figure 37. Spanwise Shear,  $u$  vs.  $z$ , flat/ribletted,  $x = 500$  mm,  $y = 0.5$  mm.

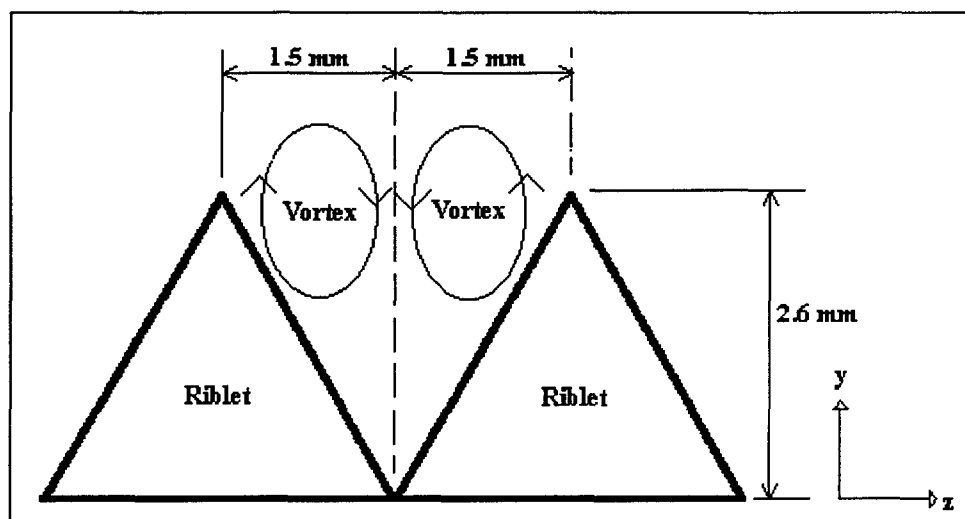


Figure 38. Paired Riblet Valley Vortices Schematic.

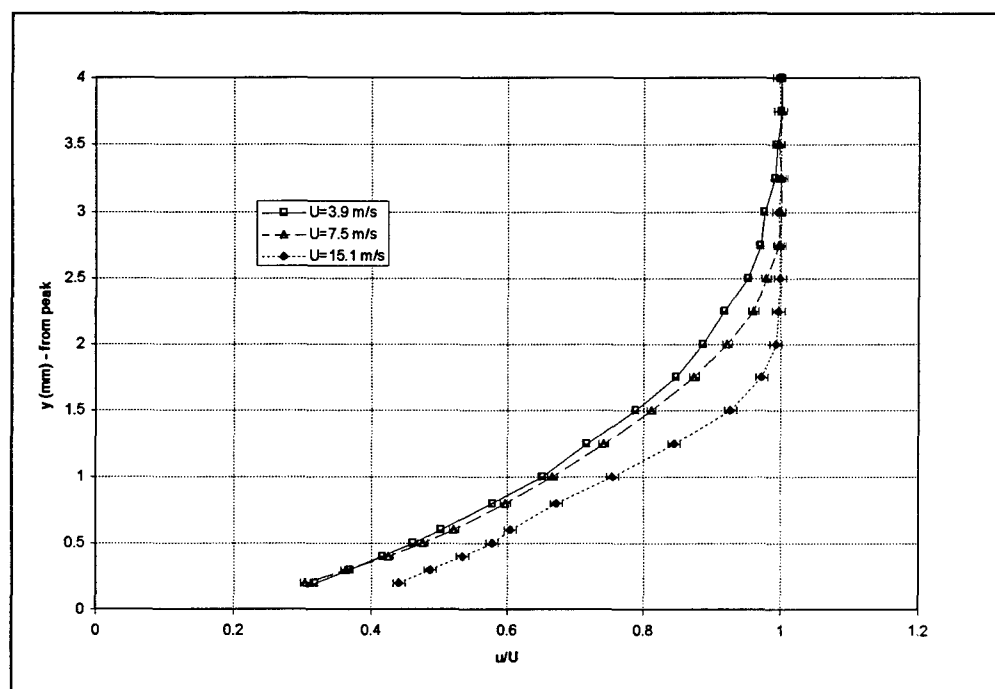


Figure 39. Riblet Peak  $u$  vs.  $y$ , flat/ribletted,  $x = 105$  mm.

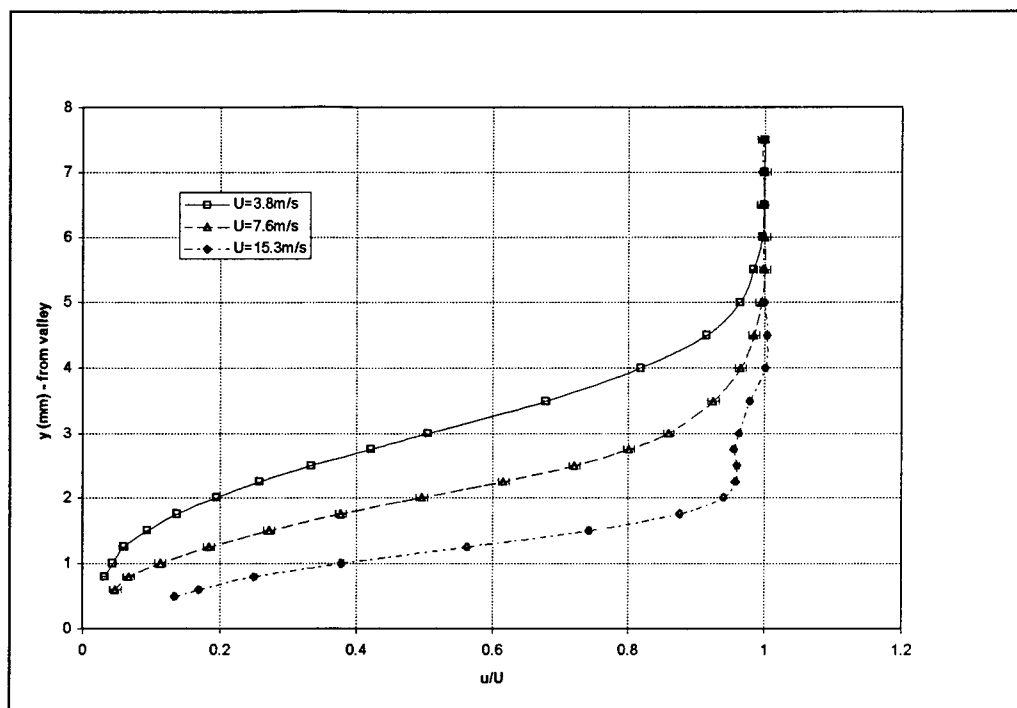


Figure 40. Riblet Valley,  $u$  vs.  $y$ , flat/riblet,  $x = 105$  mm.

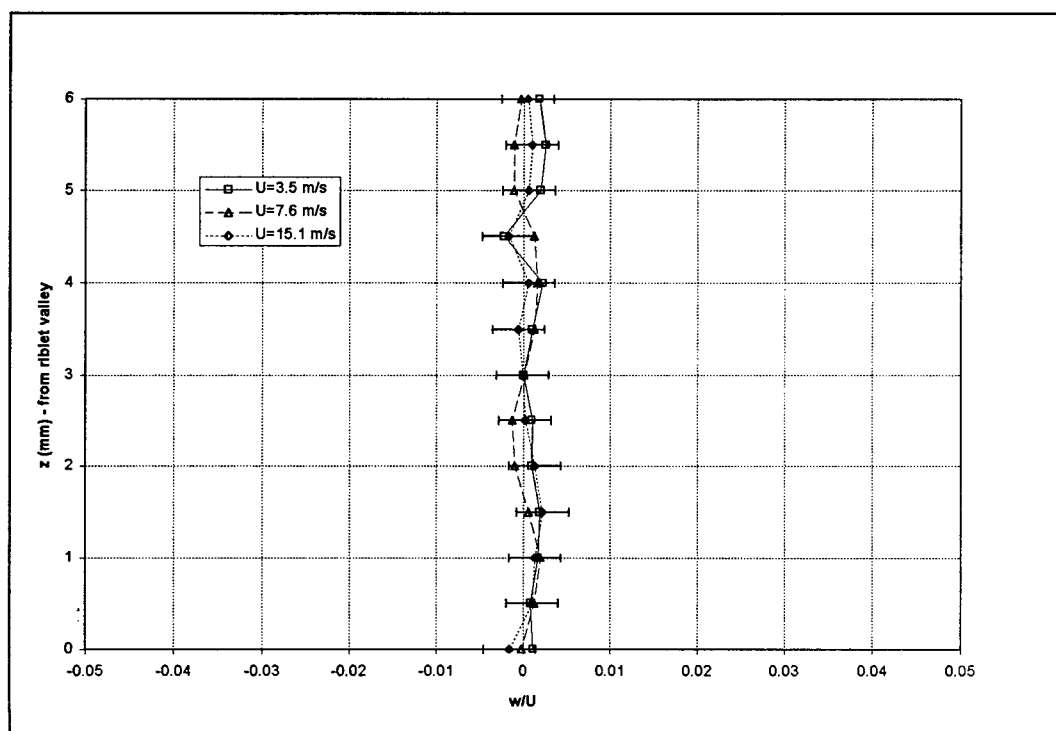


Figure 41.  $w$  vs.  $z$ , flat/riblet,  $y = 0.5$  mm,  $x = 105$  mm.



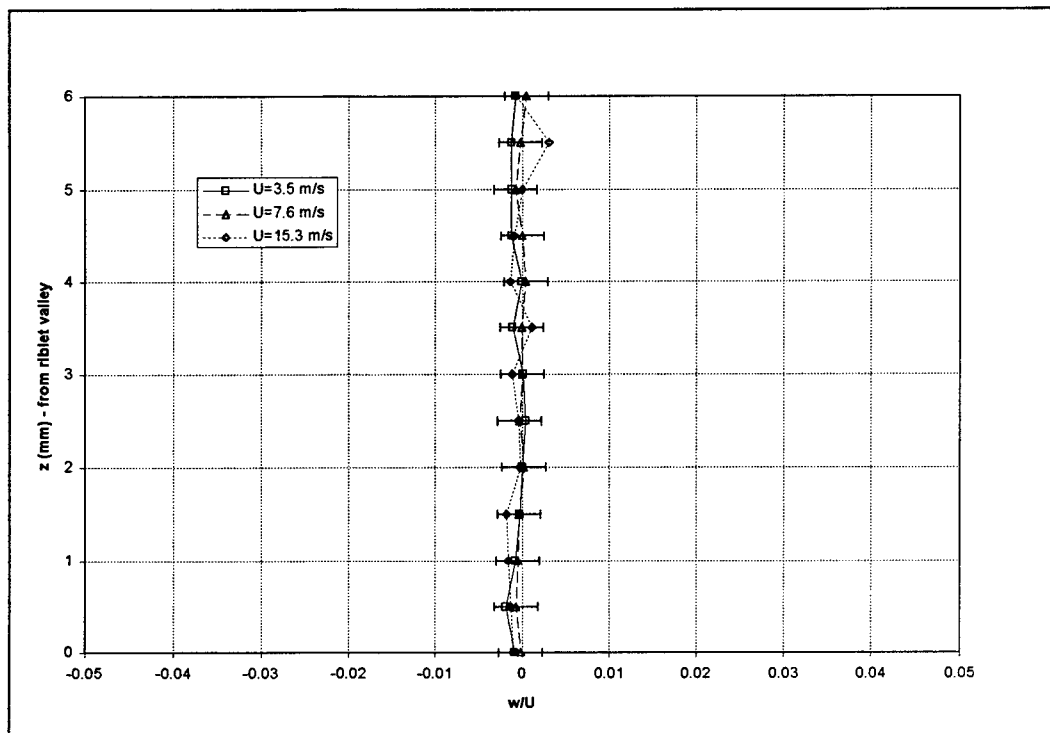


Figure 42.  $w$  vs.  $z$ , flat/riblet,  $y = 0.5$  mm,  $x = 200$  mm.

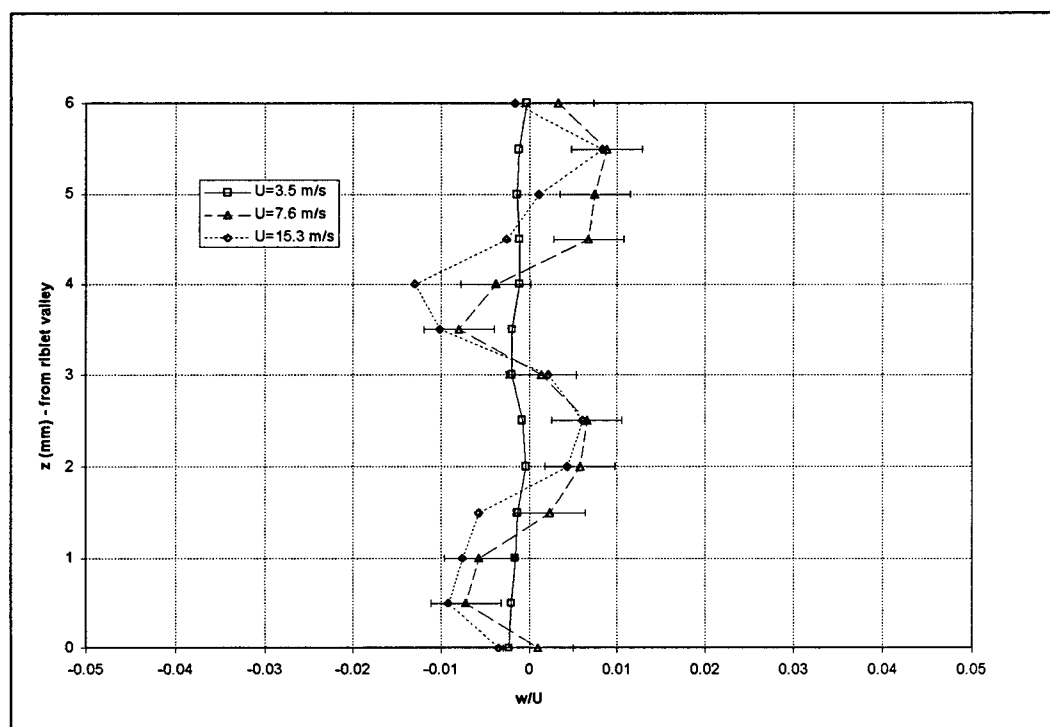


Figure 43.  $w$  vs.  $z$ , flat/riblet,  $y = 0.5$  mm,  $x = 300$  mm.

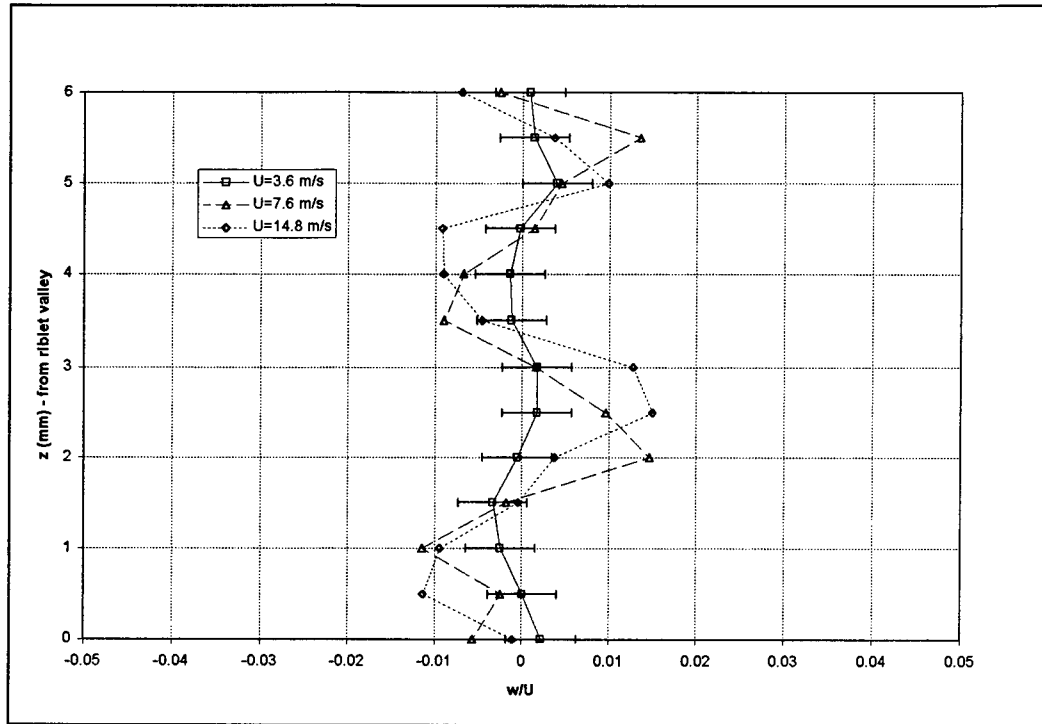


Figure 44.  $w$  vs.  $z$ , flat/ribletted,  $y = 0.5$  mm,  $x = 400$  mm.

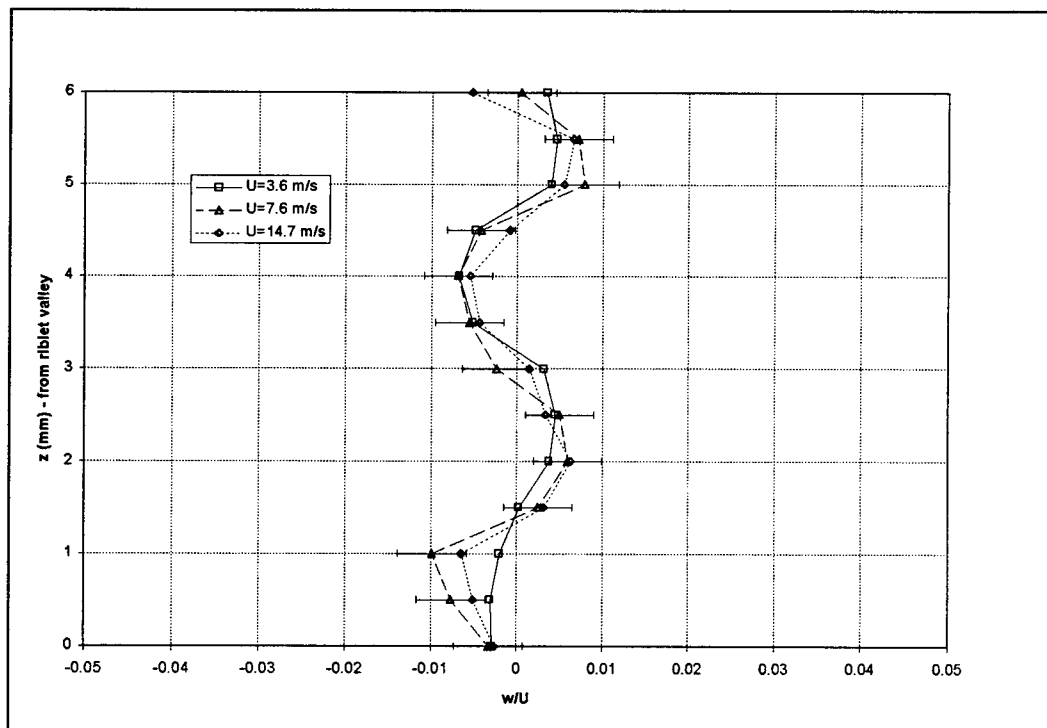


Figure 45.  $w$  vs.  $z$ , flat/ribletted,  $y = 0.5$  mm,  $z = 500$  mm.

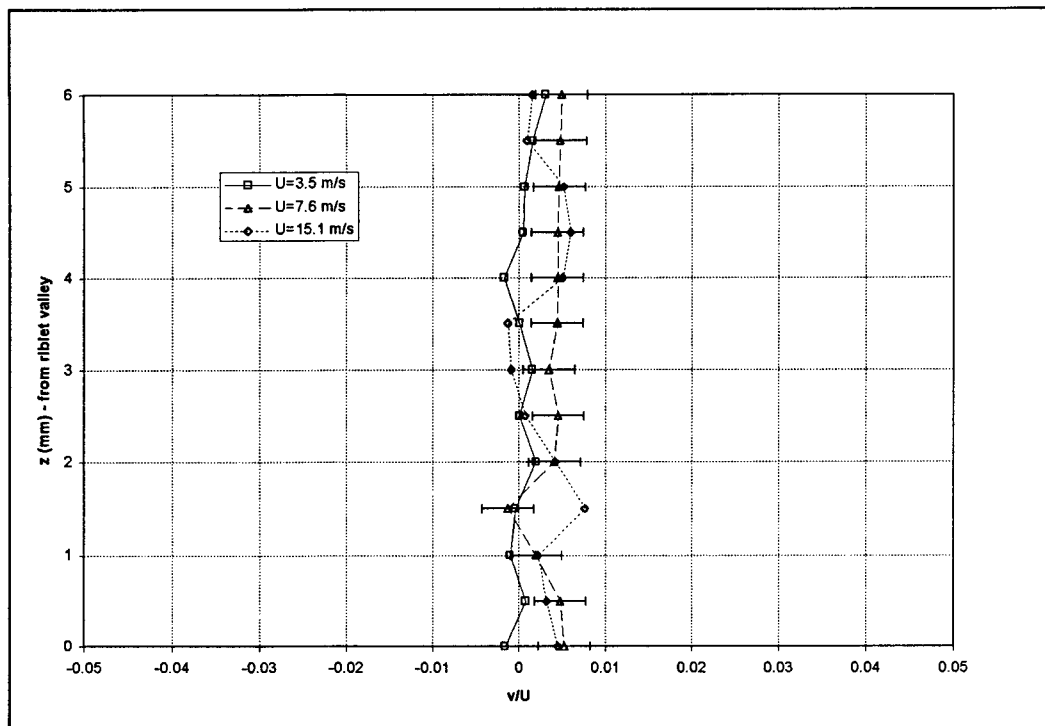


Figure 46.  $v$  vs.  $z$ , flat/ribletted,  $y = 0.5$  mm,  $x = 105$  mm.

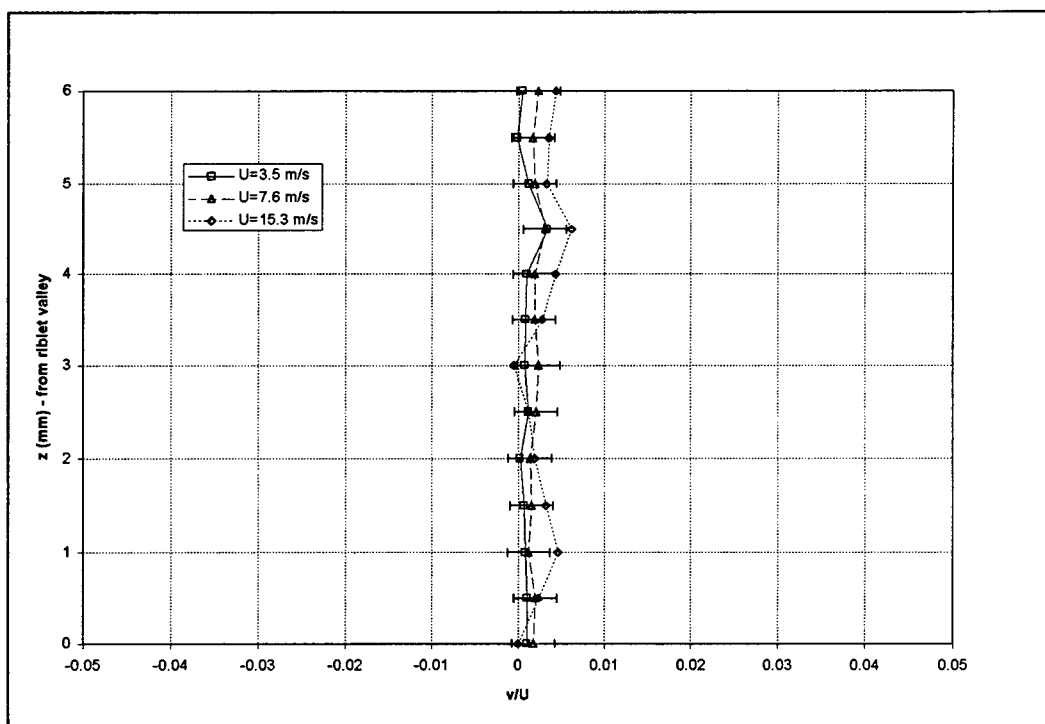


Figure 47.  $v$  vs.  $z$ , flat/ribletted,  $y = 0.5$  mm,  $x = 200$  mm.

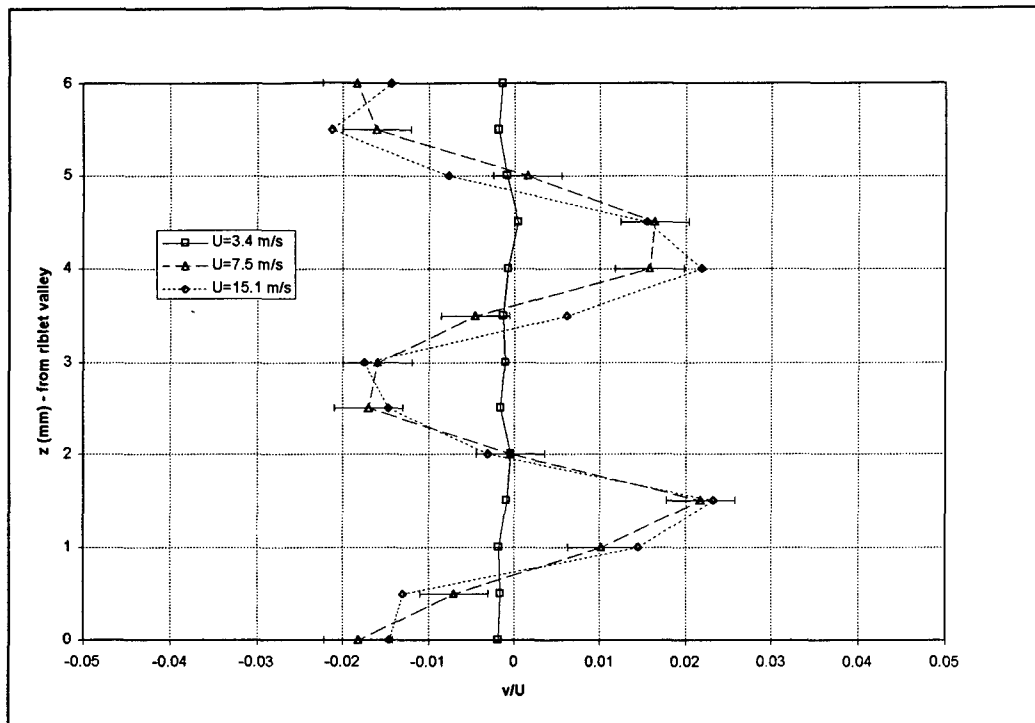


Figure 48.  $v$  vs.  $z$ , flat/ribletted,  $y = 0.5$  mm,  $x = 300$  mm.

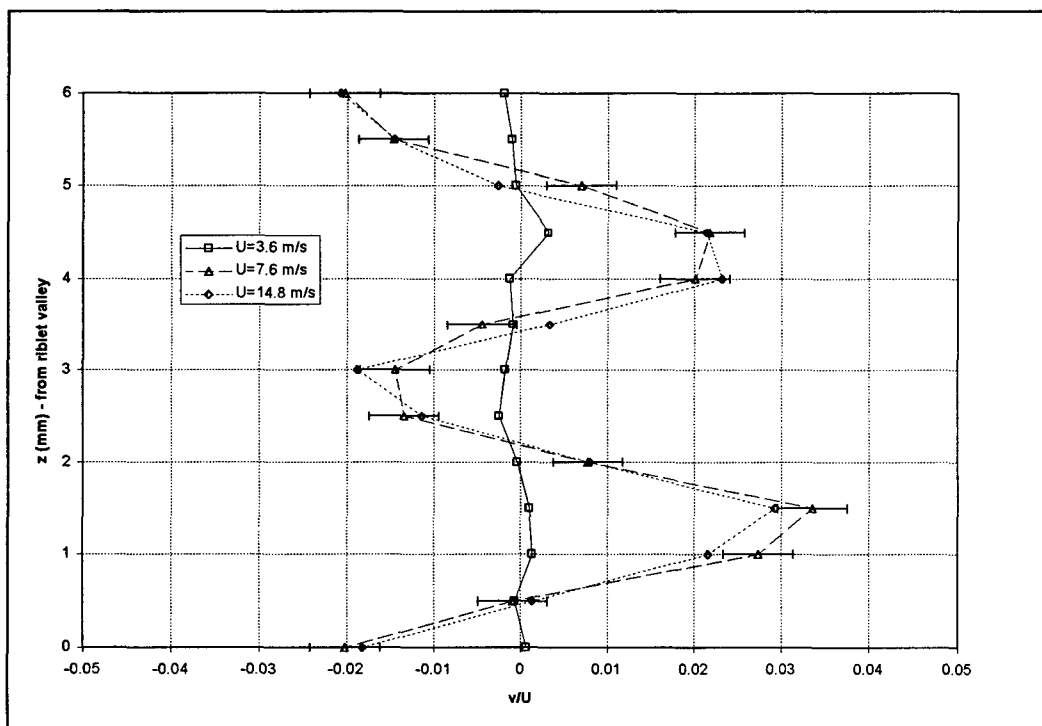


Figure 49.  $v$  vs.  $z$ , flat/ribletted,  $y = 0.5$  mm,  $x = 400$  mm.

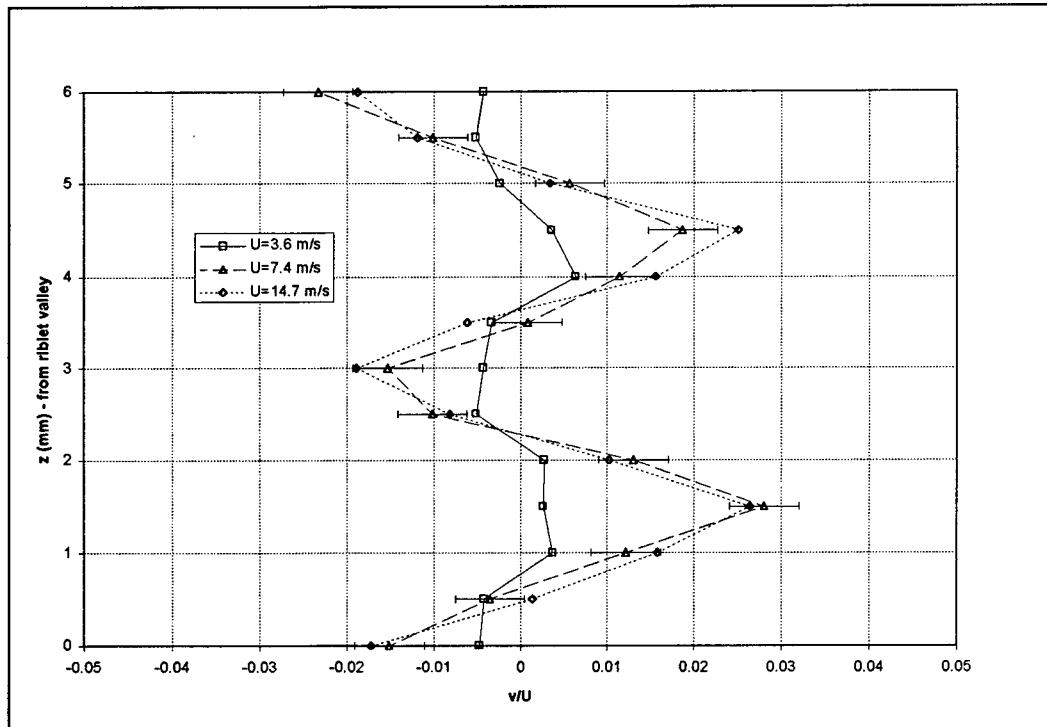


Figure 50.  $v$  vs.  $z$ , flat/ribletted,  $y = 0.5$  mm,  $x = 500$  mm.

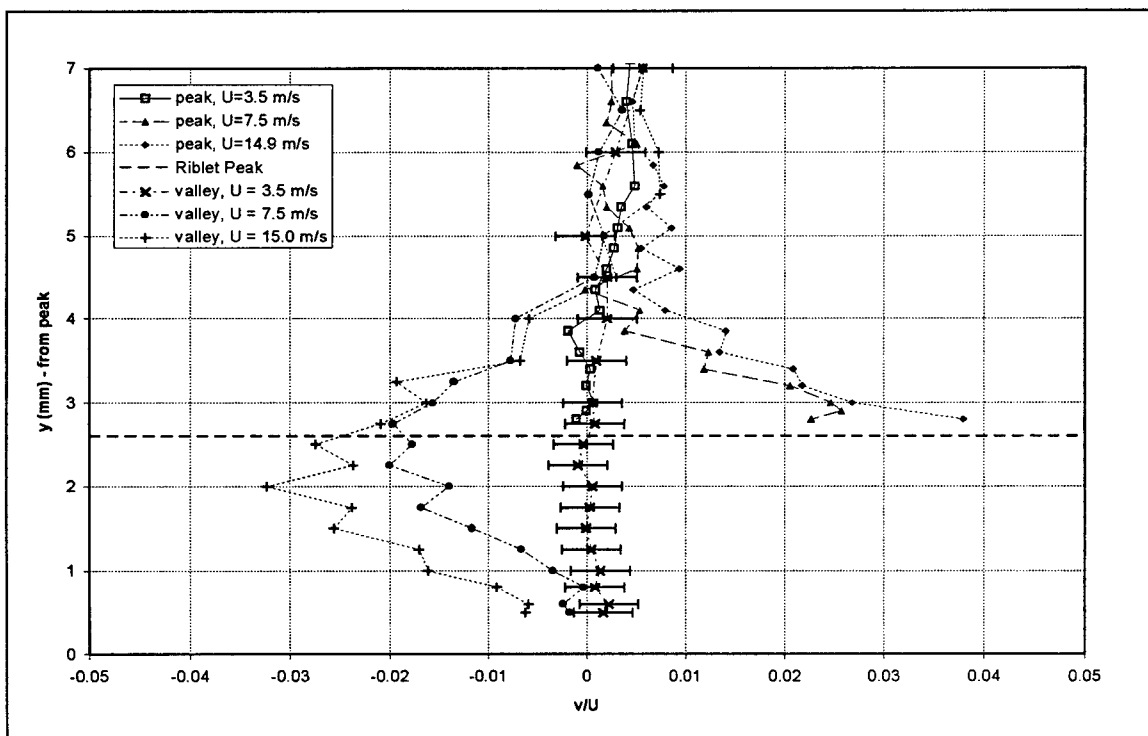


Figure 51. Peak and Valley Comparison,  $v$  vs.  $y$ , flat/ribletted,  $x = 300$  mm.

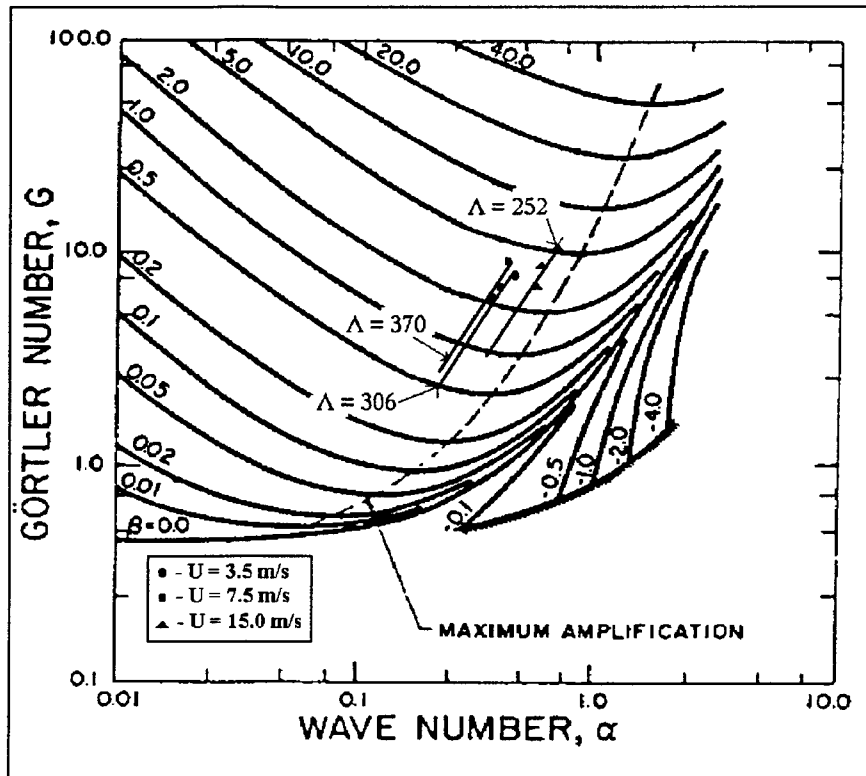


Figure 52. Measured GV's, Curved/Smooth Plate.

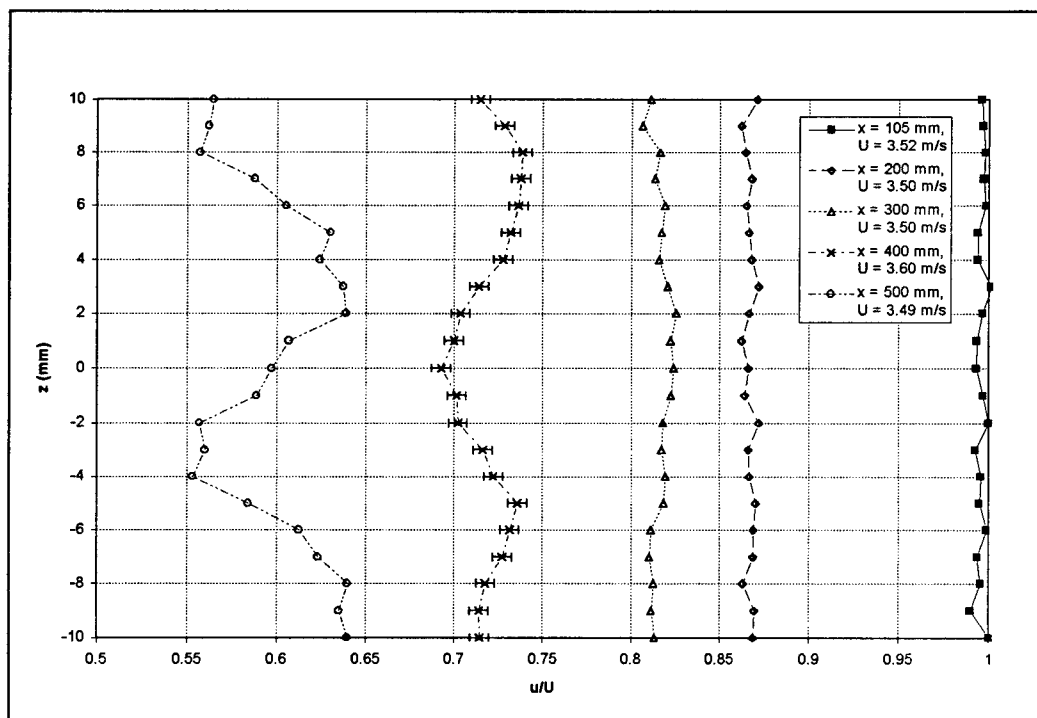


Figure 53.  $u$  vs.  $z$ , curved/smooth,  $U \approx 3.5$  m/s,  $y = 3.0$  mm.

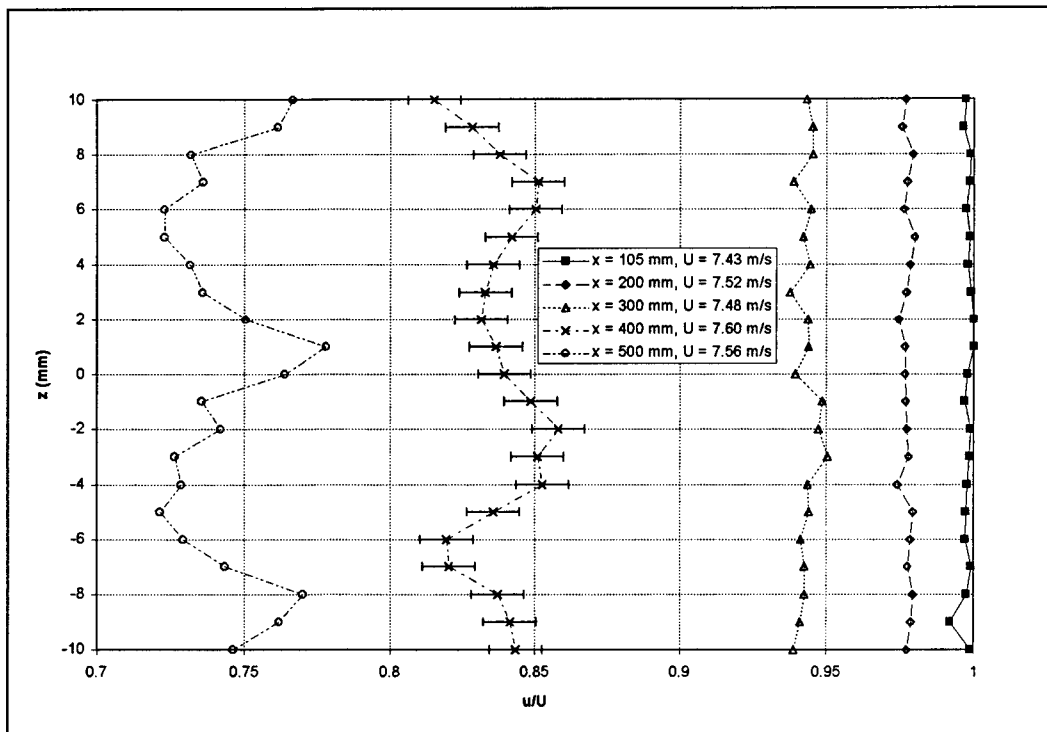


Figure 54.  $u$  vs.  $z$ , curved/smooth,  $U \approx 7.5$  m/s,  $y = 3.0$  mm.

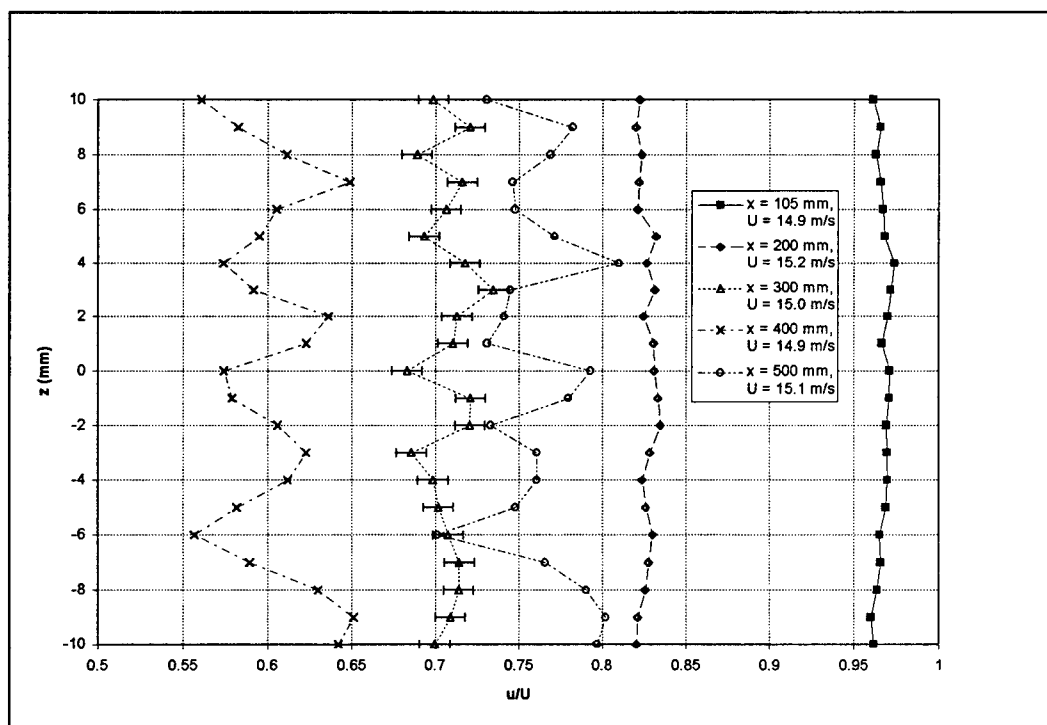


Figure 55.  $u$  vs.  $z$ , curved/smooth,  $U \approx 15.0$  m/s,  $y = 1.0$  mm.

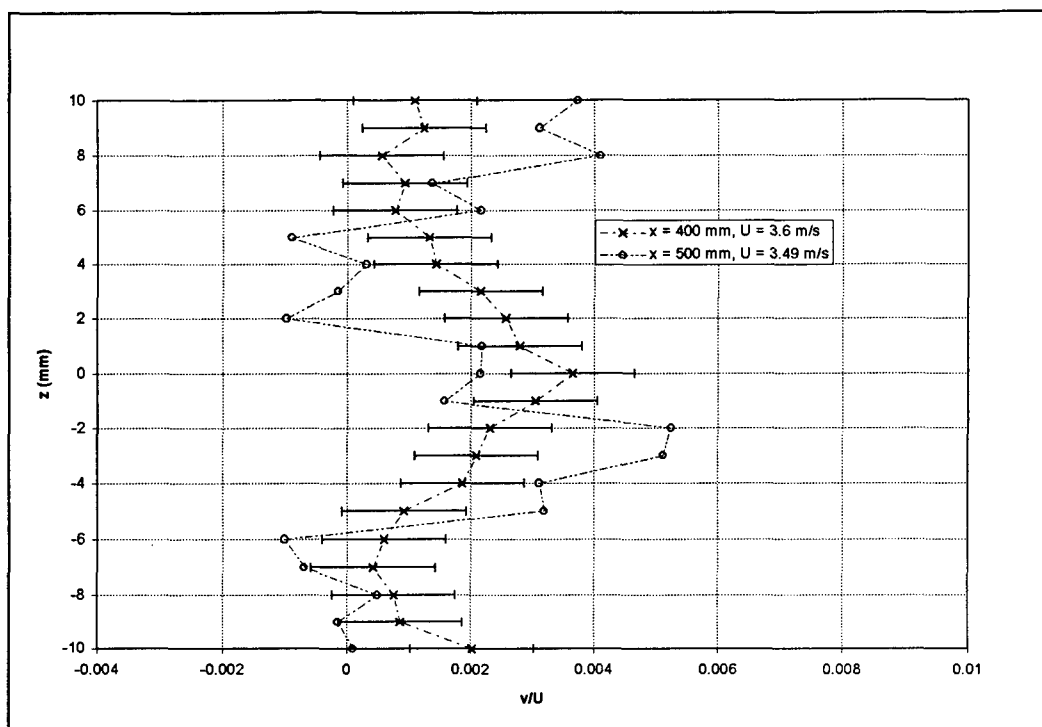


Figure 56.  $v$  vs.  $z$ , curved/smooth,  $U \approx 3.5$  m/s,  $y = 3.0$  mm.

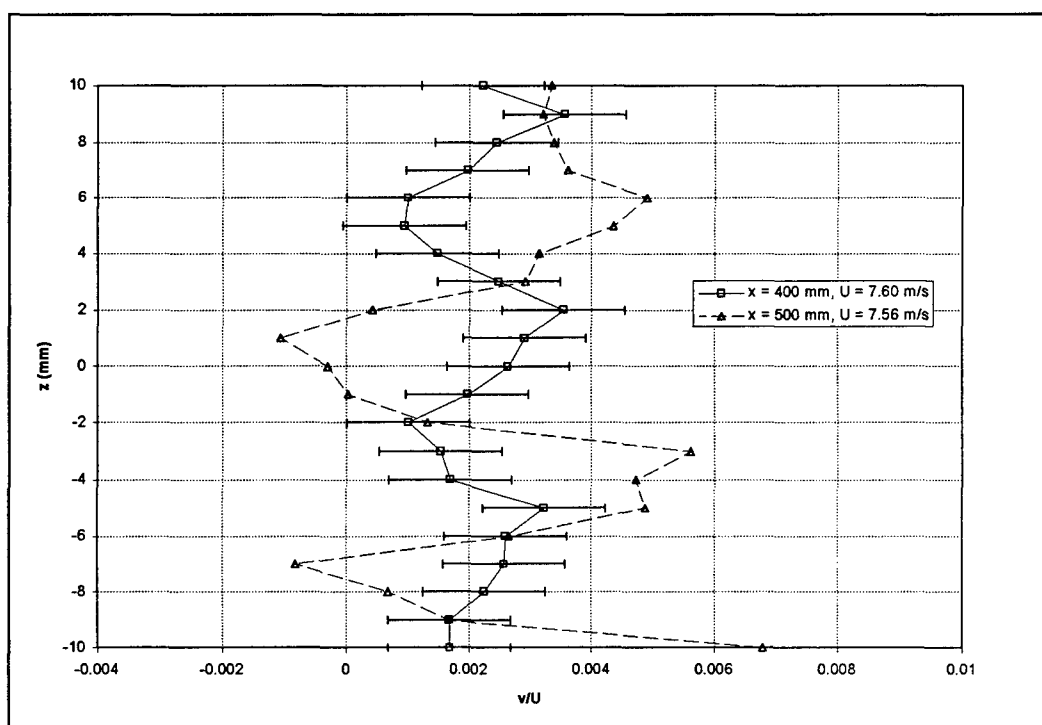


Figure 57.  $v$  vs.  $z$ , curved/smooth,  $U \approx 7.5$  m/s,  $y = 3.0$  mm.



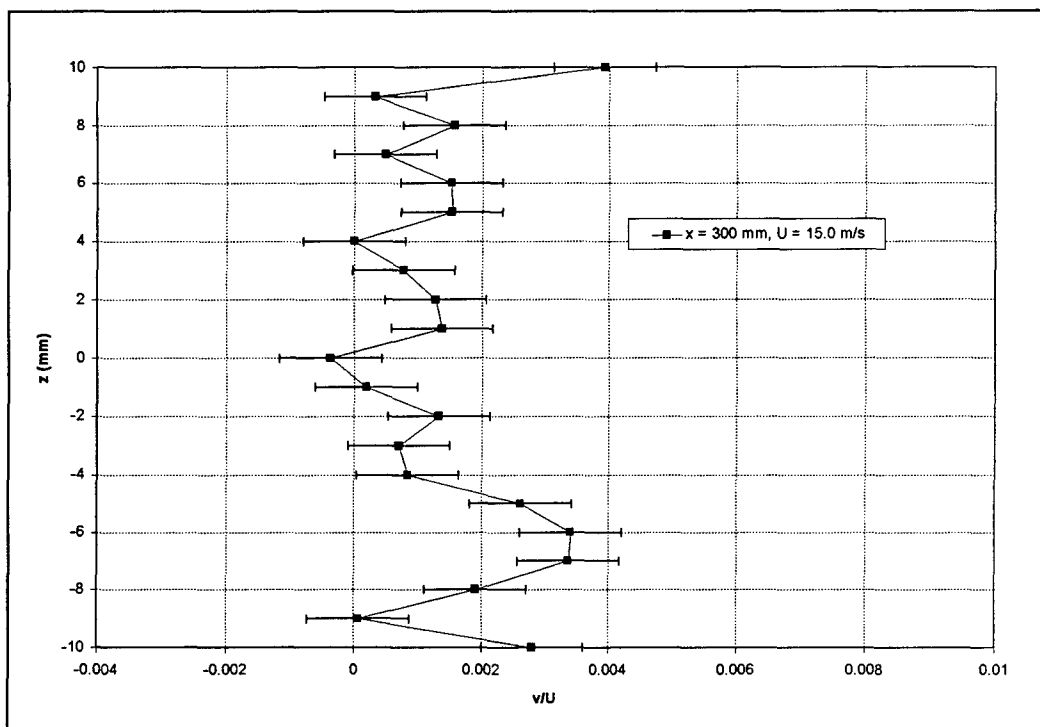


Figure 58.  $v$  vs.  $z$ , curved/smooth,  $x = 300$  mm,  $U \cong 15.0$  m/s,  $y = 1.0$  mm.

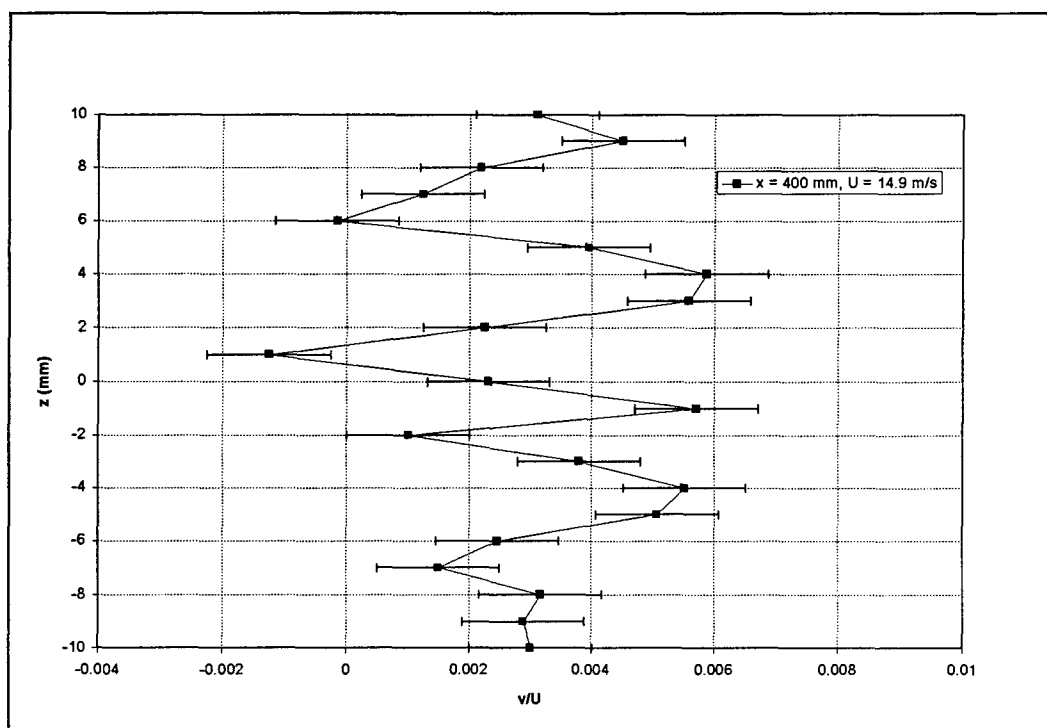


Figure 59.  $v$  vs.  $z$ , curved/smooth,  $x = 400$  mm,  $U \cong 14.9$  m/s,  $y = 0.5$  mm.

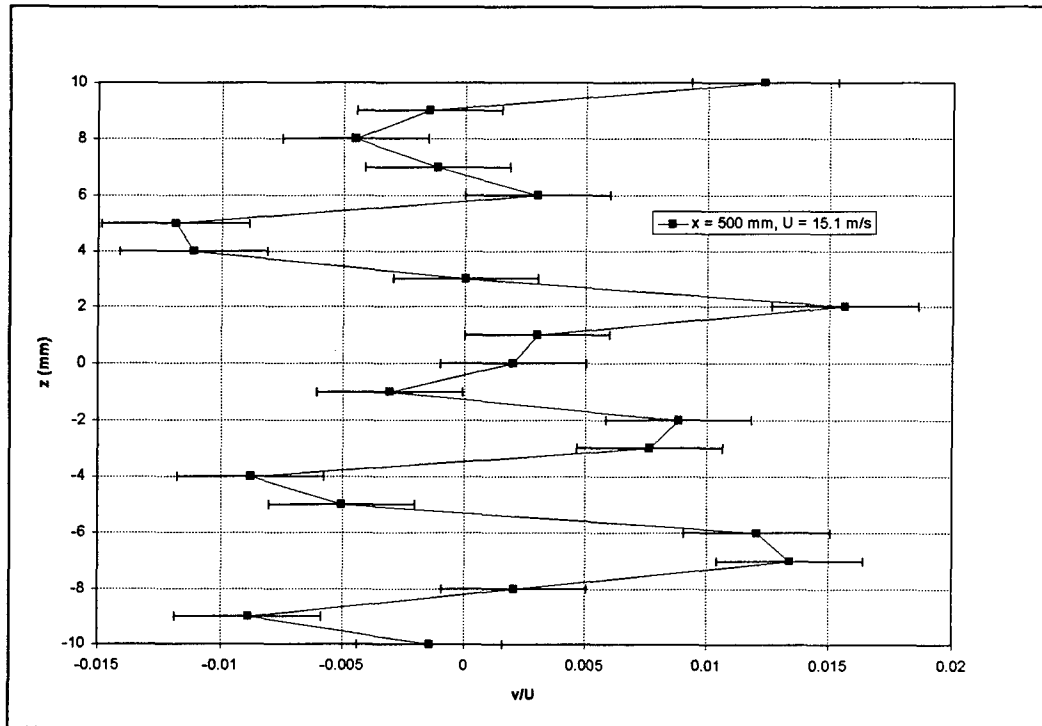


Figure 60.  $v$  vs.  $z$ , curved/smooth,  $x = 500$  mm,  $U \cong 15.1$  m/s,  $y = 0.5$  mm.

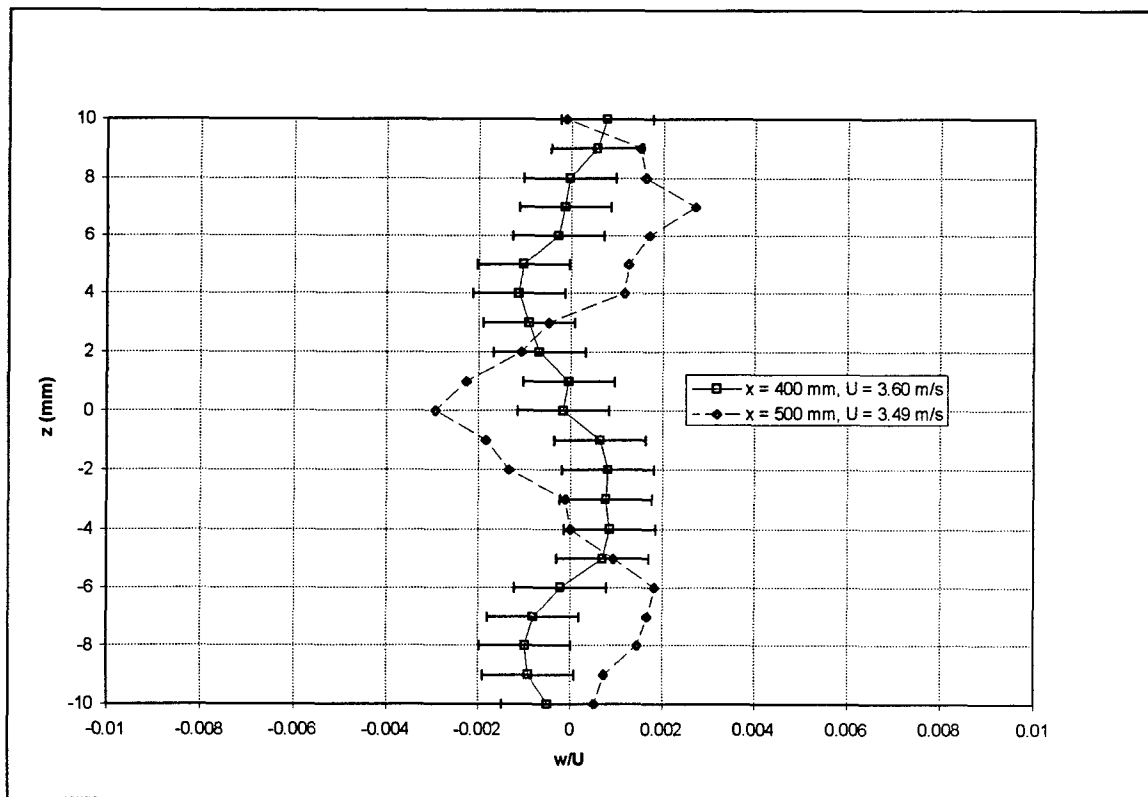


Figure 61.  $w$  vs.  $z$ , curved/smooth,  $U \cong 3.5$  m/s,  $y = 1.0$  mm.

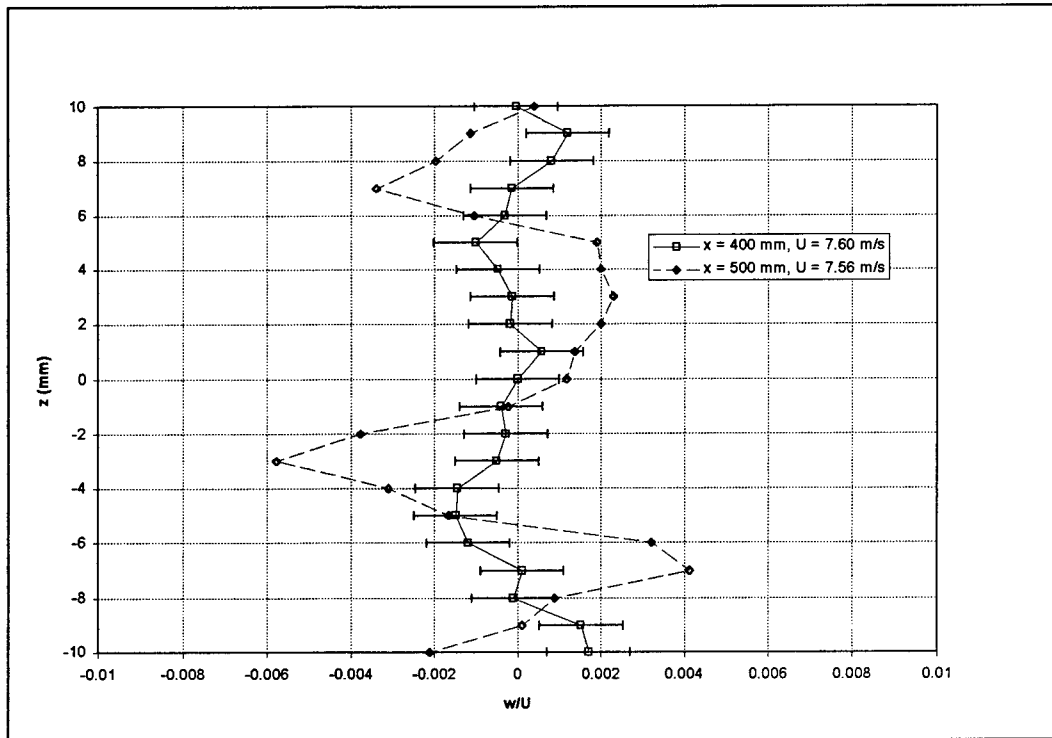


Figure 62.  $w$  vs.  $z$ , curved/smooth,  $U = 7.5$  m/s,  $y = 1.0$  mm.

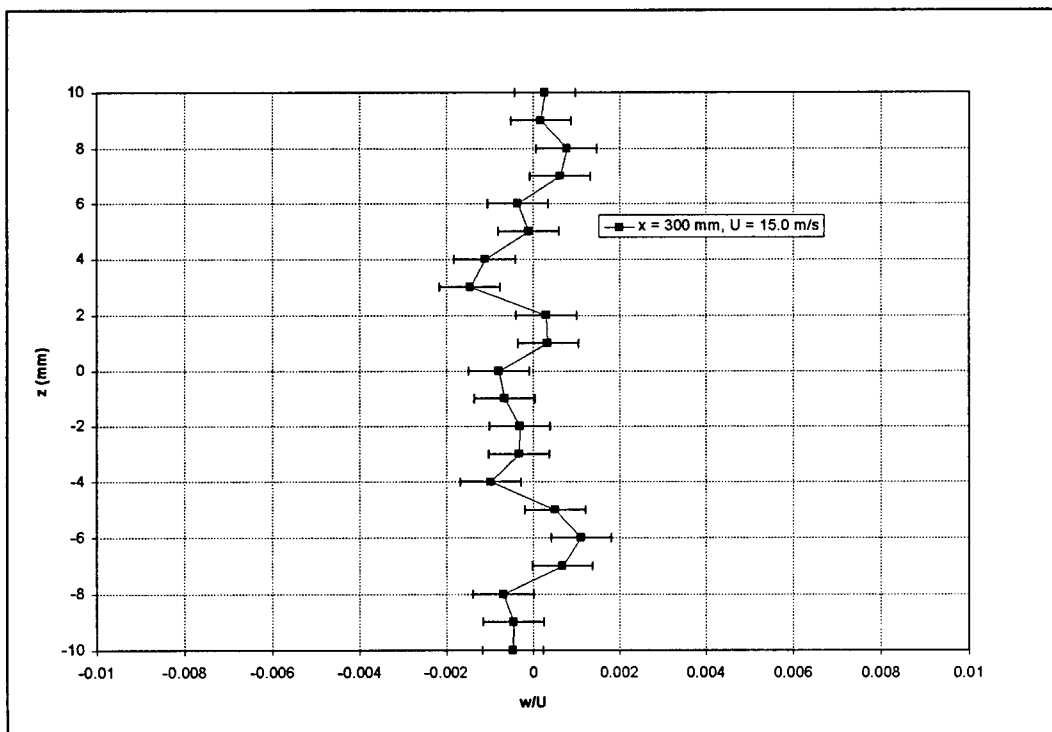


Figure 63.  $w$  vs.  $z$ , curved/smooth,  $U = 15.0$  m/s,  $x = 300$  mm,  $y = 1.0$  mm.

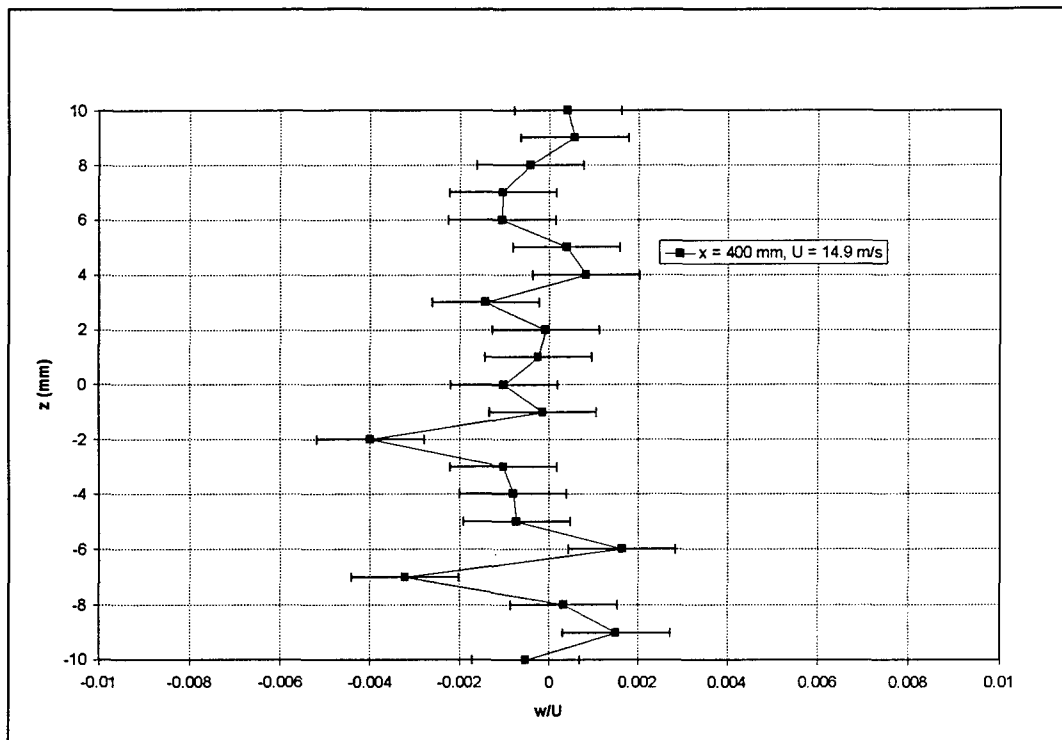


Figure 64.  $w$  vs.  $z$ , curved/smooth,  $U = 14.9$  m/s,  $x = 400$  mm,  $y = 1.0$  mm.

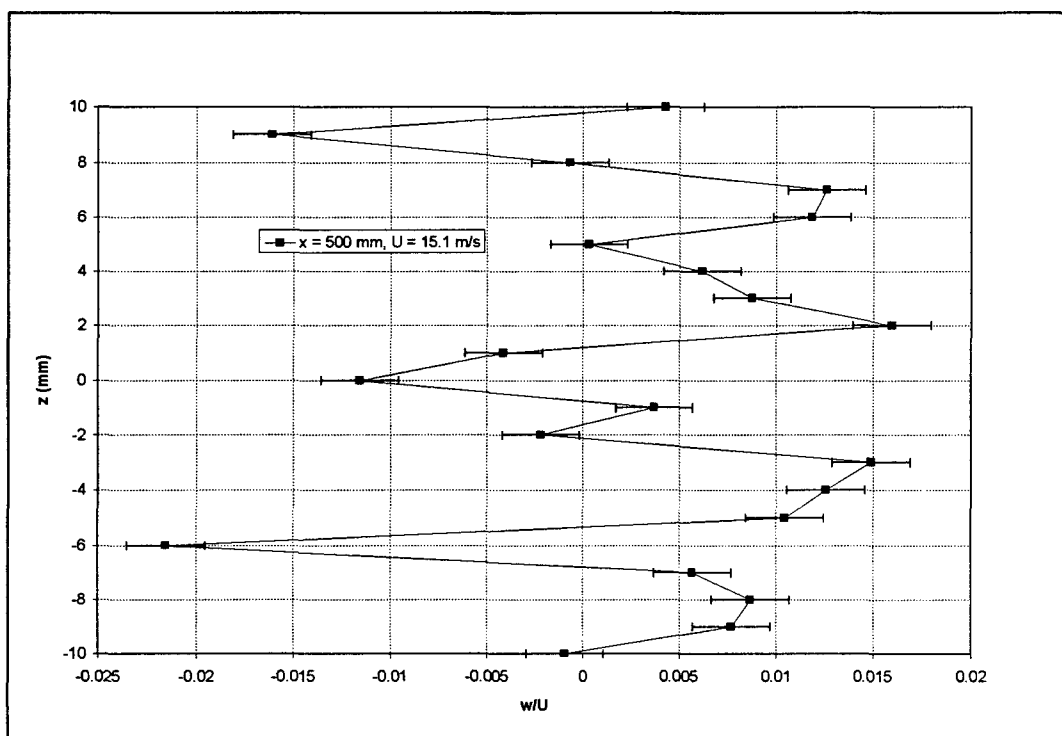


Figure 65.  $w$  vs.  $z$ , curved/smooth,  $U = 15.1$  m/s,  $x = 500$  mm,  $y = 1.0$  mm.

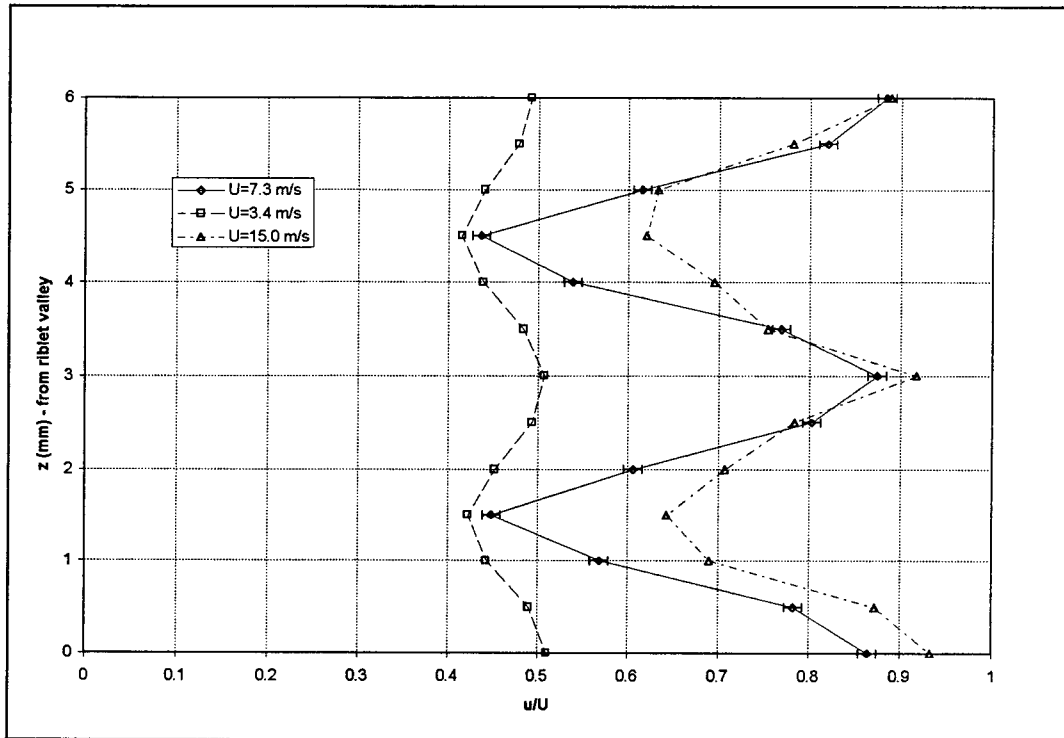


Figure 66. Spanwise Shear,  $u$  vs.  $z$ , curved/ribletted,  $x = 105$  mm,  $y = 0.5$  mm.

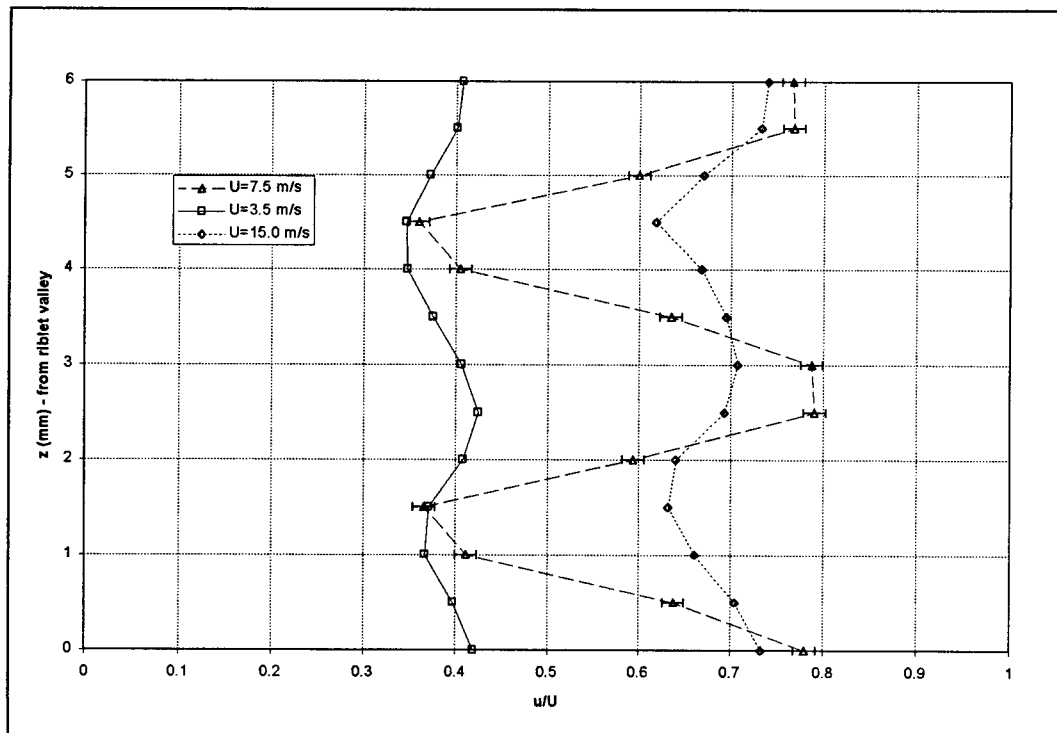


Figure 67. Spanwise Shear,  $u$  vs.  $z$ , curved/ribletted,  $x = 200$  mm,  $y = 0.5$  mm.

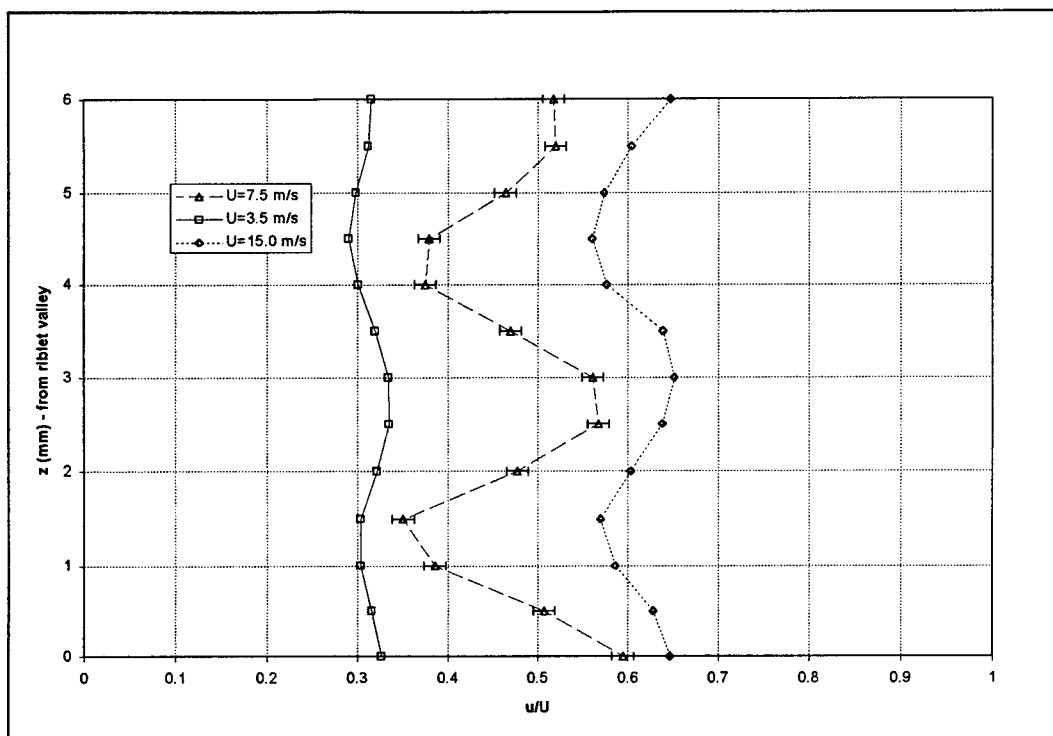


Figure 68. Spanwise Shear,  $u$  vs.  $z$ , curved/ribletted,  $x = 300$  mm,  $y = 0.5$  m/s.

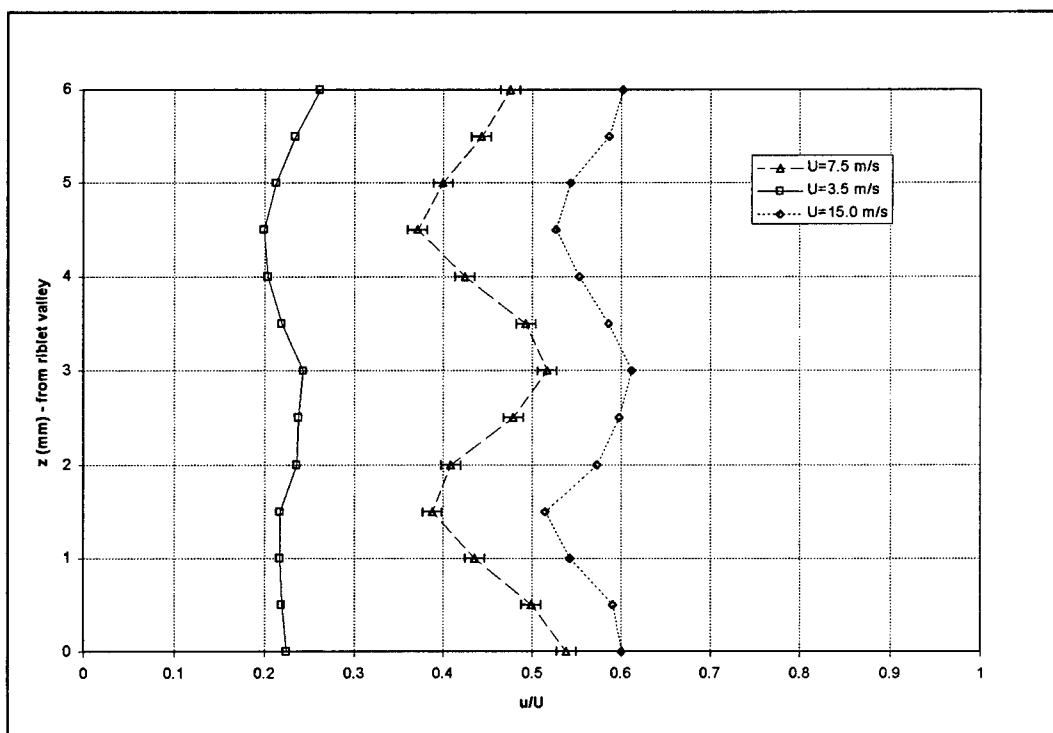


Figure 69. Spanwise Shear,  $u$  vs.  $z$ , curved/ribletted,  $x = 400$  mm,  $y = 0.5$  mm.

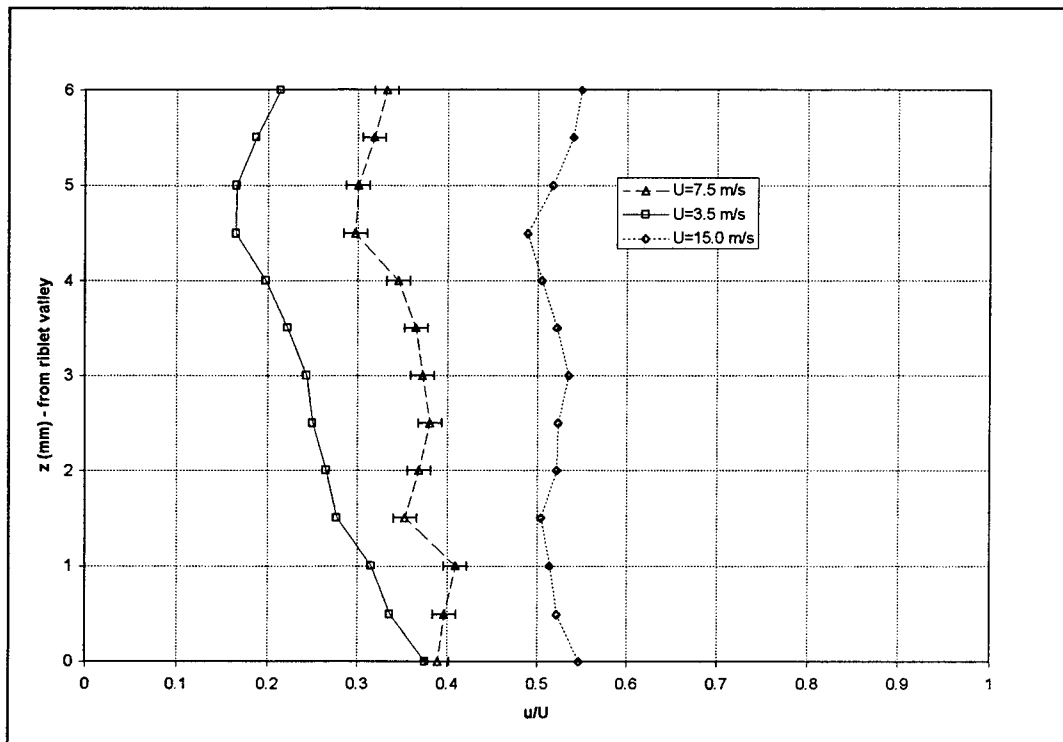


Figure 70. Spanwise Shear,  $u$  vs.  $z$ , curved/ribletted,  $x = 500$  mm,  $y = 0.5$  mm.

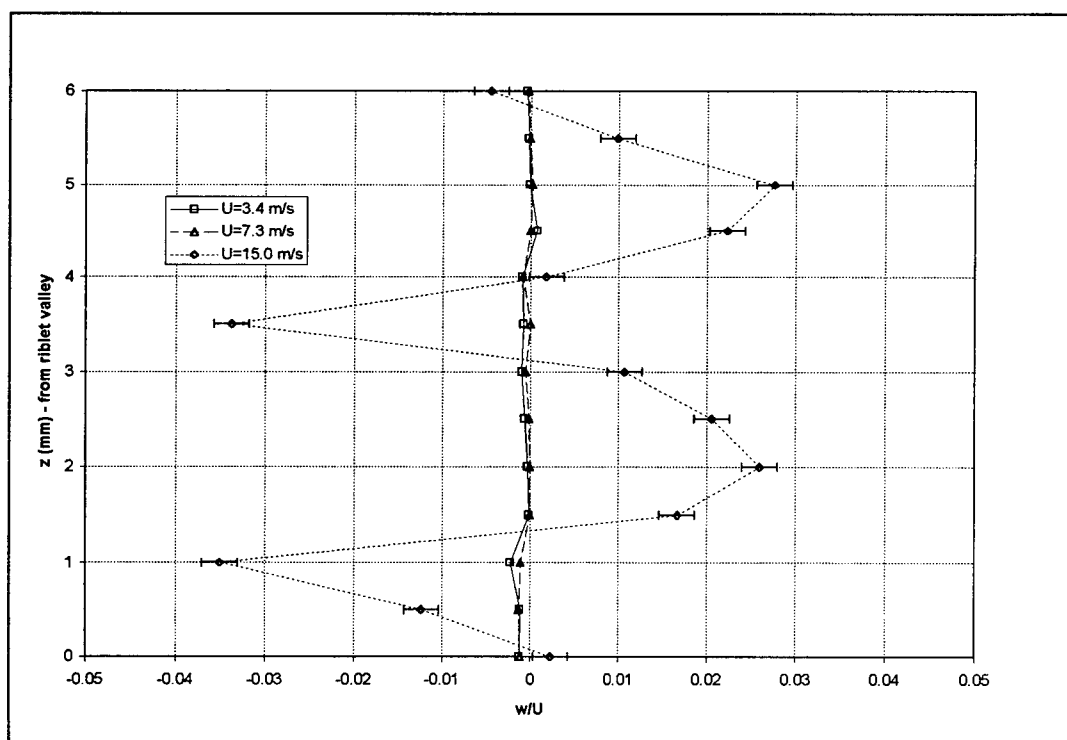


Figure 71. Lower Boundary Layer,  $w$  vs.  $z$ , curved/ribletted,  $x = 105$  mm,  $y = 0.5$  mm.

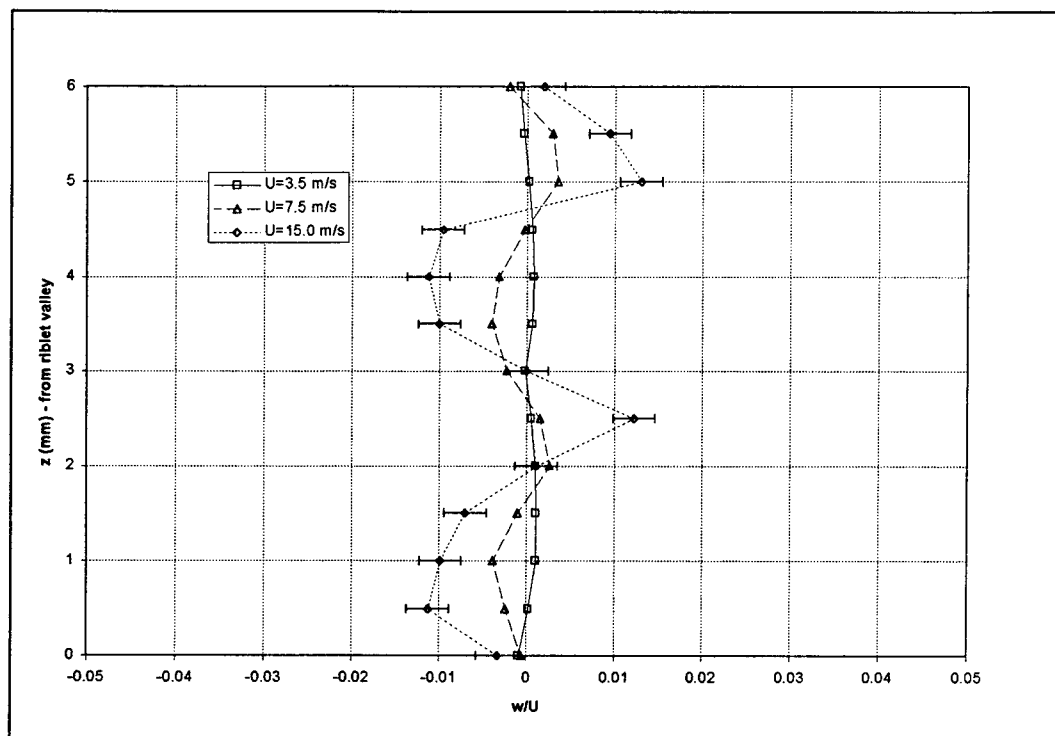


Figure 72. Lower Boundary Layer,  $w$  vs.  $z$ , curved/riblet,  $x = 200$  mm,  $y = 0.5$  mm.

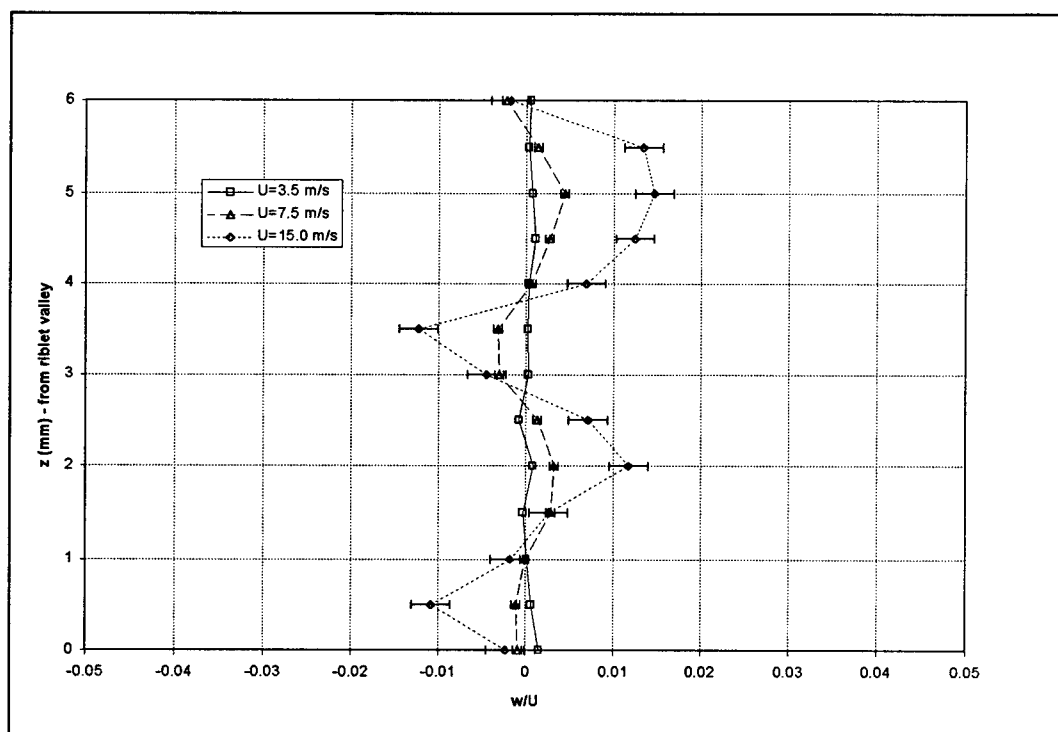


Figure 73. Lower Boundary Layer,  $w$  vs.  $z$ , curved/riblet,  $x = 300$  mm,  $y = 0.5$  mm.



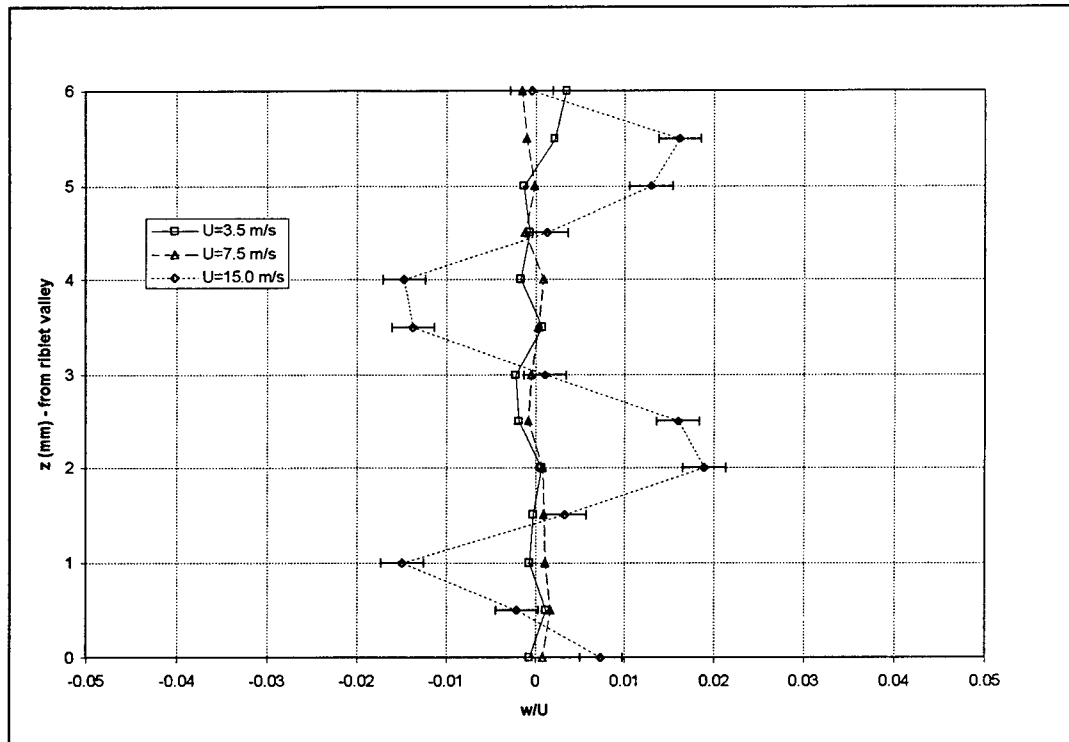


Figure 74. Lower Boundary Layer,  $w$  vs.  $z$ , curved/ribletted,  $x = 400$  mm,  $y = 0.5$  mm.

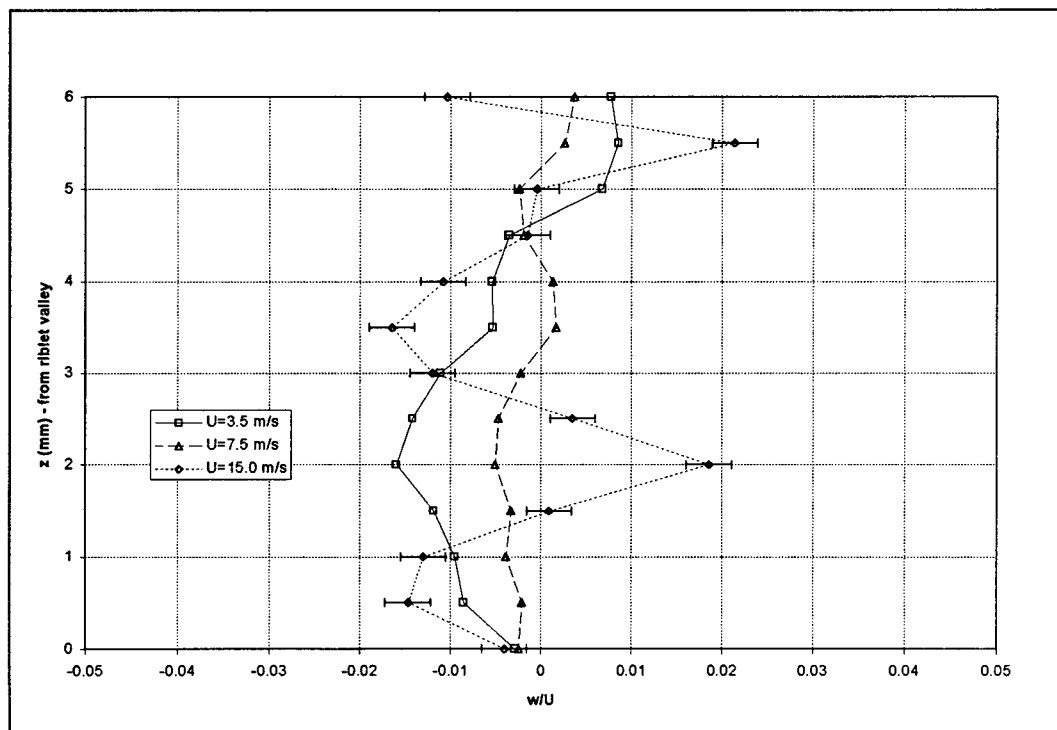


Figure 75. Lower Boundary Layer,  $w$  vs.  $z$ , curved/ribletted,  $x = 500$  mm,  $y = 0.5$  mm.

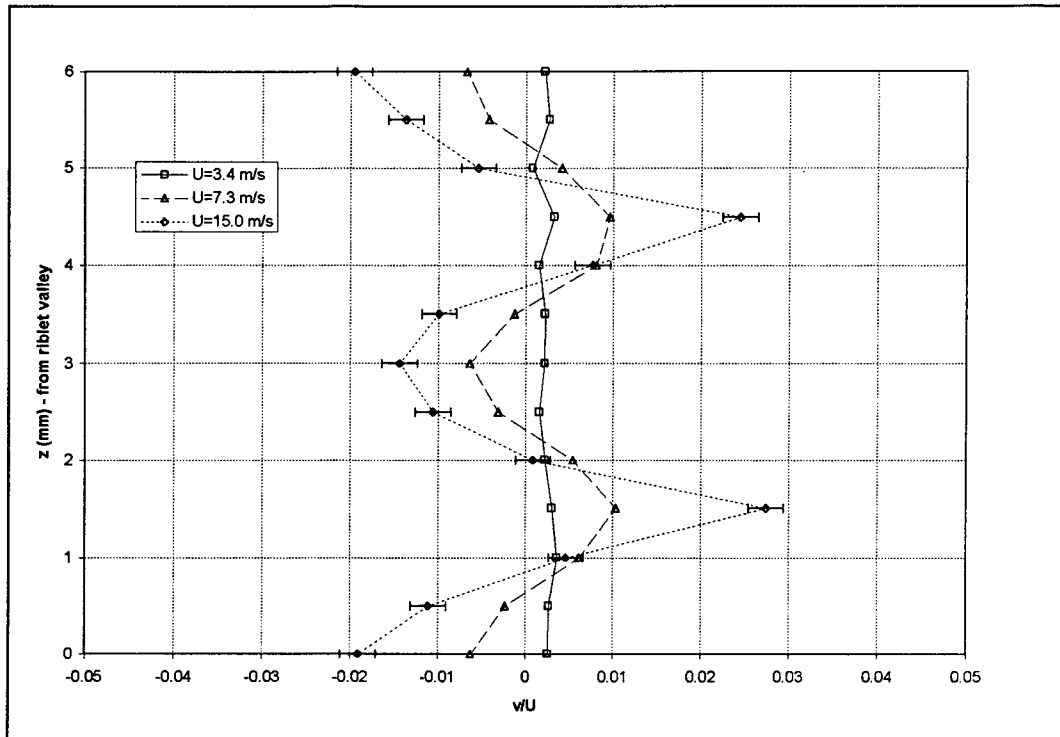


Figure 76. Lower Boundary Layer,  $v$  vs.  $z$ , curved/ribletted,  $x = 105$  mm,  $y = 0.5$  mm.

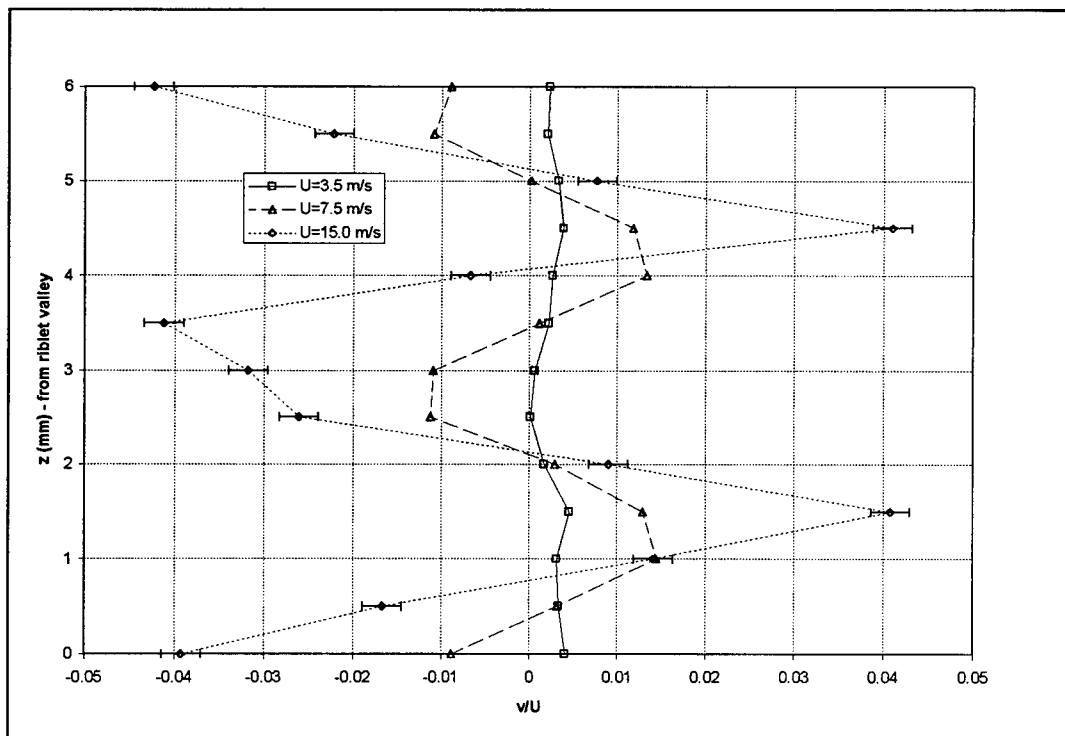


Figure 77. Lower Boundary Layer,  $v$  vs.  $z$ , curved/ribletted,  $x = 200$  mm,  $y = 0.5$  mm.

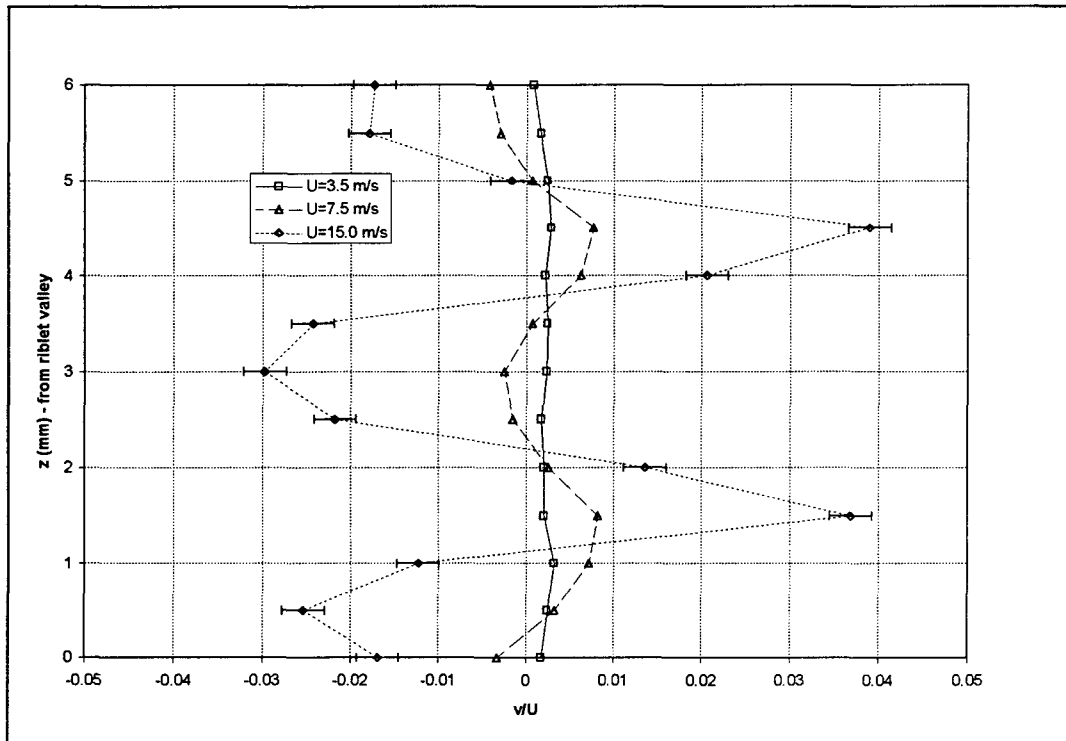


Figure 78. Lower Boundary Layer,  $w$  vs.  $z$ , curved/ribletted,  $x = 300$  mm,  $y = 0.5$  mm.

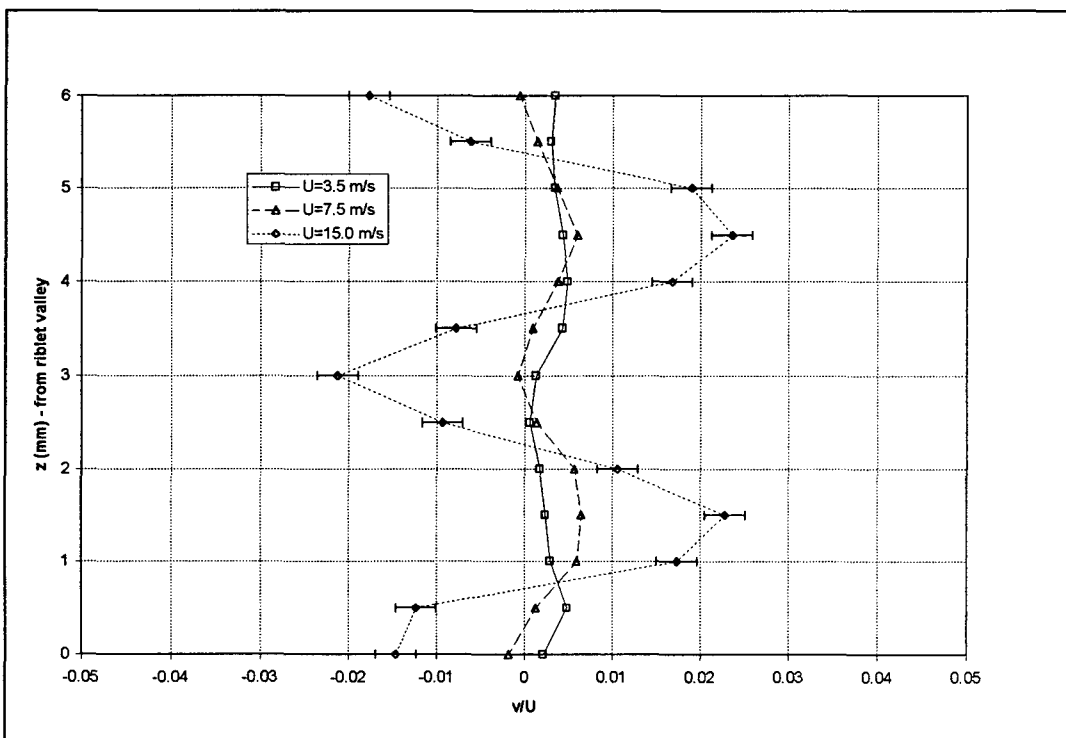


Figure 79. Lower Boundary Layer,  $w$  vs.  $z$ , curved/ribletted,  $x = 400$  mm,  $y = 0.5$  mm.

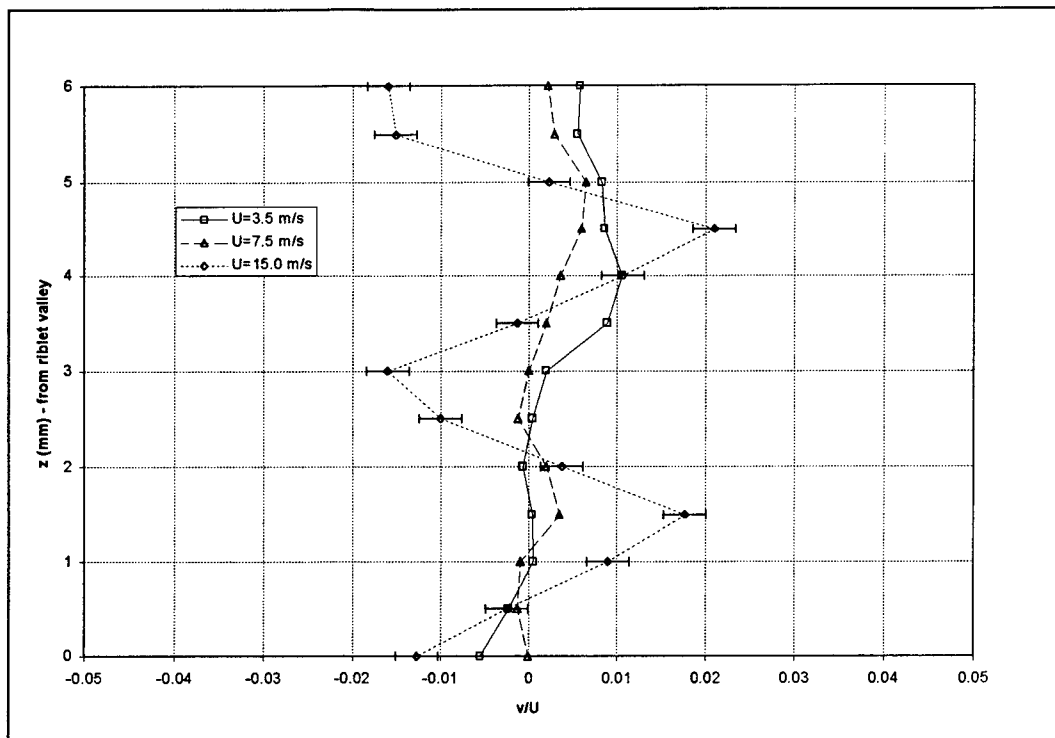


Figure 80. Lower Boundary Layer,  $v$  vs.  $z$ , curved/ribletted,  $x = 500$  mm,  $y = 0.5$  mm.

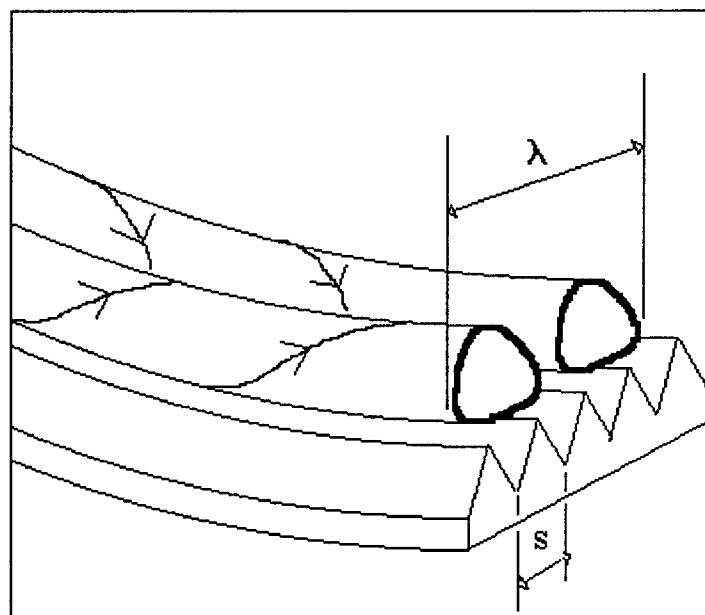


Figure 81. Upper Boundary Layer GV Formation Example.

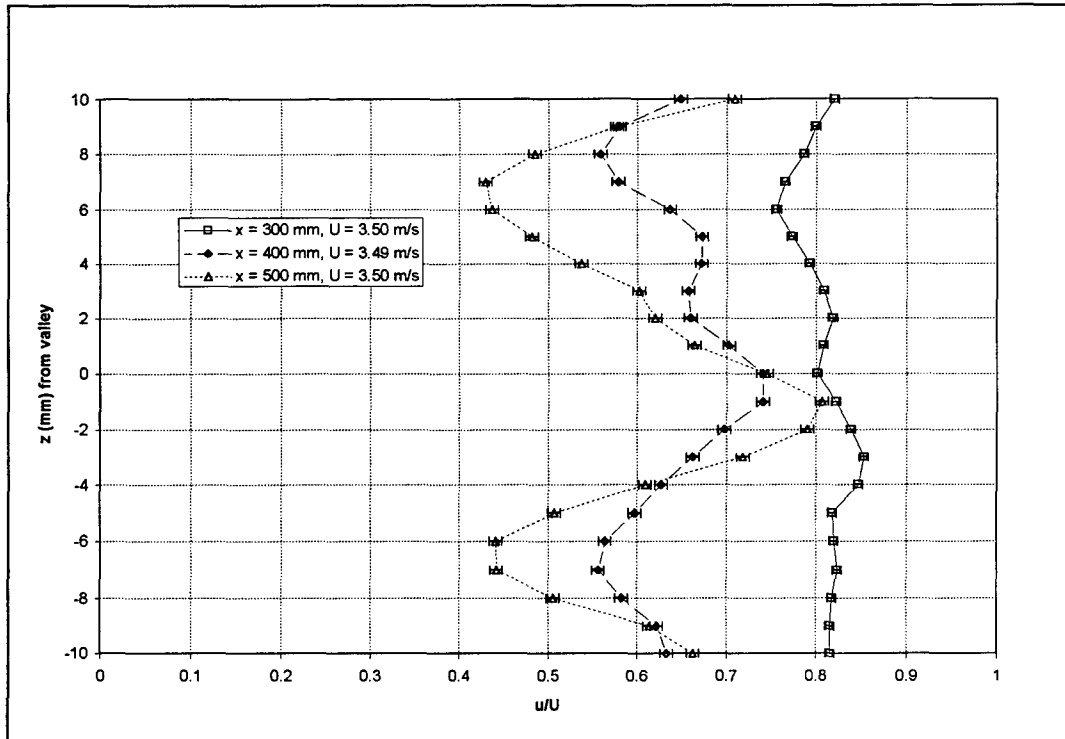


Figure 82. Upper Boundary Layer,  $u$  vs.  $z$ , curved/ribletted,  $U \approx 3.5$  m/s,  $y = 3.0$  mm.

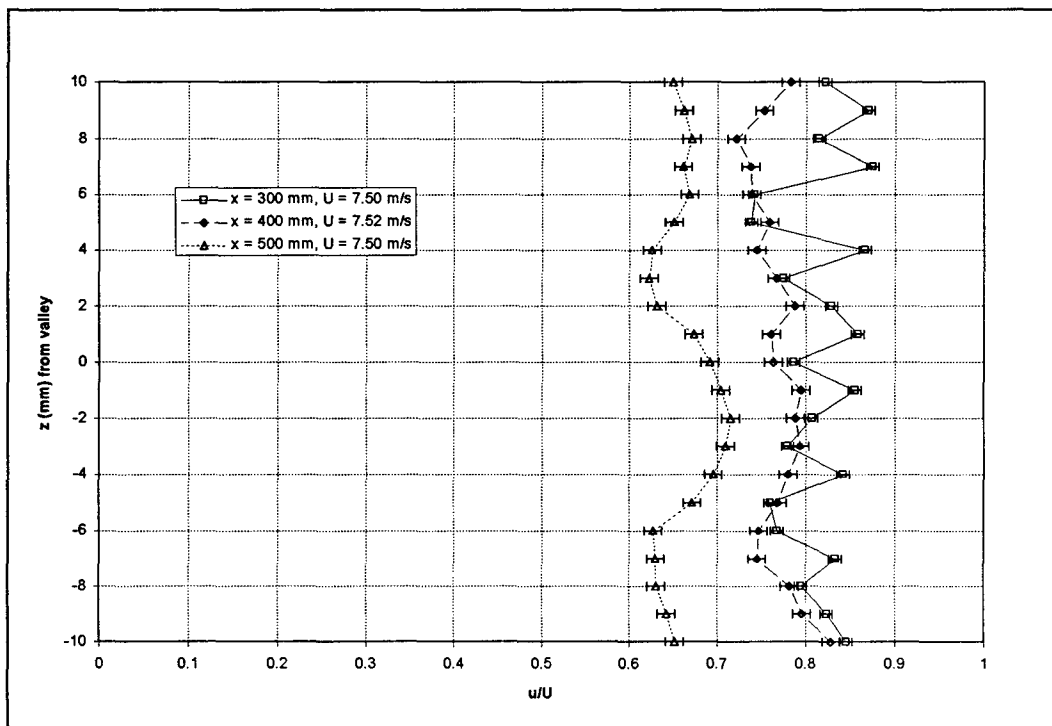


Figure 83. Upper Boundary Layer,  $u$  vs.  $z$ , curved/ribletted,  $U \approx 7.5$  m/s,  $y = 3.0$  mm.

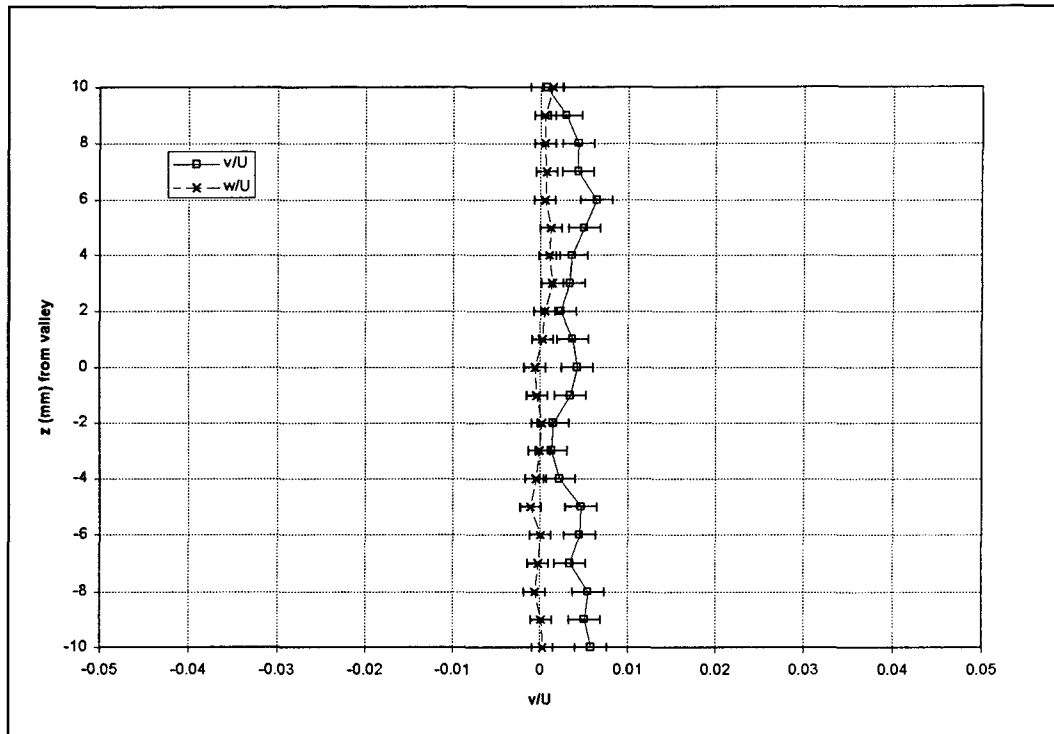


Figure 84.  $v$  and  $w$  vs.  $z$ , curved/ribletted,  $U \cong 3.5$  m/s,  $x = 300$  mm,  $y = 3.0$  mm.

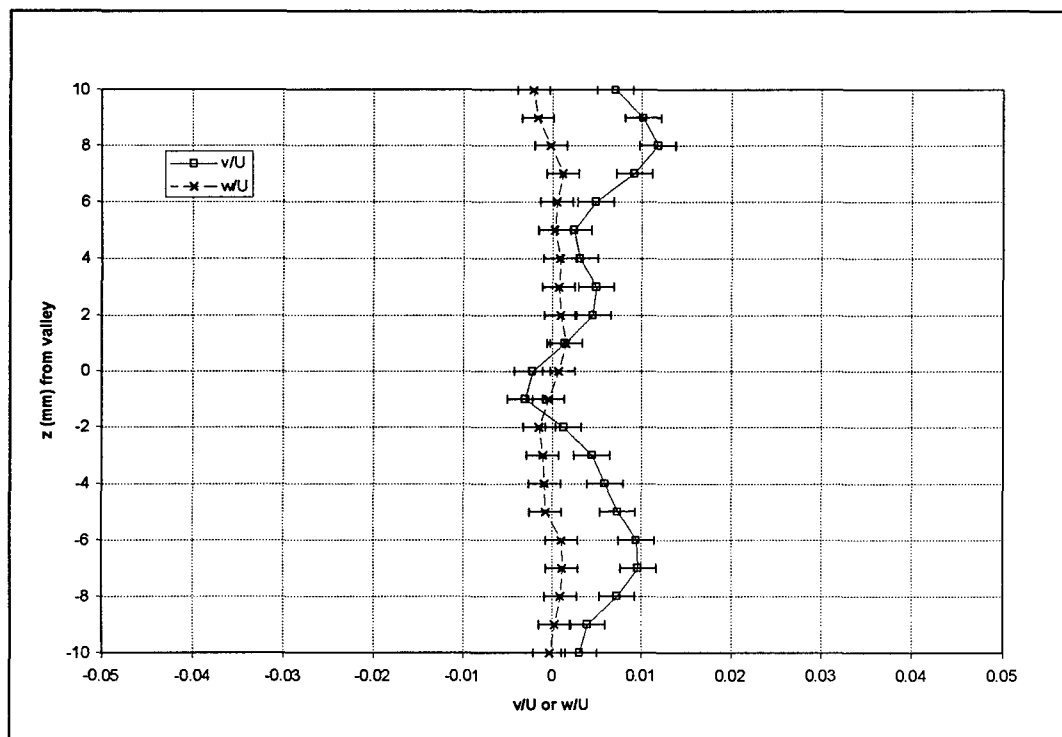


Figure 85.  $v$  and  $w$  vs.  $z$ , curved/ribletted,  $U \cong 3.5$  m/s,  $x = 400$  mm,  $y = 3.0$  mm.

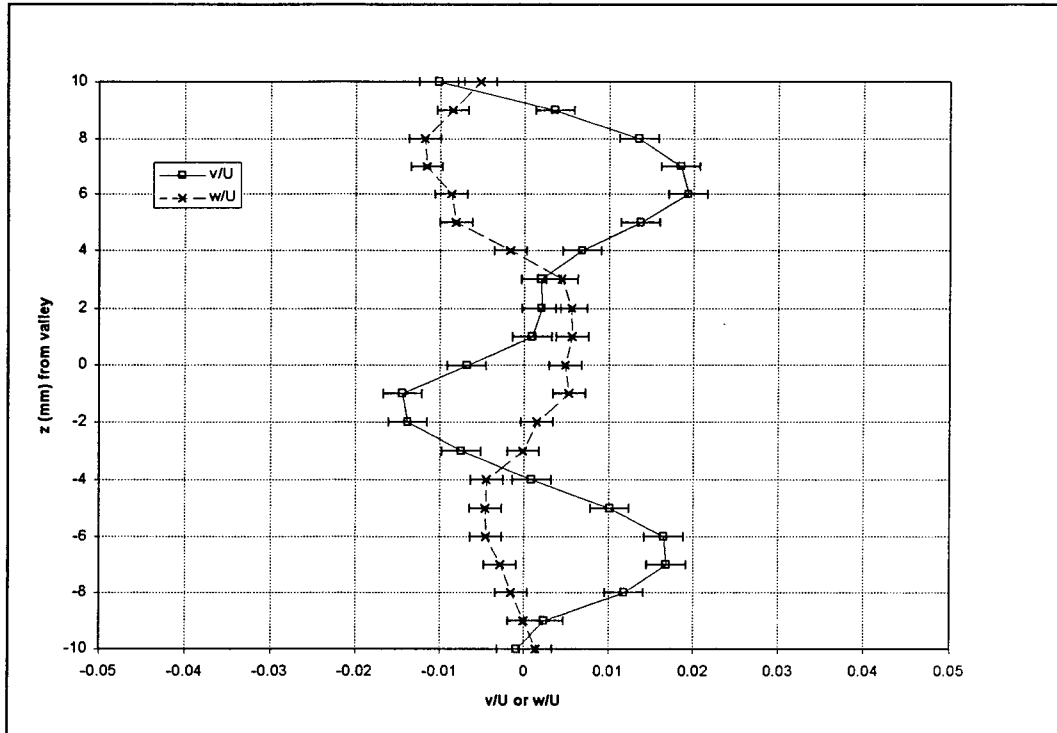


Figure 86.  $v$  and  $w$  vs.  $z$ , curved/ribletted,  $U \cong 3.5$  m/s,  $x = 500$  mm,  $y = 3.0$  mm.

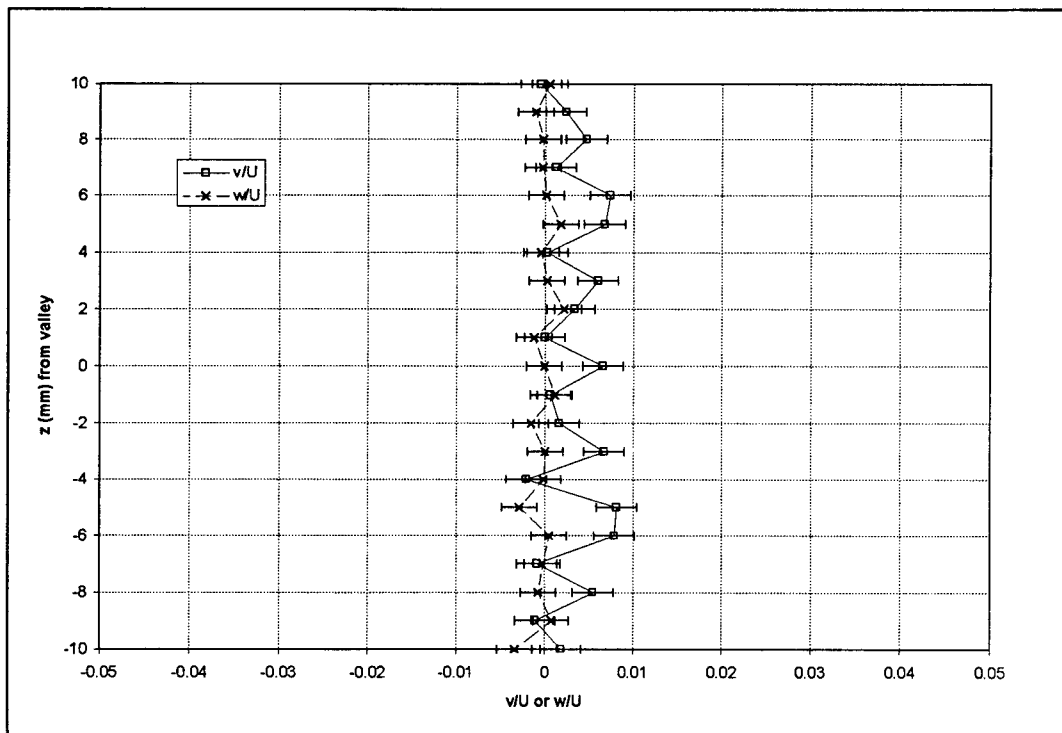


Figure 87.  $v$  and  $w$  vs.  $z$ , curved/ribletted,  $U \cong 7.5$  m/s,  $x = 300$  mm,  $y = 3.0$  mm.

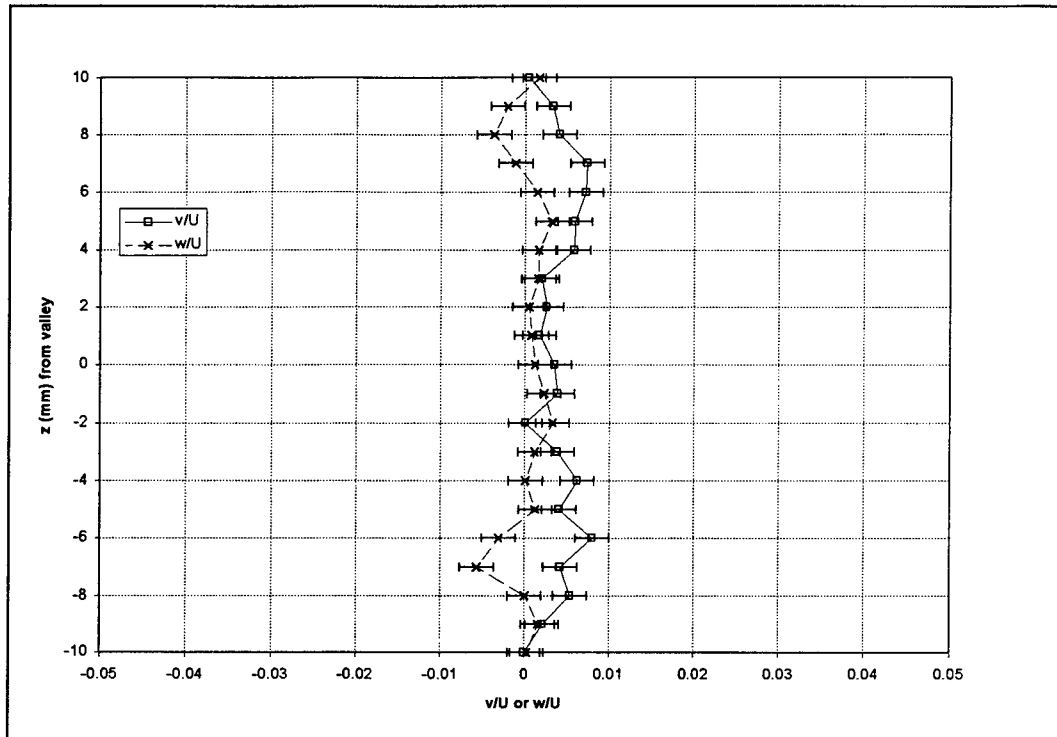


Figure 88.  $v$  and  $w$  vs.  $z$ , curved/ribbletted,  $U \cong 7.5$  m/s,  $x = 400$  mm,  $y = 3.0$  mm.

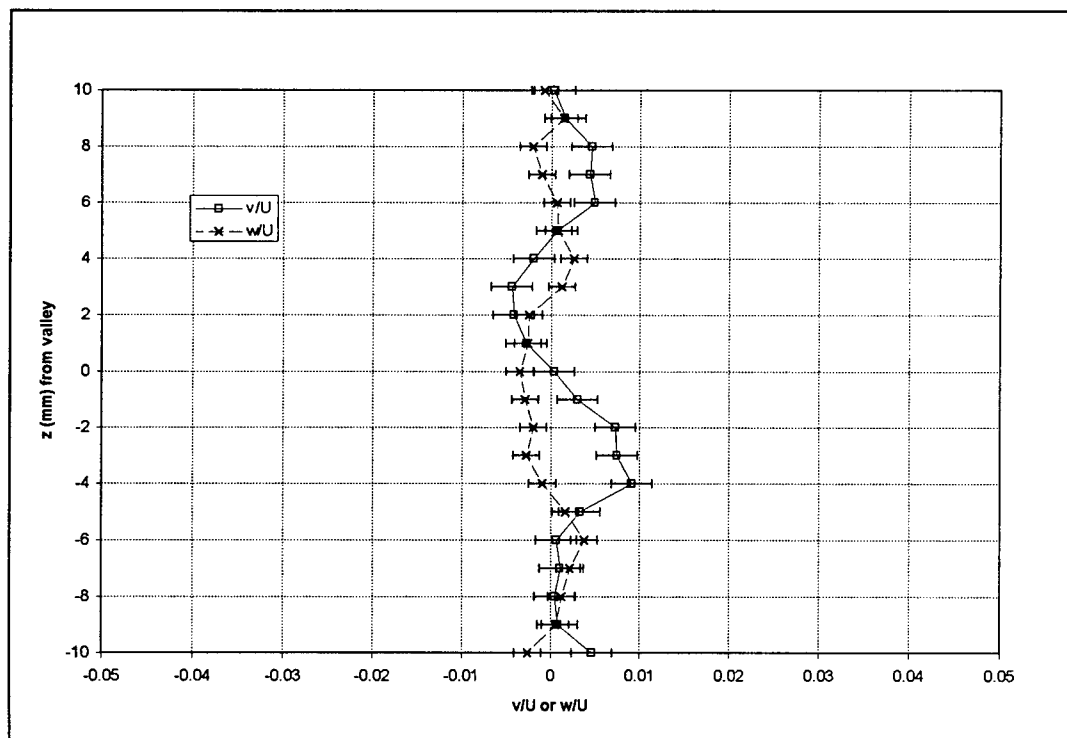


Figure 89.  $v$  and  $w$  vs.  $z$ , curved/ribbletted,  $U \cong 7.5$  m/s,  $x = 500$  mm,  $y = 3.0$  mm.



## VI. Conclusions and Recommendations

### 6.1 Conclusions

1. The accuracy of the three-dimensional laser-Doppler anemometry system was validated through the measurement of a classical laminar boundary layer.

2. Riblets on a flat plate induced spanwise velocity perturbations in the boundary layer flow not seen on a smooth surface. The resulting sheared flow deformations roll-up into streamwise vortices which nest in riblet valleys and induce early transition to a turbulent boundary layer. These vortices persist in the turbulent boundary layer, a result in contrast with the destruction of streamwise vortices found on a smooth-curved surface in a turbulent boundary layer.

3. Görtler vortices found on the curved/smooth plate had wavelengths in a range of values considered most likely to occur from Görtler stability theory. The ability to measure weak cross-stream components, the first ever to be reported, was verified.

4. Riblets on a curved surface can accelerate the formation of GVs if sized to match vortices likely to appear; but riblets sized to extinguish naturally occurring vortices do not eliminate vortices that would otherwise appear in the absence of riblets, but simply delay their formation to a point farther downstream.

This research demonstrated that riblets can delay boundary layer transition over a concave surface. Since laminar viscous drag is smaller than turbulent drag, further research could identify particular  $\Lambda_s$  regimes in which riblets reduce the net drag on a concave surface, such as found on the highly cambered laminar flow regions of turbine and compressor blades. In addition, although heat transfer was not measured in this research,

GVs have been shown to increase laminar flow heat transfer (Floryan (1991)). Since riblets can accelerate or delay GV development, their use could enhance or reduce heat transfer from a surface.

## 6.2 Recommendations

Several extensions to this work would provide valuable additional information.

1. A more extensive analysis of boundary layer transition with more streamwise locations over the curved plate would clarify the connection between  $\Lambda_s$  and transition location. This greater number of streamwise locations at which boundary layer turbulence profiles are measured (perhaps every 20 cm) should extend downstream into the fully turbulent boundary layer for all test cases.

2. Removal of the streamwise freestream turbulence gradient would facilitate direct comparisons of boundary layer transition to the empirical correlations of other researchers. This would require a window to allow the laser beams to enter the test section at a number of streamwise locations while covering the remainder of the slot in the test section wall.

3. A larger range of  $\Lambda_s$  should be investigated. In particular, values nearer to and above 210 would identify the extent to which GVs can be made to develop in nested pairs. In addition, since very small riblets (e.g.,  $\Lambda_s < 10$ ) may have a negligible effect on GV development, it would be of interest to determine the size below which no effect on GV development occurs. This study would ideally be performed using particle image velocimetry (PIV) since the precise location of the vortices within and above the riblet valleys could be monitored as  $\Lambda_s$  varies.

4. Various riblet shapes should be investigated, including riblets with flat valleys, rectangular profiles, or any of the other profiles used by riblet researchers in the past. This would extend this research to see if the various riblet profiles affected the boundary layer vortical structures differently. In particular, the use of riblets with a larger height to spacing ratio may decrease skin friction by reducing the area at the riblet peaks exposed to high speed fluid in the boundary layer.

5. It would be of interest to repeat this research for riblets over a convex surface, a condition which is centrifugally stable for a smooth plate. This would indicate whether the viscosity-induced riblet-valley vortices seen on a flat-ribletted plate would be observed and possibly attenuated by the centrifugal forces rather than reinforced as they are over a concave surface.

6. Varying the wall curvature and/or the freestream pressure gradient would yield valuable insight into the riblet-GV interaction. This is because the majority of flows in which riblets might be used involve both a pressure gradient and variable wall curvature, such as on the aerodynamic components of compressors and turbines. In particular, monitoring GV development over the pressure surface of a compressor or turbine blade with and without riblets would yield very practical information.

## References

1. Barlow, R. S. and J. P. Johnston. "Roll-Cell Structure in a Concave Turbulent Boundary layer," AIAA paper 85-0297, AIAA 23rd Aerospace Sciences Meeting, Reno, January, 1985.
2. Bassom, Andrew P. "Time-Dependent Inviscid Vortices in Three-Dimensional Boundary Layers," The Quarterly Journal of Mechanics and Applied Mathematics, vol. 45, pt. 3, Newark, NJ: Oxford University Press, 1992.
3. Bippes, H. "Experimentelle Untersuchung des Laminar-Turbulenten Umschlags an einer Parallel Angeströmten Konkaven Wand," NASA-TM-72243, March 1978.
4. Choi, Kwing-So. "Drag Reduction Mechanisms and Near Wall Turbulence Structure With Riblets," Structure of Turbulence and Drag Reduction: Proceedings of the IUTAM Symposium. New York: Springer-Verlag, 1990.
5. Clauser, M. and F. Clauser. "The Effect of Curvature on the Transition From Laminar to Turbulent Boundary Layer," NACA TN 613, 1937.
6. Coustols, M. and A. M. Savill. "Turbulent Skin-Friction Reduction by Active and Passive Means," Special Course on Skin Friction Drag Reduction, AGARD report no. 786, Loughton, Essex: Specialized Printing Services Limited, 1992.
7. Crane, R. and H. Umur. "Concave-Wall Laminar Heat Transfer and Görtler Vortex Structure: Effects of Pre-Curvature Boundary Layer and Favourable Pressure Gradients," ASME paper no. 90-GT-94, N.Y., 1990.
8. DANTEC, "Burstware Users Manual, Version 3.0," DANTEC Measurements, Inc., 1990.
9. Decook, Stephen J. "Experimental Investigation of Trailing Edge Crenelation Effects on Losses in a Compressor Cascade," MS Thesis, School of Engineering, Air Force Institute of Technology (AU), Wright-Patterson AFB, OH, December, 1991.
10. Desaint Victor, X. "Résolution des Equations de Navier-Stokes Appliquées à l'Etude de l'Ecoulement Laminaire dans des Riblets," Rapport Technique OA 18-5025 AYD, ONERA/CERT, June 1987.
11. Eshbach, Ovid D., and Mott Souders. Handbook of Engineering Fundamentals, 3rd edition, NY: John Wiley and Sons, Inc., 1975.

12. Fang, Chen, Tang Yan-Ping, and Chen Mao-Zhang. "An Experimental Investigation of Loss Reduction With Riblets on Cascade Blade Surfaces and Isolated Airfoils," ASME paper 90-GT-207, New York: ASME, 1990.
13. Floryan, J.M. "Görtler Instability of Boundary Layers Over Concave and Convex Walls," The Physics of Fluids, vol. 29, American Institute of Physics, NY, August, 1986, pp. 2380-2387.
14. Floryan, J. M. "Görtler Instability of Boundary Layers," National Aerospace Laboratory Technical Report, TR-1120T, Tokyo: National Aerospace Laboratory, 1991.
15. Floryan, J. M. and W. S. Saric. "Stability of Görtler Vortices in Boundary Layers," AIAA Journal, vol. 20, AIAA, 1985, pp. 316-324.
16. Floryan, J. M. "The Second Mode of the Görtler Instability of Boundary Layers," AIAA Journal, vol. 23, 1828-1830, AIAA, 1985.
17. Goglia, G. L. and S. M. Mangalam. "Experimental Studies on Taylor-Görtler Vortices," Final Report under Research Grant NAG-1-353, J. R. Dagenhart. Technical Monitor, Hampton VI: NASA Langley Research Center, 1985.
18. Görtler, H. "On the Three-Dimensional Instability of Laminar Boundary Layers on Concave Walls," NACA TM 1375, June, 1954.
19. Gregory, N. and W. S. Walker. "The Effect on Transition of Isolated Surface Excrescence's in the Boundary Layer," ARC Repl., R&M No. 2779, 1956, pp. 1-10.
20. Hall, P. "The Nonlinear Development of Görtler Vortices in Growing Boundary Layers," NASA Contractor Report No. 178215, Contract No. NAS1-18107, Hampton VI: NASA Langley Research Center, 1986.
21. Herbert, T. "On the Stability of the Boundary Layer Along a Concave Wall," Archives of Mechanics, vol. 28, Polish Academy of Sciences, Institute of Fundamental Technological Research, Polish Scientific Publishers, Warszawa, 1976, pp. 1039-1055.
22. Huber, Franz J. A. "Subsonic Aerodynamic Research Laboratory Inlet Studies," University of Dayton Research Institute, 30 September, 1982.
23. Kalburgi, V., S. M. Mangalam, J. R. Dagenhart. "Görtler Instability on an Aerofoil: Comparison of Marching Solution With Experimental Observations,"

AGARD-CP-438, paper no. 8, Specialized Printing Services Limited, Essex, England, 1989.

24. Kottke, V. "Taylor-Görtler Vortices and Their Effect on Heat and Mass Transfer," Proceedings of the Eighth International Heat Transfer Conference, edited by C. Tien, V. Carey, and J. Ferrell, San Francisco, CA, 1986.
25. Kreyszig, E. Advanced Engineering Mathematics. Sixth Edition, NY: John Wiley and Sons, 1988.
26. Liepmann, H. W. "Investigation of Boundary Layer Transition on Concave Walls," NACA Wartime Report W-87, 1945.
27. Liepmann, H. W. "Investigations on Laminar Boundary Layer Stability and Transition on Curved Boundaries," NACA Wartime Report W-107, August, 1943.
28. McCormack, P. D., H. Welker, and M. Kelleher. "Taylor-Görtler Vortices and Their Effect on Heat Transfer," Journal of Heat Transfer, Transactions of the ASME: ASME, February, 1970, pp. 101-112.
29. Michel, R. "Etude de la transition sur les profils d'aile-etablissement d'un point de transition et calcul de la trainée de profil en incompressible," ONERA Report No. 1/1578A, 1952.
30. Rothenflue, James A. "Experimental Investigation into the Effects of Riblets on Compressor Cascade Performance," MS Theses GAE/ENY/91D-5. School of Engineering, Air Force Institute of Technology (AU), Wright-Patterson AFB OH, December, 1991.
31. Smith, F. T. "Nonlinear Interaction of Near Planar Waves and Longitudinal Vortices in Boundary-Layer Transition," NASA CR-181751, 1988.
32. Suzuki, Y. and N. Kasagi. "Turbulent Drag Reduction Mechanism Above a Riblet Surface," AIAA Journal, vol. 32, no. 9, AIAA, NY, September 1994, pp. 1781-1790.
33. Tani, I. and J. Sakagami. "Boundary Layer Instability at Subsonic Speeds," Proceedings of the Third Congress of International Council of Aerospace Sciences, Stockholm, 1962, Spartan, Washington D.C., 1964, pp. 391-403.
34. Tennekes, H., J.L. Lumley. A First Course in Turbulence. 3rd edition, Cambridge Mass: M.I.T. Press, 1990.

35. Van Driest, E. R., and C. B. Blumer. "Boundary Layer Transition, Freestream Turbulence, and Pressure Gradient Effects," AIAA Journal, vol. 1, Washington, AIAA, 1963, pp. 1303-1306.
36. Walsh, Michael J. "Riblets," Viscous Drag Reduction in Boundary Layers. vol. 123, Progress in Astronautics and Aeronautics, edited by Dennis M. Bushnell and Jerry N. Heffner, Washington: AIAA, 1990.
37. White, Frank M. Viscous Fluid Flow. Second Edition, NY: McGraw-Hill, 1991.
38. Walpole, Ronald E., and Raymond H. Myers. Probability and Statistics for Engineers and Scientists. 4th edition, NY: Macmillan Publishing Company, 1989.

## Appendix A. Component Listing

<u>Component</u>	<u>Model/Serial No.</u>
Burst Spectrum Analyzers	
BSA1 (green)	Dantec 57N20 Enhanced
BSA2 (blue)	Dantec 57N35 Enhanced Slave
BSA3 (purple)	Dantec 57N35 Enhanced Slave
Transmitter	Dantec FiberFlow S/N FF127
Photomultipliers (x3)	Dantec Photomultiplier 57x08
Laser Probes	
1-D	Dantec 60x10
2-D	Dantec 60x11
Beam Expanders (x2)	Dantec 55x12
Main Aperture Optics (x2)	Dantec 55x58 (f = 600 mm)
Color Separator	Dantec 55x35, SN 9055x0353
Fog Generator	Dantec Model with Dantec Fog Fluid
Atomizer	TSI model 9306 6 Jet
Computer	Gateway 2000, 486DX/33
Mass Flow Regulator	Grove Model 83, SN 94710
Control Regulator	Grove Model 829 Pilot, SN 11509
Pressure Gauge	American Inst. Corp. 25 x 1/4 psi
Triple Scale Laser Power Meter	US Instruments, model 33s



## Appendix B. BLRF Component Specifications

### Contracting Section (Nozzle)

The section connecting the stilling chamber to the aluminum attachment piece to the test section is based on a bi-circular contour with a 10 degree initial angle of contraction. The drawing as submitted to the AFIT Model Fabrication Shop is given in Figure 90. The initial radius of curvature was 18.9 inches and the final radius was 9.4 inches. Other dimensions are as given on the drawing.

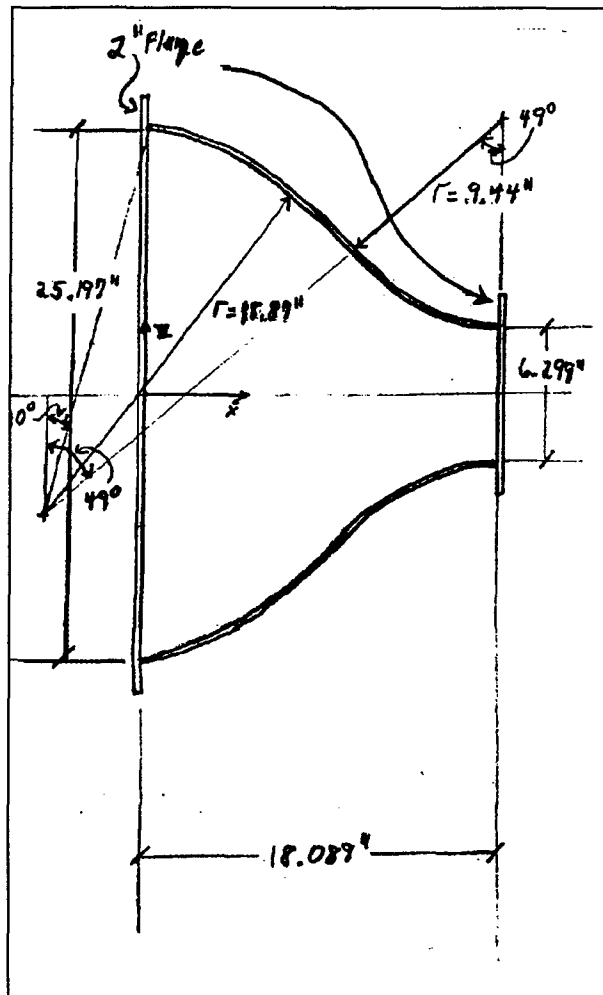


Figure 90. Nozzle Top View Shop Drawing.

### Stilling Chamber Stand

The stilling chamber stand holds the stilling chamber and is leveled using adjustable feet. One shop drawing, containing the important dimensions is given in Figure 91.

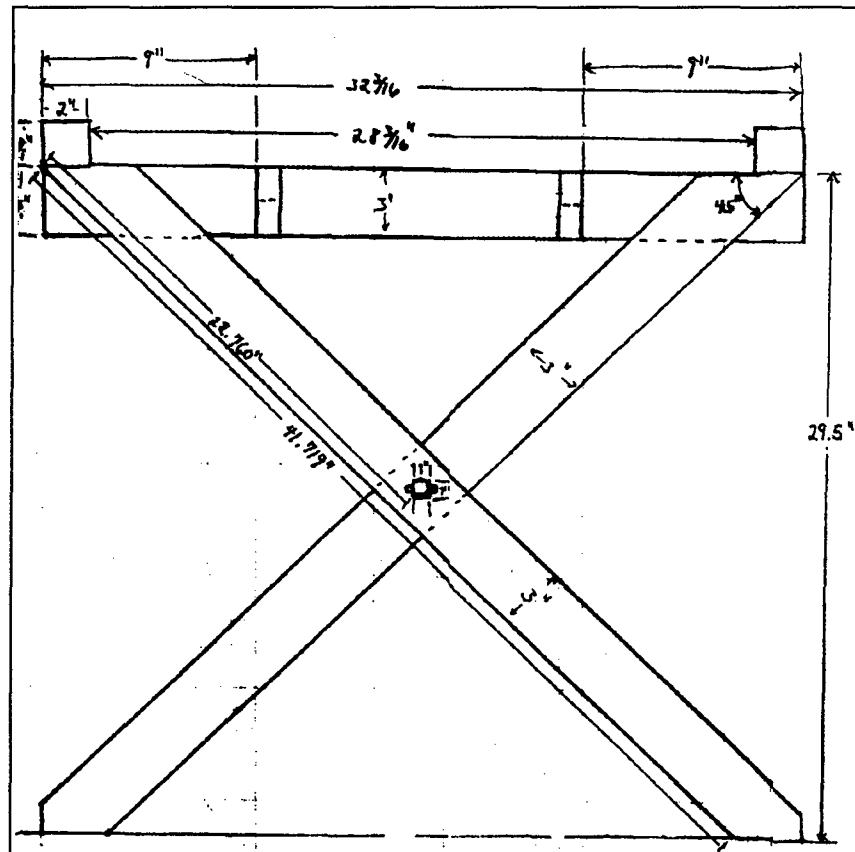


Figure 91. Stilling Chamber Stand.

## Appendix C. Laser Doppler Anemometry - Basic Principles

### The Laser Doppler Problem.

A laser Doppler anemometer is designed to measure the frequency shift of laser light reflected from a particle within a fluid flow. Theoretically, if this frequency shift could be directly measured, the particle's velocity component in the axis of the laser beam could be calculated. However, since laboratory particles travel at speeds which are many orders of magnitude smaller than the speed of light, conventional spectroscopic methods of measuring frequency shift are too insensitive and cannot be used. In addition, direct measurement of light frequency is impossible because modern-day electronics are several orders of magnitude too slow to measure the variations in the instantaneous electronic and magnetic fields associated with the propagation of a light wave through space. For these reasons, a laser Doppler anemometer must rely on indirect methods of measuring the frequency shift associated with particle motion. Although the details of these methods will vary from one apparatus to another, the basic principles described herein are generally universal.

### Intersecting Lasers, Doppler Frequency, and Directional Ambiguity.

Consider a volume of space defined by the region of intersection of two laser beams of identical frequency. A particle traversing this volume will scatter light from both beams. However, since the angle between each laser beam and the particle's velocity vector is different, the frequency of the reflected light from each beam will also be different. Therefore, the intensity of the scattered light from the particle will vary with time in a "beating" pattern due to the alternating constructive and destructive interference of the light from each laser. The electrical

signal from a photodetector measuring the intensity of this scattered light would reveal the particle's passage with what is called a "Doppler burst", illustrated in Figure 92.

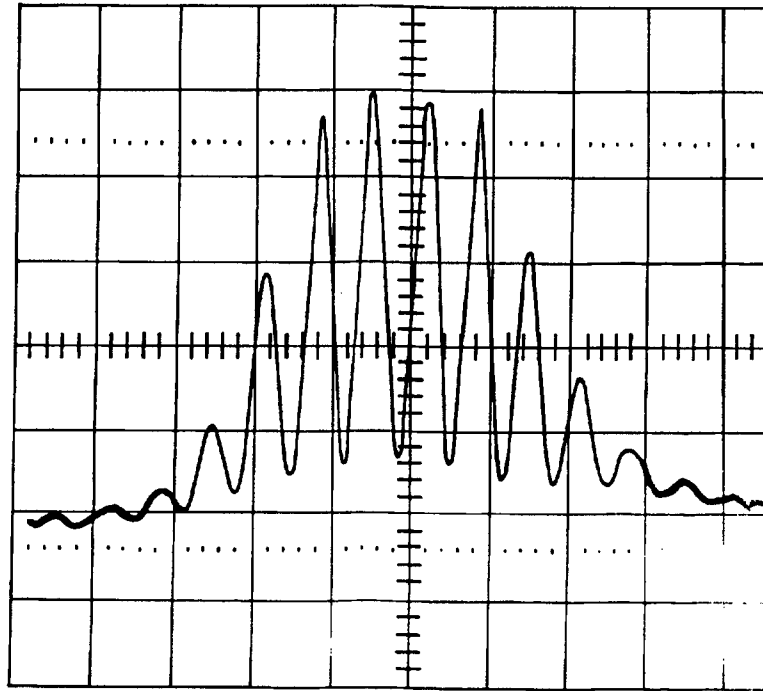


Figure 92. Doppler Burst as Seen on Oscilloscope.

The frequency of the oscillating signal in the Doppler burst is proportional to the particle's velocity component normal to the angular bisector of the two laser beams and in the plane of the lasers, illustrated in Figure 93. The first order approximation of this relationship, assuming the particle speed is much less than the speed of light, is

$$U_N = f \frac{\lambda}{2 \sin(\theta / 2)}, \quad (42)$$

where  $U_N$  is the velocity component,  $f$  is the burst frequency,  $\lambda$  is laser wavelength, and  $\theta$  is the angle between the lasers. For most practical applications, the frequency,  $f$ , is low enough to be accurately measured using current electronics.

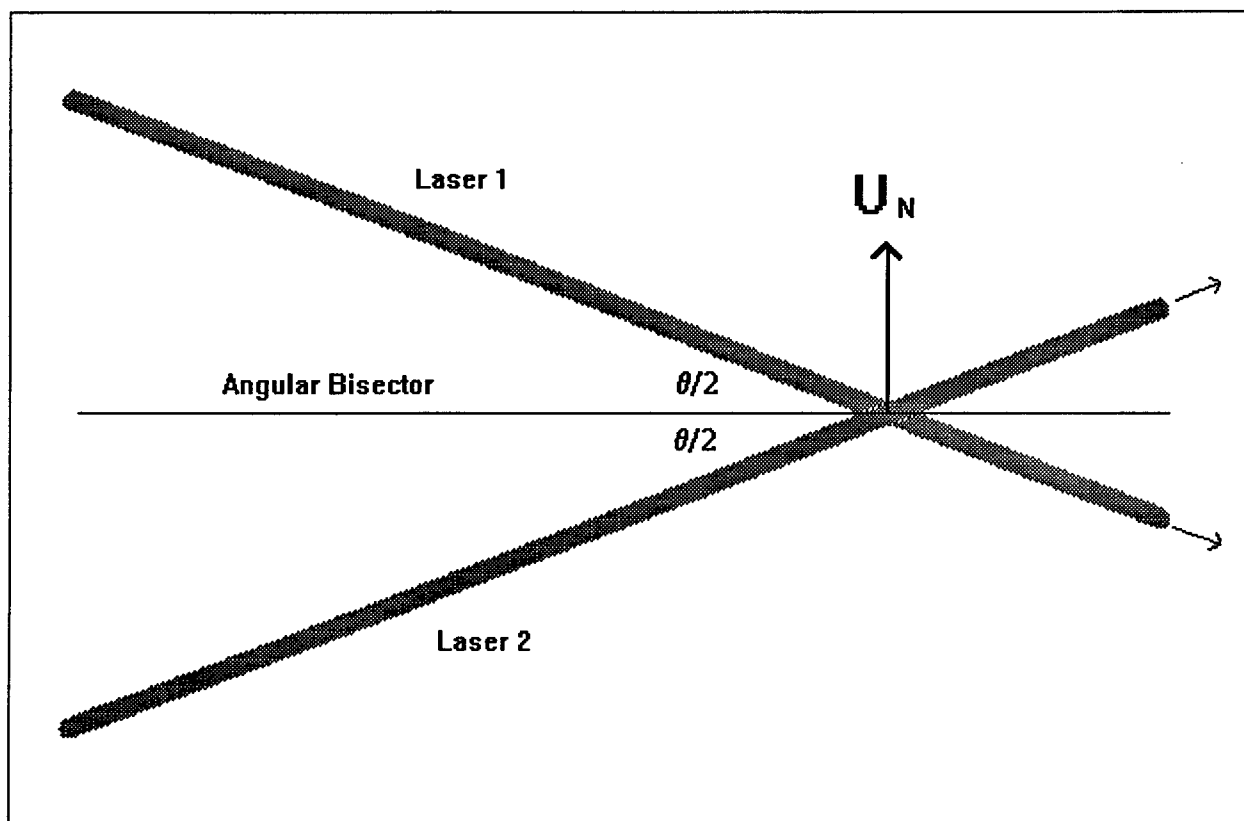


Figure 93. Direction of  $U_N$ .

Equation (42) will yield the magnitude of  $U_N$  but not its sign. This ambiguity can be resolved by slightly shifting the frequency of one of the laser beams by a known value,  $f_0$ . The shift in laser frequency will create an identical shift in the burst frequency,  $f$ . In effect, this shifts the velocity-frequency curve to the left, as illustrated in Figure 94. In this figure,  $f_0 = 40$  MHz, and the velocity of the particle is now directionally unambiguous down to a velocity of  $u = -f_0\lambda/[2\sin(\theta/2)]$ . Thus, if the experimenter knows a priori that the largest negative particle velocities within the flow, due to any reason including turbulent fluctuations, will be less than  $u$ , then his measurements will be directionally unambiguous. For this case, the burst frequency from a stationary particle in the volume would be equal to  $f_0$ .

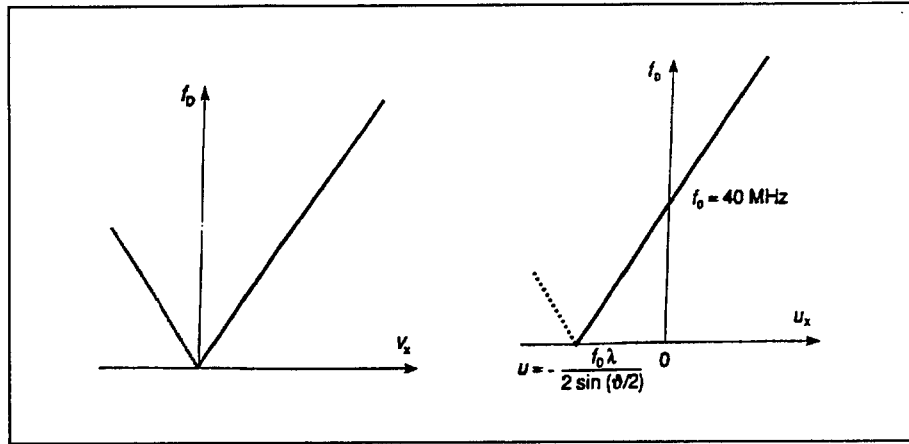


Figure 94. Velocity-Frequency Relationship with Frequency Shift.

### The Fringe Model.

The concept of fringe patterns is central to laser Doppler anemometry, and the "fringe model" is a more intuitive first order approximation of the theory described in the previous section. Consider, once again, the volume defined by the region of intersection of two laser beams. The interference of the two coherent beams will produce a set of alternating planar dark and bright regions in space called fringes. This phenomenon is illustrated in two dimensions in Figure 95.

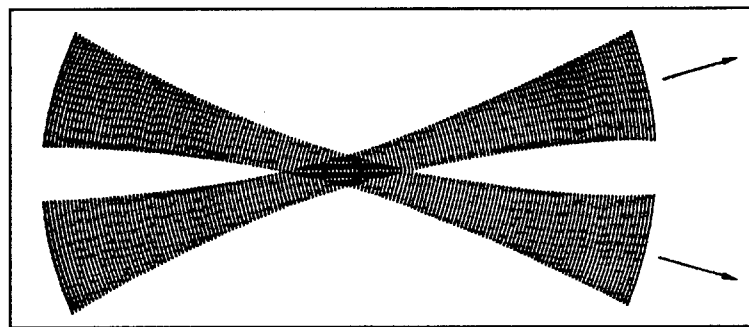


Figure 95. 2-D Fringe Pattern from Two Coherent Beams.

The intersection of three-dimensional laser beams with Gaussian power distributions will create an ellipsoidal volume of fringes, called the probe volume, whose exact dimensions are determined by

the reflectivity of the transiting particle and the sensitivity of the detecting photomultiplier. An example of such a probe volume is given in Figure 96.

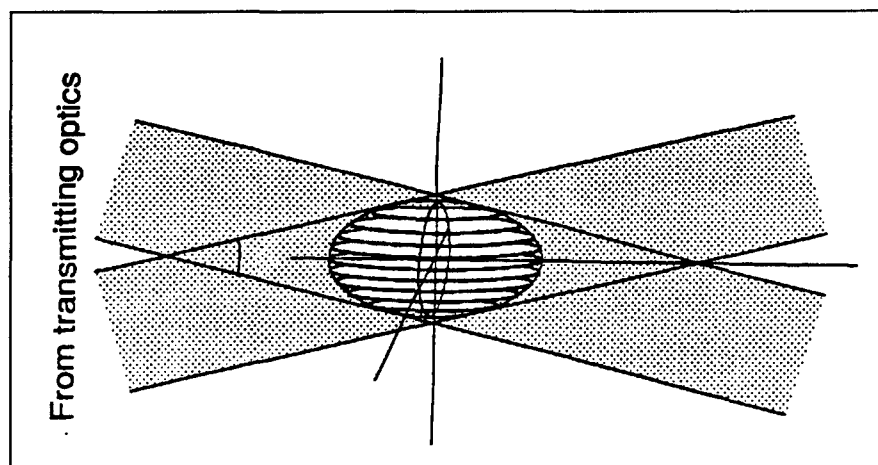


Figure 96. 3-D Fringe Pattern.

The distance between the fringes,  $s$ , is given by,

$$s = \frac{\lambda}{2 \sin(\theta / 2)}. \quad (43)$$

The Doppler frequency of a particle passing through this volume is  $f = v/s$ . Direct substitution of this formula into Equation (43) yields Equation (42), indicating that the two approaches to the problem yield the same result.

The aforementioned frequency shift used to address the directional ambiguity causes the fringe pattern to scroll within the probe volume. Thus, a stationary particle would be swept by alternating light and dark regions, resulting in a Doppler frequency equal to the shift frequency,  $f_0$ . Particle velocity is now directionally unambiguous, given the same constraints discussed in the previous section.

### Multidimensional Measurements.

The principles for single component velocity measurements extend easily to two or three dimensions. A separate pair of lasers is focused into the same region of space for each additional dimension. These additional pairs each have a unique color (wavelength) and spatial orientation. Each pair of lasers has a separate set of receiving optics designed to detect only that color, thus allowing simultaneous and independent velocity measurements of each velocity component for a particle which is passing through the superimposed fringe patterns generated by each pair of lasers.



## Appendix D. Optical to Test Section Coordinate Transformation

### Purpose of Transformation.

It is generally impractical or impossible to construct an experimental apparatus for three axis laser Doppler anemometry in which the three measured velocity components from the LDA correspond exactly with the defined  $u$ ,  $v$ , and  $w$  velocities (which are often mutually perpendicular) within the test section. Although two dimensional laser probes are usually designed so that the measured velocity components are perpendicular, it is rarely possible to arrange the apparatus so that the one dimensional probe velocity component is perpendicular to the 2-D components. In addition, slight misalignments between the laser Doppler equipment and the wind tunnel test section must also be accounted for. Therefore, measured velocity components must be converted into test section coordinates using an appropriate transformation matrix, named the optical-to-test section (OTT) matrix. For the remainder of this discussion, the functions  $\sin(\theta)$  and  $\cos(\theta)$  will be replaced by the abbreviations  $s\theta$  and  $c\theta$  respectively.

### Laser Probe Alignment (LPA) Matrix.

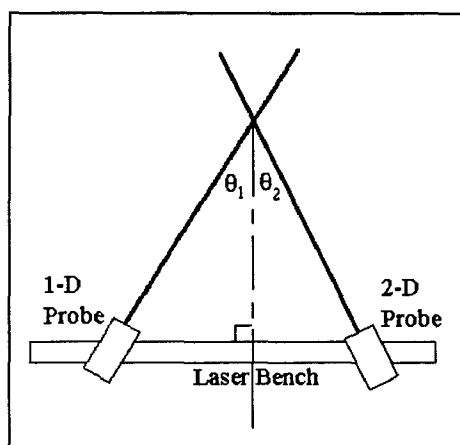


Figure 97. Laser Probe Angles.

The most convenient method for determining the OTT matrix is to define it as the product of two simpler matrices: the laser probe alignment (LPA) matrix and the optical misalignment (OM) matrix. The LPA matrix accounts for the angles between the 1-D and 2-D laser probes, illustrated in Figure 97, and the OM matrix accounts for the angles (misalignments) between laser bench and the test section. This section addresses the derivation of the

LPA matrix.

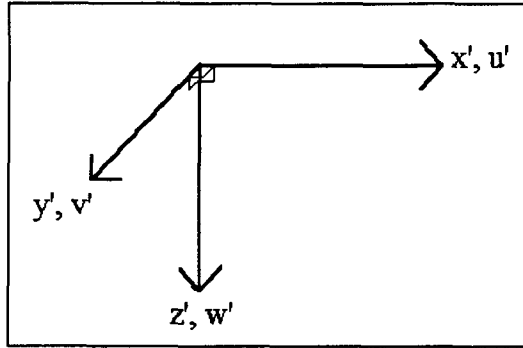


Figure 98. Laboratory Coordinates.

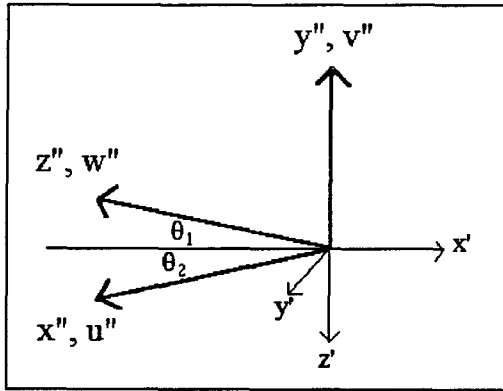


Figure 99. LDA Measurement Axes.

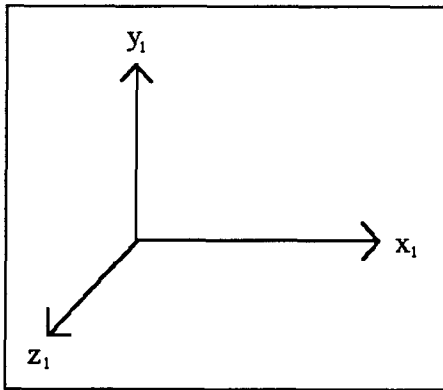


Figure 100. After 1st Rotation.

where

$$[B] = \begin{bmatrix} -c\theta_2 & 0 & s\theta_2 \\ 0 & 1 & 0 \\ -s\theta_2 & 0 & -c\theta_2 \end{bmatrix} \begin{bmatrix} 1 & 0 & 0 \\ 0 & 0 & -1 \\ 0 & 1 & 0 \end{bmatrix} = \begin{bmatrix} -c\theta_2 & s\theta_2 & 0 \\ 0 & 0 & 1 \\ -s\theta_2 & -c\theta_2 & 0 \end{bmatrix} \quad (46)$$

Consider the orthogonal laboratory coordinate system given in Figure 98. Now, assume an LDA apparatus measuring velocities along the axes given in Figure 99, where  $u''$ ,  $v''$ , and  $w''$  are the measured velocities along the non-orthogonal  $x''$ ,  $y''$ , and  $w''$  axes. Transforming the coordinate system in Figure 98 to that in Figure 99 involves two rotations and one coordinate transformation. Begin by rotating the laboratory coordinates (Figure 98) about the  $x'$  axis by  $270^\circ$ , resulting in Figure 100.

Mathematically, this is expressed by

$$\begin{Bmatrix} x_1 \\ y_1 \\ z_1 \end{Bmatrix} = [A] \begin{Bmatrix} x' \\ y' \\ z' \end{Bmatrix} = \begin{bmatrix} 1 & 0 & 0 \\ 0 & 0 & -1 \\ 0 & 1 & 0 \end{bmatrix} \begin{Bmatrix} x' \\ y' \\ z' \end{Bmatrix}. \quad (44)$$

Next, rotate Figure 100 about the  $y_1$  axis through  $180+\theta_2$  degrees as illustrated in Figure 101. Thus,

$$\begin{Bmatrix} x_2 \\ y_2 \\ z_2 \end{Bmatrix} = \begin{bmatrix} -c\theta_2 & 0 & s\theta_2 \\ 0 & 1 & 0 \\ -s\theta_2 & 0 & -c\theta_2 \end{bmatrix} \begin{Bmatrix} x_1 \\ y_1 \\ z_1 \end{Bmatrix} = [B] \begin{Bmatrix} x' \\ y' \\ z' \end{Bmatrix}, \quad (45)$$

The  $x_2$  and  $y_2$  coordinates are now parallel to the  $x''$  and  $y''$  coordinates. In terms of the  $\{x_2\}$  coordinate system, the  $z''$  coordinate is now  $z'' = x_2 \cos(\theta_1 + \theta_2) + z_2 \sin(\theta_1 + \theta_2)$ , yielding

$$\begin{Bmatrix} x'' \\ y'' \\ z'' \end{Bmatrix} = \begin{bmatrix} 1 & 0 & 0 \\ 0 & 1 & 0 \\ c(\theta_1 + \theta_2) & 0 & s(\theta_1 + \theta_2) \end{bmatrix} \begin{Bmatrix} x_2 \\ y_2 \\ z_2 \end{Bmatrix} = [C] \begin{Bmatrix} x' \\ y' \\ z' \end{Bmatrix}, \quad (47)$$

where

$$[C] = \begin{bmatrix} 1 & 0 & 0 \\ 0 & 1 & 0 \\ c(\theta_1 + \theta_2) & 0 & s(\theta_1 + \theta_2) \end{bmatrix} \begin{bmatrix} -c\theta_2 & s\theta_2 & 0 \\ 0 & 0 & -1 \\ -s\theta_2 & -c\theta_2 & 0 \end{bmatrix} \quad (48)$$

$$= \begin{bmatrix} -c\theta_2 & s\theta_2 & 0 \\ 0 & 0 & -1 \\ -c\theta_2 c(\theta_1 + \theta_2) - s\theta_2 s(\theta_1 + \theta_2) & s\theta_2 c(\theta_1 + \theta_2) - c\theta_2 s(\theta_1 + \theta_2) & 0 \end{bmatrix}$$

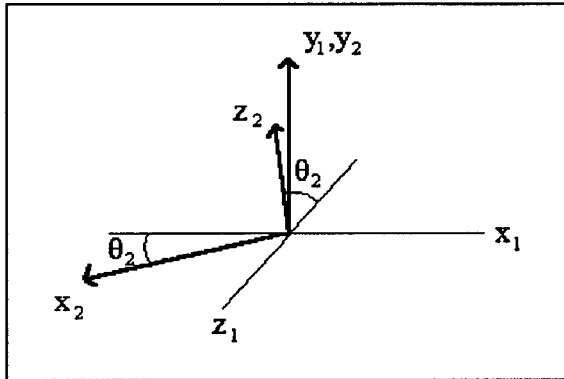


Figure 101. Second Rotation.

The LPA matrix is equal to  $[C]^{-1}$  and it converts measured velocity components ( $u''$ ,  $v''$ , and  $w''$ ) to laboratory velocities ( $u'$ ,  $v'$ , and  $w'$ ) by calculating  $\{u'\} = [C]^{-1}\{u''\}$ . For this research,  $\theta_1 = 34.75^\circ$  and  $\theta_2 = 35.25^\circ$ .

### Optical Misalignment (OM) Matrix.

The laboratory coordinate system given in Figure 98 is the datum defined by the orientation of the LDA system. In the real world, the physical orientation of the test section will differ slightly from the laboratory datum, unless measures are in place to allow for precise alignment of the test section with the LDA equipment. Since both the laboratory and test section

coordinate systems are orthogonal, the transformation matrix from one system to the other is the product of cosine matrices. This matrix,  $[D]$ , is the OM matrix and is used to convert velocities from laboratory (laser probe bench, by definition) to test section coordinates by calculating  $\{u, v, w\} = [D]\{u', v', w'\}$ .

For this research, rotations of  $\alpha$ ,  $\beta$ , and  $\gamma$  degrees were performed about the  $z'$ ,  $y'$ , and  $x'$  axes respectively to arrive at the test section orientation. This results in an OM matrix given by,

$$[D] = \begin{bmatrix} c\alpha c\beta & c\beta s\alpha & s\beta \\ -s\alpha c\gamma - s\gamma c\alpha s\beta & c\gamma c\alpha - s\gamma s\alpha s\beta & s\gamma c\beta \\ -s\gamma s\alpha - c\gamma c\alpha s\beta & -s\gamma c\alpha - c\gamma s\alpha s\beta & c\gamma c\beta \end{bmatrix} \quad (49)$$

For this research, these angles varied with test configuration from  $-0.5^\circ < \alpha < 1.0^\circ$ ,  $0.7^\circ < \beta < 2.8^\circ$ , and  $\gamma \approx 0^\circ$ .

#### Optical-to-Test Section Matrix.

The OTT matrix,  $[E]$ , is the product of the LPA and OM matrices:  $[E] = [C]^{-1}[D]$ . Thus, the calculation of test section velocities ( $u$ ,  $v$ , and  $w$ ) given the raw velocities from the LDA equipment ( $u''$ ,  $v''$ , and  $w''$ ) is as follows:  $\{u, v, w\} = [E]\{u'', v'', w''\}$ .

## Appendix E. Boundary Layer Turbulence Profiles

### Curved/Smooth Plate.

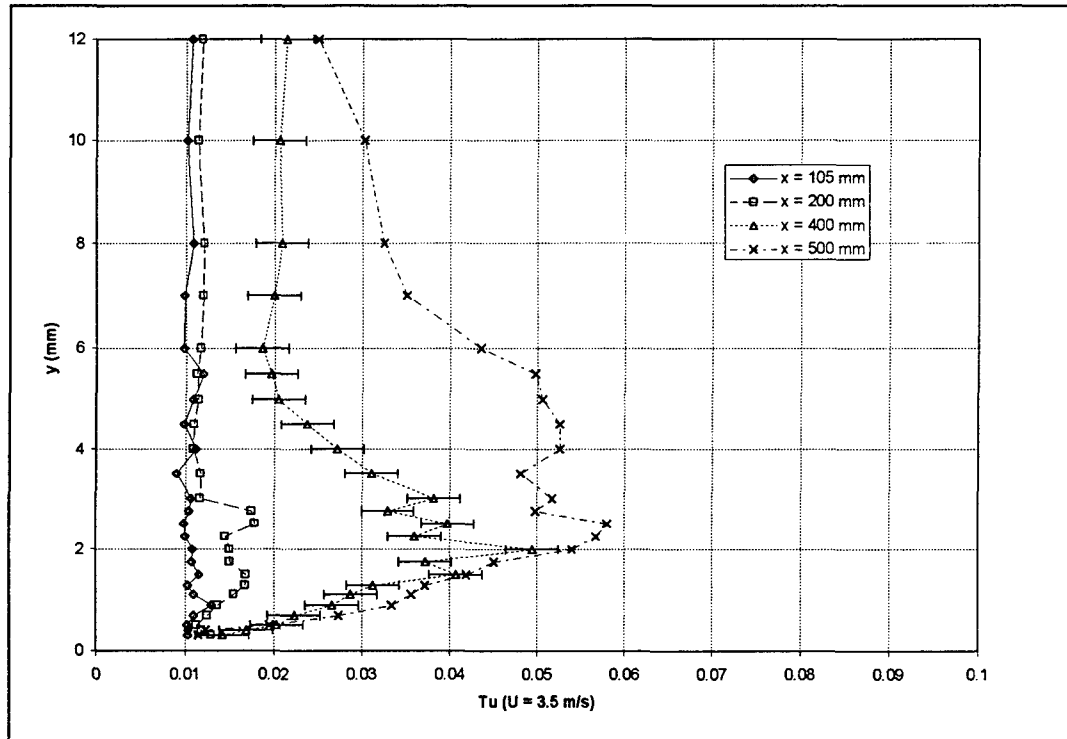


Figure 102.  $Tu$  vs.  $y$ : Curved/Smooth,  $U = 3.5$  m/s.

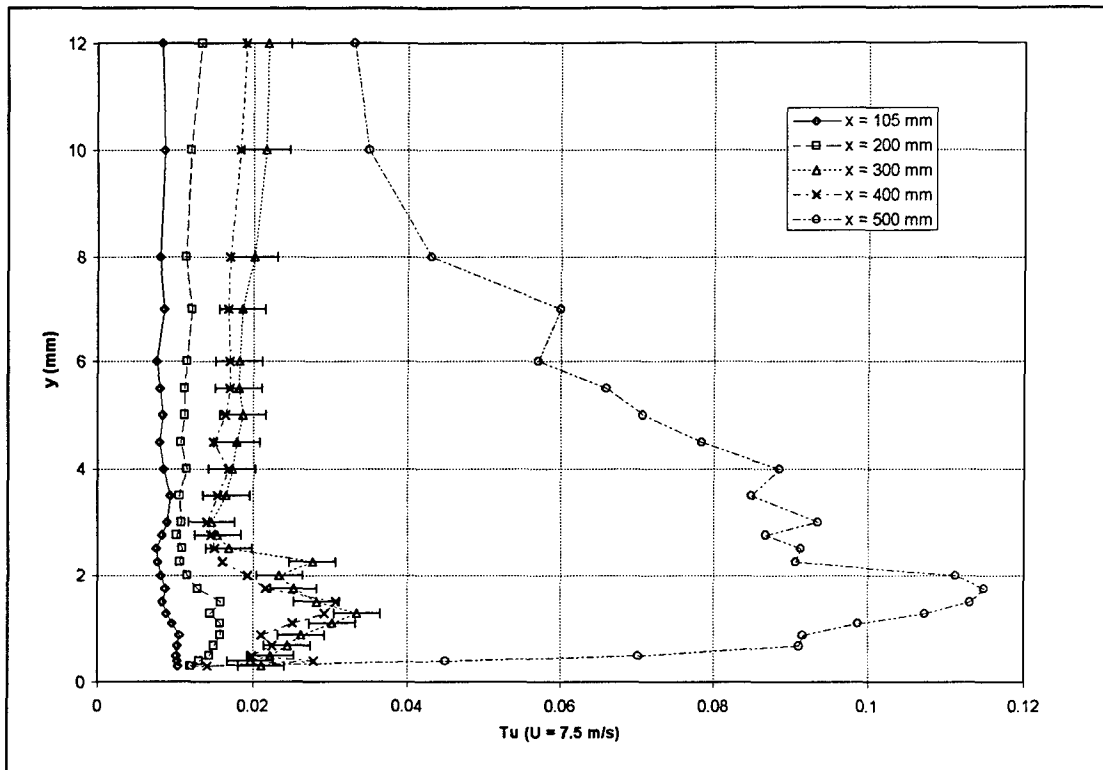


Figure 103. Tu vs. y: Curved/Smooth,  $U = 7.5$  m/s.

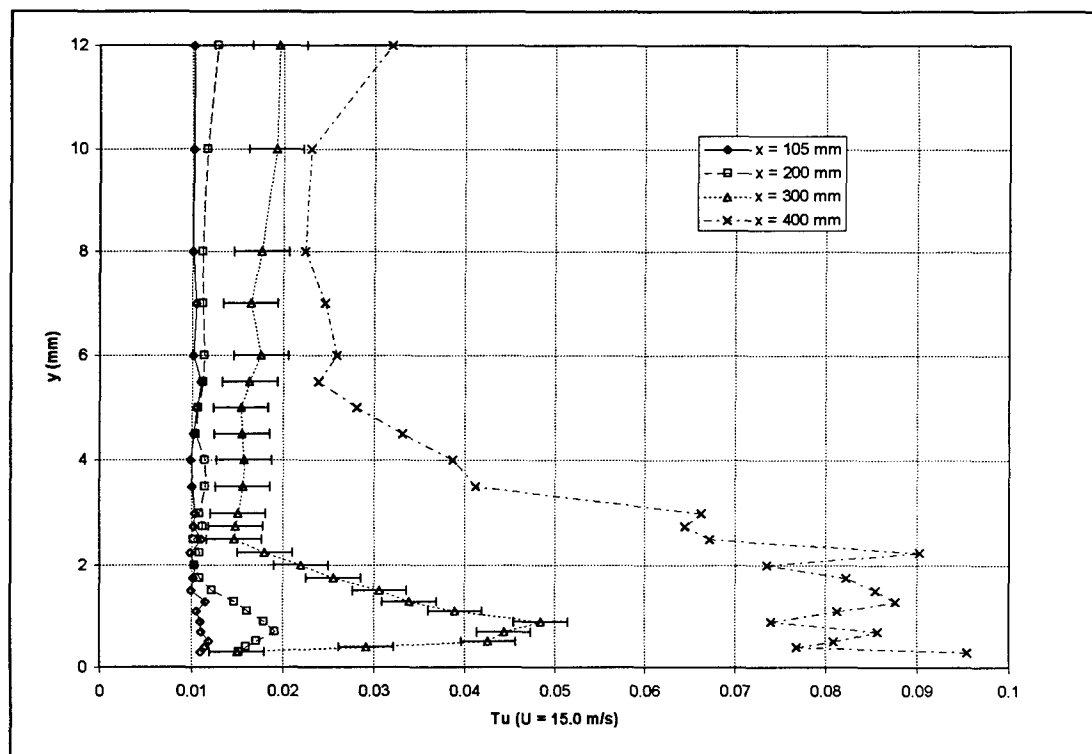


Figure 104. Tu vs. y: Curved/Smooth,  $U = 15.0$  m/s.

# Flat/Ribletted Plate.

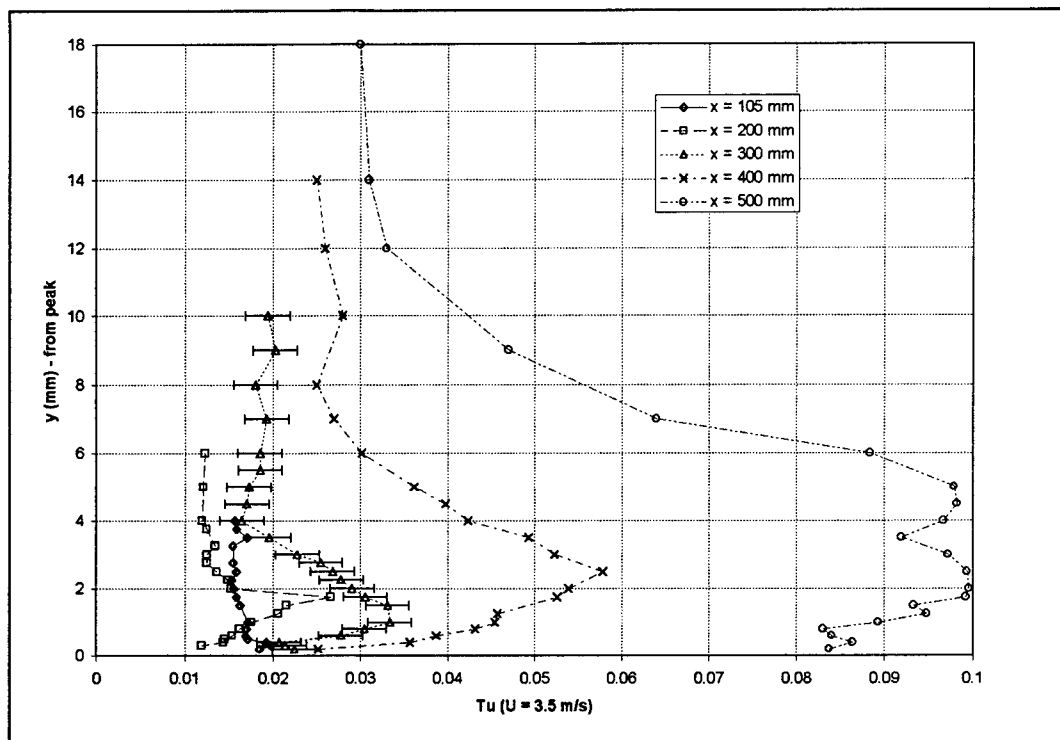


Figure 105.  $Tu$  vs.  $y$ : Flat/Ribletted,  $U = 3.5$  m/s, Riblet Peak.

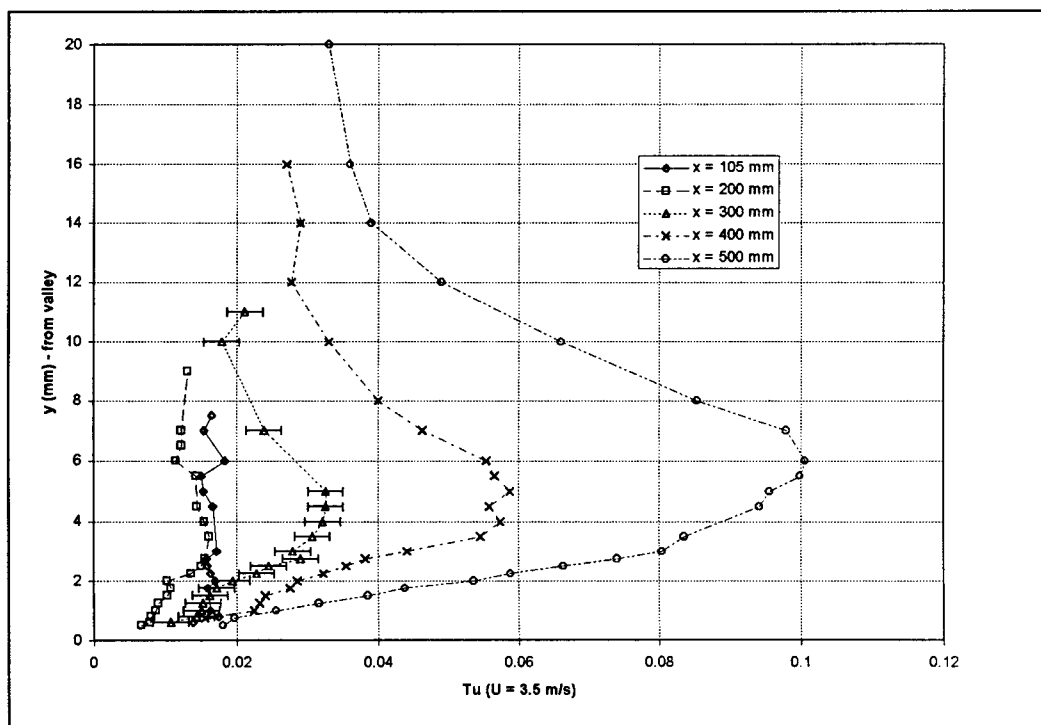


Figure 106.  $Tu$  vs.  $y$ : Flat/Ribletted,  $U = 3.5$  m/s, Riblet Valley.

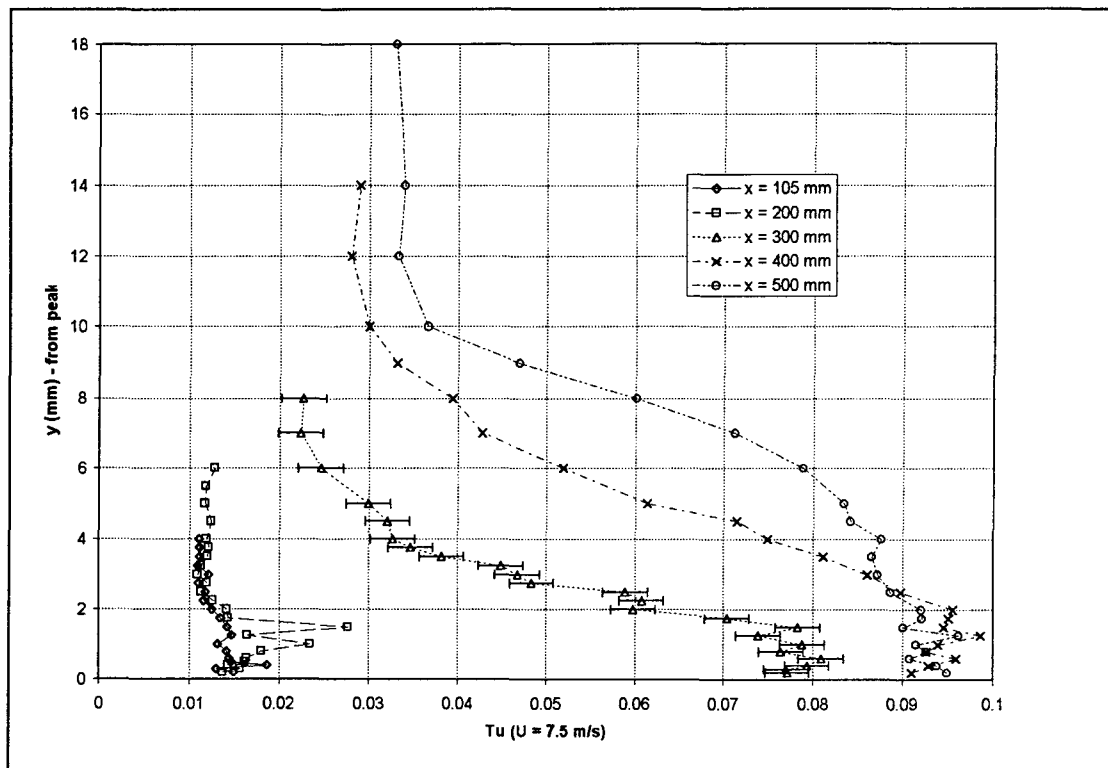


Figure 107.  $Tu$  vs.  $y$ : Flat/Ribletted,  $U = 7.5$  m/s, Riblet Peak.

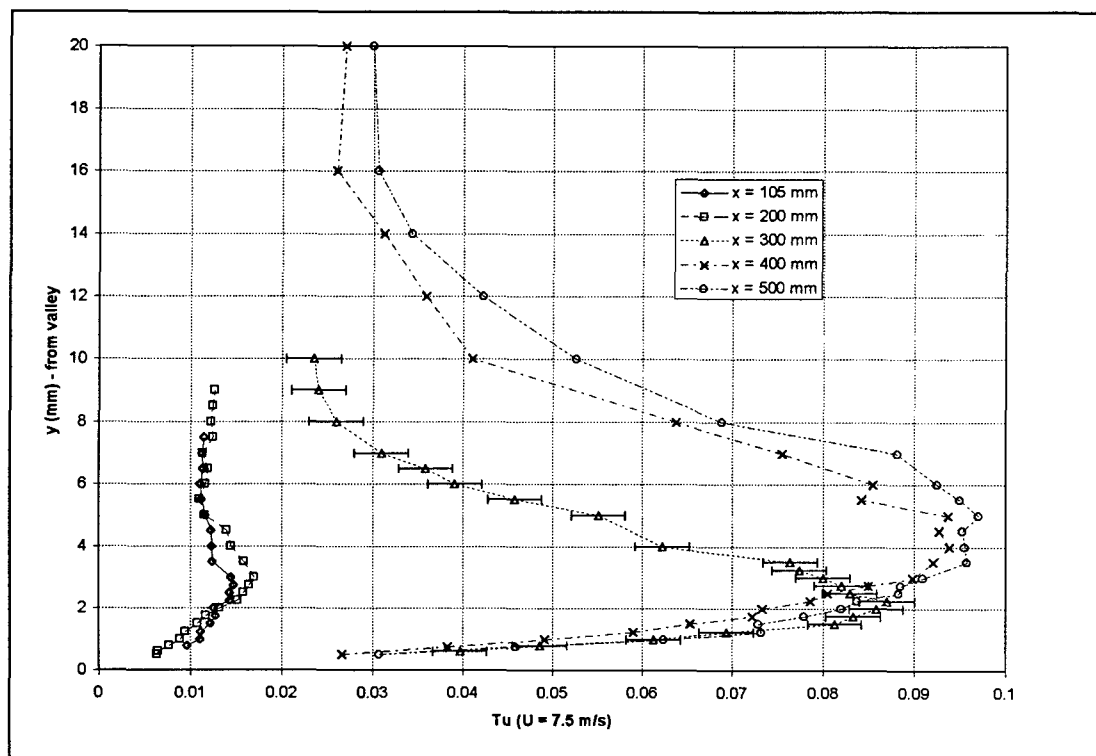


Figure 108.  $Tu$  vs.  $y$ : Flat/Ribletted,  $U = 7.5$  m/s, Riblet Valley.



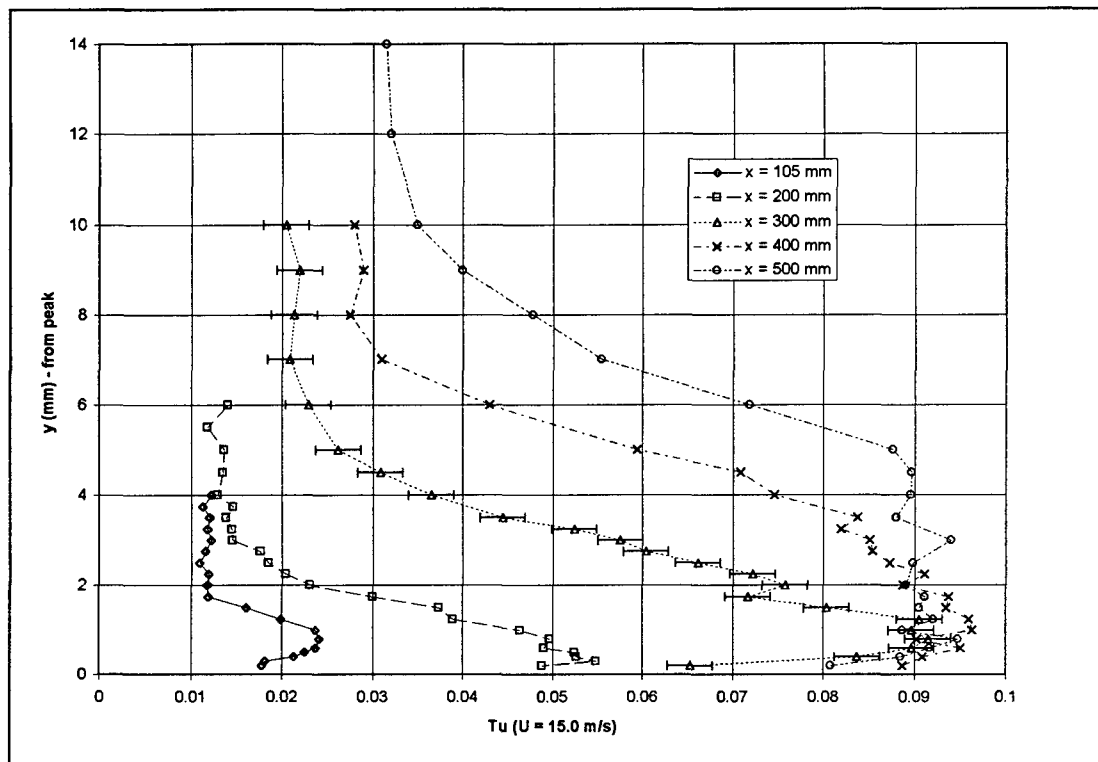


Figure 109.  $Tu$  vs.  $y$ : Flat/Ribletted,  $U = 15.0$  m/s, Riblet Peak.

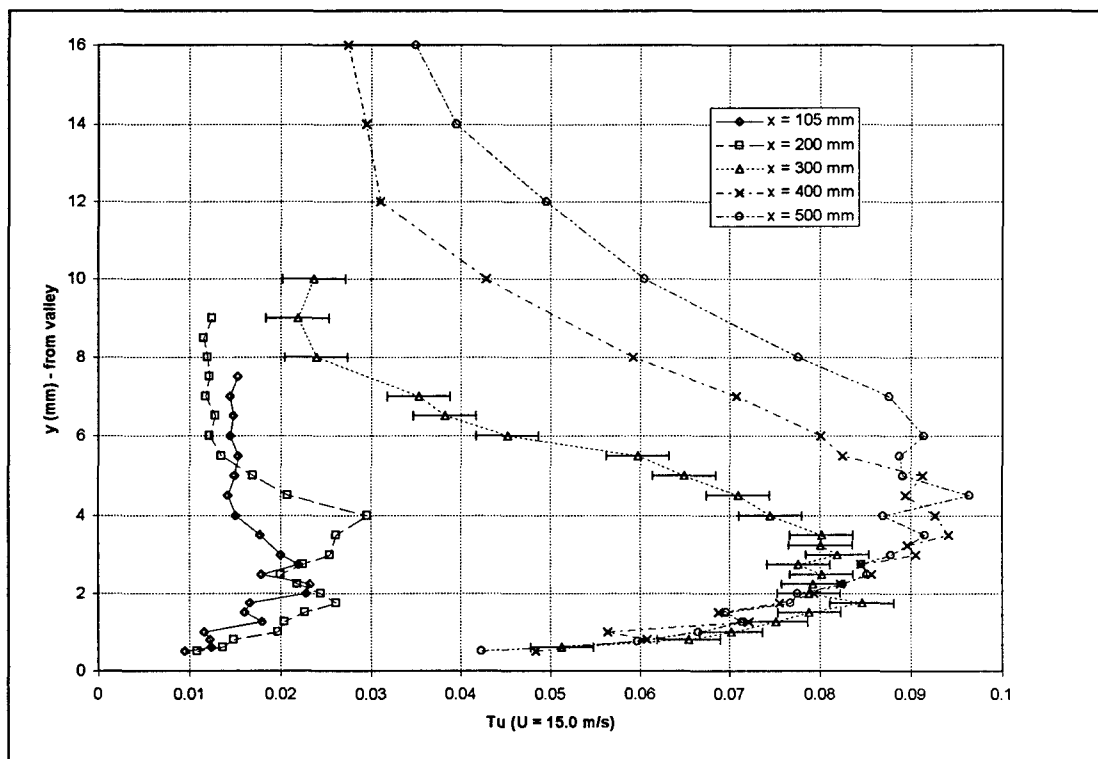


Figure 110.  $Tu$  vs.  $y$ : Flat/Ribletted,  $U = 15.0$  m/s, Riblet Valley.

# Curved/Ribletted Plate.

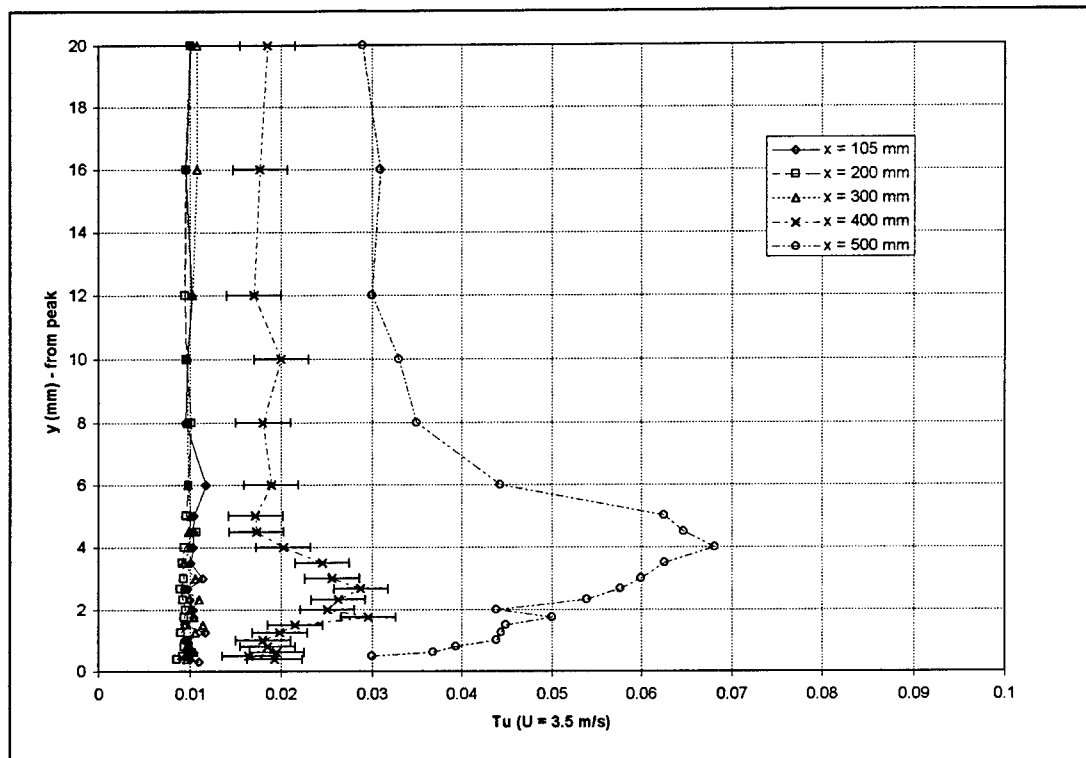


Figure 111. Tu vs. y: Curved/Ribletted, U = 3.5 m/s, Riblet Peak.

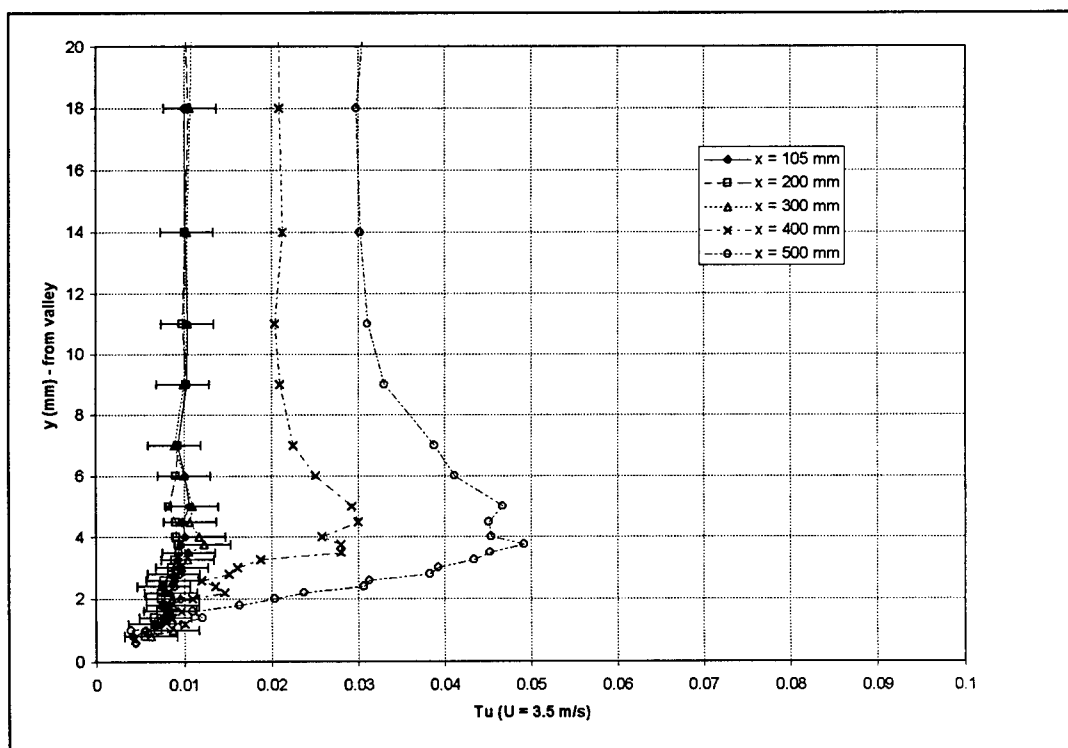


Figure 112. Tu vs. y: Curved/Ribletted, U = 3.5 m/s, Riblet Valley.

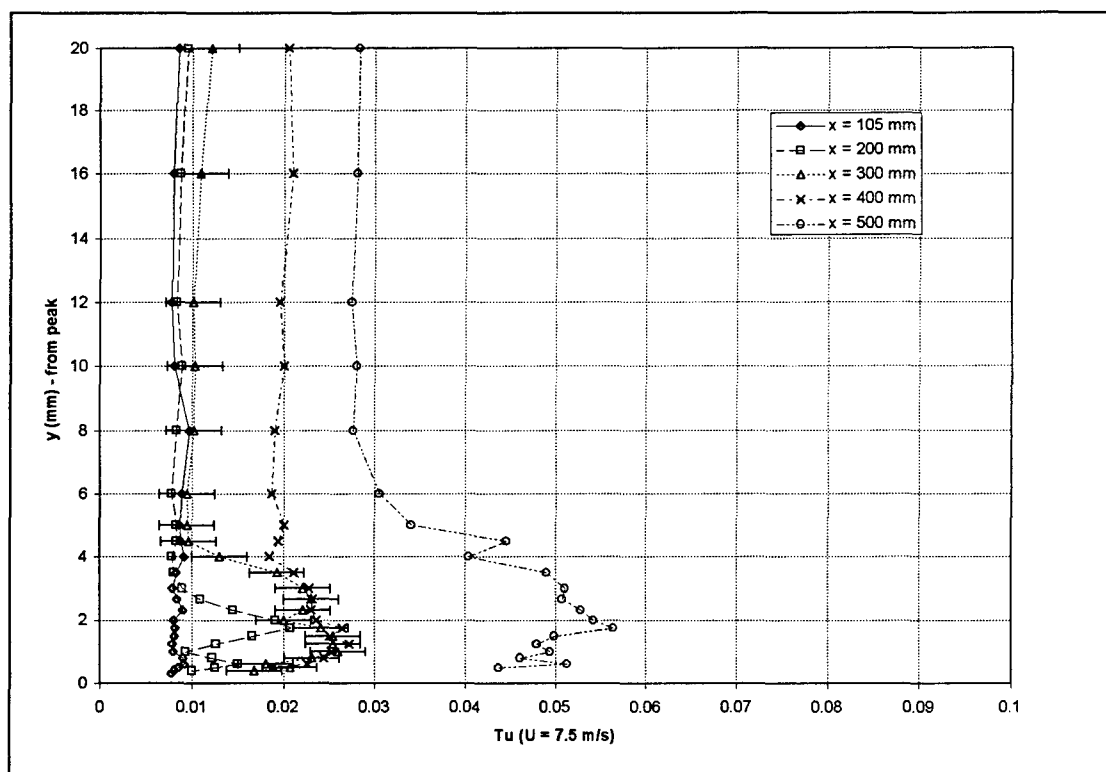


Figure 113.  $Tu$  vs.  $y$ : Curved/Ribletted,  $U = 7.5$  m/s, Riblet Peak.

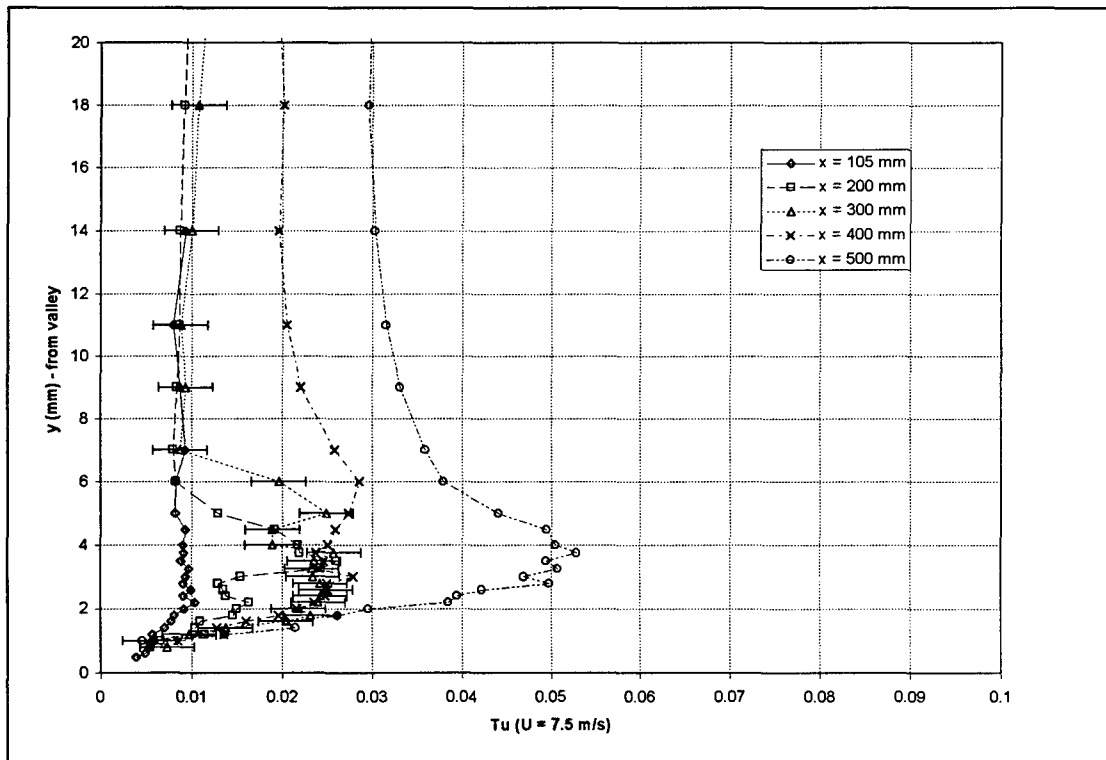


Figure 114.  $Tu$  vs.  $y$ : Curved/Ribletted,  $U = 7.5$  m/s, Riblet Valley.

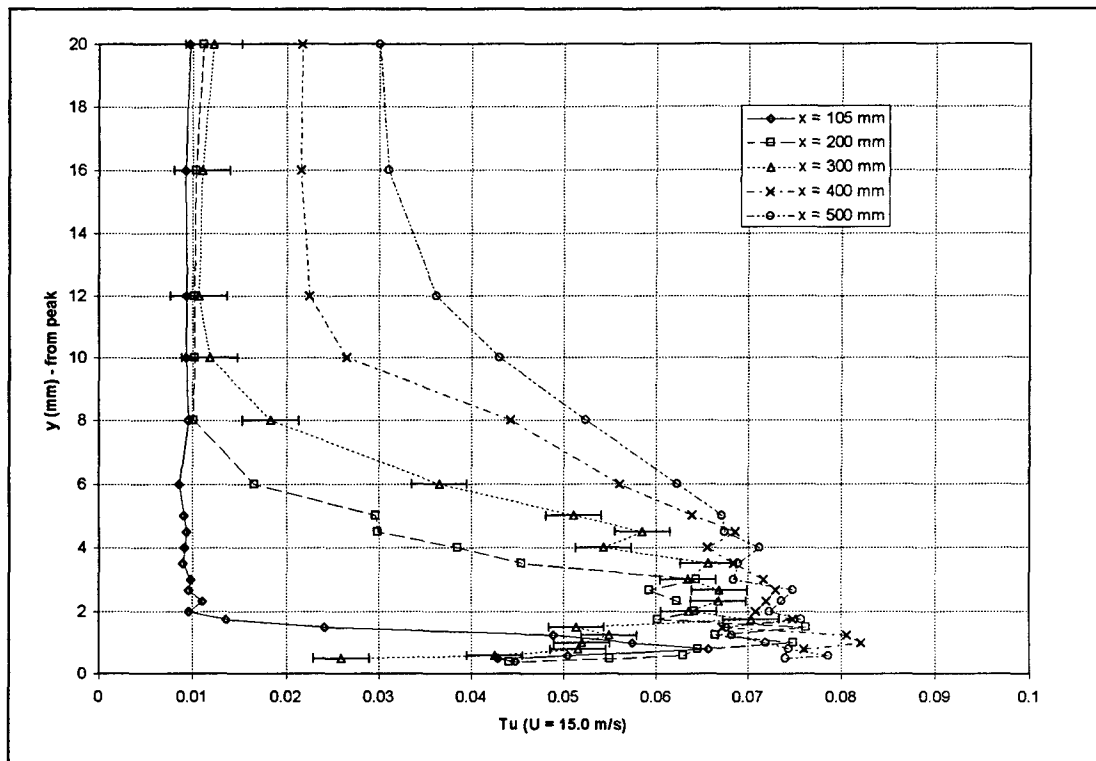


Figure 115. Tu vs. y: Curved/Ribletted,  $U = 15.0$  m/s, Riblet Peak.

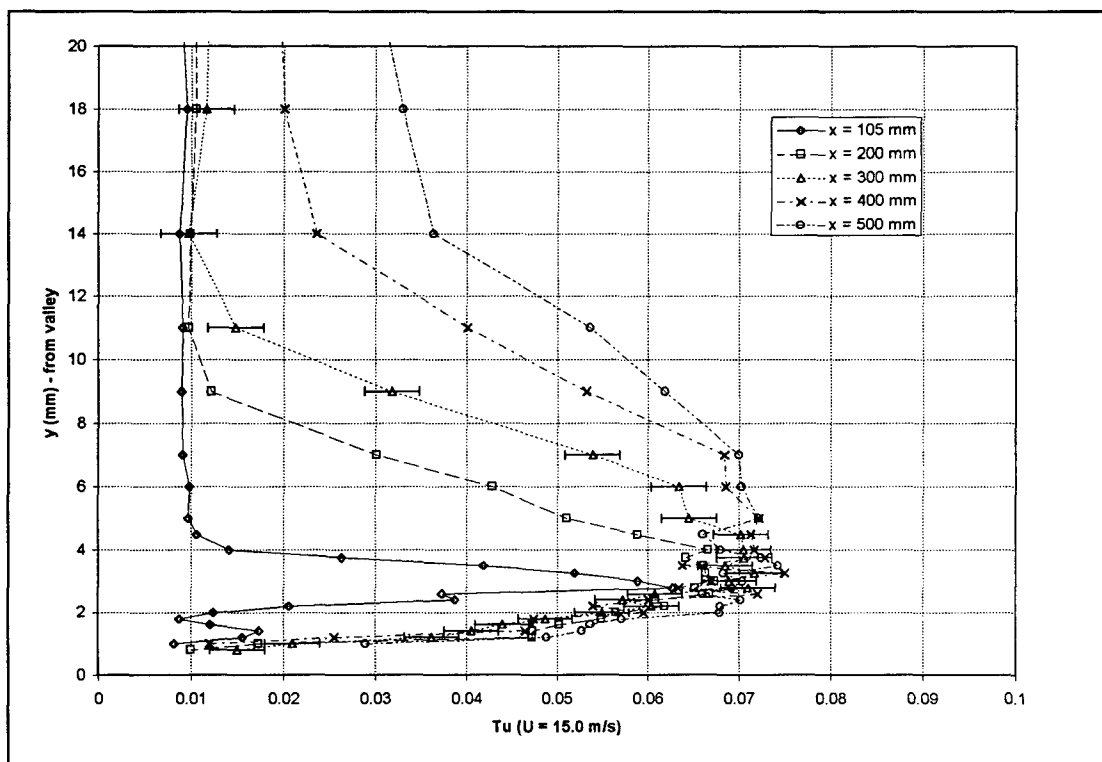


Figure 116. Tu vs. y: Curved/Ribletted,  $U = 15.0$  m/s, Riblet Valley.

## Appendix F. Boundary Layer Velocity Profiles

### Curved/Smooth Plate.

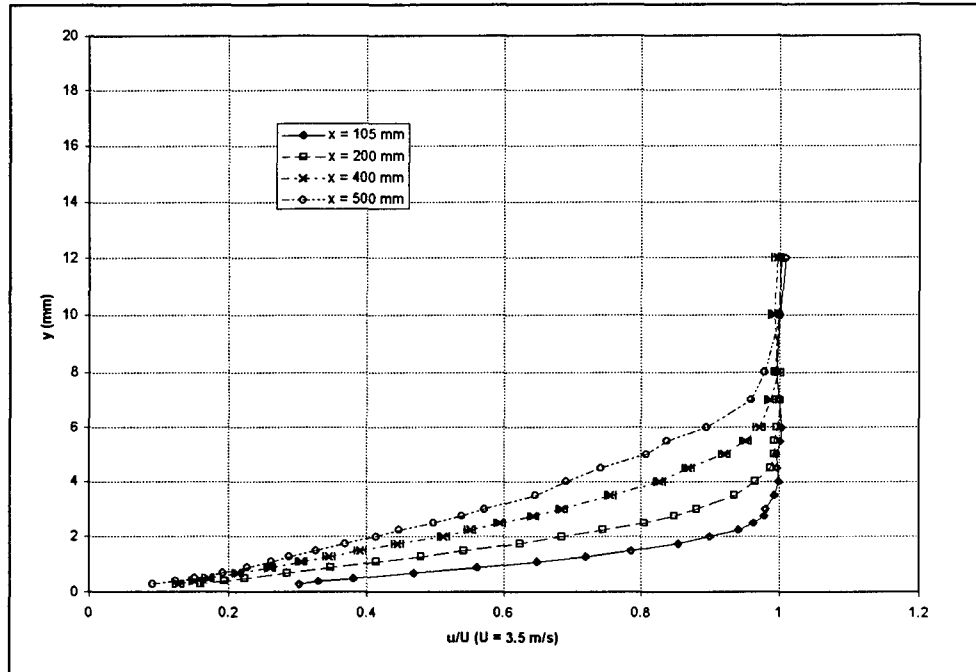


Figure 117.  $u$  vs.  $y$ : Curved//Smooth,  $U = 3.5$  m/s.

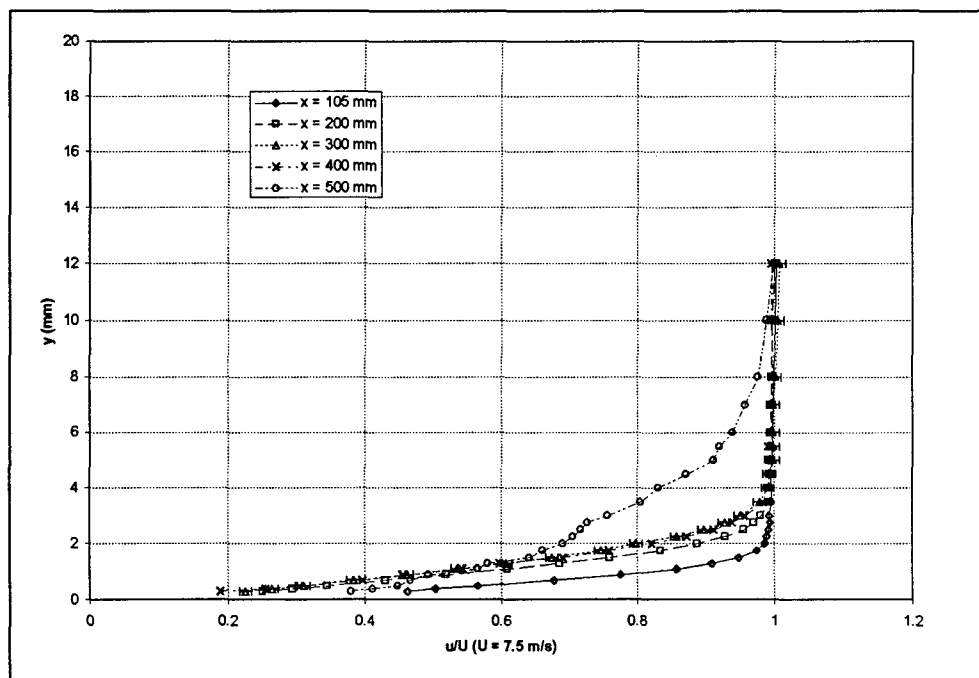


Figure 118.  $u$  vs.  $y$ : Curved/Smooth,  $U = 7.5$  m/s.

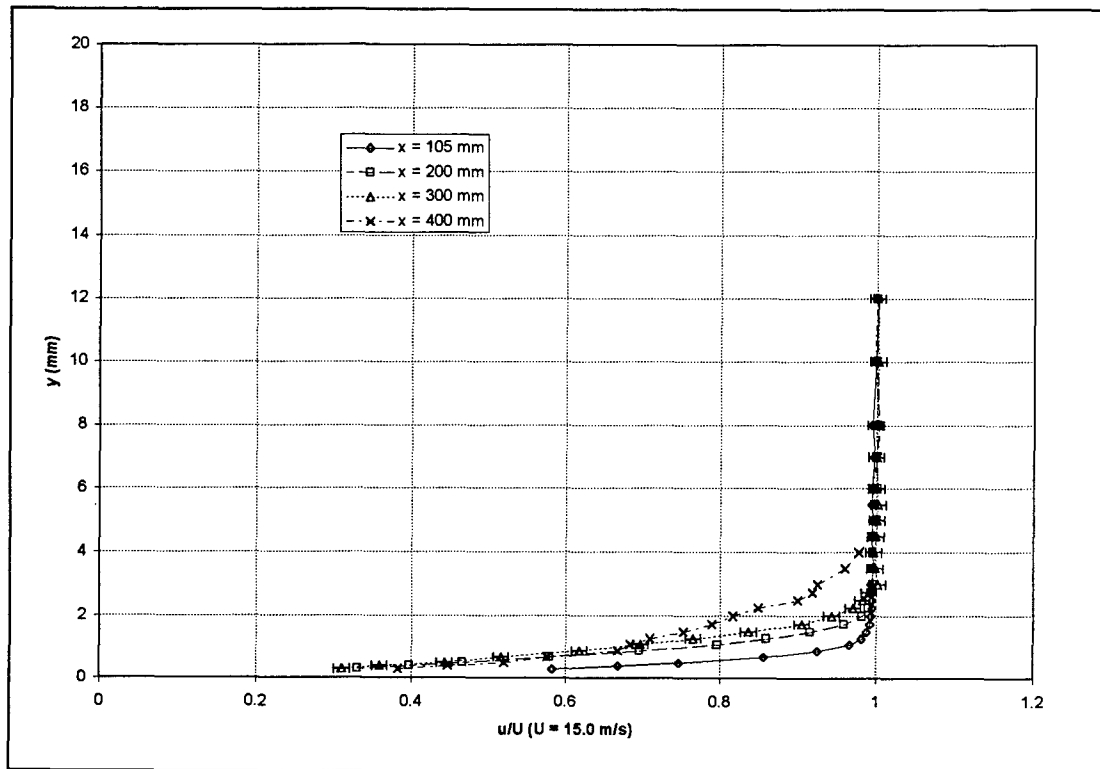


Figure 119.  $u$  vs.  $y$ : Curved/Smooth,  $U = 15.0$  m/s.

# Flat/Ribletted Plate.

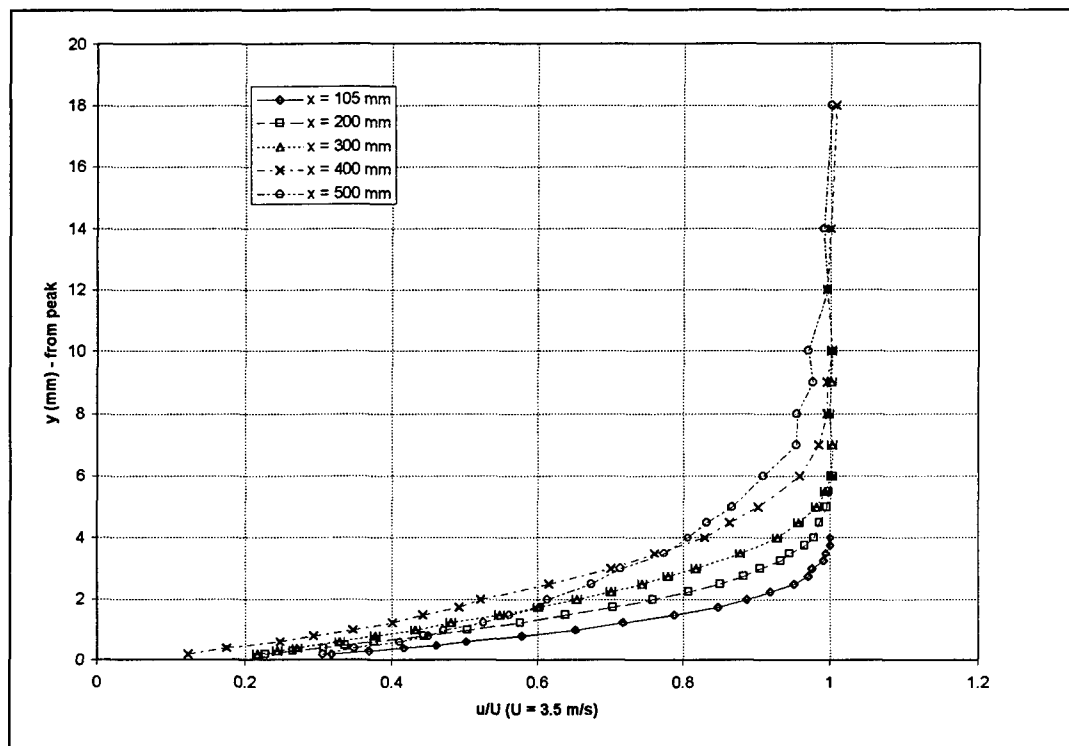


Figure 120.  $u$  vs.  $y$ : Flat/Ribletted,  $U = 3.5$  m/s, Riblet Peak.

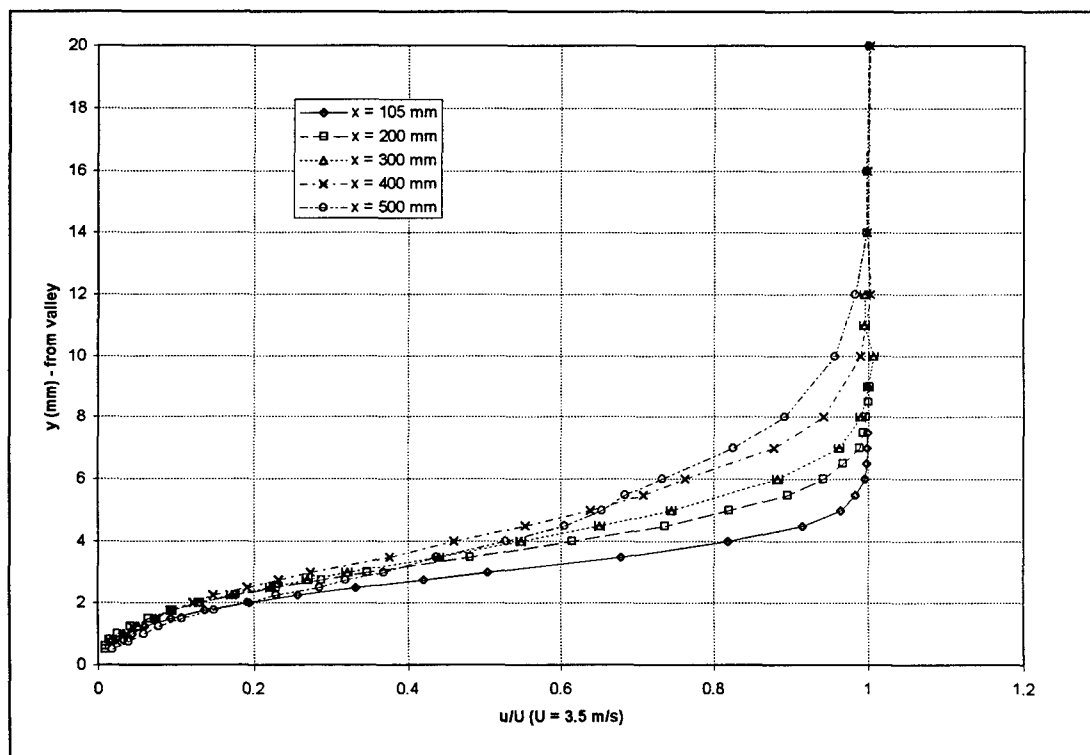


Figure 121.  $u$  vs.  $y$ : Flat/Ribletted,  $U = 3.5$  m/s, Riblet Valley.

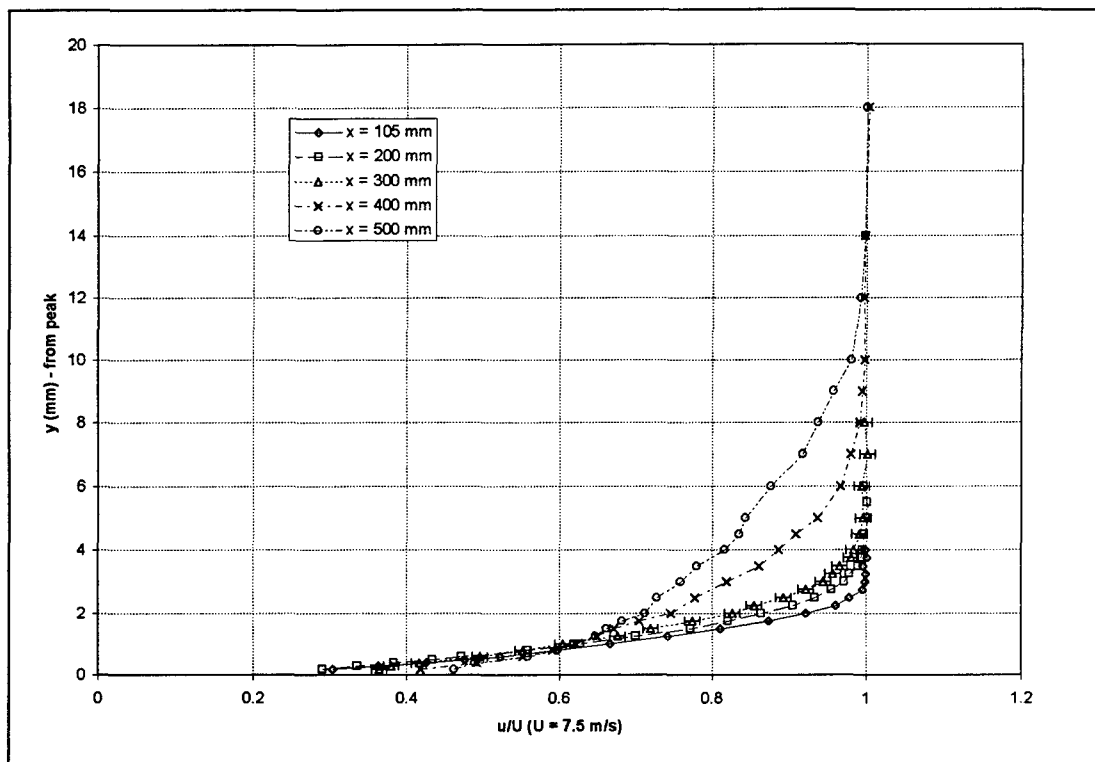


Figure 122.  $u$  vs.  $y$ : Flat/Ribletted,  $U = 7.5$  m/s, Riblet Peak.

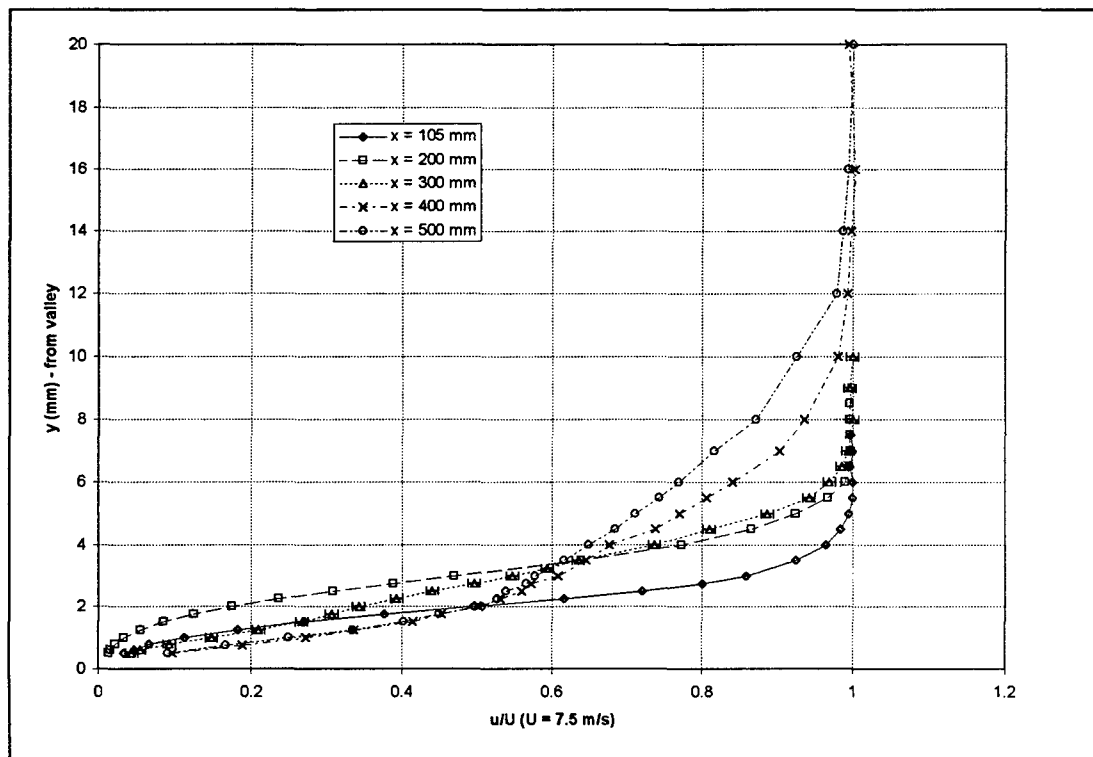


Figure 123.  $u$  vs.  $y$ : Flat/Ribletted,  $U = 7.5$  m/s, Riblet Valley.



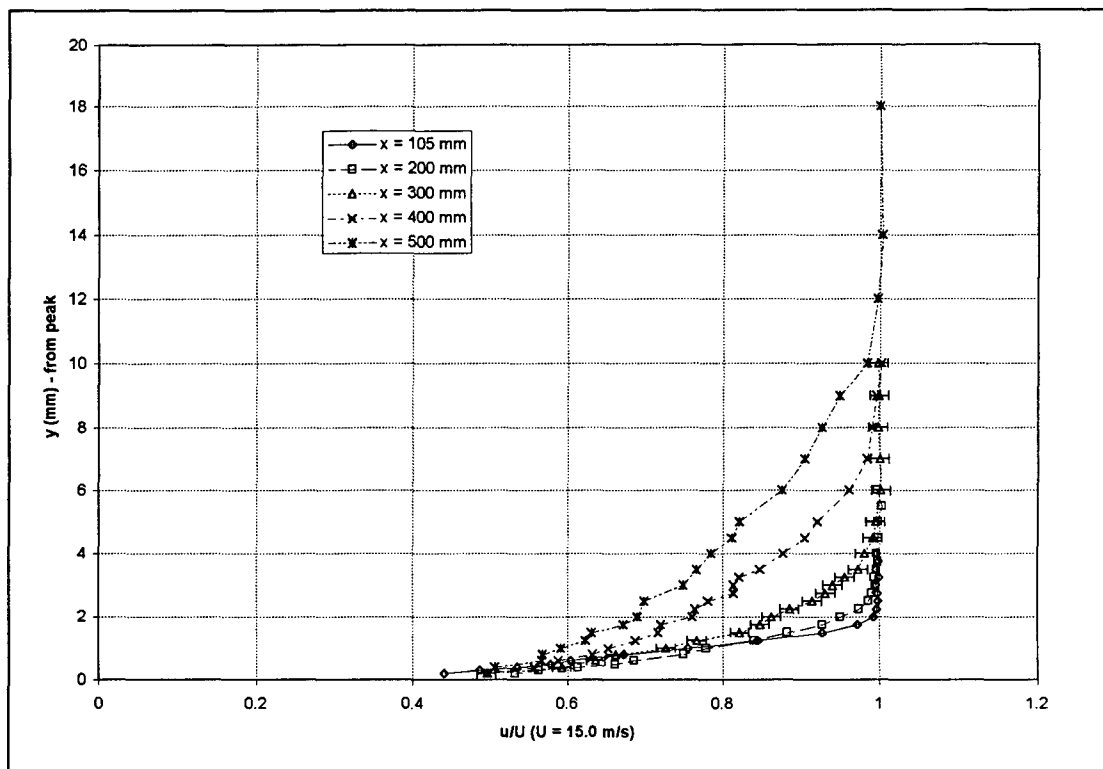


Figure 124.  $u$  vs.  $y$ : Flat/Ribletted,  $U = 15.0$  m/s, Riblet Peak.

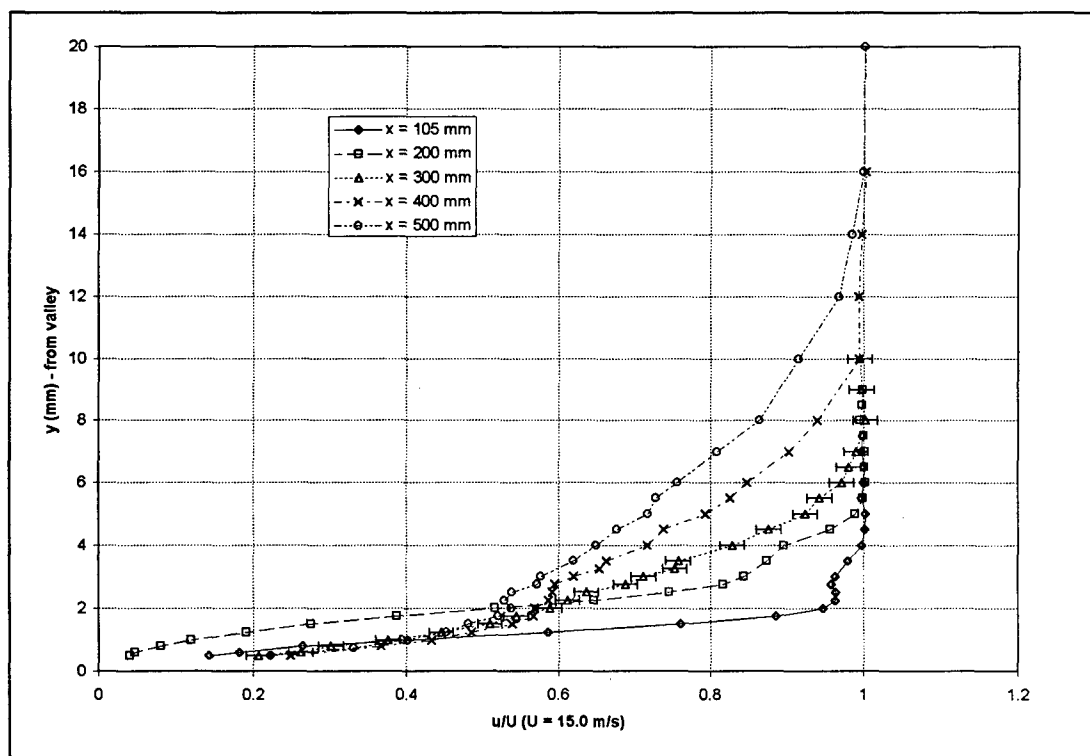


Figure 125.  $u$  vs.  $y$ : Flat/Ribletted,  $U = 15.0$  m/s, Riblet Valley.

# Curved/Ribletted Plate.

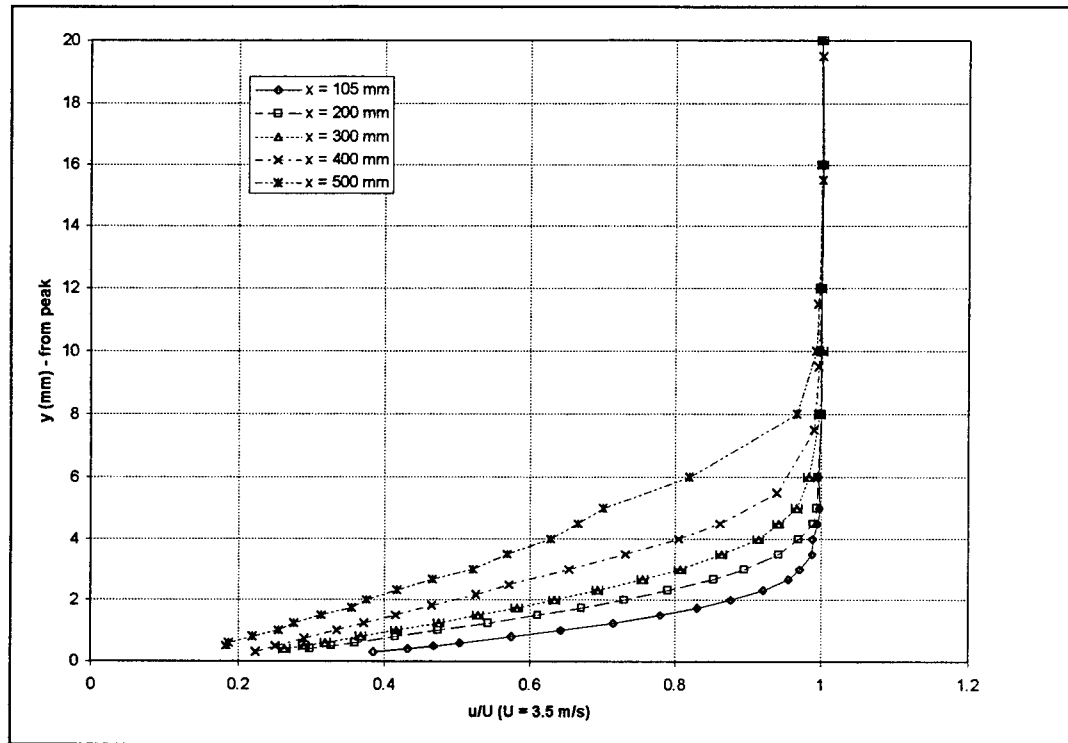


Figure 126.  $u$  vs.  $y$ : Curved/Ribletted,  $U = 3.5$  m/s, Riblet Peak.

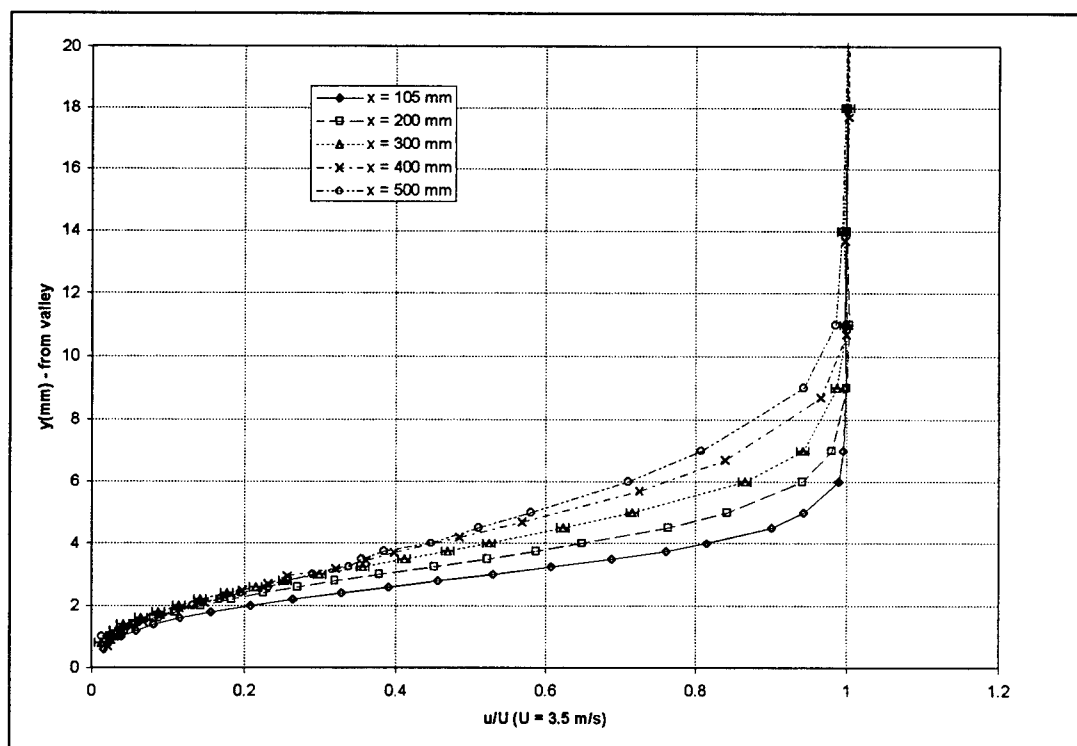


Figure 127.  $u$  vs.  $y$ : Curved/Ribletted,  $U = 3.5$  m/s, Riblet Valley.

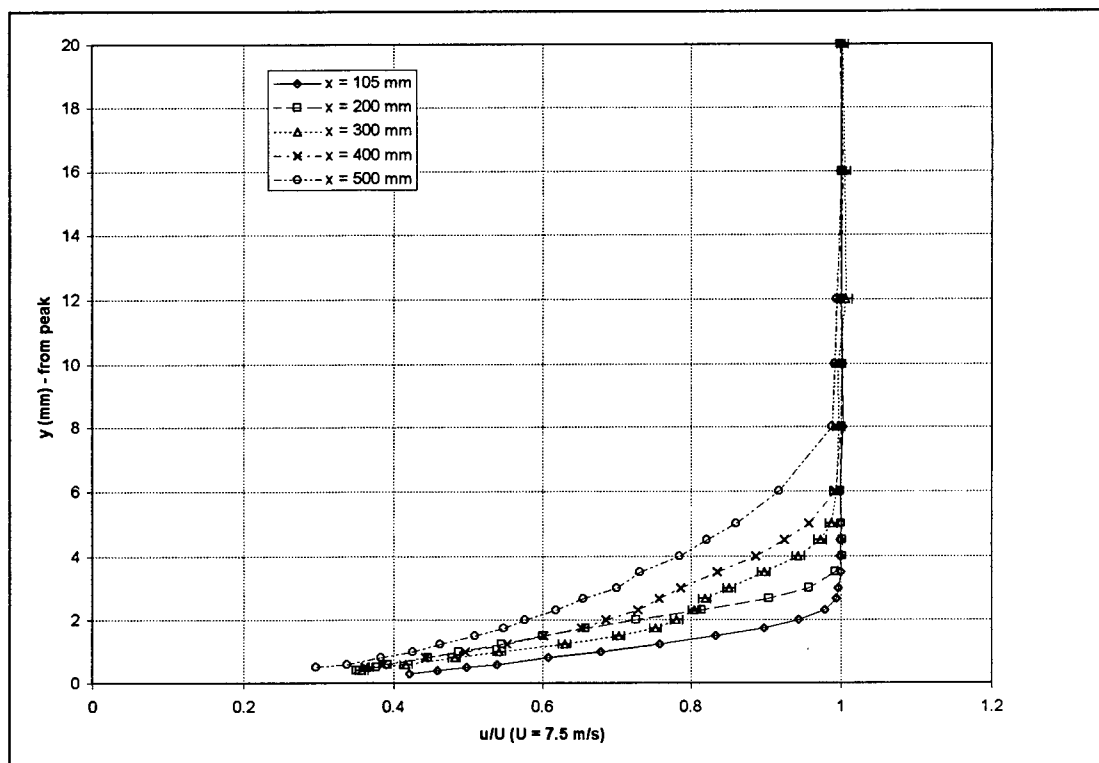


Figure 128.  $u$  vs.  $y$ : Curved/Ribletted,  $U = 7.5$  m/s, Riblet Peak.

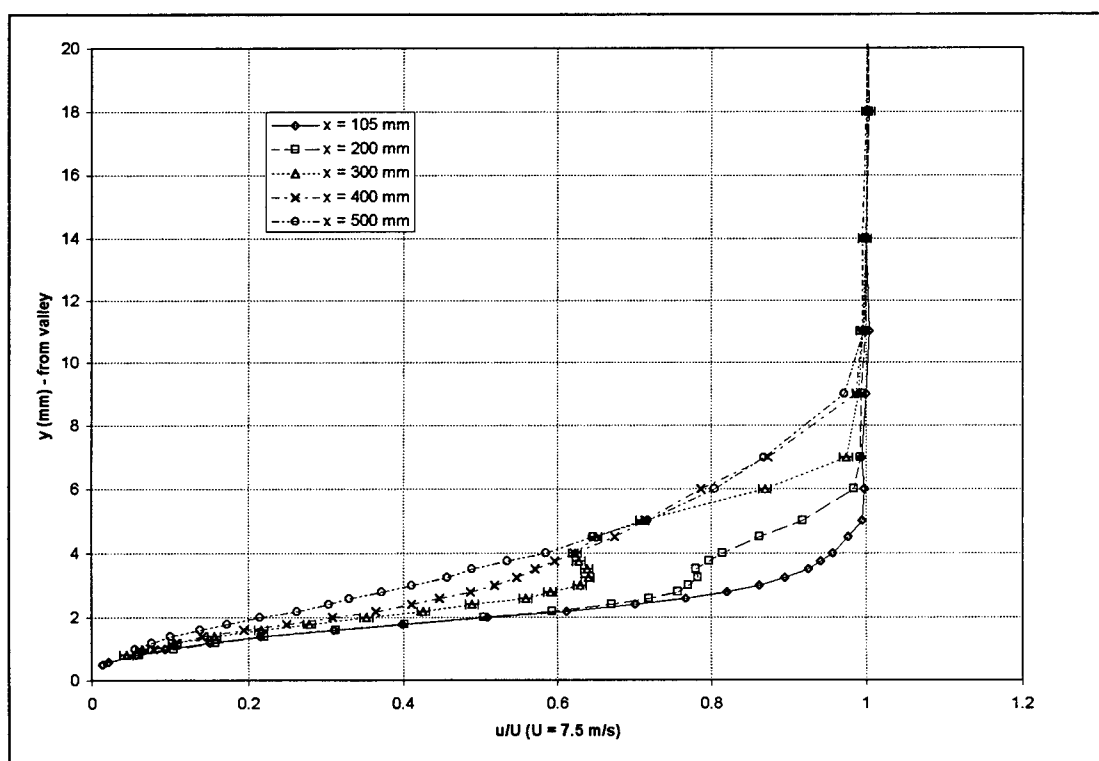


Figure 129.  $u$  vs.  $y$ : Curved/Ribletted,  $U = 7.5$  m/s, Riblet Valley.

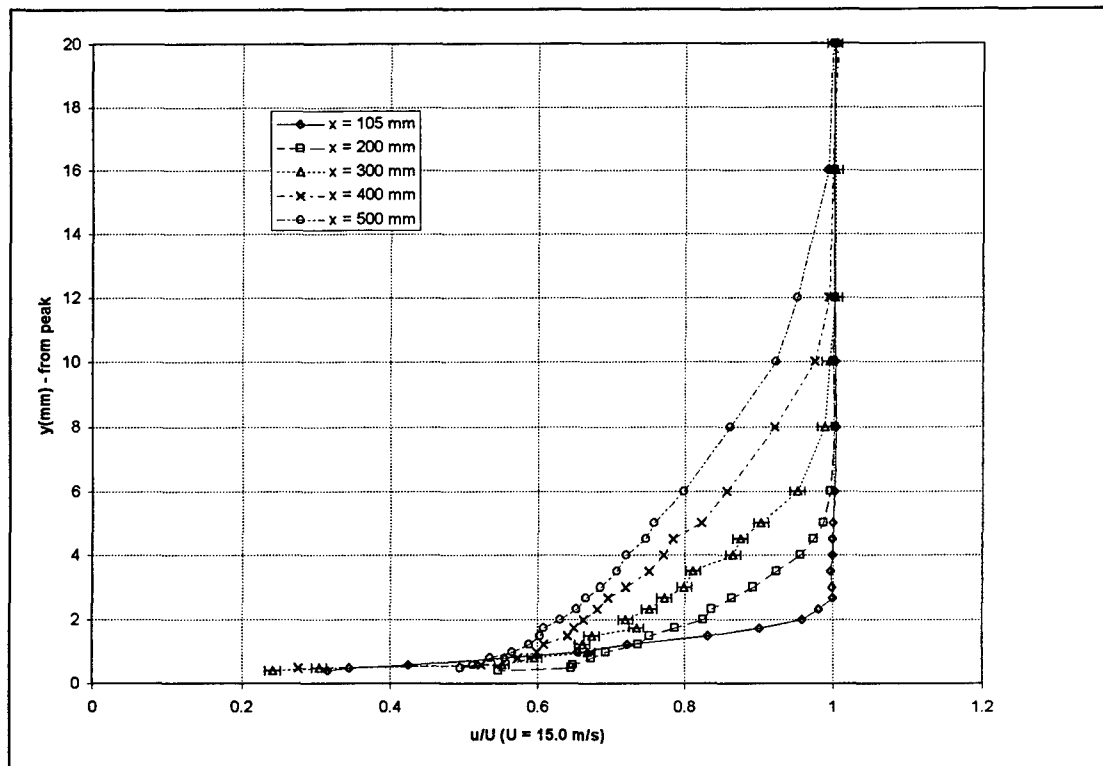


Figure 130.  $u$  vs.  $y$ : Curved/Ribletted,  $U = 15.0$  m/s, Riblet Peak.

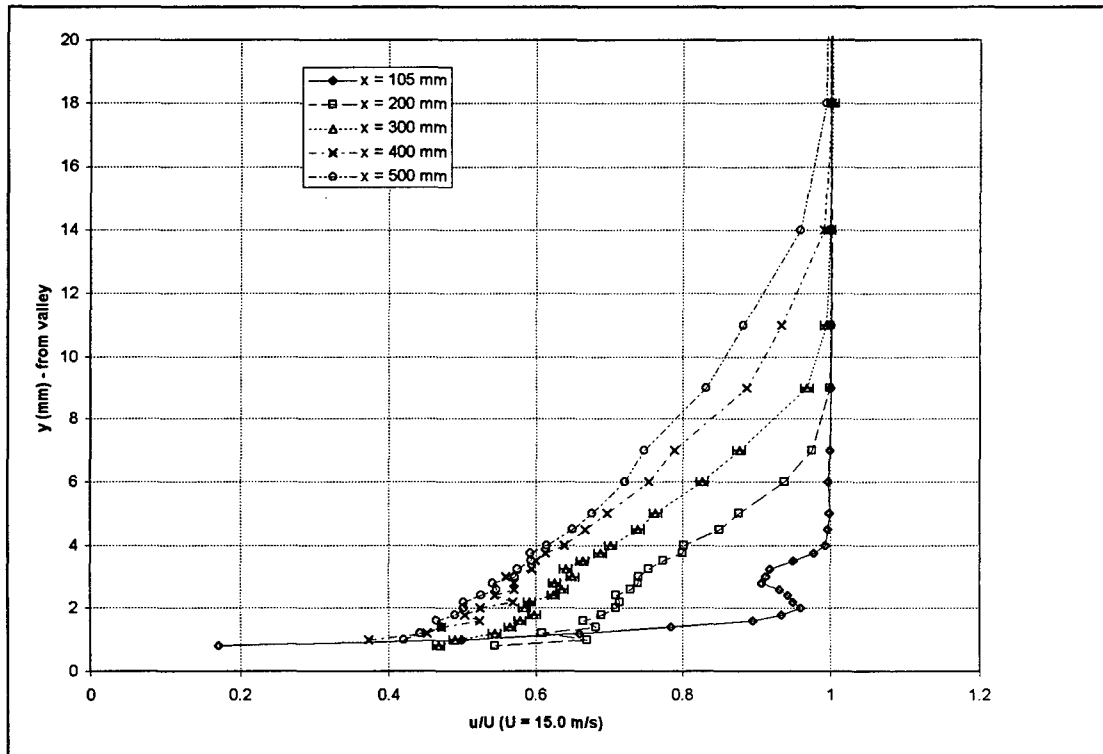


Figure 131.  $u$  vs.  $y$ : Curved/Ribletted,  $U = 15.0$  m/s, Riblet Valley.

---

Vita

Captain James Andrew Rothenflue [REDACTED]

[REDACTED] Upon graduation from Bryan Adams High School in Dallas, Texas, he attended the University of Texas at Arlington where he earned a Bachelor of Science in Aerospace Engineering in 1987. He entered the Air Force under the College Senior Engineering Program and received his commission from the Air Force Officer Training School at Lackland Air Force Base, Texas in 1987. He was assigned to the Foreign Technology Division at Wright-Patterson Air Force Base as an Astronautical Systems Analyst until 1990.

Captain Rothenflue was assigned to the Air Force Institute of Technology (AFIT) at Wright-Patterson Air Force Base in 1990, and completed his Masters degree in Aeronautical Engineering in 1991. He remained at AFIT under the Continuing Scholars Program in order to earn a Ph.D. in Aeronautical Engineering.

[REDACTED]

REPORT DOCUMENTATION PAGE			Form Approved OMB No. 0704-0188	
Public reporting burden for this collection of information is estimated to average 1 hour per response, including the time for reviewing instructions, searching existing data sources, gathering and maintaining the data needed, and completing and reviewing the collection of information. Send comments regarding this burden estimate or any other aspect of this collection of information, including suggestions for reducing this burden, to Washington Headquarters Services, Directorate for Information Operations and Reports, 1215 Jefferson Davis Highway, Suite 1204, Arlington, VA 22202-4302, and to the Office of Management and Budget, Paperwork Reduction Project (0704-0188), Washington, DC 20503.				
1. AGENCY USE ONLY (Leave blank)	2. REPORT DATE February 1996	3. REPORT TYPE AND DATES COVERED Doctoral Dissertation		
4. TITLE AND SUBTITLE  RIBLET EFFECTS ON GÖRTLER VORTEX DEVELOPMENT OVER A CONCAVE SURFACE		5. FUNDING NUMBERS		
6. AUTHOR(S)  James A. Rothenflue, Captain, USAF				
7. PERFORMING ORGANIZATION NAME(S) AND ADDRESS(ES)  Air Force Institute of Technology (AFIT) 2950 P St. Wright-Patterson AFB, OH 45433		8. PERFORMING ORGANIZATION REPORT NUMBER  AFIT/DS/ENY/96-4		
9. SPONSORING / MONITORING AGENCY NAME(S) AND ADDRESS(ES)  Air Force Phillips Laboratory (PL) 3550 Aberdeen Ave. S.E. Kirtland AFB, NM 87117		10. SPONSORING / MONITORING AGENCY REPORT NUMBER		
11. SUPPLEMENTARY NOTES				
12a. DISTRIBUTION / AVAILABILITY STATEMENT  Approved for Public Release; distribution unlimited			12b. DISTRIBUTION CODE	
13. ABSTRACT (Maximum 200 words)  Riblet effects on Görtler vortex development in laminar and transitional flows were measured using three-dimensional laser-Doppler anemometry. Three freestream velocities were tested such that riblet spacing corresponded to Görtler vortex (GV) wavelengths which presumably would be either strongly amplified, weakly amplified, or attenuated by centrifugal forces on a curved surface. Experiments revealed the development of paired, counterrotating vortices within the riblet valleys over both flat and concave surfaces. For riblet spacings equivalent to weakly or non-amplified GV wavelengths, GV development on a curved surface was above the riblets and was delayed by the addition of riblets. The GV wavelength was larger than the riblet spacing, but was approximately the same as for the smooth surface. For the strongly amplified case, streamwise vorticity developed earlier than for the smooth plate and was confined to paired, counterrotating, riblet-valley vortices with wavelength equal to the riblet spacing. Boundary layer transition was accelerated by the addition of riblets to the curved surface for the strongly amplified case, but was delayed for the other two cases. Thus, riblets with spacing equal to strongly amplified GV wavelengths accelerate boundary layer transition; whereas, riblet spacings equal to smaller, less strongly amplified or attenuated GV wavelengths delay transition. Surface skin friction was increased in all test cases by the addition of riblets.				
14. SUBJECT TERMS  Riblets, Görtler Vortices, boundary layer transition, centrifugal instability, concave surface			15. NUMBER OF PAGES 187	
			16. PRICE CODE	
17. SECURITY CLASSIFICATION OF REPORT Unclassified	18. SECURITY CLASSIFICATION OF THIS PAGE Unclassified	19. SECURITY CLASSIFICATION OF ABSTRACT Unclassified	20. LIMITATION OF ABSTRACT  UL	